

**METAGENOMIC AND
GEOCHEMICAL
CHARACTERISATION OF
MICROBIALLY INFLUENCED
CORROSION IN MARINE STEEL
PILING**

Richard Peter Brennan

A thesis submitted in partial fulfilment of the requirements
of the University of Brighton for the degree of
Doctor of Philosophy

May 2021

University of Brighton

ABSTRACT

Microbially influenced corrosion (MIC) of marine steel piling is a globally phenomenon that carries with it a financial and safety burden for the operators of harbours and ports. It has been observed to drastically reduce the service life of marine infrastructure and in extreme cases has resulted in collapse of quaysides. Despite this, it is not extensively researched, and those studies that have been conducted concentrate on the specialised form of marine MIC known as ‘accelerated low water corrosion’ (ALWC).

This study aimed to take a broader approach than other studies by identify the microbial and mineralogical composition of corrosion taken from several locations on a section of marine steel piling, rather than solely within the ‘ALWC’ region, and to contextualise these with data obtained from the surrounding environment. The sampling site was situated within an active port facility on the south coast of England. Corrosion, marine sediment, and seawater samples were all extracted from a tidal location within the port. X-ray powder diffraction, Fourier-transform infrared and inductively coupled plasma optical emission spectrometry were employed alongside GeoChip functional gene array, denaturing gradient gel electrophoresis, and high-resolution melt analysis to analyse the environmental samples, and seawater conditions monitored via a site-installed sonde.

The data obtained allowed construction of a model to explain the presence of microbes within marine corrosion formations. Diversity and cluster analysis of environmental samples revealed a strong link between key microbial groups in marine sediment and corrosion, with seawater providing a lesser influence. Turbidity measurements provided evidence for periodic exposure of corrosion formations to significant levels of re-suspended marine sediment. Analysis of fifteen functional genes identified 116 microbial genera of prokaryote linked to MIC. Comprising eight microbial groups, these indicated the microbial diversity within MIC formations and demonstrated the microbial continuity that exists between MIC in different environments.

Mineralogical, chemical and gene analysis of a vertical section of carbon steel piling discerned regions in which MIC was active and regions of normal water corrosion. MIC was found to be characterised by the presence of reduced sulfur species as well as the mineral maghemite, whereas normal water corrosion was characterised by the minerals

akaganeite and hematite, and chloride green rust. As well as a clearly defined mineralogy, the microbial communities in the corrosion formed clusters of similar genetic composition in line with the mineral groups. It was confirmed that the region of piling affected by MIC was not limited to the low water region but extended throughout the intertidal zone, from the sediment bed up to mean tide level.

CONTENTS

ABSTRACT	ii
LIST OF FIGURES	x
LIST OF TABLES	xvi
LIST OF ABBREVIATIONS	xvii
ACKNOWLEDGEMENTS.....	xxi
DECLARATION.....	xxii
Chapter 1 Introduction	1
1.1 Microbially influenced corrosion.....	1
1.2 Research aims	2
1.3 Research objectives.....	2
1.4 Thesis structure	2
Chapter 2 Literature Review	4
2.1 Mechanisms of Microbially influenced corrosion	4
2.2 Microbial groups and genera associated with MIC	6
2.3 Functional genes associated with MIC	12
2.4 Biofilms	16
2.5 Corrosion in marine steel piling.....	18
2.5.1 Introduction to piling in harbours and ports	18
2.5.2 Design and construction of modern steel piling	19
2.5.3 Normal Water Corrosion: formation and mineralogy	20

2.5.4	Normal Water Corrosion profiles in steel piling	26
2.5.5	Microbially influenced corrosion profiles in steel piling	28
2.5.6	Microbially influenced corrosion: structure and mineralogy	29
2.6	Global distribution and financial implications of marine MIC.....	32
2.7	Corrosion control	33
2.7.1	Alternative materials.....	34
2.7.2	Cathodic protection.....	35
2.7.2.1	Sacrificial anode.....	35
2.7.2.2	Impressed current	35
2.7.3	Anodic Protection	37
2.7.4	Biocide treatment.....	37
2.7.5	Protective coatings.....	38
2.8	Techniques in microbial influenced corrosion research	39
2.8.1	Functional gene analysis by GeoChip microarray	39
2.8.2	Functional gene analysis by Next Generation Sequencing	40
2.8.3	Genetic diversity analysis using High-resolution melt.....	43
2.8.4	Genetic diversity analysis using Denaturing gradient gel electrophoresis	44
2.8.5	X-ray powder diffraction	45
2.8.6	Fourier-transform infrared.....	46
2.8.7	Inductively coupled plasma optical emission spectrometry	47

2.9	Summary	47
Chapter 3	Methodology.....	49
3.1	Field work	49
3.1.1	Overview of sampling site	49
3.1.2	Seawater monitoring	52
3.1.3	Corrosion sampling.....	53
3.1.4	Marine sediment sampling.....	55
3.1.5	Seawater sampling	56
3.2	Laboratory analysis.....	58
3.2.1	Laboratory Work Overview.....	58
3.2.2	Functional gene analysis using GeoChip.....	59
3.2.3	Genetic diversity analysis (High-resolution melt).....	62
3.2.4	Genetic diversity analysis (Denaturing gradient gel electrophoresis).....	64
3.2.5	Mineralogical analysis	67
3.2.6	Chemical analysis (Fourier-transform infrared spectroscopy)	68
3.2.7	Chemical analysis (Inductively coupled plasma optical emission spectrometry)	68
Chapter 4	Tidal range and turbidity analysis.....	71
4.1	Tidal data	71
4.2	Turbidity data.....	77
4.3	Summary	84

Chapter 5	Spectroscopic analysis of marine sediment using inductively coupled plasma optical emission spectrometry and X-ray powder diffraction	85
5.1	Inductively coupled plasma optical emission spectrometry of sediment pore water and marine sediment	85
5.2	X-ray powder diffraction analysis of marine sediment	88
5.3	Summary	90
Chapter 6	Functional gene analysis using GeoChip microarray	91
6.1	Community diversity analysis of low tide zone corrosion, marine sediment, and seawater samples.....	91
6.2	Relative gene abundance in low tide zone corrosion, marine sediment, and seawater samples	94
6.3	Genetic similarity analysis of low tide zone corrosion, marine sediment, and seawater samples	101
6.3.1	<i>aprA</i> gene.....	101
6.3.2	<i>aprB</i> gene.....	101
6.3.3	<i>dsrA</i> gene	102
6.3.4	<i>dsrB</i> gene	102
6.3.5	<i>soxB</i> gene	102
6.3.6	<i>amoA</i> gene	103
6.3.7	<i>napA</i> gene	103
6.3.8	<i>narG</i> gene	103
6.3.9	<i>nirK</i> gene	104
6.3.10	<i>nirS</i> gene	104

6.3.11	<i>nrfA</i> gene.....	104
6.3.12	<i>fthfs</i> gene.....	104
6.3.13	<i>mcrA</i> gene	105
6.3.14	<i>iro</i> gene	105
6.3.15	<i>assA</i> gene	105
6.4	Taxonomy of low tide zone corrosion	113
6.5	Summary.....	130
Chapter 7 Genetic diversity analysis using denaturing gradient gel electrophoresis and high-resolution melt.....		132
7.1	Denaturing gradient gel electrophoresis and high-resolution melt analysis of low tide zone corrosion, marine sediment, and seawater	132
7.2	High-resolution melt analysis of vertical profile corrosion	138
7.2.1	Melt-curve for <i>aprA</i> gene	138
7.2.2	Melt curve for <i>dsrB</i> gene	139
7.2.3	Melt curve for <i>soxB</i> gene.....	140
7.2.4	Melt curve for <i>16S</i> gene.....	141
7.3	Summary.....	146
Chapter 8 Spectroscopic analysis of corrosion samples using X-ray powder diffraction 148		
8.1	Low tide zone corrosion	148
8.2	Vertical profile corrosion.....	153
8.3	Summary.....	159

Chapter 9	Spectroscopic analysis of corrosion samples using Fourier-transform infrared spectroscopy.....	160
9.1	Low tide zone corrosion	160
9.2	Vertical profile corrosion.....	167
9.3	Summary	179
Chapter 10	Project synthesis	180
10.1	Model for colonisation of carbon steel piling by microorganisms	180
10.2	Mineralogy and microbial diversity of vertical piling	188
Chapter 11	Conclusions and further work.....	196
	References.....	199
	Appendix A - Membrane filtration protocol.....	238
	Appendix B - MoBio PowerSoil protocol	239
	Appendix C - GeoChip methodology	241
	Appendix D - Alpha Diversity tests.....	242
	Appendix E - PCR primers	243
	Appendix F - PCR preparation	244
	Appendix G - Thermocycler protocols	245
	Appendix H - FTIR spectra (1650 cm ⁻¹ to 550 cm ⁻¹)	248

LIST OF FIGURES

Figure 2-1 Schematic representation of MIC mechanism via cathodic depolarisation	5
Figure 2-2 Schematic representation of MIC chemical pathways with associated microbial groups.....	15
Figure 2-3 Plan profiles of the two commonly used piling designs.....	19
Figure 2-4 Simple electrochemical corrosion cell	21
Figure 2-5 Abiotic corrosion pathways in carbon steel	25
Figure 2-6 Vertical zones on steel piling and typical NWC corrosion rates.....	28
Figure 2-7 MIC Tubercle	30
Figure 2-8 MIC formation without tubercle	30
Figure 3-1 Location of Shoreham Port within the British Isles	51
Figure 3-2 Arial view of Shoreham Port.....	52
Figure 3-3 Dredger Berth monitoring (A) and sampling (B) locations	52
Figure 3-4 Schematic diagram of steel piling at the Dredger Berth with vertical positions and height above the sediment bed of all corrosion samples	55
Figure 3-5 Corer head with extension tube	56
Figure 3-6 Sediment corer sleeve with Rhizon samplers fitted	70
Figure 4-1 Dredger Berth tidal data from 01/04/14 to 30/06/14.....	73
Figure 4-2 Dredger Berth tidal data from 01/07/14 to 30/09/14.....	73
Figure 4-3 Dredger Berth tidal data from 01/10/14 to 31/12/14.....	74
Figure 4-4 Dredger Berth tidal data from 01/01/15 to 31/03/15.....	74

Figure 4-5 Dredger Berth tidal data from 01/04/15 to 30/06/15	75
Figure 4-6 Dredger Berth tidal data from 01/07/15 to 30/09/15	75
Figure 4-7 Dredger Berth tidal data from 01/10/15 to 31/12/15	76
Figure 4-8 Dredger Berth tidal data from 01/01/16 to 24/03/16	76
Figure 4-9 Dredger Berth seawater turbidity data (0 to 100 FNU) from 01/04/14 to 30/06/14	79
Figure 4-10 Dredger Berth seawater turbidity data (0 to 100 FNU) from 01/07/14 to 30/09/14	79
Figure 4-11 Dredger Berth seawater turbidity data (0 to 100 FNU) from 01/10/14 to 31/12/14	80
Figure 4-12 Dredger Berth seawater turbidity data (0 to 100 FNU) from 01/01/15 to 31/03/15	80
Figure 4-13 Dredger Berth seawater turbidity data (0 to 100 FNU) from 01/04/15 to 30/06/15	81
Figure 4-14 Dredger Berth seawater turbidity data (0 to 100 FNU) from 01/07/15 to 30/09/15	81
Figure 4-15 Dredger Berth seawater turbidity data (0 to 100 FNU) from 01/10/15 to 31/12/15	82
Figure 4-16 Dredger Berth seawater turbidity data (0 to 100 FNU) from 01/01/16 to 24/03/16	82
Figure 4-17 Dredger Berth seawater turbidity seven day average	83
Figure 4-18 Dredger Berth seawater turbidity (between 0 and 4000 FNU)	83
Figure 4-19 Dredger Berth seawater turbidity (between 0 and 100 FNU)	83
Figure 5-1 Sediment pore water sulfate concentration vs depth	87

Figure 5-2 Sediment pore water iron concentration vs depth	87
Figure 5-3 Acid digested sediment sulfur concentration vs depth.....	87
Figure 5-4 Acid digested sediment iron vs depth.....	87
Figure 5-5 XRD diffractogram with identified minerals for marine sediment samples .	89
Figure 6-1 Diversity analysis of samples using Simpson Index	93
Figure 6-2 Diversity analysis of samples using Shannon-Wiener Index	93
Figure 6-3 Diversity analysis of samples using Shannon evenness.....	93
Figure 6-4 Median abundance of functional genes within microbial groups for corrosion samples C 14a, C 14b, and C 14c.....	97
Figure 6-5 Median abundance of functional genes within microbial groups for marine sediment samples SED 01, SED 02, and SED 03	98
Figure 6-6 Median abundance of functional genes within microbial groups for seawater samples SW 01, SW 02, and SW 03	99
Figure 6-7 Median abundance of functional genes within microbial groups for corrosion, marine sediment, and seawater samples	100
Figure 6-8 Similarity analysis of samples using <i>aprA</i> gene data.....	108
Figure 6-9 Similarity analysis of samples using <i>aprB</i> gene data.....	108
Figure 6-10 Similarity analysis of samples using <i>dsrA</i> gene data	108
Figure 6-11 Similarity analysis of samples using <i>dsrB</i> gene data	109
Figure 6-12 Similarity analysis of samples using <i>soxB</i> gene data	109
Figure 6-13 Similarity analysis of samples using <i>amoA</i> gene data.....	109
Figure 6-14 Similarity analysis of samples using <i>napA</i> gene data.....	110
Figure 6-15 Similarity analysis of samples using <i>narG</i> gene data.....	110

Figure 6-16 Similarity analysis of samples using <i>nirK</i> gene data.....	110
Figure 6-17 Similarity analysis of samples using <i>nirS</i> gene data	111
Figure 6-18 Similarity analysis of samples using <i>nrfA</i> gene data.....	111
Figure 6-19 Similarity analysis of samples using <i>fthfs</i> gene data	111
Figure 6-20 Similarity analysis of samples using <i>mcrA</i> gene data	112
Figure 6-21 Similarity analysis of samples using <i>iro</i> gene data	112
Figure 6-22 Similarity analysis of samples using <i>assA</i> gene data	112
Figure 7-1 DGGE gel image (<i>dsrB</i> PCR products from twelve environmental samples)	134
Figure 7-2 Similarity analysis of DGGE gel image (<i>dsrB</i> PCR products from twelve environmental samples)	134
Figure 7-3 HRM curves (<i>dsrB</i> gene PCR products for twelve environmental samples)	135
Figure 7-4 Similarity analysis of HRM data (<i>dsrB</i> gene PCR products for twelve environmental samples)	135
Figure 7-5 HRM curves for fifteen <i>aprA</i> amplicons.....	142
Figure 7-6 Similarity analysis of HRM curves for fifteen <i>aprA</i> amplicons.....	142
Figure 7-7 HRM curves for fifteen <i>dsrB</i> amplicons	143
Figure 7-8 Similarity analysis of HRM curves for fifteen <i>dsrB</i> amplicons	143
Figure 7-9 HRM curves for fifteen <i>soxB</i> amplicons	144
Figure 7-10 Similarity analysis of HRM curves for fifteen <i>soxB</i> amplicons.....	144
Figure 7-11 HRM curves for fifteen <i>16S</i> amplicons.....	145
Figure 7-12 Similarity analysis of HRM curves for fifteen <i>16S</i> amplicons.....	145

Figure 8-1 XRD diffractogram with identified peaks for corrosion samples C 14a, C 14b, and C 14c	151
Figure 8-2 XRD diffractogram with identified peaks for corrosion samples C 01 to C 15	156
Figure 9-1 FTIR spectra and deconvoluted peaks for corrosion samples C 14a, C 14b, and C 14c	165
Figure 9-2 FTIR spectra and deconvoluted peaks for corrosion samples C 01, C 02, and C 03	172
Figure 9-3 FTIR spectra and deconvoluted peaks for corrosion samples C 04, C 05, and C 06	173
Figure 9-4 FTIR spectra and deconvoluted peaks for corrosion samples C 07, C 08, and C 09	174
Figure 9-5 FTIR spectra and deconvoluted peaks for corrosion samples C 10, C 11, and C 12	175
Figure 9-6 FTIR spectra and deconvoluted peaks for corrosion samples C 13, C 14, and C 15	176
Figure 10-1 Diversity analysis summary for nine environmental samples ordered by decreasing diversity	181
Figure 10-2 Similarity analysis summary for nine environmental samples and fifteen functional genes with cluster references, based on dendrogram cluster data (75%+ similarity)	184
Figure 10-3 Similarity analysis summary for twelve environmental samples for <i>dsrB</i> gene, based on dendrogram cluster data (75%+ similarity)	184
Figure 10-4 Source-pathway-receptor model for colonisation of corrosion on steel piling face at the Dredger Berth, Shoreham Port	188

Figure 10-5 Schematic diagram of steel piling at the Dredger Berth with vertical positions of corrosion samples, tidal zones, and HRM dendrogram cluster data (75%+ similarity) for *aprA*, *dsrB*, *soxB*, and *16S* genes with cluster references 194

Figure 10-6 Schematic diagram of steel piling at the Dredger Berth with vertical positions of all corrosion samples, tidal zones, and characteristic minerals and chemical species, as determined by XRD and FTIR analysis 195

LIST OF TABLES

Table 2-1 Proposed mechanism for cathodic depolarisation	5
Table 2-2 Microorganism groups and selected genes associated with MIC	14
Table 3-1 Laboratory methodology summary.....	58
Table 6-1 Results of GeoChip 5.0 analysis of samples C 14a, 14b, and 14c,.....	123
Table 8-1 XRD peaks (a to o) with corresponding minerals and chemical compounds for corrosion samples C 14a, C 14b, and C 14c	152
Table 8-2 XRD peaks (p to ad) with corresponding minerals and chemical compounds for corrosion samples C 14a, C 14b, and C 14c.....	152
Table 8-3 XRD peaks (a to o) with corresponding minerals and chemical compounds for corrosion samples C 01 to C 15	157
Table 8-4 XRD peaks (p to ad) with corresponding minerals and chemical compounds for corrosion samples C 01 to C 15.....	158
Table 9-1 Deconvoluted FTIR peaks (A to O) with wavenumbers and corresponding minerals, compounds, and chemical species for corrosion samples C 14a, C 14b, and C 14c.....	166
Table 9-2 Deconvoluted FTIR peaks (P to AD) with wavenumbers and corresponding minerals, compounds, and chemical species for corrosion samples C 14a, C 14b, and C 14c.....	166
Table 9-3 Deconvoluted FTIR peaks (A to O) with wavenumbers and corresponding minerals, compounds, and chemical species for corrosion samples C 01 to C 15.....	177
Table 9-4 Deconvoluted FTIR peaks (P to AD) with wavenumbers and corresponding minerals, compounds, and chemical species for corrosion samples C 01 to C 15.....	178

LIST OF ABBREVIATIONS

<i>16S</i>	16S ribosomal ribonucleic acid gene
ALWC	Accelerated low water corrosion
<i>amoA</i>	Ammonia monooxygenase gene
AOB	Ammonia-oxidizing bacteria
AP*	Anodic protection
AP	Acetogenic prokaryotes
APB	Acid-producing bacteria
<i>aprA</i>	Adenylyl-sulfate reductase subunit A gene
APS	Adenosine 5' phosphosulfate
<i>assA</i>	Alkylsuccinate synthase gene
CD	Cathodic depolarisation
cDNA	complementary deoxyribonucleic acid
CMIC	Chemical microbially influenced corrosion
CP	Cathodic protection
CPIC	Cathodic protection by impressed current
CPSA	Cathodic protection by sacrificial anode
CTE	Coal tar epoxy
<i>cysJ</i>	Sulfite reductase flavoprotein alpha-component gene
DC	Direct current
DGGE	Denaturing gradient gel electrophoresis
DNA	Deoxyribonucleic acid
dNTP	deoxynucleotide triphosphate
ddNTP	dideoxynucleotide triphosphate
<i>dsrB</i>	Dissimilatory sulfate reductase subunit B gene

EDTA	Ethylenediaminetetraacetic Acid
EMIC	Electrical microbially influenced corrosion
EPS	Extracellular polymeric substances
FB	Fermentative bacteria
<i>feR</i>	Ferric reductase gene
FGA	Functional gene analysis
<i>fhfs</i>	Formyltetrahydrofolate synthetase gene
FTIR	Fourier-transform infrared
FWHM	Full width half maximum resolution
GR(CO ₃ ²⁻)	Carbonate green rust
GR(Cl ⁻)	Chloride green rust
GR(SO ₄ ²⁻)	Sulfate green rust
HDB	Hydrocarbon-degrading bacteria
HRM	High-resolution melt
HTL	High tide level
<i>hydA</i>	Hydrogenase gene
ICP-OES	Inductively coupled plasma optical emission spectrometry
IOB	Iron-oxidizing bacteria
IRB	Iron-reducing bacteria
<i>iro</i>	Ferrous oxidase gene
LTL	Low tide level
MA	Methanogenic archaea
MDA	Multiple displacement amplification
<i>mcrA</i>	Methyl coenzyme M reductase gene
MIC	Microbially influenced corrosion
mRNA	Messenger ribonucleic acid

NAD	Nicotinamide adenine dinucleotide
<i>napA</i>	Nitrate reductase gene
<i>narG</i>	Nitrate reductase gene
NGS	Next Generation Sequencing
<i>nirK</i>	Nitrite reductase gene
NOB	Nitrite-oxidizing bacteria
NRP	Nitrate-reducing prokaryotes
<i>nrfA</i>	Nitrite reductase gene
<i>nirS</i>	Nitrite reductase gene
NWC	Normal water corrosion
<i>nxr</i>	Nitrite oxidoreductase gene
PCR	Polymerase chain reaction
PPi	Pyrophosphate
QUATS	Quaternary ammonium compounds
<i>sat</i>	Sulfate adenylyltransferase gene
<i>sir</i>	Sulfite reductase gene
SOB	Sulfur-oxidizing bacteria
<i>soxB</i>	Thiosulfate oxidase subunit B gene
sp./spp.	Species/Many species
SRP	Sulfate-reducing prokaryotes
<i>sqr</i>	Sulfide quinone oxidoreductase gene
STE	Sodium Chloride/Tris/EDTA solution
TAE	Tris/acetic acid/EDTA solution
TEA	Terminal electron acceptor
TEMED	N,N,N',N'-Tetramethylethylenediamine
TGGE	Temperature gradient gel electrophoresis

Tris	tris(hydroxymethyl)aminomethane
UV	Ultraviolet light
XRD	X-ray powder diffraction

ACKNOWLEDGEMENTS

There are many people that I would like to thank and without whom this thesis would not have been possible.

First, I must thank my supervisors Prof. Martin Smith, Dr Heidi Burgess, and Dr Jon Caplin for the patience, support, and encouragement they have shown me.

I would like to thank ArcelorMittal for sponsoring the first three years of this project.

I would also like to thank Dr Charles Knapp for his invaluable support, and Dr Kaiming She for perhaps the most important piece of advice I received whilst studying for this degree.

My thanks go to Tony Parker, Brian Rousell, Carl Aichroth, and the engineering staff at Shoreham Port who were always generous with their time and assistance during my site visits.

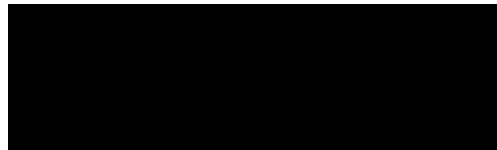
I am indebted to Peter Mathers, Peter Lyons, David Harker, Matt Leake and Georgios Oikonomou of the UoB SET technical staff for providing the best of practical support during my studies and for helping me remain grounded.

I would also like to thank my family for their unwavering support during some challenging times. I also extend my gratitude to Paul Kilkie for his help and encouragement, and to Claire Yeomans and Magdalena Grove for their support and guidance at some pivotal moments during my studies.

DECLARATION

I declare that the research contained in this thesis, unless otherwise formally indicated within the text, is the original work of the author. The thesis has not been previously submitted to this or any other university for a degree and does not incorporate any material already submitted for a degree.

Signed



Dated

31.05.21

Chapter 1 Introduction

1.1 Microbially influenced corrosion

Microbially influenced corrosion (MIC) is one of the terms commonly applied to forms of corrosion caused by microbial lifeforms, or more specifically, a process driven by the metabolic processes that occur within certain microorganisms (Angell, 1999, Shi et al., 2011, San et al., 2012, Homberg et al., 2014, Little et al., 2015, Refait et al., 2018). In other studies it is named microbially induced corrosion (Heitz et al., 1996, Roberts et al., 2002, Ilhan-Sungur et al., 2007, Pineau et al., 2008, McBeth et al., 2011); microbial corrosion (An et al., 2016, Kong et al., 2017, Hong et al., 2018); or biocorrosion (Dzierzewicz et al., 1997, Bholal et al., 2013, Delaunois et al., 2014, Jin and Guan, 2014, Forte Giacobone et al., 2015).

This study will use the term microbially influenced corrosion, as the term best fits the current understanding in the subject area.

MIC is of significance to engineers and technologists as well as to microbiologists and conservators, as it is associated with destruction of substrate at an accelerated rate: an order of magnitude greater than that expected by purely electrochemical forms of corrosion (Kumar and Stephenson, 2005) and two orders of magnitude greater than typical physical weathering processes (Waragai, 2016). To date MIC has been discerned in environments as diverse as oil pipelines (Al-Jaroudi et al., 2011), concrete sewer systems (Gomez-Alvarez et al., 2012), natural sandstone monuments (Li et al., 2008), cooling systems in nuclear power stations (Forte Giacobone et al., 2015), and structural steel in maritime installations (Phull, 2010).

This study is concerned with MIC occurrences on carbon steel piling within the coastal marine environment. The cost implications of repair and replacement of prematurely damaged infrastructure can be significant (Beech and Campbell, 2008). Though methods to mitigate the effects of MIC are available and widely used, they are expensive and can be detrimental to the surrounding environment (Liengen et al., 2014). A greater understanding of the mechanisms involved in the corrosion process as well as the key

microbes responsible may lead to improved methods for reducing or preventing MIC, thus safeguarding the environment, and reducing monetary costs.

1.2 Research aims

- To characterise corrosion formations in steel piling where microbially influenced corrosion has been reported within the marine environment.
- To determine how the adjacent marine environment links to the microbial consortia found within microbially influenced corrosion formations.

1.3 Research objectives

- Identify microbial community variability within corrosion formations at vertical positions on carbon steel piling.
- Characterise the mineralogy and chemical composition of marine mild steel piling corrosion formations.
- Determine microbial types present within low tide zone MIC formations, and contrast this with adjacent marine sediment and seawater.
- Construct a model for the inoculation processes involved in colonising MIC formations.

1.4 Thesis structure

The thesis is divided into eleven chapters:

Chapter 1 prefaces the study, introducing the concept of microbially influenced corrosion, establishing the aims and objects, and the thesis structure.

Chapter 2 outlines the mechanism and mineralogy of normal corrosion processes in the marine environment and presents a review of research in the field of MIC and current understanding of its effects, composition, the microbes associated with it, and techniques that have been used to analyse it.

Chapter 3 details the methodology adopted by this project. It includes a review of the project site and details the sampling procedures and locations. It also describes the analytical techniques employed in the study, and explains which procedures were utilised for the steel corrosion, marine sediment, and seawater samples obtained.

Chapter 4 presents the results of the tidal range and turbidity analysis for the harbour water adjacent to the corrosion sampling location.

Chapter 5 presents the results of x-ray powder diffraction (XRD) mineralogical and elemental analysis using inductively coupled plasma optical emission spectrometry (ICP-OES) of sediment adjacent to the corrosion sampling location.

Chapter 6 presents the results of GeoChip functional gene analysis of low tide zone corrosion, marine sediment, and seawater samples.

Chapter 7 presents the results of a denaturing gradient gel electrophoresis (DGGE)/high-resolution melt (HRM) comparative study of low tide zone steel corrosion, marine sediment, and seawater samples, and HRM genetic diversity analysis of corrosion samples extracted from fifteen locations on a steel piling section.

Chapter 8 presents the results of powder XRD mineralogical analysis of low water corrosion samples from Chapters 6, and fifteen vertical profile corrosion samples from Chapter 7.

Chapter 9 presents the results of chemical analysis using Fourier-transform infrared spectroscopy (FTIR) of low tide zone corrosion from Chapters 6 and 8, and vertical profile corrosion samples from Chapters 7 and 8.

Chapter 10 collates data from previous chapters and discusses the key findings of this research project.

Chapter 11 presents the project conclusions along with recommendations for future studies.

Chapter 2 Literature Review

2.1 Mechanisms of Microbially influenced corrosion

Since Leeuwenhoek's first observations of microbial lifeforms in the 17th century, the ubiquitous nature and ways in which these smallest of living organisms interact with the world has been of great interest to researchers (Atlas and Bartha, 1998, Gest, 2004). Early by research by scientists such as Pasteur and Koch during the 19th century was focused on isolating, culturing, and identifying individual genera; their findings provided the foundations upon which later researchers were to prove the involvement of microorganisms in cycling carbon, nitrogen, oxygen and sulfur (Atlas and Bartha, 1998, National Research Council (US) Committee on Metagenomics, 2007).

The involvement of microbial organisms in the corrosion of ferrous metals had been suspected since the late 19th Century but it was not until the early 20th century that research provided compelling evidence of the involvement of specific microbial genera in the corrosion of structural metal and machinery components. In 1910, Gaines noted the presence of sulfur compounds in iron pipe corrosion, and suggested the involvement of anaerobic soil bacteria. Corrosion of aircraft fuel tanks associated in the presence of sulfur-cycling bacteria were reported in the 1930s (Neihof, 1988) and subsequent studies revisited the causes of damage to buried cast iron pipework. A connection was made to the sulfur-reducing prokaryotes (SRP) of genus *Desulfovibrio* present in the surrounding soil (Wolzogen-Kuhr and Van der Vlugt, 1934). From this they subsequently proposed a mechanism known as cathodic depolarisation.

Cathodic depolarisation theory consists of six main steps (Table 2-1 and Figure 2-1). Firstly, a small proportion of iron atoms at the metal surface oxidise in the presence of water. Secondly, the dissociation of water molecules produces hydrogen ions and hydroxide ions. The hydrogen ions are then reduced to hydrogen gas by free electrons from the first step. SRP utilise sulfate ions as terminal electron acceptor and hydrogen as reducing agent, producing hydrogen sulfide, water, and hydroxide ions. The hydrogen sulfide and hydroxide then react with the ferrous ions in solution forming ferrous sulfide

(FeS) and ferrous hydroxide (Fe(OH)₂). The rate of hydrogen production and subsequent consumption by SRP was posited as the main driver of microbially influenced corrosion.

Table 2-1 Proposed mechanism for cathodic depolarisation

Anodic reaction	$4\text{Fe} \rightarrow 4\text{Fe}^{2+} + 8\text{e}^-$	(1)
Water dissociation	$8\text{H}_2\text{O} \rightarrow 8\text{H}^+ + 8\text{OH}^-$	(2)
Cathodic reaction	$8\text{H}^+ + 8\text{e}^- \rightarrow 4\text{H}_2$	(3)
Hydrogen oxidation	$\text{SO}_4^{2-} + 4\text{H}_2 \rightarrow \text{H}_2\text{S} + 2\text{H}_2\text{O} + 2\text{OH}^-$	(4)
Precipitation (1)	$\text{Fe}^{2+} + \text{H}_2\text{S} \rightarrow \text{FeS} + 2\text{H}^+$	(5)
Precipitation (2)	$3\text{Fe}^{2+} + 6\text{OH}^- \rightarrow 3\text{Fe}(\text{OH})_2$	(6)
Total reaction	$4\text{Fe} + \text{SO}_4^{2-} + 4\text{H}_2\text{O} \rightarrow \text{FeS} + 3\text{Fe}(\text{OH})_2 + 2\text{OH}^-$	(7)

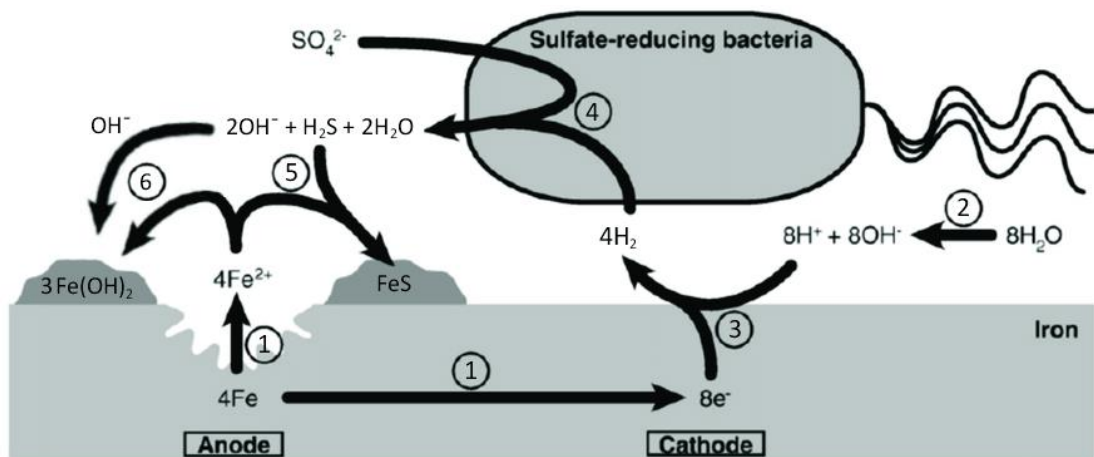
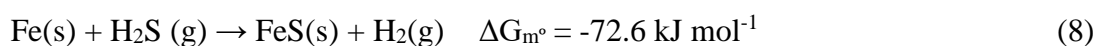


Figure 2-1 Schematic representation of MIC mechanism via cathodic depolarisation
(adapted from Mori et al. (2010))

MIC research from the 1960s through to the 1980s produced little systematic progress. The importance of sulfate-reducing prokaryotes as a primary driver of MIC was widely accepted, much research time was taken up either refuting or validating the cathodic depolarisation theory (Videla, 2001). Modifications to the mechanism included those proposed by King and Miller (1971) in which hydrogen adsorbed onto the ferrous sulfide is more easily accessed by SRP thus increasing the rate of corrosion; and Obuekwe et al.

(1981) whose anodic depolarisation theory promoted precipitation step 2 to the main driver of the MIC, and ferrous hydroxide the main corrosion product. The greatest challenges to Wolzogen-Kuhr and Van der Vlugt's original mechanism occurred following research that employing additional organic electron acceptors such as lactate. These studies showed that it was the rate of hydrogen sulfide production that determined the rate of corrosion, and not the rate of hydrogen oxidation. Indeed, it rapidly became accepted that the reactivity of iron with biogenic hydrogen sulfide (equation 8) alone could account for most of the corrosive effects of SRP (Enning and Garrelfs, 2014).



However, even during that time there had been speculation about MIC mechanisms based on directly utilised free electrons in the metal surface. Dinh et al. (2004) provided some of the earliest firm evidence for just such a mechanism. It was found that SRP communities could reduce sulfate without consumption of cathodic hydrogen. Additionally, the observed activity was associated with rates of corrosion up to 71 times those observed with hydrogen utilisation alone. Enning et al. (2012) and Venzlaff et al. (2013) conducted similar studies but focused on isolating specific strains of *Desulfobulbus*, *Desulforhopalus*, *Desulfopila* and *Desulfovibrio*. As well as confirming earlier findings, they were able to determine that this mechanism was specific to certain species of SRP only. Therefore, whilst all sulfate-reducing prokaryotes are able to contribute to iron corrosion due to their production of H₂S, only a limited number can cause the more damaging form of corrosion caused by direct utilisation of free electrons. Enning et al. (2012) coined the term 'Electrical microbially influenced corrosion' or 'EMIC' for this direct form of corrosion to differentiate it from corrosion by biogenic H₂S which was termed 'Chemical microbially influenced corrosion' or 'CMIC'.

2.2 Microbial groups and genera associated with MIC

In addition to the genera of SRP mentioned above, many others have been isolated from biofilms in contact with accelerated corrosion of marine carbon steel. These include species of *Desulfobacter*, *Desulfobacula*, *Desulfocella*, *Desulfotignum* (Usher et al.,

2014); *Desulfomicrobium* (AlAbbas et al., 2013, An et al., 2016), and *Desulfospira* (Paissé et al., 2012).

Sulfate-reducing prokaryotes of various genera have also been isolated from MIC biofilms found within other environments: *Desulfocaldus*, *Desulfoglaeba* (Suo et al., 2012), *Desulfonauticus*, *Desulfothermus* (Bonifay et al., 2017), *Desulfonatronospira*, *Desulfonatronovibrio*, and *Kytococcus* have all been found within biofilms associated with corroded crude oil pipelines (Zhilina et al., 1997, Rodríguez-Rodríguez et al., 2009, Summer et al., 2014, Bonifay et al., 2017). *Dethiosulfovibrio* has been linked to MIC in off-shore oil rig installations (Magot et al., 1997). *Desulfobotulus*, *Desulfustis*, *Desulfofaba* (Lamine and Azzedine, 2013) and *Desulfohalobium* (Liang et al., 2016) have been implicated in MIC damage to gas processing pipelines. Steel pipelines and water injection studies have revealed the presence of *Brevibacterium* (Li et al., 2019), *Desulfocapsa* (An et al., 2016), *Desulfotalea* (Bodtker et al., 2008), *Desulfurivibrio* (Yang et al., 2014), and *Fibrobacter* species (Costerton et al., 1978). *Chlorobaculum* and *Desulforudis* have been found in both biodigestion plant and geothermal plant corrosion formations (Lerm et al., 2013, Haosagul et al., 2019). *Corynebacterium* has been found in seawater biofilms around copper alloy corrosion formations (Schiffrin and De Sanchez, 1985). *Desulfotoregula* and *Desulfotobulbus* have been found in biofilms associated with MIC of concrete sewer systems (Santo Domingo et al., 2011). MIC research has also discovered SRP genera such as *Halorhodospira* in natural stone constructions (Otlewska et al., 2017).

Laboratory-based MIC studies utilising either marine or crude oil samples have also revealed the presence of the genera *Desulfobacterium* (Amann et al., 1991, Dinh et al., 2004), *Desulfococcus*, *Desulfosarina* (Amann et al., 1991), *Desulfotomaculum* (Beech and Gaylarde, 1999, Cetin and Aksu, 2009), *Desulfuromonas* (Amann et al., 1991), *Desulfitobacterium* (Comensoli et al., 2020), *Desulfosporosinus* (Telegdi et al., 2017), *Clavibacter* (San et al., 2012), and *Chlorobium* (Eashwar et al., 2004).

SRP are not believed to be the sole agent responsible for MIC; however, as several other groups of microorganisms have been isolated from corrosion formations. These often also possess properties capable of causing corrosion, either directly or by facilitating other

microorganisms to do so (Little and Lee, 2007, Javaherdashti, 2009, McBeth et al., 2011, Jin et al., 2015, Bonifay et al., 2017).

One of the most important groups are the acetogens or acid-producing bacteria (APB), which cause surface corrosion due their metabolic production of either organic or inorganic acids. Sulfur-oxidizing bacteria (SOB) are a diverse group of chemolithotrophs that fall into this category. They utilise reduced sulfur species and elemental sulfur as electron donors (Li et al., 2008, Madigan et al., 2009) which results in sulfuric acid production. Their cycling of sulfur species into sulfate and oxygen consumption also encourages SRP activity by providing these microorganisms with a terminal electron acceptor along with promoting anaerobic conditions (Iverson, 2001). Dong et al. (2016) observed the damaging effects of *Acidithiobacillus* sp. in stainless steel pipework, whilst Sowards and Mansfield (2014) noted the accelerated corrosion of carbon steel storage tanks in the presence of *Acetobacter* sp. Acid-producing bacteria of the genus *Propionibacterium* have also been linked to MIC in marine steelwork. These microorganisms uniquely produce propionic acid as a final product in the electron-transport chain (Machuca et al., 2016). SOB genera such as *Thiocapsa* are implicated in MIC of stainless steel (Otero et al., 2004), whilst *Acidithiobacillus*, *Acidiphilium*, *Halothiobacillus*, *Lactobacillus*, *Thiothrix*, *Thiobacillus*, and *Thiomonas* have also been observed in MIC damage to concrete sewer systems (Okabe et al., 2007, Bielefeldt et al., 2010) and sewerage infrastructure (Babu et al., 2006, Huber et al., 2016). *Thioalkalivibrio* is a genus of SOB that has been associated with SRP communities in MIC in petroleum reservoirs.

Another important group of APB are the nitrite-oxidizing bacteria (NOB). These aerobic microorganisms utilise the reduced nitrogen species nitrite (NO_2^-) as an electron donor, producing corrosive nitric acid. They include the genera *Nitrobacter*, *Nitrospina*, *Nitrococcus*, and *Nitrospira* (Madigan et al., 2009).

NOB are unable to utilise more reduced nitrogen species and are thus reliant upon other organisms such as: ammonia-oxidizing bacteria (AOB) which exploit the reducing properties of ammonia (NH_3) and ammonium (NH_4^+), generating nitrite (Madigan et al., 2009); and nitrate-reducing prokaryotes (NRP). *Nitrosovibrio*, *Nitrosomonas*, and *Nitrosospira* are three genera of ammonia-oxidizing bacteria that have been isolated from

biofilms associated with MIC damage to sewers (Islander et al., 1991) and natural stone constructions (Bock et al., 1988, Meincke et al., 1989).

NRP are mostly facultative aerobes that can switch terminal electron acceptor from oxygen to nitrate under anaerobic conditions producing ammonium and nitric oxide (Zumft, 1997). Some genera of NRP, such as *Thiomicrospira* and *Desulfotignum* are also capable of oxidizing sulfide to sulfate, a property that has been utilised in corrosion prevention (Section 2.7.4). Recent research indicates that some NRP can promote corrosion by sulfide production. Yuk et al. (2020) observed corrosion damage in the presence of a strain of *Marinobacter*. They proposed that an assimilatory sulfate reduction pathway regulated by the sulfite reductase hemoprotein gene (*cysI*) was responsible. Chang et al. (2014) similarly suggested a link between species of the genus *Methyloversatilis* with MIC occurrences in carbon steel (Chang et al., 2014). Species of the genus *Neisseria* have been isolated from biofilms associated with MIC of carbon steel and concrete exposed to dairy effluent (Babu et al., 2006), whilst *Thauera* is an NRP that has been discovered in light crude lines and linked to oil souring and possible corrosion (Conlette, 2016).

The acetogens are an important group of microorganisms that have been observed within MIC formations (Mand et al., 2014). Included in this group are species of the genera: *Acetobacterium*; *Actogenium*; *Bacillus*, *Clostridium*; *Moorella*; *Desulfotomaculum*; *Eubacterium*; and *Treponema* (Babu et al., 2006, Madigan et al., 2009). Acetogens are strictly anaerobic prokaryotes that utilise hydrogen as electron donor, carbon dioxide as electron acceptor, and secrete acetate as a waste product. As discussed above, hydrogen utilisation promotes proton reduction and electron removal from the metal surface which leads to iron ions entering solution, thus degrading the metal surface. Many acetogens can also reduce nitrate and thiosulfate, qualifying them as NRP and SRP respectively also (Madigan et al., 2009).

Iron-reducing bacteria (IRB) are obligate anaerobes that use ferric ion as terminal electron acceptors. They are another class that have been associated with MIC (Herrera and Videla, 2009). Sun et al. (2014) indicates that IRB promote corrosion by reducing passive ferric surface layers to soluble ferrous ions, rendering the surface liable to attack by other microorganisms. IRB overcome the problems of ferric ion insolubility by using

membrane-bound ferric reductase enzymes, which necessitate direct contact with the substrate surface (Lovley, 1993). However, it has also been suggested that certain species such as *Geobacter shewanella* and *G. geothrix* can utilise secreted electron carriers, greatly increasing rates of ferric reduction (Lovley et al., 2004). Some studies, whilst not contradicting the reduction mechanism above, suggest that ferric reduction by IRB can inhibit steel corrosion. Nagiub and Mansfeld (2002) demonstrated how pure cultures of *Shewanella algae* and *S. ana* successfully reduced corrosion rates in low-carbon steel. Similarly, Dubiel et al. (2002) and Lee and Newman (2003) indicated the corrosion inhibiting properties of *S. oneidensis*, in sterile media. In each case it was suggested that aqueous ferrous ions formed a reducing layer above the metal surface which shielded it from dissolved oxygen, thus maintaining anaerobic conditions. Despite the involvement of IRB species, these studies were only applied to normal water corrosion (NWC) mechanisms, and therefore do not constitute evidence of IRB as a corrosion mitigant in MIC formations. Iron-reducing species of the genus *Acidobacterium* have been noted in biofilms associated with MIC in cast iron pipework (Zhu et al., 2014), and bacteria of the genus *Leifsonia* was isolated from suspected MIC obtained from a nuclear waste pool during a study by Forte Giacobone et al. (2011), though their significance to the corrosion process was not determined.

Fermentative bacterial activity can be significant in environments low in electron acceptors such as sulfate, nitrate, and ferric ions. The group includes many genera of anaerobes that can use organic compounds as both electron donors and electron acceptors mostly via substrate-level phosphorylation. Their metabolic waste products vary according to the type of fermentable substance catabolised but can include carbon dioxide, molecular hydrogen, and hydrogen ions (Madigan et al., 2009). The involvement of fermentative processes in MIC of carbon steel piling specifically has not been widely investigated, though a study by Procópio (2019) connects fermentative hydrogen production with the activity of SRP and methanogens on steel in marine environments. Other environments are more fully investigated along with the directly corrosive effect of hydrogen waste products (Babu et al., 2006, Briggs et al., 2019, Stamps et al., 2020).

The group of microorganisms known as the hydrocarbon-degrading bacteria (HDB) include many species from other groups including SRP. HDB which utilise aliphatic and aromatic hydrocarbon substrates as electron donors. Where conditions favour a

proliferation of these microorganisms, a corresponding increase in corrosion is also commonly observed. Research into this group and their effects upon MIC has been considerable within the oil processing and transportation infrastructure environments (Rajasekar, 2017, Parthipan et al., 2018, Zhao et al., 2019), but not as extensive within the field of marine steel piling. Studies by Païssé et al. (2012), Kostka et al. (2014), Salerno et al. (2018) do indicate, however, that HDB can be a contributive factor in marine MIC especially in regions of significant hydrocarbon pollution.

Research also indicates that archaea contribute to MIC. These prokaryotes form a domain distinct from bacteria and eukaryotes, though sharing characteristics such as circular chromosomes, a lack of membrane-bound organelles, and reproduction via horizontal gene transfer, with the former, and methionine-initiated protein synthesis, and many RNA polymerases, with the latter (Madigan et al., 2009).

Methanogens (MA) include specific forms of archaea that have been found within MIC, especially in the presence of SRP (Bryant et al., 1977). They produce methane as part of their energy metabolism, and like the acetogens use hydrogen and various organic substrates as electron donor. In the absence of hydrogen some methanogens can also directly utilise alcohols to produce carbon dioxide leading to a lowering of pH, and a subsequent increase in corrosion (Madigan et al., 2009). Several species of methanogen have also been found to directly oxidize Fe^0 to Fe^{2+} in the presence of hydrogen ions and carbon dioxide (Daniels et al., 1987), and so also fall within a group known as Iron-oxidizers. Many known iron-oxidizing microorganisms belong to the domain Bacteria. Most iron-oxidizing bacteria (IOB), however, utilise dissolved ferrous ions as a source of energy which they oxidize to ferric ions. Liu et al. (2015) and Xu et al. (2007) observed how IOB activity was enhanced by the presence of SRP and corrosion damage was increased. Wang et al. (2014) observed the damaging effects of *Rhodospirillum* spp. containing biofilms in corrosion of cast iron pipes. Both *Gordonia* and *Enterobacter* IOB genera have been isolated from MIC samples taken from wastewater treatment plant (Ashassi-Sorkhabi et al., 2012). As IOB tended to colonise the transition region between aerobic and anaerobic zones, it was implied that the formation of ferric minerals away from the metal surface prevent the formation of a passivating layer. However, the species *Ralstonia pickettii* has also been studied in relation to MIC of aluminium alloys and copper pipes, and there are indications that its presence can reduce corrosion rates in

mixed consortia (Galyon Dorman et al., 2014, Galarce et al., 2019). The inhibition mechanism was not fully explored, but it was postulated that the bacteria was adhering closely to the metal surface and forming a passivating oxide layer and stabilising its immediate environment by secreting an extracellular polymeric substance (Section 2.4).

As well as methanogenesis, some genera of archaea, especially the phylum Crenarchaeota, are capable of sulfate-reduction. *Methanobacterium* is a genus of methanogenic archaea capable of reducing elemental sulfur to sulfide; H₂S was observed by Stetter and Gaag (1983). Chaban et al. (2006) noted that the effects of accelerated steel corrosion in the presence of *Methanotorris*, *Methanoculleus*, *Methanofollis*, *Methanoplanus*. These methanogenic archaea were determined to be hydrogen-users, causing damage via H⁺ production. *Archaeoglobus* and *Caldivirga* are thermophilic genera of archaea noted by Telegdi et al. (2017) for their sulfate-reducing properties and association with MIC in crude oil installations. *Pyrobaculum* is a genus of hyperthermophilic (T_{opt} > 80°C) iron-reducing archaea that are capable of sulfate reduction (Feinberg, 2007). Similarly, the extremophiles *Thermoproteus* and *Vulcanisaeta* have been isolated from MIC of hydrothermal power plant (Navarrette-Bedolla et al., 1999, Kozubal et al., 2012). Archaea also include several genera of nitrate-reducer: *Haloarcula* (Han et al., 2009) and *Haloferax* are obligately halophilic nitrate-reducing archaea associated with biofilms in stainless steel corrosion (Haque et al., 2020).

2.3 Functional genes associated with MIC

The use of functional genes in environmental studies has been explored in several environmental studies (He et al., 2007, Van Nostrand et al., 2009, Wang et al., 2009, Zhou et al., 2010, He et al., 2018, Luo et al., 2018). Analysis of specific functional genes can provide data on chemical processes occurring within an environment, and interactions occurring between the various members of the microbial community. In MIC research, several genes have been identified that link with the microbial groups described previously (Section 2.2). Table 2-2 lists these genes, and Figure 2-2 provides a schematic summary of the chemical pathways associated with these genes.

The presence of sulfate-reducing prokaryotes (SRP) can be determined by the presence of *aprA*, *aprB*, *dsrA*, and *dsrB* gene activity. The *aprA* and *aprB* genes code for the

adenosine 5' phosphosulfate (APS) reductase (AprAB) protein complex which forms part of the chemical pathway between sulfate and sulfite in the dissimilatory sulfate reduction process (Barton and Hamilton, 2007, Dong et al., 2017). Similarly, the *dsrA* and *dsrB* genes also code for a protein complex: the sulfite reductase (DsrAB) protein, which is responsible for reduction of sulfite to sulfide as part of the dissimilatory sulfate reduction pathway (Jørgensen et al., 2019).

The presence of sulfate-oxidizing bacteria (SOB) is indicated by activity of the *soxB* gene. The *soxB* protein forms part of the sulfur oxidation (SOX) pathway from thiosulfate to sulfate (Luo et al., 2018).

Nitrite-oxidizing bacteria (NOB) can be detected by activity of the *nxr* gene, which encodes for the nitrite oxidoreductase protein (Boddicker and Mosier, 2018). Activity of sub-unit A of the ammonia monooxygenase gene (*amoA*) is seen as evidence for nitrification by ammonia-oxidizing bacteria (AOB) (Li et al., 2014, Remmas et al., 2016).

Nitrate-reducing prokaryotes (NRP) are indicated by the presence of activity of the *napA* and *narG* nitrate reductase genes (Smith et al., 2007), and *nirK*, *nirS*, and *nrfA* nitrite reductase genes (Remmas et al., 2016, Cannon et al., 2019, Reji et al., 2019).

Acetogenic bacteria (AB) can be detected by the formyltetrahydrofolate synthase gene (*fthfs*) (Müller et al., 2016), and methanogenic archaea (MA) by activity of the gene that codes for the alpha subunit of methyl coenzyme M reductase (*mcrA*) (Rajala et al., 2019).

According to Schroder et al. (2003) iron-reducing bacteria (IRB) have been detected using the ferric reductase gene *fer*. Whereas iron-oxidizing bacteria are indicated where the *iro* (ferrous oxidase) gene is active (Hedrich et al., 2011).

The final microbial group are the fermentative bacteria (FB) and the hydrocarbon-degrading bacteria (HDB); these are indicated by activity of the *hydA* (hydrogenase encoding) gene, and *assA* (Alkylsuccinate synthase encoding) gene respectively (Zhao et al., 2019, Liu et al., 2020).

Table 2-2 Microorganism groups and selected genes associated with MIC

Group	Gene	Encoding function	Reference
Sulfate-reducing prokaryotes (SRP)	<i>aprA</i>	AprA component of the dissimilatory adenosine 5' phosphosulfate reductase complex	Barton and Hamilton (2007), Dong et al. (2017)
	<i>aprB</i>	AprB component of the dissimilatory adenosine 5' phosphosulfate reductase complex	Barton and Hamilton (2007), Dong et al. (2017)
	<i>dsrA</i>	DsrA component of the dissimilatory sulfite reductase complex	Jørgensen et al. (2019)
	<i>dsrB</i>	DsrB component of the dissimilatory sulfite reductase complex	Jørgensen et al. (2019)
Sulfur-oxidizing bacteria (SOB)	<i>soxB</i>	SoxB component of the periplasmic thiosulfate oxidizing complex	Luo et al. (2018)
Nitrite-oxidizing bacteria (NOB)	<i>nxr</i>	Nitrite oxidoreductase	Boddicker and Mosier (2018)
Ammonia-oxidizing bacteria (AOB)	<i>amoA</i>	Ammonia monooxygenase	Li et al. (2014), Remmas et al. (2016)
Nitrate-reducing prokaryotes (NRP)	<i>napA</i>	Nitrate reductase	Smith et al. (2007)
	<i>narG</i>	Nitrate reductase	Smith et al. (2007)
	<i>nirK</i>	Nitrite reductase	Reji et al. (2019)
	<i>nirS</i>	Nitrite reductase	Remmas et al. (2016)
	<i>nrfA</i>	Nitrite reductase	Cannon et al. (2019)
Acetogenic prokaryotes (AP)	<i>fthfs</i>	Formyltetrahydrofolate synthase	Müller et al. (2016)
Methanogenic archaea (MA)	<i>mcrA</i>	Methyl coenzyme M reductase	Rajala et al. (2019)
Iron-reducing bacteria (IRB)	<i>feR</i>	Ferric reductase	Schroder et al. (2003)
Iron-oxidizing bacteria (IOB)	<i>iro</i>	Ferrous oxidase	Hedrich et al. (2011)
Fermentative bacteria (FB)	<i>hydA</i>	Hydrogenase	Zhao et al. (2019)
Hydrocarbon-degrading bacteria (HDB)	<i>assA</i>	Alkylsuccinate synthase	Liu et al. (2020)

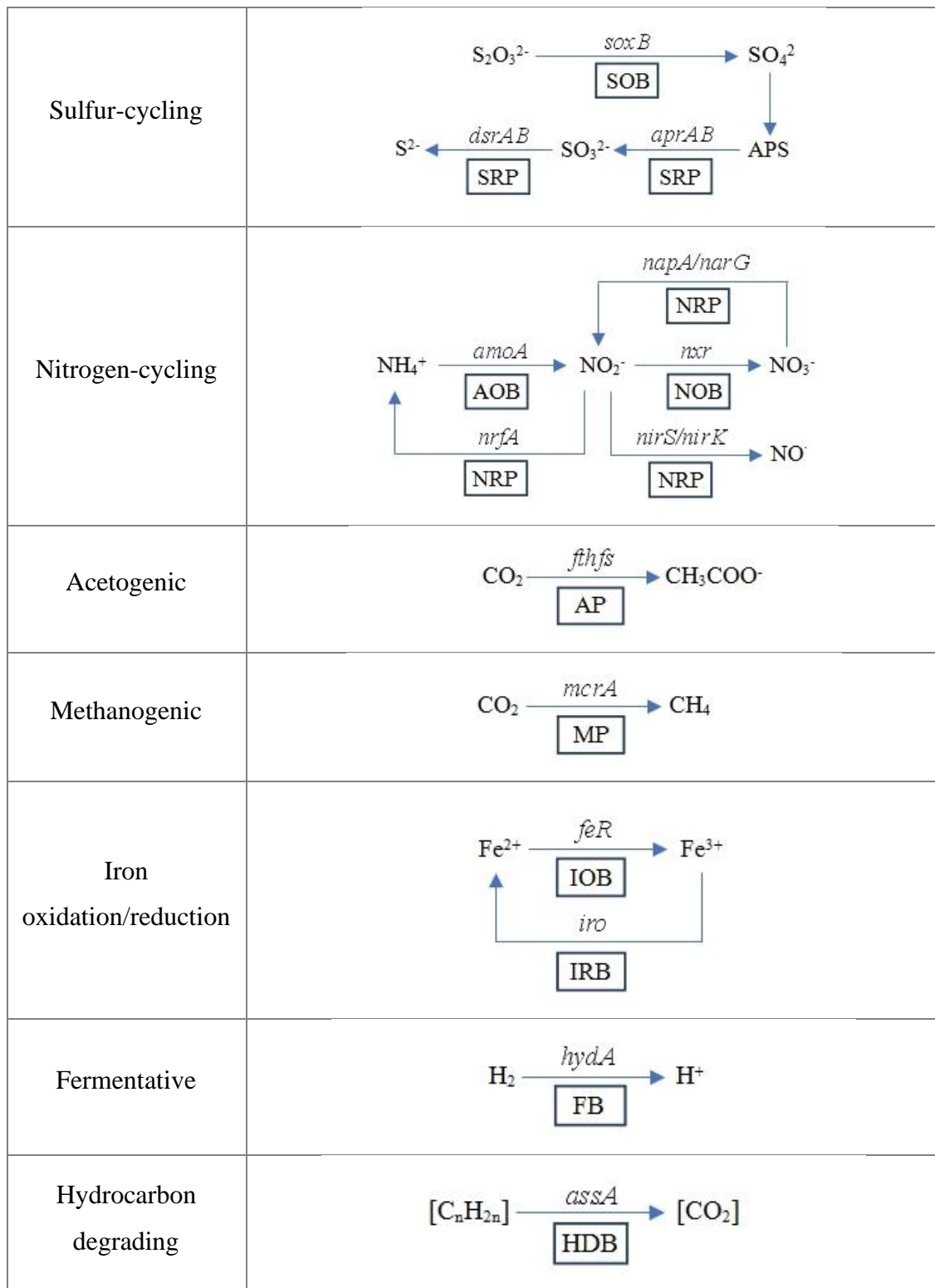


Figure 2-2 Schematic representation of MIC chemical pathways with associated microbial groups

2.4 Biofilms

Section 2.2 detailed various microbial groups that are implicated in accelerated corrosion and outlined the mutually beneficial and symbiotic relationships between certain groups such as between sulfate-reducing prokaryotes and sulfate-oxidizing bacteria, and sulfate-reducing prokaryotes and iron-oxidizing methanogens. However, the differing environmental conditions that these groups often require would seem to preclude this. For example, sulfate-reducing prokaryotes are obligate anaerobes but are often associated with obligate aerobic sulfate-oxidizing bacteria. It was indicated previously that certain microorganisms can occupy marginal regions that allow interaction with microbes in adjacent anoxic environments whilst allowing access to oxygen, but what has not been discussed is how the microorganisms themselves construct and maintain these environments. This is where the concept of the biofilm becomes relevant.

Microorganisms can survive and grow most readily when in contact with a physical surface, either organic or inorganic in nature (Donlan, 2001, Liengen et al., 2014). When planktonic microbes encounter a surface, they may fail to adhere and be carried away, or become attached. Attachment at this stage is weak and reversible, being due to Van der Waals forces between the microorganism and the surface or hydrophobic interactions with the environment. Under favourable conditions the attached microbes can multiply and begin to modify their immediate surroundings. Surface adherence is increased by involvement of appendages such as flagella, pili, fimbriae, or glycocalyx (Donlan, 2001). Genes, which were inactive in the planktonic form of the microbe, are expressed encoding proteins that produce extracellular polymeric substances (EPS) and intercellular signalling molecules (Szttyler, 2014). The EPS forms a porous and layered three-dimensional matrix in and around the growing community. Typically composed of mainly polysaccharides, lipids, and proteins it also incorporates water molecules as well as abiotic particles such as silt and sand (Liengen et al., 2014). The matrix serves several functions, including structurally stabilising the community, trapping nutrients, and regulating water availability. Structural stabilisation ensures surface adhesion is maintained, but also that cells can become effectively fixed in locations advantageous to their metabolic requirements (Madigan et al., 2009, Procópio, 2019). Collectively, the assemblage of microbial cells and the EPS matrix is known as a biofilm.

Biofilms have been observed that include one or two species of microorganisms, but more commonly they comprise of hundreds or thousands of bacteria and archaea. Biofilms are always dynamic environments that are in continuous development, expanding along with their microbial population, constantly reacting to environmental changes, and regulating internal conditions. Communication between cells is key to this process. Signalling molecules are released by microbial cells stimulate gene expression in other cells leading to a modification in the form and composition of the biofilm. This mechanism is known as quorum sensing, which as well as providing intraspecies communication is believed to facilitate interspecies signalling also (Madigan et al., 2009).

Biofilms are routinely reported in the presence of microbial influenced corrosion. Studies by Melchers (2008) and Melchers and Jeffery (2008) demonstrated that abiotic processes initially dominate relatively slow corrosion processes in the presence of seawater, and that corrosion rates rapidly increased upon maturation of a biofilm. They demonstrated this model to apply to a range of steels from low carbon (mild) steel through to several high nickel and chromium steels in the marine environment. Studies of microbial communities found in the presence of MIC confirm the matrices are composed mainly of humic substances, proteins, and polysaccharide. Zhang and Fang (2001) calculated that 89% of the overall volume of a corrosion formation could be thus composed; whilst research by AlAbbas et al. (2013) showed that the organic composition of inner corrosion layers was approximately 10% by weight, suggesting that despite being extensive within an MIC formation, the EPS matrix is a low-density entity. The proportion of each of the main biofilm components also appears to be dependent upon the microbial composition of the mature biofilm: carbohydrates predominate in the presence of acid-producing bacteria (Section 2.2); proteins are in highest concentration in communities dominated by methanogenic archaea; and biofilms higher in humic substances are found in the presence of methanogens and aerobic prokaryotes (Liu and Fang, 2002). As discussed above, the composition of the matrix varies according to the requirements of the microbial community. A common characteristic of each however is the presence of anionic functional groups; these bind metal ion within the EPS matrix. It is believed that this is significant to the corrosion process, as metal cations in varying oxidation states can act as 'electron shuttles' (Beech and Sunner, 2004) providing pathways for direct electron transfer (e.g., oxidation of surface iron layers) or cathodic depolarisation (Section 2.1).

With regard to maintaining and preserving the microbial community, Jia et al. (2019) noted the efficacy of a mature biofilm to resist physical and chemical damage in carbon steel installations; a characteristic that is enhanced when in the presence of intercalated corrosion products as well as hard external mineral layers.

2.5 Corrosion in marine steel piling

As noted above, MIC is a recognised phenomenon within the marine environment. Where its effects can compromise commercial efficiency and safety, port authorities have a keen interest in MIC research. Studies have been conducted within active harbour sites with the intention of understanding the how the microbial biota degrade structural steelwork and in particular, support piling (Cheung et al., 1994, Beech and Campbell, 2008, Melchers and Jeffery, 2012, Melchers, 2013).

2.5.1 Introduction to piling in harbours and ports

To facilitate efficient and safe loading and unloading of cargo from moored ships, systems of constructed wharves have been used since antiquity. Initially the method of construction would be directed by the nature of locally available materials: Northern Europe, which was abundant in timber has a history of wharves constructed from dressed logs piled into the sediment bed. These piles were either widely spaced and used to support a horizontal platform or close set to act as a retaining wall, behind which the area was filled with stone and rubble. Cast iron had been used as a building material since the late 18th century but it saw limited use in quayside construction due to its tendency to undergo brittle fracture under load. Reinforced concrete was developed during the later stages of the 19th century, and it proved an adequately durable material in marine environments which could either be piled or cast in situ. Also, by the end of the 19th century carbon steel began to be adopted as a piling material following the wide-scale availability of high purity steel following development of the Bessemer process. Today carbon steel piling is ubiquitous in harbour installations due to its relatively low cost and ease of handling (Tomlinson and Woodward, 2014, Pile Buck International Inc., 2015).

2.5.2 Design and construction of modern steel piling

The method of installing each steel pile and securing it to its neighbour has changed relatively little since introduction: a pile is lifted into position and then either machine hammered, pressed, or vibrated into the sediment to a depth determined by sediment bed properties and other local environmental conditions. Each successive pile is positioned close to its neighbour so the integral full-length clamp or ‘clutch’ on each pile can interlock. In addition in order to resist further outward bowing due to pressure from rubble backfill, anchor ties are routinely fixed at key locations to the rear of the piling (ThyssenKrupp GfT Bautechnik., 2008, Pile Buck International Inc., 2015).

There are several common forms of piling steel in modern use: box section; straight web; composite; and normal section. Normal section piles are the most common and comprise of two main designs: Z-profile (also known as Frodingham piles) and U-profile (also known as Larssen piles)(ArcelorMittal Commercial RPS S.à r.l., 2008). The key difference in configuration between Z and U-profile piles is the position of the ‘clutch’ connecting the adjacent pile (Figure 2-3). Z-profile piles are coupled at positions known as the out-pan and in-pan (Cheung et al., 1994), whereas U-profile sections are coupled along their interconnecting diagonal face. The choice of piling profile for a wharf is mainly determined by the intended layout of the installation, though Z-profile and U-profile piles are highly suitable for linear berths, and share similar installation and load-bearing characteristics so are commonly encountered (Skyline Steel LLC., 2014).

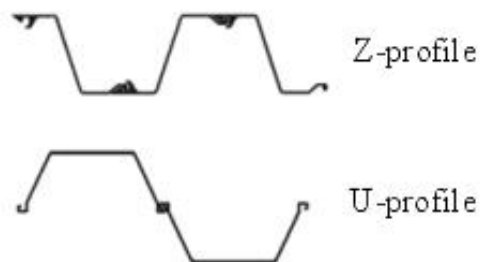


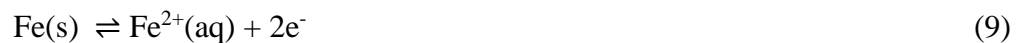
Figure 2-3 Plan profiles of the two commonly used piling designs
(Engineering and Construction., 2013)

2.5.3 Normal Water Corrosion: formation and mineralogy

The iron used to produce steel is derived from various mined ores, most significantly magnetite (Fe_3O_4), hematite ($\alpha\text{-Fe}_2\text{O}_3$), goethite ($\alpha\text{-FeO(OH)}$), limonite ($\text{FeO(OH)} \cdot n\text{H}_2\text{O}$) and siderite (FeCO_3) (Komatina and Gudenau, 2004, Filippov et al., 2014). The processing required to separate iron from its ore requires specialist plant and the input of significant energy due to the thermodynamically unfavourable nature of iron reduction reactions. Thus, iron is thermodynamically unstable with respect to the elements such as are found in these ores, most notably oxygen, so an iron surface will therefore tend to return to an oxidized state if left unprotected. Iron is alloyed with other elements to produce steel with specific characteristics, including how it responds to corrosion. Indeed, stainless steels are formulated to resist corrosion and would thus appear to be suited to environments that promote this form of degradation. However, as discussed in section 2.5.1, carbon steel is almost universally employed in marine environments. This can be explained in terms of projected lifespan of such a material (section 2.5.4) relative to the cost of corrosion resistant steels, which are typically three to four times more expensive than carbon steels of the same weight (MEPS International Ltd, 2020).

Under anhydrous conditions, a carbon steel surface exposed to oxygen will form an oxide corrosion layer on exposed surfaces composed mainly of hematite and magnetite. As the layer thickens, its oxygen permeability decreases rapidly, resulting in an effective halt to further corrosion once it reaches an approximate thickness of 10 nm (Bolton, 2002). This type of corrosion is possible to produce under laboratory conditions and may occur in the environment to a minor degree, especially immediately following steel production, but is easily overtaken by other processes when water is present along with oxygen. The reactions associated with this produces the more commonly recognised form of steel corrosion or rust characterised by red-brown layers of friable scale. The presence of oxygen with water also changes the corrosion process from purely chemical reactions to electrochemical interactions.

The following two half equations apply under aqueous conditions:



The standard electrode potentials (E^\ominus) for these reactions are +0.44 V and +0.401 V respectively, so when coupled the resulting total cell potential is $(0.401 \text{ V} + 0.44 \text{ V}) = +0.841 \text{ V}$. Therefore, iron will become oxidized to the ferrous ion, whilst water and oxygen are reduced to hydroxide ions. A schematic model for how this process occurs within a water droplet placed on a carbon steel surface and how these reactions apply to then initial formation of rust are shown in Figure 2-4.

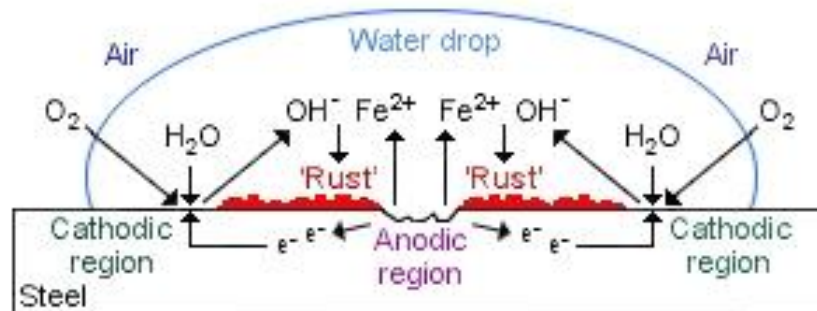


Figure 2-4 Simple electrochemical corrosion cell
(based on Todorova, 2020, and Stansbury and Buchanan, 2000)

The basic corrosion mechanism is one of a short-circuited galvanic cell: the centre of the water droplet has least access to atmospheric oxygen so the adjacent metal will form the anode of the cell; the outer edges of the droplet are able to absorb oxygen more readily so act as the cathode. Oxidation of the iron at the anode provides electrons, which are free to travel through the body of metal where they can be utilised in in the cathodic region. As iron(II) hydroxide is poorly soluble in water ($1.43 \times 10^{-3} \text{ g l}^{-1}$ at 25 °C, pH 7) the ferrous ions and hydroxide ions combine to form a precipitate, which becomes deposited on the metal surface. Where oxygen is present, the ferrous hydroxide can subsequently oxidize to iron (III) oxide-hydroxide (FeOOH) minerals. According to De la Fuente et al. (2016) lepidocrocite ($\gamma\text{-FeOOH}$) is the first oxy-hydroxide polymorph to form, but then a partial change occurs to the more stable goethite ($\alpha\text{-FeOOH}$) as the rust thickens. Morcillo et al. (2015) attributes this transition from lepidocrocite to goethite to the presence of hydrogen ions within a reducing environment. Over time goethite can convert to hematite ($\alpha\text{-Fe}_2\text{O}_3$) or maghemite ($\gamma\text{-Fe}_2\text{O}_3$) (Balasubramaniam et al., 2003). In addition, maghemite can form as the result of magnetite oxidation, which can

subsequently transform to hematite (Nasrazadani and Raman, 1993). Nasrazadani and Raman (1993) showed how this process can occur during wetting and drying cycles of a corrosion surface and that lepidocrocite can result from magnetite oxidation. They also observed a subsequent transition from lepidocrocite to goethite. If the region closest to the metal surface becomes oxygen depleted, hematite can subsequently become partially reduced producing magnetite. Feroxyhyte (δ -FeOOH) is another ferric oxyhydroxide polymorph, which was first described by Chukhrov et al. (1977), and is now accepted as a common component of marine corrosion of carbon steel (Arroyave and Morcillo, 1997, Mei et al., 2015). According to Mei et al. (2015) and Majzlan et al. (2008) feroxyhyte is a fine grained mineral found close to the metal surface. Its formation mechanism is not well documented but is believed to be produced as the result of rapid oxidation of ferrous ions, as such it appears to follow a separate formation path from lepidocrocite and goethite. Whether feroxyhyte thus produced subsequently transforms to other minerals is unclear. Cornell and Schwertmann (2003) notes that the transformation of feroxyhyte to hematite can occur under vacuum and at temperatures above 150 °C via dehydroxylation reactions, and direct transformation to goethite can occur in the presence of strong base. Clearly these conditions are not experienced in marine corrosion, but the reactions outlined may be possible albeit at a very slow rate. Mei et al. (2015) notes that it forms compact layers that reduce corrosion at the metal surface, and in this way is similar to goethite (Cook et al., 1999).

Free hydroxide ions (Equation 10) can also produce a localised increase in pH which can be significant enough to allow reaction with aqueous hydrogen carbonate and calcium ions. This results in formation of aragonite (CaCO_3) thus:



Hydroxide ions can also react with aqueous magnesium ions, forming brucite ($\text{Mg}(\text{OH})_2$):



The precipitation of these compound can be significant in slowing subsequent corrosion as they tend to form a passivating layer at the metal surface (Guezennec, 1994, Tu and Cottis, 2009, Yang et al., 2015). The mineral siderite (FeCO_3) has also been observed in the presence of carbonate under similar pH conditions. Formation of siderite via reaction of ferrous hydroxide with carbonate is thermodynamically unfavourable ($\Delta G_m^\circ = +33.35 \text{ kJ mol}^{-1}$) (Atkins, 2006), so is possibly the result of a similar reaction pathway to aragonite above. Research indicates that this mineral can subsequently be oxidized to both maghemite and magnetite (Kim et al., 2013).

Morcillo et al. (2015) and De la Fuente et al. (2016) indicate that where iron oxyhydroxides form in the presence of high chloride ion concentrations akaganeite ($\beta\text{-FeOOH}$) can form, either due to the stabilizing effects of intercalated chloride ions in the presence of oxygen or as a result of hydrolysis of ferrous chloride (FeCl_2) under high chloride conditions (Mei et al., 2015, Guerra et al., 2018). This polymorph forms a porous and loose structure and has been associated with increased rates of carbon steel corrosion. However, as with goethite this mineral transforms with time into ferric oxides, most commonly maghemite ($\gamma\text{-Fe}_2\text{O}_3$) (Ma et al., 2008). Another ferric oxyhydroxide common to rust is ferrihydrite, which is present as a fine-grained nanomaterial. Whilst its formula is ill defined due to its variable water content, it has commonly been given as $\text{Fe}_5\text{HO}_8 \cdot 4\text{H}_2\text{O}$ (Morcillo et al., 2015, De la Fuente et al., 2016). Similarly, there is no unified mechanism for the formation of ferrihydrite (Weatherill et al., 2016); however, research indicates ferrihydrite requires stabilization by other species in order to form such as silicon, calcium, and chromium (Furukawa et al., 2002).

Schwertmann and Fechter (1993) note that ferrous hydroxides subject to oxidizing conditions and pH conditions between weakly acidic and weakly basic can form compounds known as green rusts. These corrosion products are composed of Fe(II)(OH)_6 octahedra layers in which a proportion of Fe(II) ions are replaced with Fe(III) . Water molecules form interlayers along with anionic species assimilated to balance the net positive charge of the iron hydroxide sheets (Thomas et al., 2018). Three types of green rust are commonly isolated: chloride green rust ($\text{GR(Cl}^-)$); sulfate green rust ($\text{GR(SO}_4^{2-})$); and carbonate green rust ($\text{GR(CO}_3^{2-})$) (Usman et al., 2018). Schwertmann and Fechter (1993) place green rust formation as an intermediate step between ferrous hydroxide and lepidocrocite, and Ma et al. (2008) states that chloride green rust is a precursor to

akaganeite formation. Research by Legrand et al. (2001) and Hansen (1989) indicates that carbonate green rust can form in the presence of carbonate and hydrogencarbonate ions, and that subsequent oxidation forms ferrihydrite. The reaction was also observed to be reversible under reducing conditions. Drissi et al. (1995) performed a similar study and derived goethite from carbonate green rust oxidation. A study by Jones et al. (2017) connects these two sets of observations: ferrihydrite can transform into lepidocrocite and goethite under anaerobic conditions. Drissi et al. (1995) also noted that oxidation of sulfate and chloride green rusts produce lepidocrocite, an observation which agrees with Schwertmann and Fechter (1993) above. Conversely Guilbaud et al. (2013) showed that goethite and lepidocrocite can revert to sulfate green rust or chloride green rusts if subjected to reducing conditions.

Overall, the processes involved in the corrosion of carbon steel are dynamic and do not ultimately finish with the formation of a specific mineral. Many of the steps produce an increase in ferric ion content, and there is a general tendency towards more stable oxides of iron; however, many reactions can be reversed if environmental conditions change, or the mineral composition alters the degree to which oxygen or certain ionic species can influence the processes. This is especially relevant in the formation of green rusts and iron oxides. Figure 2-5 summarises the processes outlined above. Of note are the lepidocrocite relationship to chloride green rust and sulfate green rust, which is separate from the ferrihydrite and carbonate green rust reactions; the formation of feroxyhyte and siderite, neither of which are involved with green rust formation unlike lepidocrocite and goethite; and the maghemite-hematite-magnetite cycle.

minerals form expanded layers of friable, poorly adherent scale which provides little or no protection to the underlying metal surface. So, unlike metals such as copper and aluminium, which form essentially uniform layers of metal oxide in the presence of water and oxygen, iron surfaces will not generally achieve surface passivation. The result is that carbon steel structures have the potential to turn entirely to rust if left untreated.

2.5.4 Normal Water Corrosion profiles in steel piling

Analyses of vertical NWC profiles often categorise areas according to their position relative to sediment bed level and specific tidal conditions (Morley and Bruce, 1983, Cheung et al., 1994, Phull, 2010, Tomlinson and Woodward, 2014). The averaged NWC rates measured from several sites in the UK, Cyprus, and the United Arab Emirates are shown in Figure 2-6 (Tomlinson and Woodward, 2014). The profile exhibits the presence of discrete vertical zones, each of which is subject to a differing degree of submersion and exhibits a different mean rate of corrosion. The two areas displaying the highest rates of corrosion are the ‘splash zone’ (supralittoral zone), which is situated above the mean high tide level, and the ‘low tide zone’ (lower littoral) which lies below mean low tide level. The splash zone is partially covered during spring high tides (HTL on Figure 2-6) and is subject at other high tide conditions to sea spray and wave action. Conversely the low tide zone is mostly submerged but can be partially exposed especially during spring low tides (LTL on Figure 2-6). The atmospheric zone is defined as the region above the splash zone; it does not have direct contact with seawater other than from spray, and it typically experiences rates of corrosion comparable to the intertidal zone.

Visualising corrosion as a series of zones is an effective way of indicating typical corrosion rates at a location, and therefore useful for targeted monitoring of piling for maintenance purposes. It does not provide information about variations in corrosion rates within a zone, however. The upper portion of the immersion zone for example will experience shorter periods of immersion compared with the lower part of this zone; in effect this vertical location may experience conditions which are closer to the low tide zone and suffer a greater rate of corrosion as a result, despite being below mean low tide level. Additionally, averaging data from geographically separate marine environments, each with its own environmental conditions, will only provide an indication of corrosion

rates. The data does, however, provide a suitable base-line from which to assess the seriousness of MIC occurrences.

In addition, rates of NWC at different positions on the piling face can vary within the same corrosion zone. A study by Wall and Wadso (2013) of piling sections within the Baltic Sea Port of Halmstad, Sweden indicates that average corrosion rates are greatest on the outpan section of piling, whilst inpan sections, corrode at the slowest rate on average within all vertical zones above bed level. They recorded corrosion rates of up to 0.06 mm yr^{-1} on the outpan of five separate sections of piling whereas in all but one location the corrosion rate of inpans averaged 0.03 mm yr^{-1} . They noted the highest rate of corrosion occurred on each piling face between mean water level and 6 m depth. Despite being located in the tidal area of the port, the low tidal range experienced at Halmstad of 0.2 m (Meteo365.com Ltd., 2015) means that the majority of the sampling areas were within the immersion zone. Their data is consistent, however, with the averaged corrosion rates obtained by Tomlinson and Woodward (2014) for this zone.

The buried zone is subject to the slowest rate of corrosion. Anoxic conditions within the marine sediment should produce a differential aeration cell with piling regions above sediment bed level: the buried piling face, having a lower exposure to oxygen, forms the anode of the corrosion cell, and the exposed region form the cathode, resulting in increased rates of corrosion in the buried section (Cheung et al., 1994, Bolton, 2002, Borda et al., 2003). As a high rate of corrosion is not observed are evidently processes that mitigate the process. The Immersion zone is exposed to seawater continually but growth of marine organisms, such as barnacles and algae, provides a partial barrier to seawater abrasion and reduce steel surface exposure to oxygen. This may produce an environment sufficiently anoxic to prevent macro scale differential aeration cell from forming with the buried piling sections. In addition Refait et al. (2018) reported the formation of significant layers of pyrite (FeS_2) and siderite (FeCO_3) in steel sections buried in marine sediment; it is feasible that these mineral form a passive layer which retards the rate of corrosion in this section. The intertidal zone is periodically exposed to the atmosphere but similarly benefits from protection by marine organisms. It had been proposed that the splash zone and low tide zone exhibit greater corrosion rates due to the abrasive effect of wash from shipping, waves, and floating debris; these zones having a greater localised contact time with both areas during periods of slack tide. The splash

zone is also exposed to sea spray and atmospheric weather conditions which provide additional wetting of the piling. Unlike the intertidal, low tide and immersion zones this area will lack surface protection provided by marine growth (Tomlinson and Woodward, 2014). The low tide zone may also be subject to macro scale differential aeration cells (Bolton, 2002, Borda et al., 2003).

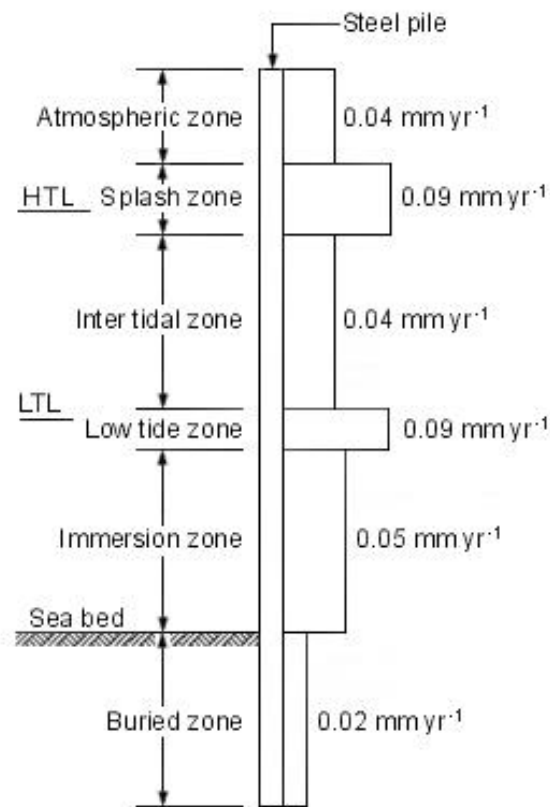


Figure 2-6 Vertical zones on steel piling and typical NWC corrosion rates (based on Alcántara et al. (2017) and Tomlinson and Woodward (2014))

2.5.5 Microbially influenced corrosion profiles in steel piling

As previously indicated in section 2.5.4, corrosion of exposed carbon steel piling which is not associated with microbial influence (NWC) typically proceeds at between 0.05 and 0.09 mm yr⁻¹ in a marine environment (Cheung et al., 1994, Kumar and Stephenson, 2005, Tomlinson and Woodward, 2014). Corrosion of piling steel in the presence of MIC is routinely associated with significantly higher corrosion rates. A study

by Marty et al. (2014) found that steel piling in the presence of MIC exceeded 0.3 mm yr^{-1} , whilst Beech and Campbell (2008) reported rates of loss exceeding 1.0 mm yr^{-1} (Beech and Campbell, 2008). Steel piling in harbours around the Danish coast was monitored as part of a study conducted by Melchers and Jeffery (2012); where MIC had been detected, perforation of steel piling occurred after 25-35 years of installation. As modern sheet steel piling is commonly manufactured with a wall thickness of between 12 and 20 mm (ArcelorMittal Commercial RPS S.à r.l., 2011) this indicates a corrosion rate in excess of 1.0 mm yr^{-1} . If these values are typical, perforation and subsequent failure of piling could occur in fewer than twenty years compared with a life span of over 100 years in the absence of MIC. Unlike for NWC profiles, there are currently no studies that provide MIC corrosion rate or microbial composition data in any location other than at the low tide zone. Important papers by Beech and Campbell (2008), Marty et al. (2012) and Melchers and Jeffery (2012) make reference only to the low tide zone as a site for MIC. The reasons why other zones were omitted, or at least discounted in their studies is not made clear. It is possible that site observations indicated the absence of MIC in other vertical zones, or it may be simply that the low tide zone is the area most at risk from elevated corrosion rates (both from NWC and MIC), and so has become the focus of research due to the dangers of catastrophic piling failure.

2.5.6 Microbially influenced corrosion: structure and mineralogy

Microbially influenced corrosion (MIC) can be quite distinct in external appearance compared to normal water corrosion (NWC). This is especially true when comparing subsurface structure. As discussed previously, NWC is comprised of flaky, porous, and scale-like layers bonded directly to the corroding metal surface; these adherent layers needing to be grinded or otherwise mechanically removed to reveal uncorroded steel beneath. MIC surface morphology can vary considerably forming hollow structures such as red-orange rusticles and chimneys, and protuberant and blister like tubercles (Little et al., 2014). In permanently submerged environments the soft and delicate tubular structures of the former two morphologies are found often mixed with tubercles, whereas in locations subject to periodic exposure to air the bulbous tubercles are common. Unlike rusticles and chimneys, these possess a hard and friable outer crust. Additionally, where MIC develops behind a layer of organic growth these characteristic surface formations

may not occur. Melchers et al. (2014) studied low tide zone MIC in a tidal location, and were able to select sampling regions according to the position of protuberant corrosion blooms that formed through a barnacle and seaweed layer (Figure 2-7). Beech and Campbell (2008), during a similar study, apparently encountered no tubercles, and were directed to MIC formations by the presence of raised and discoloured regions and vertical breaks in the concretion layer accompanied by a black liquid effusion (Figure 2-8). The mineral composition of the outer layer is mainly of goethite, ferrihydrite, maghemite, and some lepidocrocite, between layers of magnetite which provides most of its structural rigidity. Where this outer layer forms through a barnacle layer this often becomes augmented with calcium carbonate (Sarin et al., 2004, Pineau et al., 2008, Little et al., 2015).



Figure 2-7 MIC Tubercle
(Melchers et al., 2014)



Figure 2-8 MIC formation without tubercle
(Beech and Campbell, 2008)

Whichever form the outer layer manifests, the corrosion products beneath appear to adopt a consistent structure and composition. This core region has been found to comprise of weakly bonded minerals interspersed with a green-black sulfurous smelling semi-solid slurry that is easily scraped or rubbed away. Removal of this invariably reveals a pitted or striated shiny metallic surface beneath (Beech and Campbell, 2008, Pineau et al., 2008). Within this core region analysis has indicated the consistent presence of goethite, lepidocrocite, ferrihydrite, ferrous hydroxide, oxides of iron in the form of magnetite and maghemite (Beech and Gaylarde, 1999, Duan et al., 2008, Alcantara et al., 2015), and

silica (Little and Lee, 2007). Sulfate green rusts and the iron sulfides greigite (Fe_3S_4), mackinawite (FeS_{1-x}), marcasite (FeS_2), smythite (Fe_9S_{11}), pyrrhotite (Fe_7S_8), and pyrite (FeS_2) have also been identified (Lennie and Vaughan, 1996, Refait et al., 2003, Vaughan, 2006, Rickard and Luther, 2007, Pineau et al., 2008). It is stated that these sulfide compounds, along with the sulfate green rust, constitute a proportion of the green-black semi-solid layers found within MIC formations and the black effusion noted previously (Dong et al., 2011, Little et al., 2015). As described in Section 2.1, sulfide can subsequently react with free iron ions to form iron sulfides. Jack et al. (1995) state that mackinawite is the first form of crystalline ferrous sulfide formed and that biological processes can subsequently convert this to greigite and pyrite. Jørgensen and Kasten (2006) state that mackinawite is both unstable and amorphous. According to the same report marcasite and pyrrhotite also form from mackinawite but are the product of abiotic pathways only. Research by Neal et al. (2001) disagrees as to the first sulfide mineral formed. They observed that formation of pyrrhotite was produced initially, though they suggest that this different observation was due to the presence of oxide minerals at the metal surface. Smythite has been shown to originate from both siderite (FeCO_3) and pyrrhotite (Furukawa and Barnes, 1996): it is the abiotic product of carbonate displacement by sulfide under neutral to basic conditions; and the product of the exsolution of high-temperature pyrrhotite. Pyrite was also observed to form directly without these intermediates in pore water already saturated with pyrite (Giblin and Howarth, 1984).

Refait et al. (2003) noted the preferential formation of sulfate green rust over chloride green rust during microbially influenced corrosion despite high chloride conditions in the surrounding environment. This was taken as evidence of the greater stability of sulfated forms of green rust over chloride green rust, but due to the affinity of ferrous and ferric ions for chloride, the explanation may be the high concentrations of biogenic sulfate in the immediate corrosion environment. As discussed previously the microbial activity within MIC is associated with local increases in acidity. Carbonate is thermodynamically unstable in low pH environments, thus making carbonate green rust formation unfavourable. Herro (1998) noted the occurrence of a final liquid layer at the metal surface composed of mainly ferrous, chloride and sulfate ions. A study by Sarin et al. (2004) made no reference to this final layer but noted an increasing degree of porosity to

the core region closer to the metal surface. They were also able to differentiate three main regions within the core: the outermost has a composition most closely reflecting the outer crust layer and is mostly composed of goethite and magnetite; the middle is the location for mainly green rusts and veins of magnetite (Little and Lee, 2007); and the innermost region is richest in goethite and maghemite. The occurrence of ferric minerals transitioning to mixed oxidation state iron compounds and then to ferrous compounds is evidence for an increasingly anoxic environment towards the metal surface.

When comparing the chemical composition of microbially influenced corrosion found in tidal environments to that of normal water corrosion (Section 2.5.3) it is evident that there are many similarities. However, there are also significant mineralogical differences. Hematite is noticeably absent despite conditions within the formations favourable to the formation of another common ferric oxide maghemite. Hematite was reported in deep sea rusticles by Stoffyn-Egli and Buckley (1993) but does not appear to be a feature of tidal MIC. Research by Little et al. (1998) and Neal et al. (2001) suggests that hematite is not stable in the presence of sulfate-reducing prokaryotes, and that this form of ferric oxide is rapidly reduced to the iron sulfide pyrrhotite. Studies also fail to describe akaganeite and chloride green rust despite high chloride conditions. This is consistent with the preferential formation of sulfate green discussed above. Due to this, it is probable that maghemite formation occurs via either the sulfate green rust pathway, the direct oxidation pathway to lepidocrocite and then goethite, or the oxidation pathway via ferrihydrite to lepidocrocite and/or goethite (Figure 2-5). Conditions also do not seem to favour the fast oxidation pathway to ferrihydrite as this mineral is also not apparently described. Siderite is also not observed within MIC. Its formation would require neutral to basic conditions, as described in Section 2.5.3, and would therefore not be stable in the low pH core region. It is therefore feasible that these minerals may provide a diagnostic method to differentiate between MIC and NWC, despite not currently being a recognised methodology.

2.6 Global distribution and financial implications of marine MIC

In step with the research to understand the mechanisms of MIC, there was also a gradual increase in general awareness as to the diverse environments that could be affected; what started with buried iron pipes and fuel tanks expanded into almost every environment

where microorganisms contact with unprotected metals. Research interest into the microbial corrosion of carbon steel in the presence of seawater has always apparently been low in comparison with that into oil and gas pipelines, or concrete sewer infrastructure. Nevertheless, marine MIC was being reported in Australia, Canada, South Africa, the United States, and areas of Northern Europe by the 1980s. Within the British Isles marine MIC was firmly identified during the mid-1980s (British Standards Institute, 2000) and by the turn of the 21st century over 80 coastal port locations alone had reported its effects (International Navigation Association Work Group 44 of Maritime Navigation Commission, 2005). The financial cost of this to port authorities, companies and governments is difficult to estimate, however. It has been estimated that financial costs due to all forms of MIC are 0.4% to 0.8% of GNP within industrialised nations (Liengen et al., 2014), and that globally 6% of costs to maintain in-land steel infrastructure are due to MIC damage (Heitz et al., 1996, Bolton, 2002). The damage to oil and gas industries amounts to 2 billion USD per annum (Zhu et al., 2003); in Northern Europe MIC damage to sewers constitutes 10% of total sewage treatment costs (Zhang et al., 2008); and globally the total cost of MIC is in the order of billions of US dollars per year (Hewayde and Nehdi, 2007). Little data is available to indicate the financial burden upon coastal port facilities in combating MIC on steel piling. This is possibly because MIC remediation costs are relatively small and become subsumed into the overall cost to regularly maintain marine steel installations, but perhaps also because the ramifications of marine MIC are fewer compared with oil pipeline infrastructure for example. Corrosion monitoring and structural assessment of exposed piling sections is relatively simple to perform even in permanently submerged locations, and thus catastrophic failure is rarely an issue in properly maintained installations. Buried oil pipelines are considerably less accessible, more difficult to monitor, and thus unexpected failure, possibly leading to loss of life, far more common (Li, 2015).

2.7 Corrosion control

In general, marine steel piling is often not actively protected from corrosion following installation, though several methods are available to mitigate its effects. The cost to install piling made from materials other than carbon steel or to maintain corrosion-reducing systems are weighed against the cost to repair and re-pile, and the overall efficacy of the

techniques available. The inevitable corrosion and subsequent loss of bulk material due to exposure of seawater immersion is often mitigated by installing piling with a thickness greater than that necessary to perform its designed task. If corrosion proceeds at a predictable rate the period before replacement or repair can be estimated and planned for.

2.7.1 Alternative materials

Perhaps the most effective way of avoiding degradation of marine piling is to substitute an alternative material that is not subject to the same damaging effects. Any potential material must possess suitable compressional and tensional properties and be cost effective to manufacture and install.

Reinforced concrete is a robust construction material and is used to a limited extent in quayside installations; it is also one of the least expensive alternatives to manufacture compared with carbon steel piling, and precast piles can be driven in a similar fashion (Section 2.5.2). However, installation costs of the nearest equivalent concrete construction are typically double that of piled steel and the material lacks its versatility (iSheetPile, 2009). In addition, concrete is not immune to environmental damage. The material is susceptible to many forms of attack, though that of naturally occurring metal sulfates is one of the most common. These compounds react with the hydrated calcium aluminate cement paste forming calcium sulfoaluminate, which leads to expansion and eventual breakdown (Tomlinson and Woodward, 2014).

Stainless steel possesses many key properties that make it an ideal alternative to carbon steel: it is both strong and significantly more corrosion resistant even in marine environments (Akpa, 2013). However, as discussed in section 2.5.3, its manufacturing costs normally preclude its use in this field.

Composite materials such as fibre-reinforced polymer and structurally reinforced plastic have been adopted for some piling applications in the marine environment. Composite piles are both corrosion and impact resistant, as well as being lighter and easier to handle than either steel or concrete piles. Their current marine use is limited however and is mostly to provide an alternatives to timber in protective fenders. A fuller utilisation of these types

of pile currently appears to be held back by a lack of long-term load bearing and structural characteristics data (Zyka and Mohajerani, 2016).

2.7.2 Cathodic protection

Two forms of cathodic protection (CP) are commonly used to reduce normal corrosion: sacrificial anode (CPSA) and impressed current (CPIC). Their value in mitigating the effects of MIC is a subject of current research.

2.7.2.1 Sacrificial anode

Cathodic protection by sacrificial anode (CPSA) is a relatively simple passive technique which utilises metal blocks of a lower electrode potential than the material to be protected. The blocks are connected to the protected surface by electrical cable or physical contact so that a free flow of electrons can occur. The short-circuited galvanic cell model (Section 2.5.3) is still applicable, except whereas iron was the source of electrons before the sacrificial metal now provides these, and so the corrosion current is reversed. The sacrificial anode thus corrodes in preference to the protected material, which becomes the cathode in the circuit. Blocks of the sacrificial metal such as zinc are welded or bolted directly to the surface of the material to be protected. The technique is associated with low installation costs but is relatively expensive to maintain despite its simple technology due to the reoccurring cost of replacement sacrificial anodes. As the technique also requires an electron pathway between the sacrificial metal and the oxidizing agent, it is commonly employed in immersed environments and so is commonly used to protect ship and boat hulls (Botha, 2000). The technique has also been applied to marine steel piling (Guezennec, 1994, Roberge, 1999), but its efficacy in controlling MIC is uncertain. Currently research into MIC control using cathodic protection mainly focuses on impressed current systems.

2.7.2.2 Impressed current

Cathodic protection by impressed current (CPIC) utilises an external direct-current (DC), or, more usually, a rectified alternating-current (AC) power source in place of a sacrificial anode. The negative terminal of the power supply is connected to the protected structure,

and its positive terminal is connected to an auxiliary anode. The auxiliary anode is constructed from a material of low electronegativity such as graphite or platinum plated titanium and located within the same electrolyte as the protected material, thus completing the circuit. The power supply opposes the corrosion current by providing a flow of electrons into the protected material, turning it into the cathode of the circuit. As the input voltage is regulated the system has the advantage of controllable levels of corrosion protection. Additionally, CPIC promotes a secondary corrosion impeding process previously discussed in Section 2.5.3; the inflow of electrons tends to force the cathodic reaction of oxygen and water forming hydroxide ions (Equation 2), which promotes subsequent reaction with seawater calcium and magnesium ions producing surface layers of aragonite and brucite (Equation 11, 12, and 13) (Smith and Paul, 2015, Yang et al., 2015). Tu and Cottis (2009) suggested that promotion of these minerals could impede the progress of MIC. However, their research was conducted on clean steel coupons and excluded any form of microbial investigation. A study by Jansen et al. (2017) revealed that MIC-related biofilms were unaffected by CPIC once established. Furthermore, they observed that localised CPIC-induced pH increases were insufficient to promote formation of aragonite and brucite layers.

Compared with sacrificial anode, capital costs for impressed current systems are higher due to the necessary power supply, auxiliary anode, and cabling. Also, the recurring cost of supplying the system with electricity must be considered (Roberge, 1999). In addition, if the protected material is made excessively negative direct reduction of water can occur (Equation 14).



The hydrogen can be absorbed by the steel which subsequently suffer from surface cracking and loss of ductility due to increased pressure at the metal grain boundaries (Dear and Skinner, 2017, Industrial Metallurgists LLC, 2020).

2.7.3 Anodic Protection

Anodic protection (AP*) superficially resembles CPIC as it too utilises an externally applied DC current to control corrosion. However, the current flow is reversed so that the protected structure is made the anode in the circuit and the auxiliary electrode becomes the cathode (Bolton, 2002). Current is precisely controlled to promote the formation of layers which render the metal surface passive to corrosion and consolidate existing layers (Snow, 2001). The technology is relatively new compared to CPIC and requires more active components to operate, resulting in a high establishment cost. Operating costs are considerably lower, however, as there are no perishable components, unlike CPSA, and current levels are considerably less than used in CPIC. Careful design of installations is necessary, and it is mainly effective in controlling corrosion in stable environments only: protection of carbon steel storage tanks is a common application. Its value in controlling either NWC or MIC in marine environments is uncertain due to the inability of the steel to form reliably passive layers in this environment (Roberge, 2006).

2.7.4 Biocide treatment

To control the growth of biofilms and microbial communities, chemical treatment of affected infrastructure is often carried out. This technique lends itself mostly to enclosed environments such as water pipework networks, drilling rigs or water injection plant, where biocide doses can be circulated at precise concentrations to all parts of a system. Chemicals that have been successfully used to reduce damage due to MIC in water and oil systems include oxidizing agents such as chlorine dioxide and ozone; and non-oxidizing compounds such as isothiazolones, quaternary ammonium compounds (QUATS), and glutaraldehyde (Videla and Herrera, 2005, Sztyler, 2014). An alternative approach to chemical biocides is to introduce chemicals that selectively promote microbes that can mitigate the effects of other microorganisms. Nitrate and nitrite treatment are examples of such a technique. Addition of nitrate compounds encourages growth of bacteria, such as *Thiomicrospira* sp. and *Desulfotignum* sp. within an existing biofilm. These nitrate-reducers oxidize sulfide to sulfur or sulfate whilst reducing nitrate and nitrite to nitrous oxide, or nitrogen. The removal of sulfide produced by the sulfate-reducing prokaryotes mitigates subsequent acid corrosion (Voordouw et al., 2002).

Studies indicate that stable biofilms can form under these circumstances, resulting in long-term corrosion reduction comparable to that obtained using biocides, but without the risk of eventual community immunity (Bodtker et al., 2008).

2.7.5 Protective coatings

Any coating that isolates a vulnerable surface from attack will provide some degree of protection. Perhaps the simplest form of protective coating is that offered by layers of paint. Most applicable to external metal surfaces, these forms a barrier to water and oxygen, preventing electrochemical reactions associated with normal corrosion. As observed by Little et al. (2020), methods designed to protect against MIC are typically based on those used against conventional corrosion, though unmodified paint finishes can be ineffective against MIC as abraded pits or pinholes can form points of attack for microorganisms (Tomlinson and Woodward, 2014). For this reason, coatings based on polyurethanes, epoxy resins, polyvinyl chlorides, and silicones are often utilised to reduce microbial adherence and inhibit the growth of biofilms (Guo et al., 2018). To protect a pipe section, where the most important surface is internal, these are often added during manufacture, or if the surface is external, the protective coating can be applied following installation. These coatings often incorporate biocide to enhance their efficacy. For example, the addition of coal tar to epoxy coatings (CTE) greatly enhances their ability to impede the growth of microorganisms (Videla, 2002). However, the toxicity of coal tar and similar chemicals have led to bans in Europe and the US (Jagtap et al., 2013), so alternatives have had to be developed. Quaternary ammonium compounds mentioned in the previous section have been successfully incorporated into polymer coatings and have been found effective at impeding MIC-associated biofilms. These compounds act as both effective low-toxicity biocides and corrosion inhibitors (Videla, 2002). Alternative biocide impregnated coatings exist in the form of conductive polymers; as well as impeding normal corrosion they have also been found to be effective at reducing MIC damage. These polymers possess surface nitro groups (-NO₂); the fractional positive charge on the nitrogens disrupt the negatively charged bacterial cell walls, killing the microorganisms in contact with the surface (Abdolahi et al., 2014).

2.8 Techniques in microbial influenced corrosion research

This section introduces techniques that have been utilised or are relevant in the field of MIC research.

2.8.1 Functional gene analysis by GeoChip microarray

As discussed in Section 2.2, several types of microorganism have been linked to marine MIC and within each type, several genera have been identified as significant. Mostly these data have been collected using either culture-based studies, or laboratory-based environmental simulations using identified species singly or in small complementary groups. This approach is still in widespread use in MIC research and capable of producing significant results (Beech and Campbell, 2008). Microbial culture techniques are also commonly used in MIC studies as a step prior to analysis by other techniques such as gene sequencing (Kamarisima et al., 2018, Parthipan et al., 2018, Zhao et al., 2019, Koush et al., 2020) and electrochemical impedance spectroscopy (Ribeiro and Abrantes, 2016, Rajasekar, 2017, Rajala et al., 2019).

Complementary to this approach are metagenomic techniques that analyse the composition of a whole microbial community or sections of a community, rather than focusing on isolating individual species. One of these metagenomic techniques is the DNA microarray. This type of microarray comprises of a glass slide onto which clusters of oligonucleotides are attached. These are arranged in a grid system, with each cluster bearing an oligonucleotide sequence corresponding to a gene section from a specific microorganism. DNA is extracted from a sample, randomly fragmented, denatured and labelled with fluorescent marker molecules. When the labelled DNA is exposed to the microarray the DNA fragments hybridize to complementary probes. The fluorescence of each probe cluster is then imaged to provide a qualitative representation of the abundance of each gene in the identified microorganism. It should be noted that DNA microarrays can also utilise mRNA in place of DNA, and by using a reverse transcriptase step to synthesize complementary DNA (cDNA) can provide data about the level of gene expression within a sample rather than simple gene abundance.

GeoChip has been utilised in several functional gene diversity studies, in a range of applications including clinical diagnostics (Verma et al., 2018); deep sea (Wang et al.,

2009), groundwater (Low et al., 2016, Jiang et al., 2019), and soil ecology (Tu et al., 2014, Cong et al., 2015); biomining (Niu et al., 2016), wastewater treatment (Wang et al., 2014), and agricultural (Ma et al., 2019) and ground pollution monitoring (Xie et al., 2011, He et al., 2018). The technique has also been employed in MIC studies in oil pipeline systems (Sztyler, 2014) and copper-nickel alloys in the marine environment (Cieslak, 2012).

GeoChip, like all microarrays is a ‘closed-format’ technique (Zhou et al., 2015). The finite number of probes on a microarray slide sets a practical upper limit on target genes and microbial taxonomy that can be discerned using the technique. In addition, only probe sequences which have been isolated previously using an ‘open-format’ technique such as gene-sequencing, can be included in the slide design.

2.8.2 Functional gene analysis by Next Generation Sequencing

Next Generation Sequencing (NGS) is the term given to the latest series of techniques that provide gene sequencing data from biological samples. Next Generation Sequencing systems can be classified into four main categories: Pyrosequencing; Ion semiconductor sequencing; sequencing by ligation; and sequencing by synthesis (Heather and Chain, 2016). Each have advantages over older sequencing method; one of the most significant is their extremely high through-put: a whole human genome can be sequenced using some NGS methods in a matter of days, whereas with the older, but still utilised technique, Sanger sequencing, would take more than a decade to deliver the same data (Behjati and Tarpey, 2013). Sanger sequencing was developed during the late 1970s before becoming available on a commercial scale from the mid-1980s. It is still used extensively in the clinical field and considered the gold standard technology for validating data obtained from NGS techniques (Thermo Fisher Scientific, 2021). Though it is increasingly demonstrated that NGS systems possess a reliability that often equals (Sikkema-Raddatz et al., 2013) or surpasses (Beck et al., 2016) that of Sanger sequencing.

A basic overview of Sanger sequencing is relevant to understanding the NGS methods above. Sanger sequencing is a post PCR method of gene sequencing that utilises a primer, DNA polymerase, normal deoxynucleotide triphosphates (dNTPs), and modified dideoxynucleotide triphosphates (ddNTPs). The latter lack a 3’ hydroxyl group, so act as

chain terminators, and incorporate a fluorescent dye molecule. The DNA sequence to be analysed is first amplified and the amplicons denatured. The primer anneals to the 5' end of the single stranded DNA template; and the sample is split into four subsamples. The DNA polymerase is added to each subsamples along with all four dNTPs. A single type of ddNTP is added to each subsample. The polymerase attaches nucleotides until a dideoxynucleotide is added and the chain is terminated. As the polymerase utilises both types of nucleotide equally, the termination can occur at any position on the chain, resulting in chains of all possible lengths being formed, each ending in a ddNTP. The products are then electrophoresed, and the fragments separate according to their length. The fluorescence of the ddNTP is used to construct the gene sequence.

Whilst the NGS techniques above performs sequencing using a slightly different method, they share some similar features: each requires a library of randomly fragmented target DNA to which two oligonucleotide adaptors are ligated; all utilise solid support bearing binding sites complementary to the adaptor sequences; and all carry out bridge amplification of the template prior to commencing their sequencing cycles. The solid support is located within a flow cell, which allows for rapid introduction of nucleotides; the flushing away of the same at the completion of a cycle; and measurement of the resulting signal. The array of binding sites is a significant contributor to the through-flow capacity of the systems, allowing thousands to billions of sequencing reactions to occur simultaneously (Metzker, 2010).

In Pyrosequencing, single stranded DNA fragments are ligated to an adaptor sequence onto which the primer can anneal. In addition to the DNA template, DNA polymerase, primer, and four dNTPs, the reaction mixture includes ATP sulfurylase, apyrase, luciferase, and the substrates adenosine 5' phosphosulfate (APS) and luciferin. The sequencing proceeds by exposing the sample to one type of dNTP at a time. When an addition to the chain occurs, the nucleic acid polymerisation results in the release of a pyrophosphate (PPi) group. The PPi is then involved in a series of chemical reactions with the ATP sulfurylase, apyrase, luciferin, and the substrates, thereby generating light, which can be detected and the corresponding base recorded in the sequence (Gharizadeh et al., 2007). Limitations of the technique are the number of reads (approximately 300 to 500) compared with Sanger sequencing (800 to 1000 typically); the high reagent cost; and a high rate of errors when strings of sequences of 6 or more of the same base are

present (Fakruddin and Chowdhury, 2012). In the field of MIC research Pyrosequencing has been used to investigate acetogens in biofilms (Mand et al., 2014).

The sequencing reaction used in Ion semiconductor sequencing is like that of Pyrosequencing: the DNA template with ligated adaptor is exposed to one type of dNTP at a time in the presence of a DNA polymerase. The addition of a nucleotide results in release of a hydrogen ion. A semiconductor diode in contact with the fragment detects changes in solution pH and the current nucleotide type is recorded in the sequence. This technique has cost advantages over pyrosequencing as the additional chemicals and substrates noted above are not required (Rothberg et al., 2011, Merriman et al., 2012).

Sequencing by synthesis utilises reversibly fluorescent and terminated nucleotides. All four nucleotides are added at the same time, and once the DNA polymerase incorporates the appropriate nucleotide the remainder are removed from the reaction mixture. The fluorescence signal is then recorded. Following this, the fluorescent molecule and terminator are cleaved from the chain and removed leaving a 3' hydroxyl group intact; the cycle then repeats. It improves on pyrosequencing by allowing all four nucleotides to be introduced at the same time and does not suffer from errors due to strings of the same base. Error rate increases with read length however, due to incomplete removal of fluorescent signal. This is currently the most popular NGS technique available and has been widely applied within the environmental field: Ben Abdallah et al. (2018) and Walden et al. (2017) used Illumina NGS to investigate microbial populations in hypersaline lake water and wastewater samples, respectively; Huang et al. (2019) assessed changes in microbial communities in MIC under differing steel surface conditions; whilst Liang et al. (2016) assessed community structures in oil pipelines affected by MIC using this technique.

The fourth commonly employed NGS method, sequencing by ligation, is unique amongst this group as it utilises a DNA ligase in place of a DNA polymerase. The single stranded DNA fragment with adaptor and primer is exposed to 8-mer oligonucleotide probes. Each oligo sequence begins with the target base at its 3' end, followed by a different but specific base, then six degenerate bases, and finally a fluorescent dye molecule at its 5' end. The combinations of first and second bases results in sixteen probe types, allowing all possible two base sequences to be

represented. Once a corresponding probe anneals to the DNA fragment, the remainder are removed from the solution. The fluorescence of the new probe is recorded, after which the last three degenerate bases and the fluorescent dye are cleaved and washed away and the cycle recommences. Following approximately seven ligation cycles, the DNA strand is denatured. A new primer introduced, which anneals to the adaptor offset by one base, and the whole process repeats. This overall operation is carried out a total of five times, forming sequences that when collated identify each base present in the DNA fragment (Ho et al., 2011, Huang et al., 2012).

2.8.3 Genetic diversity analysis using High-resolution melt

High-resolution melt (HRM) is an analytical technique that has been utilised in studies to detect mutations, polymorphisms, and methylation in DNA samples (Thermo Fisher Scientific, 2018). It is a technique that usually takes place immediately following and in the same apparatus as polymerase chain reaction (PCR). As PCR proceeds, dye molecules previously included in the reaction mixture begin to chelate with the PCR products. Once PCR is complete the cycler will switch to the HRM cycle, during which time the temperature will be gradually increased to a pre-set maximum (generally ≈ 95 °C). As the temperature increases, the double-stranded amplicons begin to denature. The dye molecules are designed to fluoresce only when bound to double stranded amplicons, so the sample fluorescence is at a maximum initially that decreases as the temperature increases. The decrease in fluorescence is measured at each temperature change step and the data plotted as a melt curve. By comparing the profiles of different samples, variations in base-pair composition can be determined. The resolution is such that single base-pair variations can theoretically be differentiated. This technique has been mainly used as a high-throughput method in single genera and single species studies in food safety (Liu et al., 2018) and human (Woksepp et al., 2011, Gurtler et al., 2012, Sánchez et al., 2017), animal (Souza and Falcão, 2012, Titov et al., 2015) and plant pathology (Gori et al., 2012). The techniques is also applicable to community studies, and has been adopted in a limited number of metagenomic studies (Hjelmsø et al., 2014).

2.8.4 Genetic diversity analysis using Denaturing gradient gel electrophoresis

Denaturing gradient gel electrophoresis (DGGE) utilises a denaturant containing polyacrylamide gel to differentiate samples according to base-pair composition. This contrasts with conventional electrophoresis which differentiates samples according to sequence length. The technique was first used during the 1980s to provide molecular fingerprinting data (Lerman et al., 1984, Meyers et al., 1987). Since its initial demonstration, DGGE has been extensively utilised for elucidating the microbial variations in various environments (Porcellato et al., 2012). In MIC research, it has been a primary tool in identifying sulfur-cycling microorganisms; Muyzer et al. (1993) demonstrated its value in differentiating community composition relative to reference cultures of sulfate-reducing and sulfur-oxidizing bacteria and methanogenic prokaryotes. Similarly, Geets et al. (2006) showed that the technique could be used to discern up to twenty species of sulfate-reducing prokaryotes.

As with other electrophoresis-based techniques, DGGE provides qualitative differentiation between samples; the presence and position of bands indicates variations in a gene sequence. The gene selected for analysis would be targeted by specific primers during PCR. When initially introduced, quantitative analysis using DGGE required the inclusion of known species possessing the target gene, to act as standards. The efficacy of this approach was initially limited by the number of standards that could be included in a gel relative to the number of samples, and the availability of those standards. As the cost of gene-sequencing has decreased in recent years, it has become common to include this technique as a step following to gel imaging (Heather and Chain (2016)). This has been adopted in some SRP related DGGE studies, though the process requires careful excision of individual gel bands and subsequent cleaning stages before analysis, and has been used successfully to assign species data to individual bands (Miletto et al., 2007, Besaury et al., 2012, Heather and Chain (2016)).

The denaturing component of the gel is commonly composed of urea and formamide (Wang et al., 1995); DGGE utilises the denaturing properties of these compounds to successively break the hydrogen bonds between base pairs in DNA samples across an increasing denaturing gradient. As bond strength between base pairs is determined by the

number of hydrogen bonds present and base stacking (Yakovchuk et al., 2006), guanine-cytosine (G-C) pairs possess a greater stability, compared with adenine and thymine (A-T). Therefore, the higher the proportion of G-C pairs in the PCR amplicon, the further across the gel the product will travel before becoming fully denatured. Fully denatured amplicons would continue to process through the gel, so to impede their movement a 40 to 60 guanine and cytosine nucleotide ‘GC-clamp’ is included when the forward primer is designed. This additional section of oligonucleotides does not anneal to the 3’ end of the DNA template with the primer but becomes incorporated into the amplicon during successive PCR cycles. This G-C sequence strongly resists the denaturing gradient and is long enough to remain intact across the entire denaturing gradient. The GC clamp with denatured amplicon will tend to spread out and their combined drag counteracts the potential difference across the gel, effectively halting the movement of the amplicon (Muyzer et al., 1993, Wu et al. (1998)).

2.8.5 X-ray powder diffraction

X-ray powder diffraction (XRD) is a non-destructive technique that is primarily used to identify crystalline materials. X-rays have a wavelengths close to the distance between atoms within a crystalline solid, so can interact with the atoms and become scattered. Strong amplification of this emitted signal will occur at angles related to the spacing of the atoms due to constructive interference between the X-rays. This diffraction of the X-ray beam is key to identifying the material. X-ray powder diffractometers comprise of an X-ray source, a sample platform, and an X-ray detector. The sample is first ground to obtain a uniform composition then placed in a sample holder. This holder rests on the sample platform, which is either held stationary or slowly rotated whilst the source and detector move relative to the sample. As the angle between sample, the source and detector changes, the diffraction signal is recorded. This is usually displayed as a diffractogram, with angle plotted vs signal strength. The position of peaks can be cross-referenced with known patterns and the mineral composition determined (Holder and Schaak, 2019, Dutrow, 2020, SciMed, 2021).

The technique has been used to characterise corrosion products in various normal corrosion and MIC-related studies, especially including those concerned with iron oxyhydroxide minerals (Antunes et al., 2014, De la Fuente et al., 2016), iron oxides and

hydroxides (Fei et al., 2013, Rahman et al., 2014), and green rusts (Refait et al., 2006, Guilbaud et al., 2013, Genin et al., 2014), as well as reduced sulfur minerals (Yang et al., 2016, Dong et al., 2019). Similarly, the use of XRD to investigate the composition of marine sediment has been widespread (Roberts and Turner, 1993, Dvorkin et al., 1999, Andrews et al., 2006, Veerasingam et al., 2014).

2.8.6 Fourier-transform infrared

Fourier-transform infrared (FTIR) is an important analytical technique that allows identification of minerals, compounds, and chemical species by detection of vibrations that are characteristic of their structure. Infrared spectrometers typically utilise electromagnetic radiation in the 0.7 μm to 1000 μm range. By convention, this range is stated as reciprocals of wavelength, or ‘wavenumber’ with units of cm^{-1} . In general, wavenumbers above 1500 cm^{-1} fall in area where there are relatively few responses for each functional group, as is thus known as the ‘functional group region’, and those below 1500 cm^{-1} fall into what is known as the ‘fingerprint region’. This latter region tends to possess more complicated patterns, which can be key to identify complex compounds. Conventional infrared spectrometers expose the sample to a monochromatic IR light source multiple times, adjusting the wavelength following each exposure. Fourier-transform is a development of this technique and employs several wavelengths per exposure. The process repeats several times in rapid succession with different wavelength combinations. The raw data form an interferogram containing all the sample absorption data. This is subsequently processed by computer using the Fourier transform algorithm, separating the absorption or reflectance values for each wavenumber. The technique has several advantages over conventional ‘scanning’ infrared spectroscopy including a higher signal-to-noise ratio, and greater stability and accuracy of the IR light beam (Faix, 1992, Vlachos et al., 2006, Fan et al., 2018).

This technique has also been successfully employed to characterise iron corrosion products such as magnetite, hematite, maghemite, goethite, ferrihydrite, lepidocrocite (Balasubramaniam and Kumar, 2000, Neal et al., 2001, Balasubramaniam et al., 2003, Chaki et al., 2015, Jaen and Iglesias, 2017), green rusts (Peulon et al., 2003, Legrand et al., 2004, Zegeye et al., 2007), and other minerals and chemical compounds as summarised in Appendix H.

2.8.7 Inductively coupled plasma optical emission spectrometry

Inductively coupled plasma optical emission spectrometry (ICP-OES) is a powerful tool for determining the elemental composition of a wide range of samples. It is suited to analysing both liquid and gaseous samples. Solid phase samples require preparation before they can be analysed, however: either extraction or acid digestion are necessary. (Hou and Jones, 2000). The principle of operation relies on emission of light from atoms which possess electrons above their ground state. The ICP-OES spectrometer includes an argon plasma torch that provides the necessary energy to excite electrons in the sample to higher energy states. These excited electrons then release the energy in the form of light and return to their ground state. As the wavelengths of the emitted light is characteristic of the element(s) present, identification of the elemental composition of the sample is possible. The technique can discern concentration based on intensity of emitted light as well as identifying multiple elements within a sample.

This analytical technique has been used extensively to analyse elemental composition of samples taken from It has also been routinely used for the analysis of marine sediment (Buccolieri et al., Pozebon and Martins, 2002, Hennekam and de Lange, 2012, Chand and Prasad, 2013), as well as several MIC-related environments, including those of clinical implants (Mombelli et al., 2018), geothermal installations (Madirisha et al., 2020).

2.9 Summary

Microbially influenced corrosion is a global phenomenon, that has been identified in several diverse environments. Its occurrence is associated with accelerated rates of material deterioration compared with non-biological corrosion and a premature need to repair or replace damaged infrastructure. This often carries with it a significant financial burden. Measures that can be employed to control the progress of MIC are numerous, but their applicability between environments can be variable and efficacy uncertain and are always associated with additional financial costs.

Research has identified features of MIC that appear to be consistent regardless of environment. These include a complex microbiota, the members of which drive specific chemical processes that degrade the substrate material, and the presence of biofilms that

help maintain microenvironments suitable for the microbial community along with physical protection. Sulfate-cycling bacteria have been the most extensively studied member of these biofilms and the most consistently linked to MIC processes. Other microbial groups have also been demonstrated to augment the corrosion process, including nitrogen cyclers, acetogens, methanogens, metal reducers and oxidizers, fermentative microorganisms, and hydrocarbon-degraders. Advances in genetic research have allowed these groups to be identified and quantified according to specific functional genes.

Several analytical techniques have been employed with the MIC field of research. These have ranged from microbiological methods employing functional genes to obtain an insight into the composition of microbial communities, through to techniques that can be used to detect the 'footprint' of microbial activity either through mineralogical or chemical means.

Research in the field has mostly been concentrated within the petroleum industry. Corrosion of carbon steel piling in the marine environment by MIC has been less extensively researched but is nevertheless recognised as being of concern to those operating harbour and commercial port facilities.

Chapter 3 Methodology

To address the research aims for this project, practical work was undertaken. This comprises two main parts: field work, and laboratory analysis.

The field work section comprises of an overview of the sampling site, and site work procedures. The latter is subdivided into seawater data collection (tidal range and turbidity) and sample extraction methods (corrosion, marine sediment, and seawater). The purpose of seawater data collection was to provide an environmental context for samples subsequently extracted and to assist in the interpretation of data patterns that may have arisen during analysis; the intention of corrosion, marine sediment, and seawater was to provide samples for subsequent laboratory analysis.

The laboratory work sections branch into five main analytical methodologies: functional gene analysis (Low tide zone corrosion, marine sediment, and seawater samples), genetic diversity analysis (corrosion taken from vertical locations on a steel pile, and low tide zone corrosion, marine sediment, and seawater samples), mineralogy (low tide zone and vertical profile corrosion, and marine sediment), chemical analysis (low tide zone and vertical profile corrosion), and elemental analysis (marine sediment, and seawater).

3.1 Field work

3.1.1 Overview of sampling site

The site chosen for the study was Shoreham Port, located on the South Coast of England (Figure 3-1). This is an active commercial facility situated at the mouth of the River Adur in West Sussex. The location has a history of use as a harbour and port which dates from before the European Middle Ages. The modern Shoreham Port is a busy facility which regularly receives shipping from Scandinavia, the Baltic, Spain, and Belgium as well as numerous other UK and European ports (Shoreham Port, 2013). Annually the Port handles more than 1.6 million tonnes of cargo comprising mainly timber, steel, grain, fertilizer, oil, and aggregate (Shoreham Port, 2015). Previous studies into the cause and effects of marine microbially influenced corrosion have generally focussed on similar

working environments. An important study by Beech and Campbell (2008), which looked at the local environmental causes of MIC, was conducted on the same stretch of coastline due east of Shoreham. Other studies, which focused on rates of corrosion of piling steel or analysis of the microbiota found on corroded steel piling in coastal locations like Shoreham Port include those conducted by Melchers et al. (2014), who studied corrosion of two main types of piling (Section 2.5.2) in Newcastle Harbour, NSW, Australia; Usher et al. (2014) who focused on tubercle microbiota of corrosion formations in Fremantle Harbour, WA, Australia; and Bermont-Bouis et al. (2007) who targeted biofilms in their investigation based in Cherbourg Harbour, France. Shoreham Port is therefore a site typical of previous studies: in addition to reported occurrences of MIC, it occupies a coastal position that regularly receives commercial shipping, and the sample location is exposed to a regular tidal cycle.

Shoreham Port comprises of three principal areas: the Western Arm, which includes a 1.2 km section of the river Adur; the tidal Eastern Arm, which lies close to the out-flow of the Adur River; and a non-tidal area known as the Basin, which is separated from the tidal sections via a series of locks (Figure 3-2). Berthing and loading and unloading quays are present on the north and south sides of the Eastern Arm and Basin, and the north side of the Western Arm. The south sides of the Basin and Eastern Arm deal receive cargo of mainly timber, steel, and aggregate, whereas the northern landward sides include oil-fuel depots, a scrap-metal recycling facility, and marina for small boats and yachts. The far eastern end of the basin receives sea-going trawlers and smaller fishing boats.

All berthing areas within the port are constructed in an identical fashion: vertically driven carbon steel piling form the quay face, capped in concrete, with levelled rubble infill and tarmac top layer behind. Estimates of the tidal and non-tidal areas perimeter indicate the presence of approximately 6 km of steel piling. The piling is a mixture of both U-profile and Z-profile types (See Figure 2-3). The age of much of the piling installed prior to 2005 is not known due to an incomplete record of piling events from earlier years; where Port Authority records exist, some sections of the piling wall can be dated back to the early 20th century.

Inspection of the piling wall is carried out periodically by port staff, and areas of corrosion consistent with the physical appearance of MIC were initially noted prior to 2011.

Increased rates of damage due to corrosion, and MIC-like formations have been observed in all three principle areas under port jurisdiction (Rousell, 2012).

The choice of monitoring and sampling within Shoreham Port was based upon four main criteria: a tidal location; evidence of MIC occurrence on the piling steel; accessibility at the location for sample extraction; and minimised risk working within the port environment. The presence of MIC was indicated by data from Shoreham Port authority survey reports; and the suitability of access and safe working was decided during consultation with the port management staff and subsequent visual inspection of the site.

The location selected lies within the tidal Eastern Arm, adjacent the main locks, at a place known as the Dredger Berth (latitude 50.829678; longitude -0.238702). Access to the piling face and sediment bed was via a permanently moored floating jetty (Figure 3-3). This allowed sample collection throughout the whole tidal cycle. Environmental monitoring was conducted from position A; all corrosion samples were taken from the piling at position B.



Figure 3-1 Location of Shoreham Port within the British Isles
(Mapsofuk.co.uk, 2015)



Figure 3-2 Aerial view of Shoreham Port
(Shoreham Port, 2013)



Figure 3-3 Dredger Berth monitoring (A) and sampling (B) locations

3.1.2 Seawater monitoring

Tidal depth and turbidity data were obtained at the Dredger Berth using a YSI manufactured EXO2 sonde. The onboard depth sensor was rated between 0 and 100m depth, with an accuracy over this range of ± 0.04 m. The turbidity probe was designed to measured values between 0 and 4000 FNU with a $\pm 2\%$ accuracy between 0 and 999 FNU.

The device was programmed to measure these seawater conditions at ten-minute intervals.

The sonde was deployed in a semi-permanent position on the in-pan of piling adjacent the corrosion sample location. To facilitate retrieval during any point in the tidal cycle and to provide a degree of mechanical protection for the device when deployed, the sonde was installed inside a 100 mm diameter PVC-u pipe, fitted to reach from the cope to sediment bed level. The final 500 mm of the tube were perforated allowing free flow of seawater over the sonde measuring sensors. The device was positioned 50 mm from the sediment bed level and was retrievable via an attached steel chain. The sonde was recovered on a bimonthly basis and its data downloaded. Routine maintenance was also carried out at this time, comprising of battery replacement, turbidity probe calibration (using Sigma Aldrich 1, 10, 100, and 1000 FNU standards), and removal of any marine growth from the device.

The tidal data obtained over a period of twenty-four months was used to provide guidance in choosing low tide zone sampling positions on the piling under investigation, to determine the tidal range experienced at the Dredger Berth, and to indicate changes in water conditions.

3.1.3 Corrosion sampling

Corrosion extraction at the Dredger Berth provided samples from adjacent to the top of the piling down to less than 1 metre from the sediment bed level. As indicated in Chapter 2, previous steel piling MIC studies have focused on low tide zone corrosion analysis exclusively; the inclusion of samples from other vertical positions in this study was an intentional broadening of this focus.

All samples were extracted during a falling tide and during the same site visit during May 2015. Piling profile corrosion samples (C 01 to C 15) were removed in height sequence from the out-pan (Section 2.5.2) of a single piling section. Starting at 0.8 m from the top of the cope, corrosion samples were removed sequentially at 0.4 m intervals below this. The samples assigned for analysis as low tide zone corrosion (C 14a, C 14b, C 14c, C 14d, C 14e, C 14f, and C 14g) were taken from seven separate piling out-pans to the left

of that designated for profile corrosion samples All were taken from a height of 6 m below the cope (1.0 m above sediment bed level). Sampling heights were measured from the top of the cope using a tape measure; measurement accuracy was estimated to be ± 100 mm. Once a full measurement had been taken from cope to sediment bed, sampling heights relative to the bed level were calculated. A visual summary of samples vertical positions is given in Figure 3-4.

The precise method of sample extraction depended on the morphology of the target corrosion, but all observed the sterile working procedure described by Beech and Campbell (2008). Samples resembling normal rust were prised away from the piling using a sterilised craft knife, then flakes closest to the surface dislodged and dropped directly into sample bags; formations having MIC morphology were incised with a sterilised craft knife and levered away from the piling surface before having their inner contents removed with sterile tweezers and placed into grip-top sample bags. Where liquid was observed within extracted samples, no measures were taken to dry or remove this from the sample; as noted in Section 2.5.6, the liquid portion of MIC formations often constitutes the microbially active site for corrosion processes. Following extraction, the samples were immediately placed in anaerobic jars. Samples were returned to the laboratory within 8 hours and placed in a sample freezer at -20 °C; once frozen they were taken out of the anaerobic jars and the samples returned to storage at -20 °C.

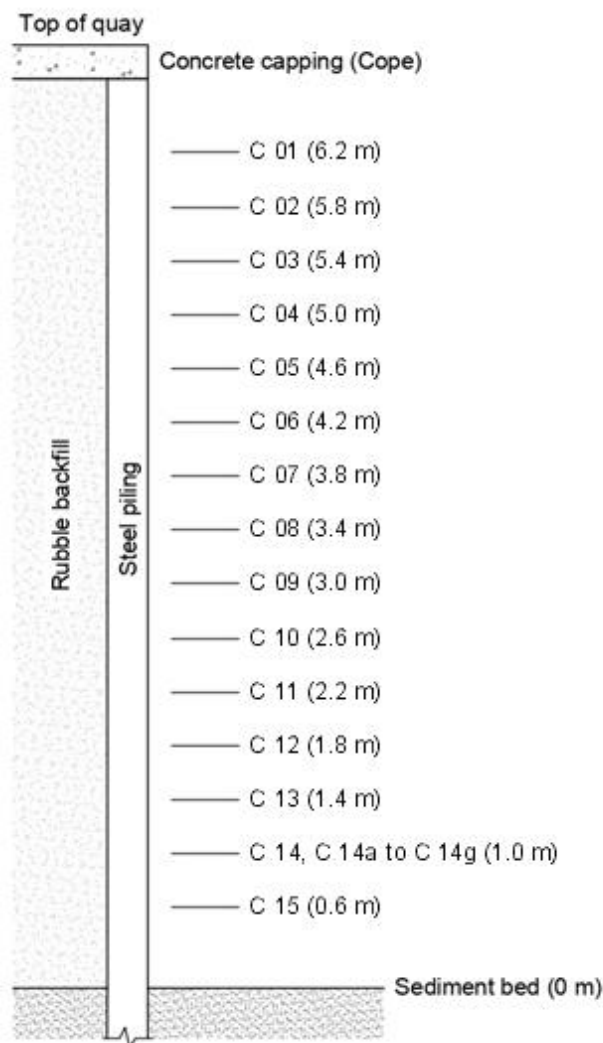


Figure 3-4 Schematic diagram of steel piling at the Dredger Berth with vertical positions and height above the sediment bed of all corrosion samples

3.1.4 Marine sediment sampling

Sediment samples were retrieved using 75mm diameter 1 m long plastic corer tubes deployed via a KC Denmark A/S Small Free Fall Corer Model 13.570 attached to an aluminium extension tube fitted hand grips (Figure 3-5). Each corer tube was pre-drilled with 5 mm diameter holes placed at 25 mm intervals along its length, to facilitate subsequent pore water extraction prior to spectroscopic analysis (Section 5.1). To allow accurate removal of sediment subsamples (Section 3.2.2) without the need to remove the core sample from the corer sleeve, each sleeve also bore a series of 5 mm high by 15 mm wide slots positioned opposite each pore water extraction hole. Both sets of apertures

were covered using duct tape prior to deployment. Practical limitations encountered during extraction resulted in removal of core sections of 500 mm, despite the length of the corer tube. Five sediment cores were thus obtained. Each was taken from adjacent to a pile used for corrosion sampling during May 2015. All were extracted from approximately 1 m from the piling face. Following extraction each core was capped and returned to the laboratory within eight hours. four cores intended for microbiological analysis were immediately placed in frozen storage at -20 °C. One core was used for pore water extraction upon return to the laboratory (Section 3.2.7), then placed in frozen storage at -20 °C with the other four cores.



Figure 3-5 Corer head with extension tube

3.1.5 Seawater sampling

Water samples were retrieved from the Dredger Berth using sterile 500 ml flasks attached to a 3 m grab arm. The flask necks were stoppered with sterile rubber bungs prior to deployment which were then released at the desired depth using an attached cord. All samples were taken during a period of low turbidity, as verified by Sonde data (see Section 4.2), during May 2015. Three batches of nine extractions were conducted on a falling tide initially. These samples were to be subsequently used for functional gene analysis; the batches were designated SW 01, SW 02, and SW 03. The sample depths

were approximately 1.0 m above sediment bed level, and whilst the seawater depth at the piling wall was approximately 2.0 m. Four additional batches of three 500 ml retrievals were carried out from adjacent to the corrosion sample piling. These were also taken from a position above the sediment bed of approximately 1.0 m, but at seawater depths relative to the piling of 4.0 m, 3.0 m, 2.0 m, and 1.0 m. The batches of three samples were designated SW 04, 05, 06, and 07, respectively. Upon retrieval the flasks were fitted with screw top lids and the water samples returned to the laboratory within eight hours of extraction. Samples were stored at 5 °C for no longer than 24 hours prior to processing.

3.2 Laboratory analysis

3.2.1 Laboratory Work Overview

The laboratory work section details the analytical techniques utilised in this study. Each method was subsequently applied to one or more environmental sample as summarised in Table 3-1. The intention to use diverse techniques on a sample type, where possible and appropriate, was to provide multiple points of verification as to the processes occurring.

Table 3-1 Laboratory methodology summary

		Environmental sample type			
		Low tide zone corrosion	Vertical profile corrosion	Marine Sediment	Seawater
Analytical category and technique	Functional gene analysis	GeoChip	n/a	GeoChip	GeoChip
	Genetic diversity analysis	DGGE/HRM	HRM	DGGE/HRM	DGGE/HRM
	Spectroscopic analysis	XRD/FTIR	XRD/FTIR	XRD/ICP-OES	n/a

Functional gene analysis via the GeoChip microarray method was applied to low tide zone corrosion, marine sediment, and seawater samples. It provides data on potential gene activity within the microbial communities of each sample group as well indicating the presence of specific microbial genera.

Genetic diversity analysis using denaturing gradient gel electrophoresis (DGGE) with high-resolution melt (HRM) was applied to low tide zone corrosion samples, marine sediment, and seawater samples. HRM alone was applied to corrosion samples taken from vertical locations on a section of piling. These techniques allow assessment of base-pair variations in specific marker gene sequences within microbially communities. Though

not providing genera or species data, they are fast and reliable methods for indicating community variability based on selected MIC-related genes.

Analysis of low tide zone and vertical profile corrosion, and marine sediment samples using powder x-ray powder diffraction (XRD) provided mineral composition data. Analysis of corrosion samples using Fourier-transform infrared spectroscopy (FTIR) provided identification of minerals, chemical compounds, and chemical species. Inductively coupled plasma optical emission spectrometry (ICP-OES) analysis was used to provide measurement of sulfur and iron concentrations at various depths in the sediment column adjacent to the corrosion sampling location.

3.2.2 Functional gene analysis using GeoChip

The microarray technique utilised in this study was GeoChip, developed by Glomics Inc. Oklahoma, USA. This is a modern functional gene microarray technique, first developed in the early 2000s (Van Nostrand et al., 2009), that has undergone continual development and improvement. The current v5.0 design utilizes more than 57000 oligonucleotide probes to discern activity in 393 gene families involved in carbon, nitrogen, sulfur, phosphorus cycling (Cong et al., 2015).

As described above the standard GeoChip microarray had been previously used in several environmental studies and has a probe composition optimised for these applications. The choice to use DNA was made instead of RNA (Section 2.8.1) due to the availability of an extraction kit of proven efficacy with corrosion samples, and the reported difficulties in obtaining high quality mRNA (Mettel et al., 2010). Before being employed its efficacy and cost were assessed relative to a custom microarray. The presence of fifteen of the eighteen genes associated with MIC chemical pathways (Table 2-2) including all the relevant sulfur and most nitrogen gene probes was judged to be suitable for this analysis and thus the standard array was employed.

Low tide zone corrosion, marine sediment, and seawater samples were subject to subsampling or separation processes prior to preparation for functional gene analysis (FGA).

Three low tide zone corrosion samples (designated C 14a, b, and c) were removed from deep freeze and examined under aseptic conditions. Sample pieces that could be subsequently split to reveal previously unexposed regions were selected. Sterile tweezers, scalpels, and spatulas were then used to remove approximately 20 g of corrosion, from which three 0.25 g subsamples were then removed for DNA extraction; the remainder being retained and refrozen for later mineralogical and chemical analysis (sections 3.2.5 and 3.2.6). The extractions were immediately processed using MoBio PowerSoil DNA isolation kit and recommended protocol (Appendix B), as utilised in corrosion studies by AlAbbas et al. (2013), Eid et al. (2018), and Liang et al. (2018). DNA quality was verified using a ThermoScientific manufactured Nanodrop Lite spectrophotometer. A DNA sample was considered viable for down-stream processing when concentration exceeded $8.5 \text{ ng } \mu\text{L}^{-1}$, and a 260/280 ratio between 1.5 and 1.9 was achieved (Glomics Inc., 2014). This was to avoid the need for multiple displacement amplification (MDA) and the risk of subsequent microbial diversity bias (Thomas et al., 2012). Extracted DNA was diluted to $8.5 \text{ ng } \mu\text{L}^{-1}$ using nuclease-free water and then stored at $-80 \text{ }^\circ\text{C}$.

To potentially increase DNA yield, a pre-extraction step based on a method by Colosi and Schaall (1993) was trialled in parallel with the protocol above. This comprised of manual sample grinding in the presence of liquid nitrogen prior to DNA extraction. However, there were no observed increases in either yield or purity, so the trial was discontinued.

Three sediment cores (SED 01, SED 02, and SED 03) were removed from $-20 \text{ }^\circ\text{C}$ storage to a sterile workspace. The duct tape covering the sediment apertures (Section 0) at 100 mm depth was removed and the exposed sediment removed to a depth of approximately 5 mm removed using a sterile scalpel. The sample depth of 100 mm was chosen following spectroscopic analysis of marine sediment samples (Section 5.1). Approximately 20 g of exposed sediment was removed from the core, from each of which three 0.25 g subsamples were removed. The 0.25 g subsamples were then immediately subject to DNA extraction using MoBio PowerSoil kit (Kerrigan et al. (2019), Ramirez et al. (2018), and Lanzen et al. (2017)), tested for concentration and purity, and stored, as per the corrosion extraction procedure above. The remaining approximate 19 g of sediment was returned to deep freeze for later processing ahead of mineralogical and chemical analysis.

Seawater samples (SW 01, SW 02, and SW 03) were subjected to membrane filtration to extract suspended solids for subsequent DNA extraction. A vacuum filtration manifold and autoclaved filtration unit with 0.45 μm filter membrane were used to remove the bulk liquid fraction of each sample. The protocol is detailed in Appendix A. Three 500 ml seawater samples were utilized per filter membrane, yielding a total of nine subsamples, in three groups of three (Section 3.1.5). DNA extraction was carried out using MoBio PowerSoil DNA (Kerrigan et al. (2019), Ul-Hasan et al. (2019)). Concentration and purity tests were immediately carried out as per corrosion and sediment subsamples, and the DNA stored as above.

Functional gene analysis using GeoChip 5.0, was carried out by a third-party specialist and developer of the technique, Glomics Inc., Oklahoma, USA. Nine each of corrosion, marine sediment, and seawater DNA samples, were transported in dry ice to the processing address. The three DNA extractions from each sample location were combined, resulting in a total of nine analytical samples: Appendix C details the subsequent sample processing.

The fluorescence data subsequently received was initially analysed using the Data Analysis Pipeline provided by The University of Oklahoma (<http://ieg.ou.edu/microarray/>). Alpha-diversity (average species diversity) was calculated using Simpson Index (1-D), Shannon-Wiener Index (H), and Shannon evenness (J) for each of the nine samples (Appendix D). Simpson Index and Shannon Index both incorporate community richness (number of groups with each sample) and abundance (number of individuals per sample) to calculate diversity. Simpson Index is a weighted arithmetic mean of proportional abundance; it measures the probability that two randomly sampled individuals will be of the same type; lower probability indicates greater diversity (Kiernan, 2020). Simpson index (D) can also be calculated in its reciprocal form, which always produces a diversity ≥ 1 but which is unbounded, so is often expressed in its complementary term 1-D. This limits diversity values to between 0 and 1; with 0 denoting no diversity and 1 indicating infinite diversity. Shannon-Wiener Index (H) is based on the measurement of uncertainty: in communities with low diversity the uncertainty of prediction is also low, so there is a higher probability that a sampled type will be a dominant within the community. The Index is sensitive to the number of species, so is often considered to be biased towards measuring species richness (Morris et al.,

2014); the minimum value for H is zero. Shannon evenness is a measure of how homogeneous a community is in terms of the abundance of the groups present. It has a range of 0 to 1, where lower values indicate a greater variation in abundance of the groups present in the community. The method is highly dependent upon sample size and extremely sensitive to small sized groups (Logan, 2011).

The GeoChip data was then analysed using Microsoft Excel 365 software. Activity data corresponding to genes implicated in MIC were extracted (Section 2.3), except for *nxr* (nitrite oxidoreductase), *feR* (ferric reductase), and *hydA* (hydrogenase) genes, probes for which were not present in the GeoChip microarray. The genes, along with the corresponding number of probe clusters present were: *aprA* (128 probes), *aprB* (52 probes), *dsrA* (582 probes), *dsrB* (428 probes), *soxB* (21 probes), *amoA* (146 probes), *napA* (123 probes), *narG* (545 probes), *nirK* (229 probes), *nirS* (271 probes), *nrfA* (141 probes), *fhfs* (467 probes), *mcrA* (101 probes), *iro* (278 probes), and *assA* (16 probes).

Bar graphs were constructed using median fluorescence data for each sample and for each of the genes present. Cluster analysis of the identified genera within the nine samples was carried out for each of the fifteen genes using Minitab v17.1.0; the unweighted pair group method with arithmetic mean (UPGMA) method was used (Gori et al., 2012, Hjelmsø et al., 2014). Dendrograms for each of the fifteen target genes were generated. Finally, taxonomical data relating to the corrosion samples was extracted from the GeoChip data and median response values calculated from the fluorescence values for each of the fifteen functional genes specified above; the indicated microorganisms and responses were then tabulated.

The use of Next Generation Sequencing techniques alongside or in place of GeoChip was considered as the methodologies would be capable of providing similar forms of data significant to this study. However, budgetary constraints precluded the use of both, and lead to the adoption of GeoChip for analysis of functional genes and identification of significant genera.

3.2.3 Genetic diversity analysis (High-resolution melt)

Corrosion, marine sediment, and seawater samples were analysed using this technique. Nineteen corrosion samples (previously designated C 01 to C15 (inclusive), C 14d, C 14e,

C 14f, and C 14g) were removed from deep freeze and examined under aseptic conditions. As with samples selected for functional gene analysis, samples were taken from previously unexposed regions. Subsamples were removed and handled as detailed in Section 3.2.2. DNA extraction was also carried out using MoBio PowerSoil DNA isolation kit and recommended protocol (Appendix B). The purity standard specified for samples undergoing functional gene analysis (8.5 ng μL^{-1} , and a 260/280 ratio between 1.5 and 1.9) was used for these samples also. This was adopted as a contingency in case cross comparison between low tide samples and vertical profile samples was able to be subsequently carried out. Following quantification, extracted DNA samples were diluted with nuclease-free water to produce a final concentration of 8.5 ng μL^{-1} and then stored at $-80\text{ }^{\circ}\text{C}$.

One sediment was removed from $-20\text{ }^{\circ}\text{C}$ storage to a sterile workspace. Cores were handled and processed as per Section 3.2.2, except that four samples were extracted from the core: from the surface layer (0 mm), then one each from 50 mm, 100 mm, and 150 mm depth. These were designated SED 04, SED 05, SED 06, and SED 07, respectively. A single subsample was removed from each 20 g section. DNA extraction was also carried out as previously described.

The seawater samples designated SW 04, SW 05, SW 06, and SW 07 (Section 3.1.5) were subjected to membrane filtration as detailed in Section 3.2.2. DNA extraction, purity testing and storage was also carried out as described in that section.

Subsequent HRM analysis was carried out in two batches. The first batch utilised DNA extracted from vertical profile corrosion only (samples C 01 to C 15) and sought to produce high-resolution melt curve data for four marker genes (*dsrB*, *aprA*, *soxB*, and *16S*). The second batch consisted of DNA extracted from four low tide zone corrosion samples (C 14d, C 14e, C 14 f, and C 14g), four marine sediment samples (SED 04, SED 05, SED 06, and SED 07) and seawater samples SW 04, SW 05, SW 06, and SW 07. These were used to produce HRM curves for the *dsrB* gene only.

For batch one, forward and reverse primers for *dsrB*, *aprA*, *soxB*, and *16S* genes were selected (Appendix E), and PCR solutions made up as per Appendix F, producing four sets of fifteen solutions. All preparation was carried out in a laminar-flow cabinet and under aseptic condition. Amplification of each set of DNA templates and subsequent melt

curve analysis was carried out using a Qiagen Rotor-Gene Q real-time PCR/HRM thermocycler programmed according to corresponding gene entry (HRM) in Appendix G. The melt region for each data set was determined manually from the HRM derivative curve (Gurtler et al., 2012, Pholwat et al., 2014, Liu et al., 2018). The attenuated melt curve data obtained were unity-based normalised (Robertson et al., 2009, Hjelmsø et al., 2014) and imported into Minitab v. 17.1.0; analysis was carried out using the UPGMA clustering method (Gori et al., 2012, Hjelmsø et al., 2014). The similarity data obtained from this were reconstructed as a dendrogram using Autodesk AutoCAD v.2012 software.

For the second batch, PCR solutions were prepared as per the previous HRM set-up. Amplification of the twelve DNA templates was carried out with the Qiagen Rotor-Gene Q thermocycler used for the first sample batch, programmed to amplify, and then perform melt curve analysis as per the *dsrB* (HRM) entry in Appendix G. Melt curve data was processed and analysed as above.

This is a relatively new technique that potentially provides faster and more accurate analysis than certain established gel-based techniques. Consequently several studies have been conducted that have sought to test its efficacy relative to established techniques such as denaturing gradient gel electrophoresis (DGGE) (Hjelmsø et al., 2014, Das et al., 2016, Pugliese et al., 2017). This study also included a comparative study of HRM versus DGGE for detecting similarities in microbial communities. It focused on variations in the *dsrB* found in environmental samples as a measure of sulfate-reducing prokaryotes diversity (Section 2.3). For both techniques, the second batch DNA extractions (See above) were used: low water corrosion (C 14d, C 14e, C 14f, and C 14g), marine sediment (SED 04, SED 05, SED 06, and SED 07), and seawater samples (SW 04, SW 05, SW 06, and SW 07).

3.2.4 Genetic diversity analysis (Denaturing gradient gel electrophoresis)

The DNA from corrosion samples C 14d, C 14e, C 14 f, C 14g, sediment samples SED 04, SED 05, SED 06, SED 07, and seawater samples SW 04, SW 05, SW 06, and SW 07, which had been previously extracted (Section 3.2.33.2.2) was utilised for denaturing gradient gel electrophoresis (DGGE) analysis (Section 2.8.4). As discussed in Section

3.2.3, this technique was compared with high-resolution melt analysis of low water corrosion, marine sediment, and seawater, in Section 7.1 of this study.

Primers for isolation of the *dsrB* gene were selected (Appendix E). These were of identical nucleotide sequence to those used for HRM analysis apart for the addition of a 31 nucleotide GC-clamp added to 5' end of the forward primer. Amplification of the twelve DNA templates was carried out with the Qiagen Rotor-Gene Q thermocycler used for HRM analysis. This was programmed to operate as per the *dsrB* (DGGE) protocol in Appendix G.

Following amplification, the PCR products were analysed using DGGE apparatus. A BioRad DCode Universal Detection System was used for employed for this, comprising of a 7-litre polycarbonate tank, control head with circulation pump and stirrer, 16-well thermoplastic comb, 20 x 20 cm glass plates, spacers, and clamps. The gel casting section consisted of Model 475 Gradient Delivery System and BioRad casting stand. External power was provided by a Hoefer PS300B power pack.

As noted above, an amplicon will resist denaturing according to its G-C composition, and so consequently the denaturing gradient necessary to provide effective separation of amplicons will reflect this. As the G-C composition of the samples in this analysis were unknown, the selection of denaturing gradient was based initially on that used in published literature and then modified according to experimental findings. The denaturing section of the polyacrylamide gel was poured using a combination of a high denaturant solution and a low denaturant solution. The strength of each solution was categorised according to the quantity of urea and formamide included; 100% denaturing solution is specified as 420 g l⁻¹ urea and 40% formamide (by volume); whereas 0% denaturing solution contains no urea and no formamide (Zhu et al., 2003). The gradient was produced by carefully controlling the proportion of each solution as the gel is poured. Zhu et al. (2003) and Meyer et al. (2007) utilised a starting denaturant of 30-35%, with a final of 60% when analysing sulfate-reducing prokaryotes in gas pipelines and pure culture; whereas Miletto et al. (2007) trialled a broad denaturing gradient of 25% to 90%, though bands were found between approximately 42% and 70% boundaries. Geets et al. (2006) used an initial 40% denaturant and 70% final concentration when differentiating SRP. In each of these studies the discriminatory region was approximately 30% wide, so

possessed broadly the same gradient despite variation in initial denaturant strengths. For this reason, an initial 30% denaturant and final 60% denaturant were used in this study. Based on Chae et al. (2006) a polyacrylamide layer of 100% denaturant was initially poured to provide a region at the base of the gel that will fully denature amplicons at this point, thus preventing them from potentially running off the gel. In addition, the sample wells were cast from 0% denaturant, to ensure denaturing of samples commenced only once the PCR products had been drawn into the gel.

The DGGE tank, with cast gel in-situ and containing 7-litres of x1 TAE buffer, was heated to 60 °C and allowed to stabilise for 30 minutes before 10 µL of each amplicon was pipetted into individual wells. The amplicons were added in a pre-determined semi-random sequence so that each sample type was separated from a similar sample by at least one lane. The final four lanes were utilised as normalisation guides; 10 µL of amplicons SW 01, SED 01, C 14d, and C14e was pipetted into these wells. It had been observed during apparatus set-up that the electrophoresis tank circulation pump produced turbulence adjacent the gel samples wells. To reduce the risk that amplicons would become dispersed, and/or mixed with adjacent samples once injected into the gel, the circulation pump was switched on 15 minutes after the start of the run period (Green et al., 2010).

As with other forms of electrophoresis, DGGE apparatus applies a potential difference across the gel to cause migration of PCR products. The optimum voltage and the period of its application will vary depending on the base-pair sequence and length of the amplicons, and must be determined empirically (Meyer and Kuever, 2007). However, studies can provide indications of setting that will yield acceptable results. In general an application of a low voltage over a period of several hours provides the best band resolution: 75 V to 120V for a period of 16 hours to 34 hours (Geets et al., 2006, Miletto et al., 2007, Besaury et al., 2012, Christiaen et al., 2013), though Liu et al. (2015) achieved a high degree of resolution when using DGGE on PCR products of *dsrB* gene at 200 V for 6 hours. This study employed 75 V and a 16-hour run period based on the studies previously mentioned and the maximum practical run-time with the apparatus available.

Upon completion of DGGE, the gel was stained in 250 ml of x1 TAE buffer containing 0.5 µg/ml ethidium bromide, for 30 minutes (Kim et al., 2015). The gel was then washed

in type 1 water and imaged under 312 nm UV light. The gel image was analysed using BioNumerics v7.6 software. Gel lanes were corrected using an averaging thickness of 15 points, 10% background subtraction, and arithmetic average filtering. Bands were normalised using the paired lanes for samples SW 01, SED 01, C 14d, and C14e. Cluster analysis was carried out using the band-based Dice similarity coefficient and UPGMA clustering method (Aydin et al., 2015, Lucena-Padros et al., 2015, Urubschurov et al., 2019). The similarity data obtained from this were reconstructed as a dendrogram using Autodesk AutoCAD v.2012 software.

3.2.5 Mineralogical analysis

The mineralogical analysis of steel corrosion and marine sediment samples was carried out using X-ray powder diffraction (Section 2.8.5). Subsamples of corrosion and sediment reserved as part of the microbiological handling protocol (Sections 3.2.2 and 3.2.3) were utilised. Both sample types were oven dried at 50 °C for 24 hours before being hand ground to a powder in approximately 10 g quantities using an agate pestle and mortar. Immediately following this they were subject to XRD analysis.

A Panalytical X'Pert Pro X-ray diffractometer with sample spinner, was used for all samples. Samples were placed in a powder mount and subjected to Cu K α radiation delivered at 40 kV and 40 mA. Diffraction angle from 0° through to 70° were used in 0.05° increments. As discussed in Mos et al. (2018), iron containing samples fluorescence under Cu K α radiation, leading to a decrease in peak intensity and possible ambiguity in peak assignments. To mitigate this effect, a nickel filter was utilised when corrosion samples were under analysis. Following each analytical run, each sample was recovered and placed in grip-top bags for later use.

The XRD data for each sample was analysed using X'Pert HighScore Plus software supplied with the diffractometer. All data were subjected to baseline subtraction using default settings (granularity=20; bending factor=3) and searched for peaks using default settings also (minimum significance=20; 2nd derivative method). Peak analysis was limited to group 1 to 7 elements of periods 1 to 5 and correlated with mineral profiles contained within the software's database. Peak were allowed an 2 θ tolerance of $\pm 0.25^\circ$. As multiple minerals within the a spectrum can be responsible for the same observed

peaks (Balasubramaniam et al., 2003, Yamashita et al., 2007, Xiao et al., 2017), each diffractogram was checked against multiple individual mineral patterns, with an emphasis on known or suspected NWC and MIC products, and minerals common to marine sediment.

3.2.6 Chemical analysis (Fourier-transform infrared spectroscopy)

Chemical analysis of corrosion samples was carried out using Fourier-transform infrared spectroscopy (Section 2.8.6). Following XRD analysis of the corrosion samples (Section 3.2.5), the previously dried and ground were analysed using a Perkin Elmer 65 Fourier-transform infrared spectrometer with universal attenuated total reflectance (ATR) sampling accessory, measuring the middle infrared region. The raw FTIR data was collected as based-lined absorbance values corrected for background carbon dioxide and water vapour absorbances. Based on its use in corrosion and mineralogical studies, which included FTIR data processing, PeakFit v.12.4 software by Systat Software, Inc. was used for spectral deconvolution and data interpretation (Rosero-Navarro et al., 2009, Wang et al., 2013, Ravin et al., 2017, Fan et al., 2018). As the absorbances associated with steel corrosion products were anticipated to occur close to the IR fingerprint region, absorbance spectrum data were cropped to wavenumbers 1650 cm^{-1} and below. The spectrometer model used was limited to wavenumber of 550 cm^{-1} and above. Peak separations were analysed using the deconvolution function, with spectral resolution set to full width half maximum (FWHM), width=33.5, and filter=78.6. Peaks were compared with published FTIR profiles of minerals, compounds, and chemical species noted within normal water corrosion and microbially influenced corrosion formations, as summarised in Appendix H. To investigate wavenumbers below 550 cm^{-1} , Raman spectroscopy was trialled. However, the available equipment produced plots with relatively high background and extremely poor peak resolution, and so this technique was not pursued further.

3.2.7 Chemical analysis (Inductively coupled plasma optical emission spectrometry)

The chemical analysis of marine sediment focussed on the sulfate and iron content of the interstitial seawater within a sediment core and of the marine sediment itself. Both were

analysed using analysis by inductively coupled plasma optical emission spectrometry (ICP-OES) (Section 2.8.7. The marine sediment was subjected to acid digestion before being subject to the same analytical technique.

Extraction of pore water samples from the samples core was carried out using Macro Rhizon soil moisture samplers as first demonstrated by Dickens et al. (2007). These samplers comprise of a porous polymer head and flexible connector finishing in a female Luer-Lok screw connection. Each sampler was manufactured with a mean pore size of 0.15 μm , so particles larger than fine clays were filtered out, alleviating the need for centrifuging prior to ICP-OES analysis. A Rhizon sampler was inserted fully into the sediment column through a pre-drilled core sleeve holes (see section 3.1.4). A 10 ml male Luer-Lok syringe was attached to each Rhizon, the plunger withdrawn to the 9 ml mark and then secured in place using a 50 mm wooden splint. Each Rhizon was left under vacuum for a 24-hour period; periodic checks were carried out during this time to monitor extraction progress and to ensure seal integrity was being maintained. A total of twenty-one pore water samples were obtained from the sediment core, from the top of the sediment (0 mm) to a depth of 500 mm in 25 mm increments. Following extraction, the syringe contents were transferred to 100 ml screw top centrifuge flasks and refrigerated at 5 °C until required for analysis. Each pore water sample was subjected to a series of ten-fold serial dilutions, obtaining x10, x 100 and x1000 test samples of 100 ml volume each and subjected to elemental analysis using an inductively coupled plasma optical emission spectrometer (PerkinElmer Optima 2100DV) (with a PerkinElmer AS90 auto-sampler) to obtain total sulfur and iron concentrations. The apparatus was calibrated using a multi-element standard solution diluted to measure a range of 0 to 10 ppm for the target element.



Figure 3-6 Sediment corer sleeve with Rhizon samplers fitted

Acid digestion of the marine sediment was carried out using a procedure based on those used by Guven and Akinci (2001), and Uddin et al. (2016). The sediment samples previously extracted from the core and used for X-ray powder diffraction analysis were utilised. Subsamples in 1g quantities were placed in 200 ml glass beakers into which 30 ml of nitric acid (70%, purified) was then added. These were left to digest for three hours, after which each mixture was added to a new beaker containing 70 ml of type 1 distilled water. Each solution was then thoroughly mixed before undergoing ten-fold serial dilution and ICP-OES analysis as described above.

Chapter 4 Tidal range and turbidity analysis

4.1 Tidal data

The tidal data obtained from approximately twenty-four months of monitoring at the Dredger Berth (from 01/04/14 to 24/03/16) are displayed below as a series of time/depth plots in Figure 4-1 to Figure 4-8. Gaps in the tidal plot were the result of depth sensor failure during the monitoring period; this resulted in five periods of data loss, totalling 51 days out of 721 days.

Early analysis of tidal depth data indicated clipping at the lower part of the tidal cycle. Examination of the monitoring apparatus during periods of low tide revealed seawater levels periodically fell below the height of the sonde's depth sensor, resulting in measurements of 0 m being taken during those sampling periods. This was not apparent during the initial site survey or during the subsequent instrument installation. Additionally, the sediment bed was found to descend approximately 0.2 m from the sonde location to the area of corrosion and sediment sampling. To allow correlation of seawater depth with corrosion sampling heights, the sonde depth data was subsequently adjusted by the addition of 0.2 m. This is reflected in the time/depth plots (Figure 4-1 to Figure 4-8) and in the calculated tidal values below.

The plots displayed characteristics of a typical semi-diurnal tidal cycle (Haslett, 2000, Masselink et al., 2011), with a measured period of 12 hours and 20 ± 5 minutes. High tide data was collated revealing the maximum spring high tide depth to be 6.0 m, and the minimum recorded neap high tide to be 3.3 m. All data at and above 3.3 m was tested for normality using Minitab 17 software; this produced a p-value > 0.05 , so average high tide was calculated as a mean of these data and was found to be 4.8 m. Analysis of the available low tide data indicated that maximum low tide at the sampling site was 1.6 m. Due to the data clipping noted above, minimum low tide data was not available. Similarly, it was not possible to calculate a mean tide height using the entire data set due to the loss of data below 0.2 m. An estimate was obtained however, by finding the mean of all neap high and neap low tide heights. This produced a mean tide height of 2.4 m from sediment bed level. A value for mean low tide was also calculated based as an offset from the mean

tide level by a distance equal to mean high tide height minus mean tide height. This produced a distance below the cropped region so was discarded.

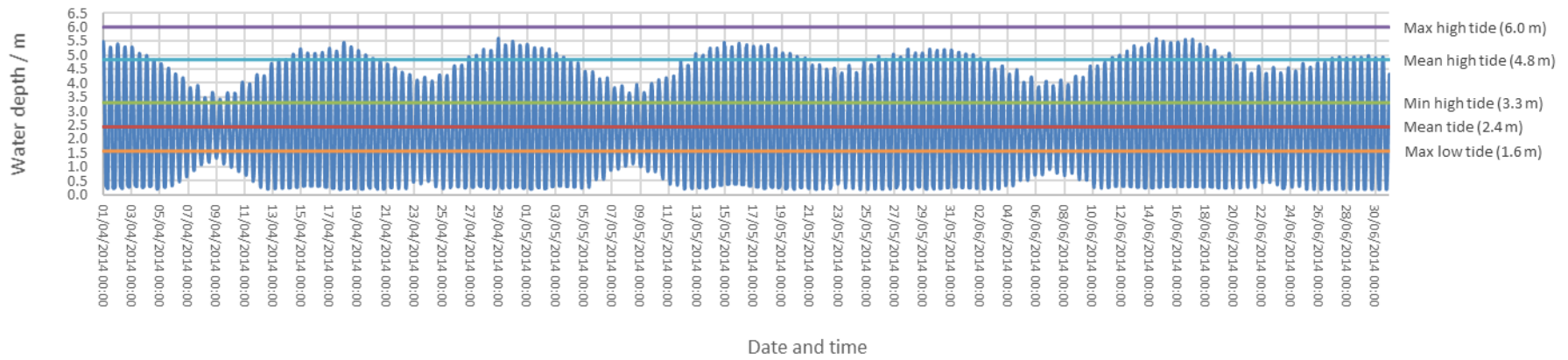


Figure 4-1 Dredger Berth tidal data from 01/04/14 to 30/06/14

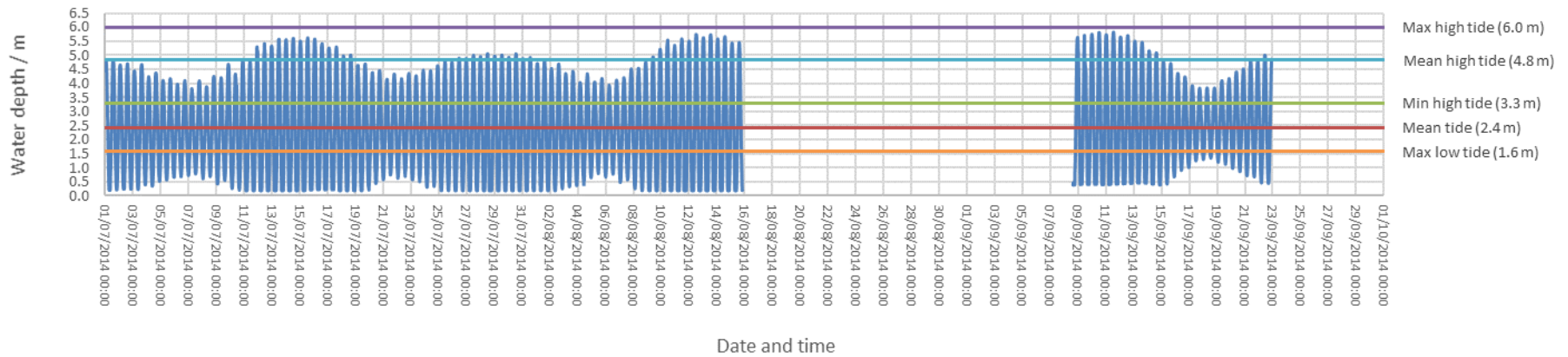


Figure 4-2 Dredger Berth tidal data from 01/07/14 to 30/09/14

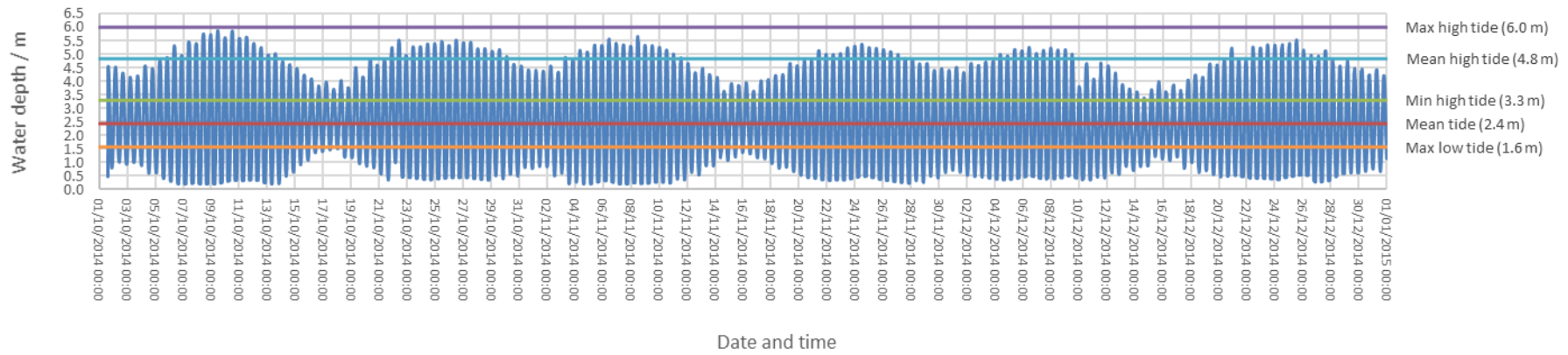


Figure 4-3 Dredger Berth tidal data from 01/10/14 to 31/12/14

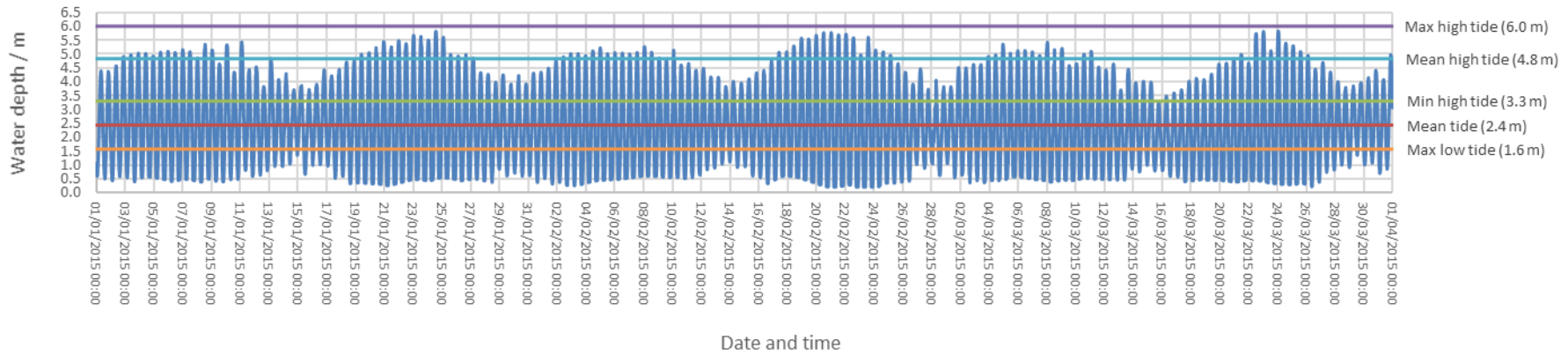


Figure 4-4 Dredger Berth tidal data from 01/01/15 to 31/03/15

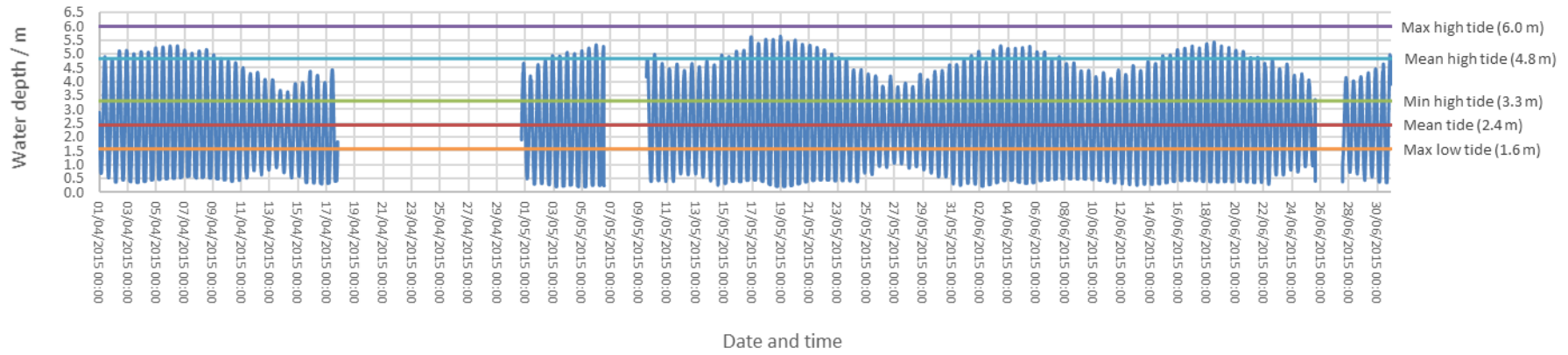


Figure 4-5 Dredger Berth tidal data from 01/04/15 to 30/06/15

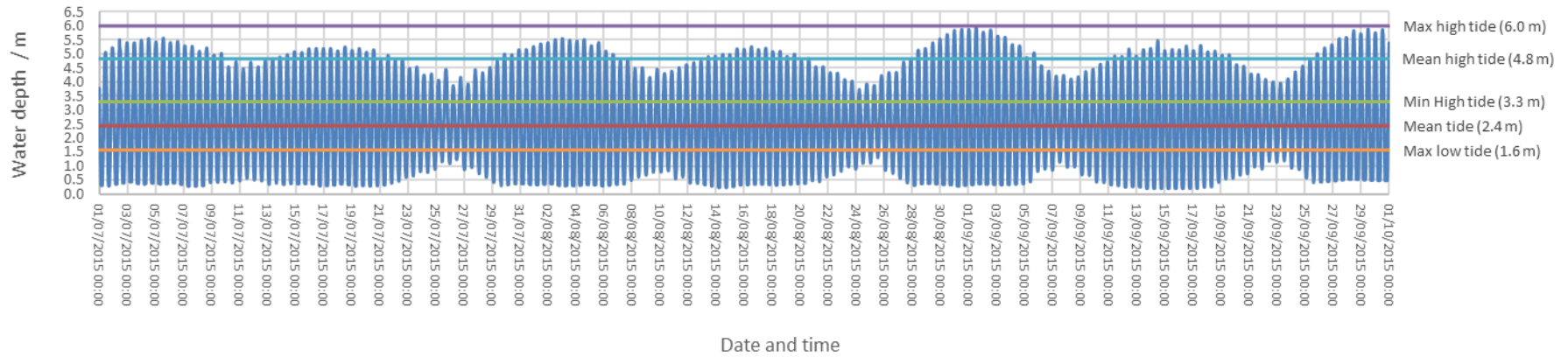


Figure 4-6 Dredger Berth tidal data from 01/07/15 to 30/09/15

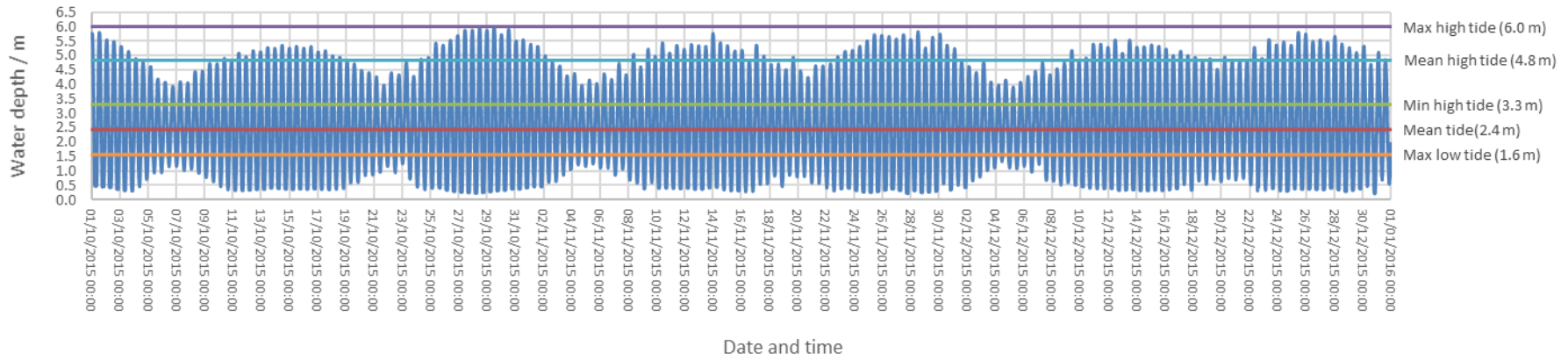


Figure 4-7 Dredger Berth tidal data from 01/10/15 to 31/12/15

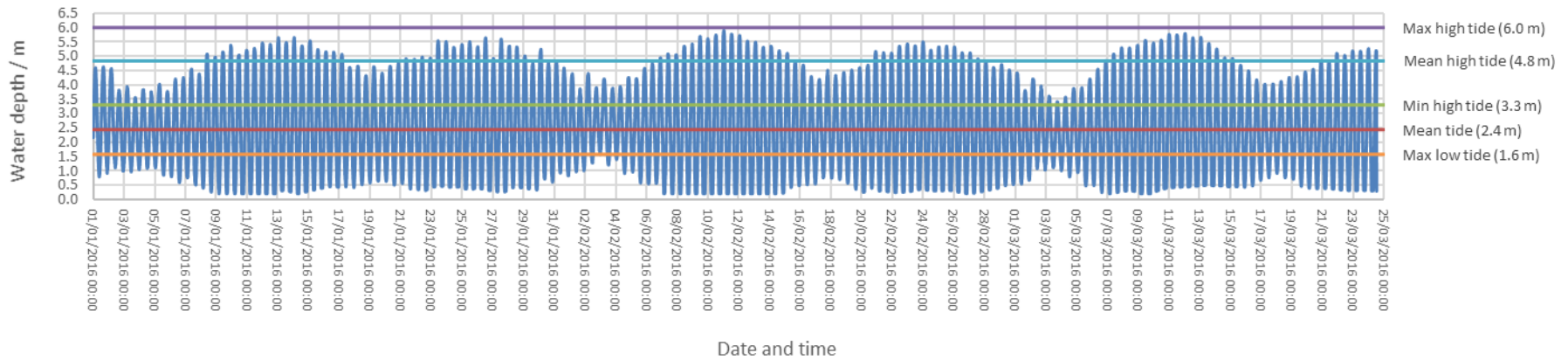


Figure 4-8 Dredger Berth tidal data from 01/01/16 to 24/03/16

4.2 Turbidity data

Turbidity data obtained from seawater monitoring equipment (Section 3.1.5) is shown as time/turbidity plots in Figure 4-9 to Figure 4-16, seven-day average turbidity plot (Figure 4-17) and cumulative frequency plots in Figure 4-18 and Figure 4-19. As per the tidal analysis, these were collected between 01/04/14 and 24/03/16. As with tidal data monitoring, sensor failure occurred periodically during the monitoring period; this resulted in four periods of data loss, totalling 26 days out of 721 days.

The turbidity data was checked for normality using Minitab 17 software. A p-value of <0.005 was obtained, so the average turbidity value was calculated as the median of the data. This produced a value of 7.04 FNU. Maximum turbidity reached the limit of 4000 FNU set by the probe. Minimum turbidity recorded was 0.09 FNU.

The time/turbidity plots indicate marked seasonal variations in the seawater conditions throughout the data collection period. Turbidity variations are smallest during spring and summer months and increase during autumn and winter months. This is more apparent in the seven-day average plot (Figure 4-17), which shows periods of increased turbidity from January 2014 to March 2015, and November to March 2016. As described previously, the Dredger Berth is a mooring for Shoreham Port Authority maintenance craft. Site observations indicated these craft visibly stir up the local sediment bed, thus contributing to turbidity levels. However, these craft operate regularly throughout the year so their contribution would be anticipated to be essentially constant. The observed turbidity increase is most probably the result of a seasonal worsening of weather leading to more turbulent seawater conditions with correspondingly greater local sediment re-suspension, as well as transport of suspended sediment into the Dredger Berth from the sea and nearby River Adur.

The first cumulative frequency plot (Figure 4-18) displays the whole turbidity data set across the full range of measurable turbidity values. As indicated by the median value calculated previously, the data tended towards the lower end of the range. Greater than 99% of the turbidity values were 85 NTU or below, and greater than 90% were 33 NTU or below.

Separating data from the four seasonal periods above (Figure 4-19) it can be seen that the spring and summer months in 2014 and 2015 (1st April to 30th September and 1st April to 31st October respectively) corresponded closely. Ninety-nine percent of turbidity values for each of these periods were 35 FNU or less. The two profiles diverged at lower values, with 90% of the former period possessing values of 12.15 FNU and below, and the latter possessing 10.6 FNU. The median turbidities for these periods were 4.48 FNU and 3.58 FNU, respectively. The period between 1st October 2014 and 31st March 2015 is characterised by 95% of samples being 52.16 FNU or below and 90% of samples being 39.97 FNU or below. The data for the final period between 1st November 2015 and 24th March 2016 indicates 95% of samples were possessed a turbidity of 65.45 FNU or less. The 90% threshold was marked by turbidity values of 50.99 FNU and less. The median turbidity values for these groups were 13.49 FNU and 19.22 FNU, respectively. In each of the four groups the maximum recorded turbidity value was 4000 FNU.

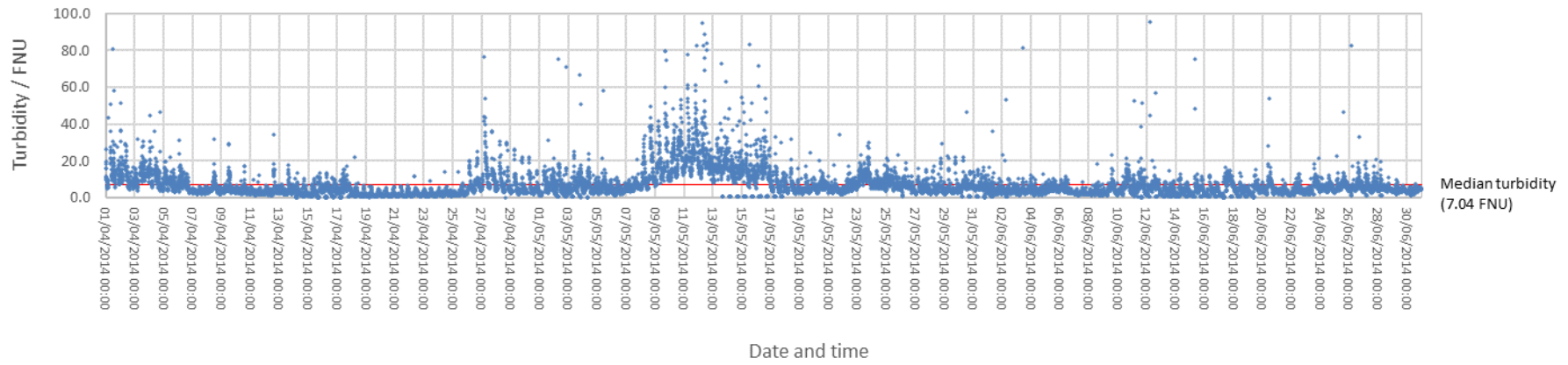


Figure 4-9 Dredger Berth seawater turbidity data (0 to 100 FNU) from 01/04/14 to 30/06/14

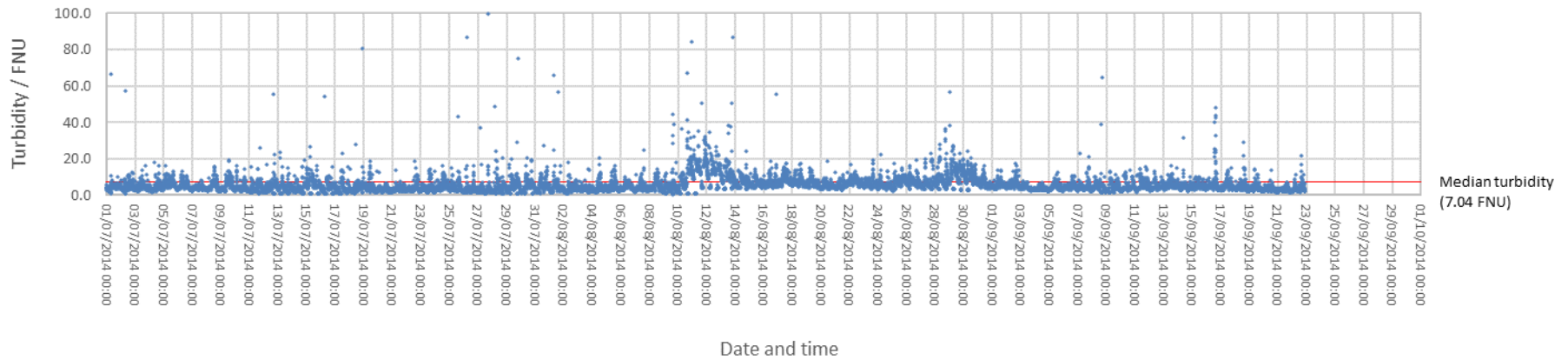


Figure 4-10 Dredger Berth seawater turbidity data (0 to 100 FNU) from 01/07/14 to 30/09/14

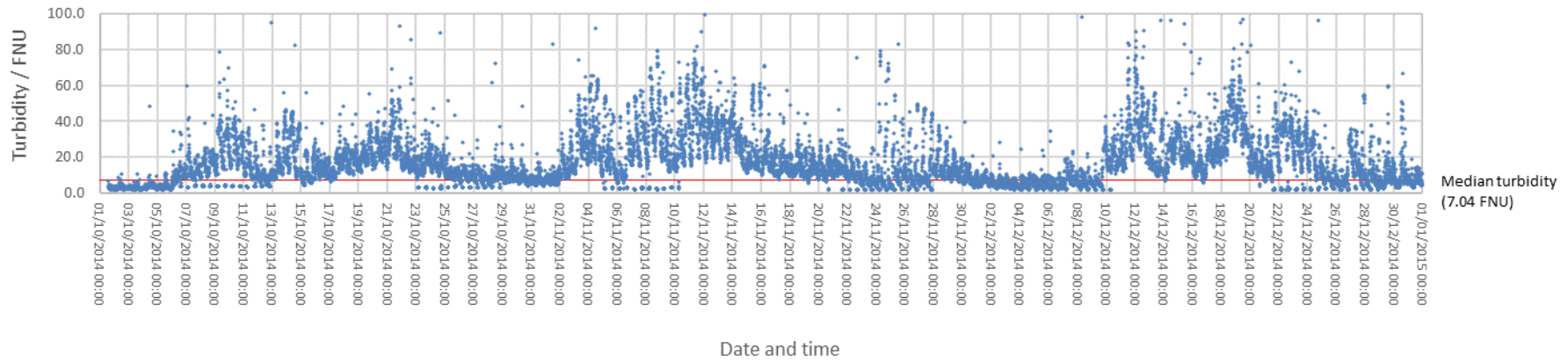


Figure 4-11 Dredger Berth seawater turbidity data (0 to 100 FNU) from 01/10/14 to 31/12/14

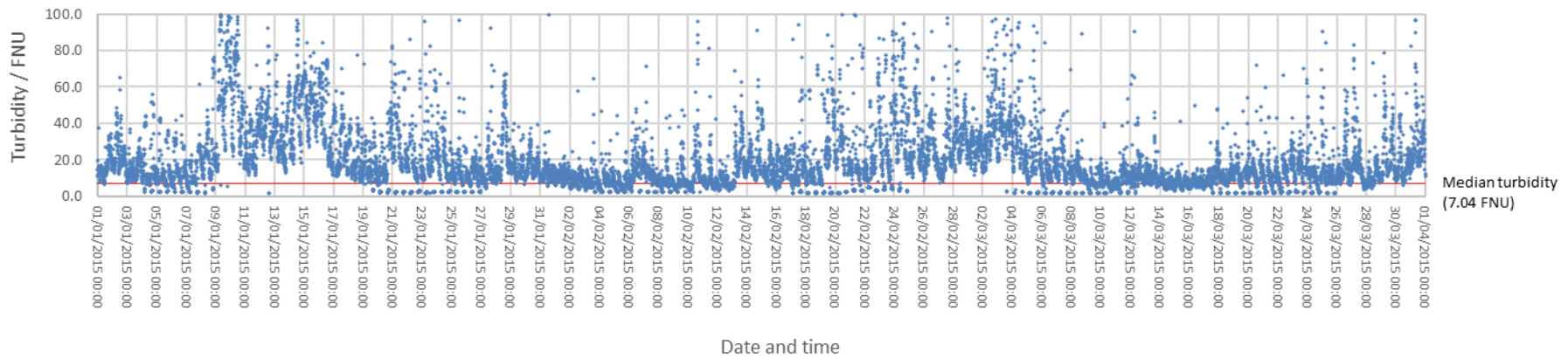


Figure 4-12 Dredger Berth seawater turbidity data (0 to 100 FNU) from 01/01/15 to 31/03/15

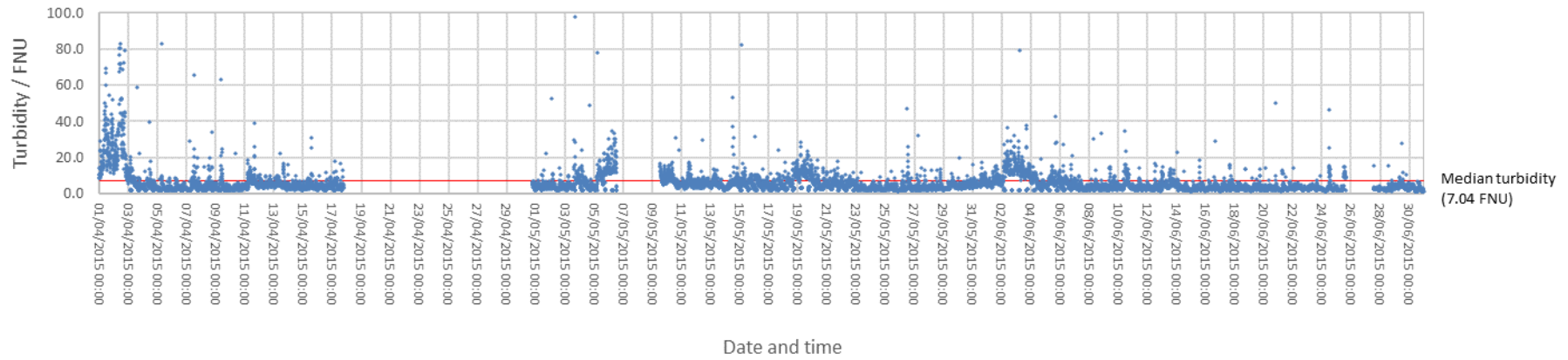


Figure 4-13 Dredger Berth seawater turbidity data (0 to 100 FNU) from 01/04/15 to 30/06/15

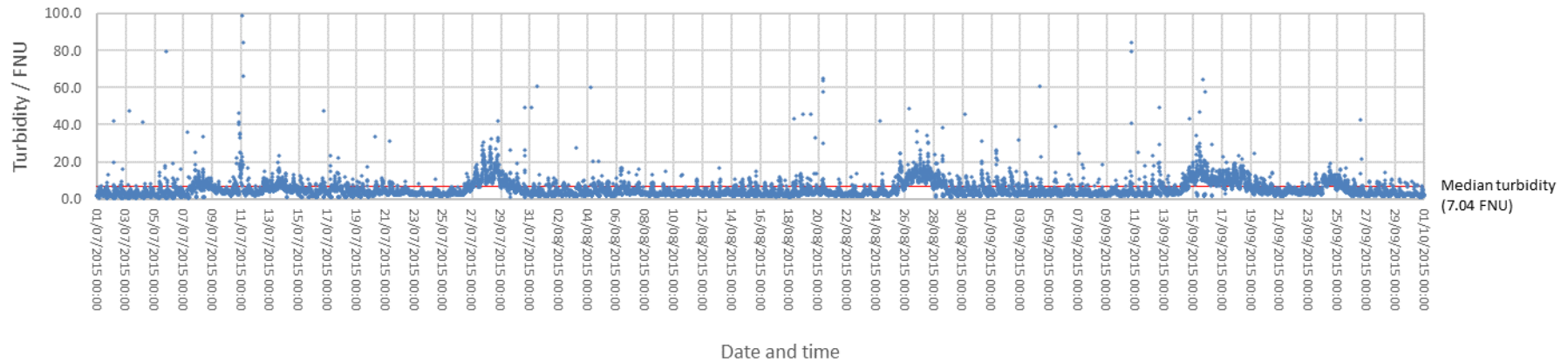


Figure 4-14 Dredger Berth seawater turbidity data (0 to 100 FNU) from 01/07/15 to 30/09/15

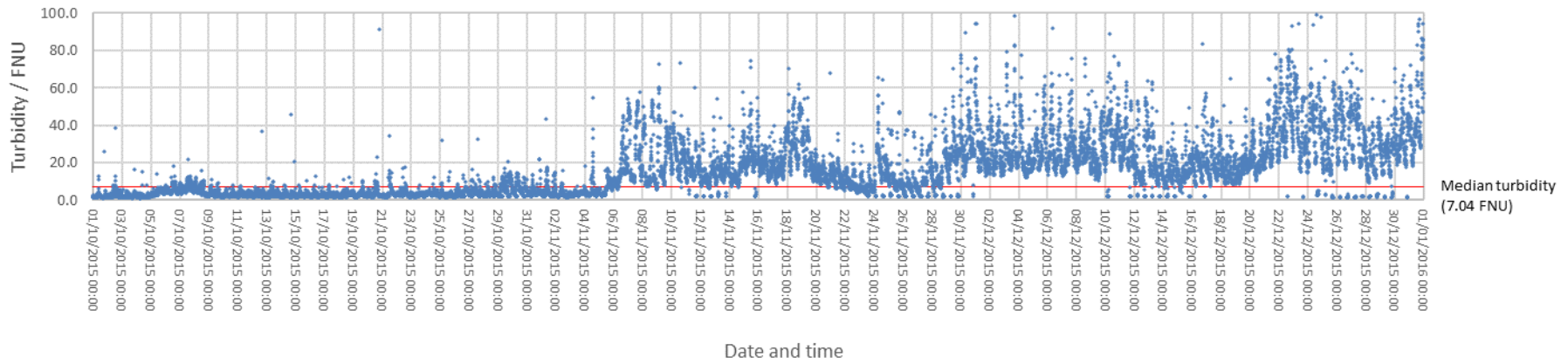


Figure 4-15 Dredger Berth seawater turbidity data (0 to 100 FNU) from 01/10/15 to 31/12/15

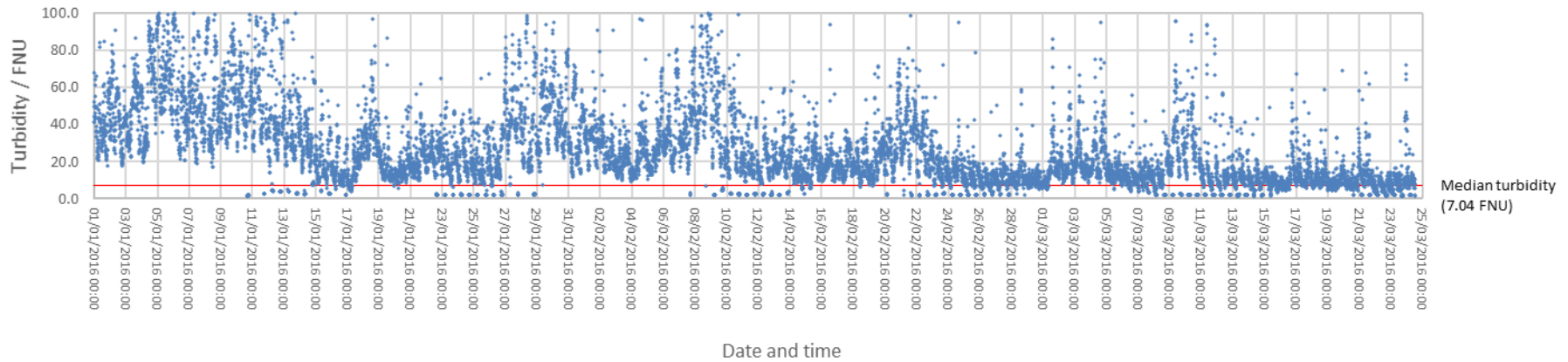


Figure 4-16 Dredger Berth seawater turbidity data (0 to 100 FNU) from 01/01/16 to 24/03/16

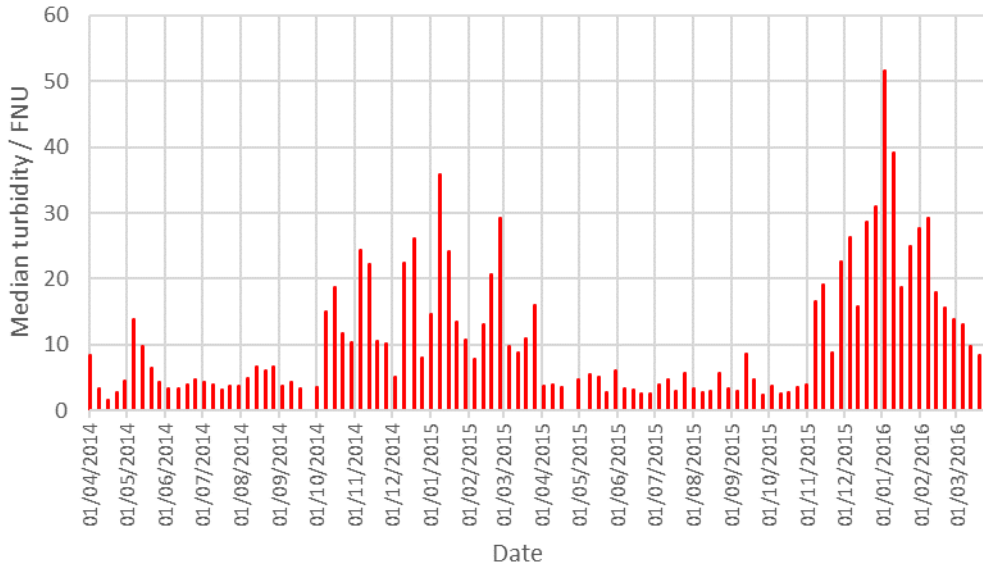


Figure 4-17 Dredger Berth seawater turbidity seven day average

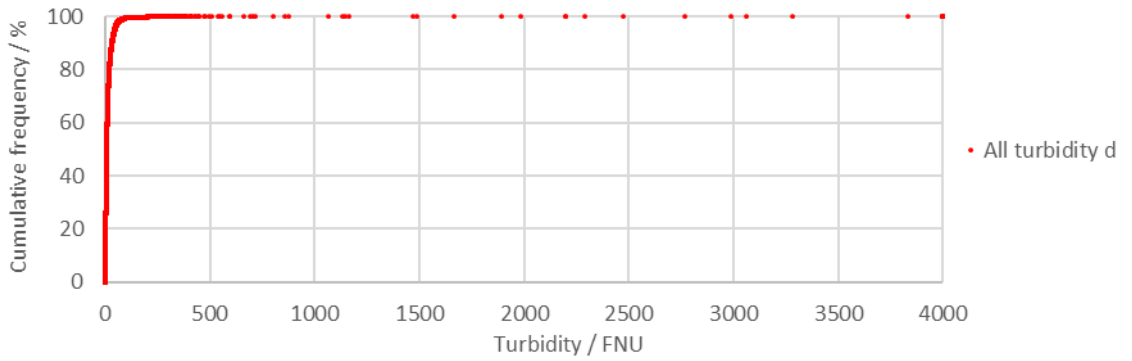


Figure 4-18 Dredger Berth seawater turbidity (between 0 and 4000 FNU)

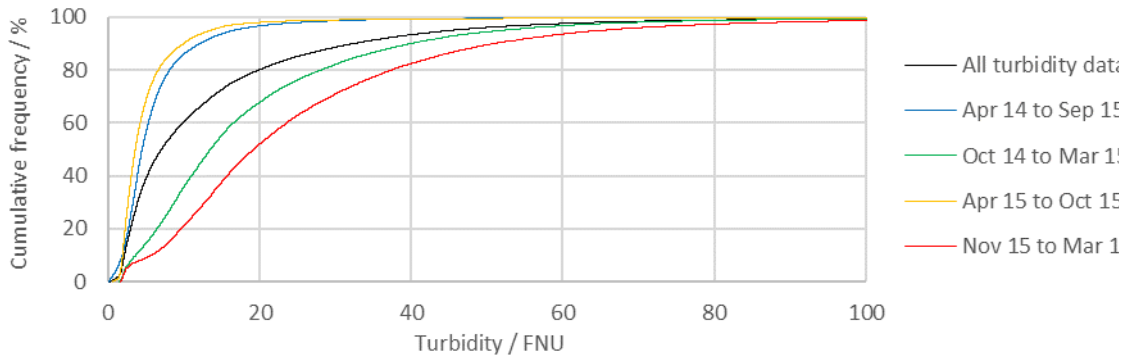


Figure 4-19 Dredger Berth seawater turbidity (between 0 and 100 FNU)

4.3 Summary

This short chapter has presented the results of the seawater monitoring section of the project. The data have allowed the tidal range and regions to be defined, as well as providing evidence of periodic turbidity events within the Dredger Berth. These findings will be relevant to the project synthesis in Chapter 10, with the former helping to contextualise the composition of the corrosion samples, and the latter to partially explain the corrosion mineralogy and help in providing a context for inoculation of the piling surface.

Chapter 5 Spectroscopic analysis of marine sediment using inductively coupled plasma optical emission spectrometry and X-ray powder diffraction

5.1 Inductively coupled plasma optical emission spectrometry of sediment pore water and marine sediment

This section details the results of the chemical analysis of pore water extracted from a sediment core (Section 3.2.7) and acid digestion of sediment samples from the same core using inductively coupled plasma optical emission spectrometry (ICP-OES). The pore water samples were extracted from a single sediment core prior to processing for XRD analysis. Samples used for acid digestion were taken from those previously utilised for XRD analysis.

Figure 5-1 shows the change in total sulfur with depth for the pore water extracted. For the sediment depths retrieved, the sulfur concentration ranged between 199 mg l⁻¹ and 583 mg l⁻¹. The highest concentration recorded was within the surface sediment; this was lower than that typically found in seawater (vanLoon and Duffy, 2005), suggesting the influence of fresh water from the nearby River Adur. There is a clear decrease in concentration the further down the column the sample was extracted. This is consistent with trends typical for this environment (Jørgensen and Kasten, 2006) where seawater infiltrates the sediment transporting with it dissolved sulfur species that are systematically utilised by sulfate-reducing prokaryotes (SRP) (Section 2.2). The aqueous iron concentrations (Figure 5-2) follow a similar trend, albeit with concentrations four orders of magnitude smaller. These ranged between 0.053 mg l⁻¹ and 0.057 mg l⁻¹. The concentration in the surface layer was significantly higher than that typically measured in seawater (0.001 to 0.003 mg l⁻¹), but as river water typically possesses iron concentrations of 0.5 to 1.0 mg l⁻¹ (Lenntech, 2020), the increase is also consistent with mixing of seawater with the adjacent fresh water outflow.

The results of the ICP-OES analysis of acid-digested marine sediment display an opposite trend to the pore water data. The sulfur concentration versus depth is shown in Figure 5-3. The minimum concentrations were found with the top 50 mm of the column. These ranged

between 27 mg l^{-1} and 31 mg l^{-1} . The plot then displays a sharp increase up to 100 mm depth. The highest sulfur concentration occurs at this point (89 mg l^{-1}), after which the concentration displays a downward trend to 250 mm. Below 250 mm the data displays an apparent vertical profile with an average value of approximately 55 mg l^{-1} . The iron concentrations for the same samples show a similar trend to the sulfur. The top 50 mm have the lowest iron concentrations (89 mg l^{-1} to 96 mg l^{-1}), followed by an increase in concentration at 100 mm (183 mg l^{-1}), and then a general decrease below this depth to an apparently vertical profile averaging approximately 150 mg l^{-1} .

The results above are consistent with the activity of SRP. Below the oxic surface region (the top 50 mm according to these data) these anaerobes utilise aqueous sulfate ions in the pore water as electron-acceptors producing hydrogen sulfide. The hydrogen sulfide then reacts with iron in solution forming iron sulfides that precipitate out. Hence, the sulfur and iron concentrations in solution decrease and the solid phase concentrations of both elements increase. The significant increase in concentrations at 100 mm depth in the acid digestion plots suggests the start of the suboxic or anoxic region and the position in the sediment column at which SRP and other anaerobes are active. It was for this reason that 100 mm was chosen as the sample depth for the marine sediment part of the functional gene analysis (Section 3.2.2).

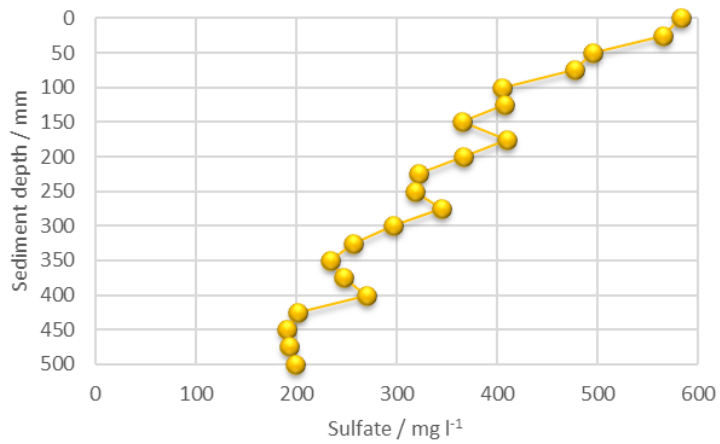


Figure 5-1 Sediment pore water sulfate concentration vs depth

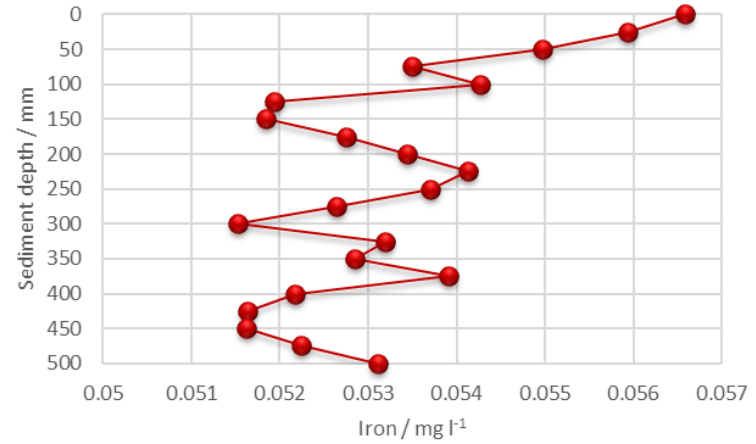


Figure 5-2 Sediment pore water iron concentration vs depth

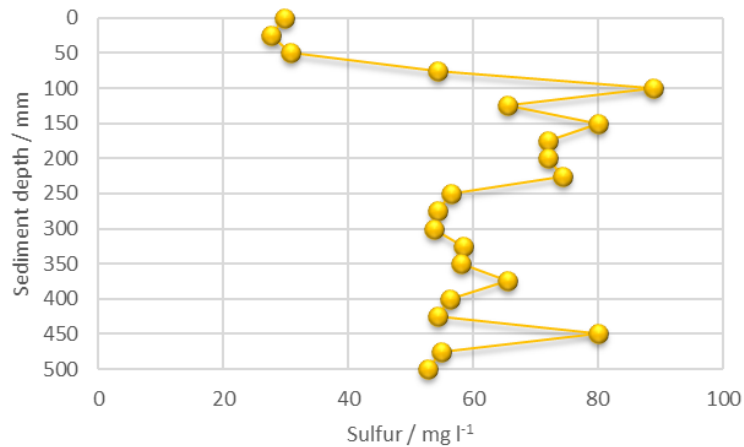


Figure 5-3 Acid digested sediment sulfur concentration vs depth

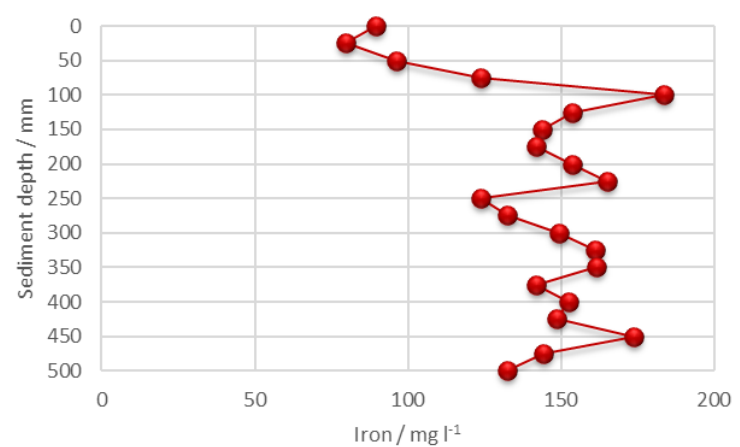


Figure 5-4 Acid digested sediment iron vs depth

5.2 X-ray powder diffraction analysis of marine sediment

The data obtained from powder X-ray powder diffraction analysis (XRD) of marine sediment core from adjacent the Dredger Berth are displayed below as a combined diffractogram (Figure 5-5). The 21 samples were plotted with an arbitrary vertical offset for the sake of clarity.

Minerals common to all depths analysed were silica, calcite, and the clays illite and kaolinite. Peaks consistent with halite and nahcolite, which will have precipitated out from seawater during the sample drying process were also present. Overall, the peak heights for each sample are of approximately consistent across the range of depths, suggesting an essentially homogenous composition up to the depth of sample retrieved. Halite peaks display a degree of increase at the lower depths. This would be consistent with seawater infiltration at depth but the shallower depths increasingly being exposed to seawater mixed with freshwater from the outflow of the nearby River Adur, surface runoff, or water percolating through the backfill behind the piling face. Most significant to this study are the peaks corresponding to pyrite (FeS_2). These were present in all samples from a depth of 50 mm and below. The 25 mm sample displays a weak response at the angles most characteristic of pyrite (33° and 56°) (Ghassa et al., 2017), and the 0 cm surface sample displays no peaks for the mineral. Below the 25 mm sample the pyrite peaks are clearly defined and show an increase in intensity down the sediment column; this being consistent with an increase in concentration with depth. As described in Jørgensen and Kasten (2006), oxygen concentrations can decrease rapidly within the first centimetres of depth resulting in suboxic and anoxic regions favourable to anaerobic microbes capable of reducing sulfate in seawater to hydrogen sulfide. The dissolved hydrogen sulfide can then react with iron from detrital minerals forming various iron sulfide minerals (Raiswell and Canfield, 1998), which can subsequently be transformed to pyrite. This latter process was discussed in Section 2.5.6.

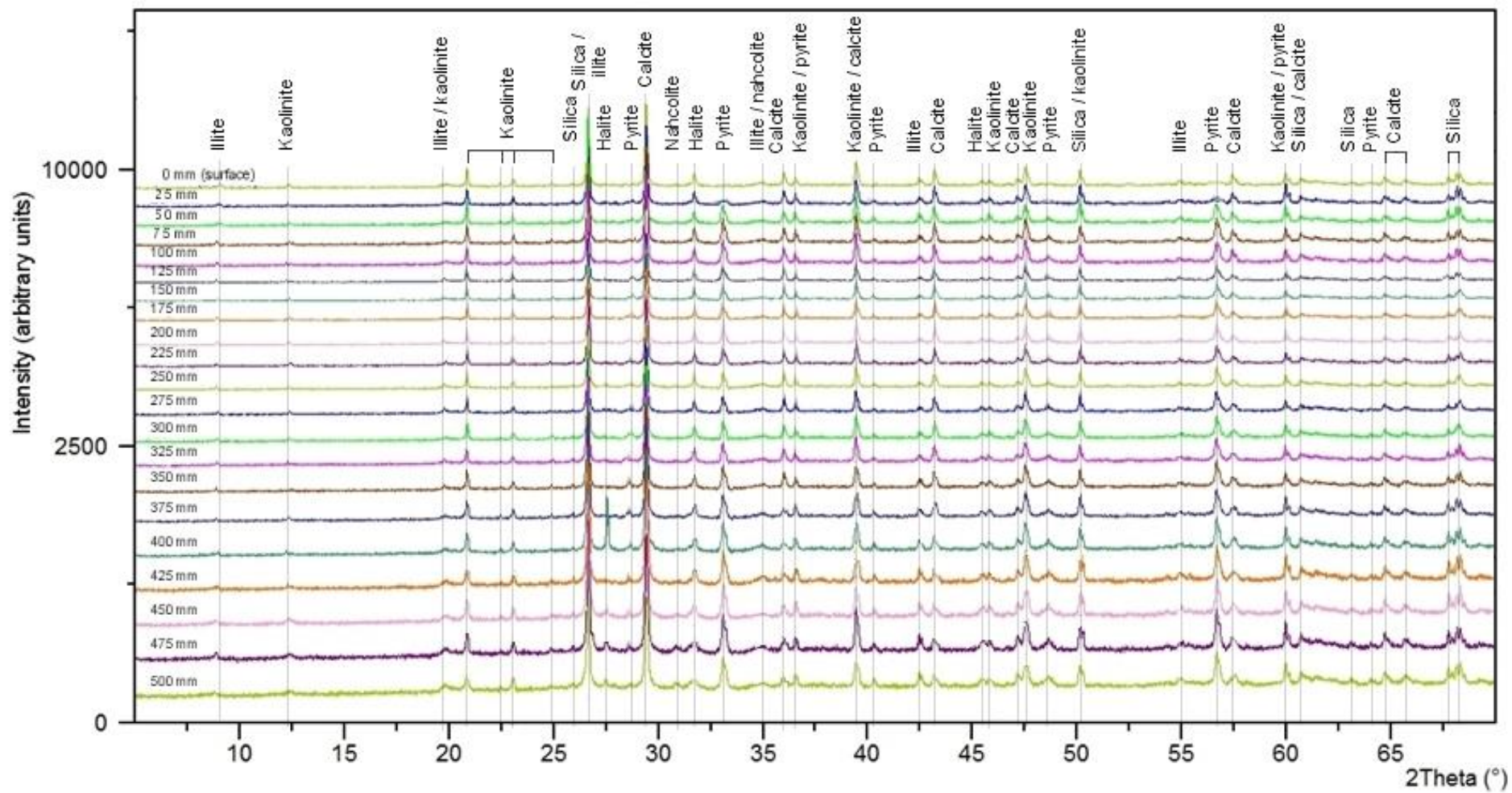


Figure 5-5 XRD diffractogram with identified minerals for marine sediment samples

5.3 Summary

Analysis of the marine sediment column by inductively coupled plasma optical emission spectrometry allowed the sulfur and iron concentrations in pore water and marine sediment to be determined according to depth. The pore water data showed a decrease in concentrations of both elements with depth; the solid phase concentrations exhibited an opposite trend with an increase occurring with depth. A rapid increase in the solid phases was noted at 100 mm below surface level. The trends observed were consistent with precipitation of iron sulfide minerals following reduction of aqueous sulfate by anaerobic microbes.

X-ray powder diffraction analysis of the marine sediment samples determined a mineralogy of mainly silica, calcite, illite, and kaolinite. Halite and nahcolite precipitated during the sample drying process were also observed. Peaks corresponding to pyrite were present at all subsurface depths. The presence of this mineral was consistent with the ICP-OES analysis in previous section.

Chapter 6 Functional gene analysis using GeoChip microarray

Part of the content of Chapter 6 is published in *npj Materials Degradation* (2019) 3(1), p 1-11)

6.1 Community diversity analysis of low tide zone corrosion, marine sediment, and seawater samples

As described in Section 3.2.2, three corrosion samples (C 14a, 14b, and 14c) from the low tide zone (corresponding with the same vertical location as sample C 14 (6.0 m from the cope / 1.0 m from the sediment bed)), three marine sediment samples (SED 01, 02, and 03) from 100 mm depth, and seawater samples (SW 01, 02, and 03) taken from 1 m above sediment bed level were subjected to community diversity analysis. The results of the community diversity analysis are shown in the figures below.

Shannon Index analysis values are shown in Figure 6-1 and range between approximately 8.99 and 9.91. The indicated diversity is therefore high for each of the samples. Numerical ordering the H values reveals the water samples (SW 01, 02, and 03) form a cluster with the most diverse microbial communities. The corrosion samples (C 14a, 14b, and 14c) also form a cluster that lies towards the bottom of the diversity scale for the samples; only sediment sample SED 01 is less diverse.

Diversity analysis using Inverse Simpson Index (Figure 6-2) displays values of $1/D$ ranging between 1629 and 5794. Despite a relatively wide data range, these data also indicate a high degree of community diversities. The diversity pattern follows that of the Shannon Index analysis with the water samples displaying the greatest diversity and all three corrosion samples forming a group towards the lower end of the diversity scale. Once again, the sediment sample SED 01 is indicated to be the least diverse.

Results of the Shannon evenness analysis revealed a range of data is between 0.86 and 0.92; these values indicated relatively low variation in the abundance of groups with the community exists. The water samples tended to possess communities with more even

distributions of identified microorganisms than those possessed by the corrosion samples. Both the corrosion and seawater samples tended to form groups that did not overlap but were interspersed by the three marine sediment samples. The distribution of the sediment samples within the table suggests they possessed greatest variability in their community evenness.

Sample ref.	Simpson Index (1-D)
SW 03	0.999827
SW 01	0.999817
SED 02	0.999737
SW 02	0.999706
SED 03	0.999680
C 14a	0.999642
C 14c	0.999591
C 14b	0.999456
SED 01	0.999386

Figure 6-1 Diversity analysis of samples using Simpson Index

Sample ref.	Shannon-Wiener Index (H)
SW 01	9.906743
SW 03	9.770932
SW 02	9.712639
SED 03	9.659099
SED 02	9.574061
C 14c	9.308528
C 14a	9.253564
C 14b	9.152567
SED 01	8.991051

Figure 6-2 Diversity analysis of samples using Shannon-Wiener Index

Sample ref.	Shannon evenness (J)
SED 02	0.919893
SW 01	0.912716
SW 02	0.903257
SED 03	0.900733
SW 03	0.899810
C 14c	0.889585
SED 01	0.877060
C 14b	0.868068
C 14a	0.860831

Figure 6-3 Diversity analysis of samples using Shannon evenness

6.2 Relative gene abundance in low tide zone corrosion, marine sediment, and seawater samples

. A plot of probe fluorescence for genes significant to MIC processes (Section 2.2) is shown in Figure 6-4. Also as previously described, three marine sediment samples and three seawater samples were similarly analysed, and their probe fluorescence plotted (Figure 6-5 and Figure 6-6).

Plots employing *total* fluorescence values have been commonly used in GeoChip analysis of environmental samples (Xie et al., 2011, Chu et al., 2014, Sztyler, 2014, Jiang et al., 2019). These have been suited to comparisons of individual genes between samples but do not allow a comparison of the abundance of different genes within a single sample. As discussed in Section 3.2.2 GeoChip microarrays comprise of a set of probes that match functional gene sequences from several genera of microbial life, however as also noted the total number of each probe cluster type varies on the GeoChip 5.0 microarray. For example, there are 128 probe clusters sensitive to the *aprA* gene; 278 probe clusters for detecting the *iro* gene; and 545 clusters for the *narG* gene. Figure 6-4 to Figure 6-7 were therefore constructed using median fluorescence values calculated to allow an estimation of activity per probe cluster to be carried out.

Initial examination of the plot for corrosion samples (Figure 6-4) revealed a measurable level of fluorescence occurs within each microbial group, confirming the presence of each target gene in each of the three samples. The relative abundance of each gene varied between each sample, with sample C14a displaying higher fluorescence for each gene apart from *narG*. Sample C 14c consistently exhibited the lowest levels of fluorescence for each gene. The highest median fluorescence was exhibited by the iron-oxidizing gene (*iro*) in C 14 a and C 14b. The genes within a microbial group tended to show the approximately similar levels of fluorescence; the four genes associated with SRP (*aprA*, *aprB*, *dsrA*, and *dsrB*) were similar within about 200 fluorescence units, as were the five genes associated with NRB (*napA*, *narG*, *nirK*, *nirS*, and *nrfA*). The variability in fluorescence relates to the number of gene fragments that have bonded to the corresponding probe, and the amount of DNA exposed to the microarray was precisely the same for each sample. In addition, this metagenomic technique utilises the whole community without the selective amplification of target genes as used in techniques such

as denaturing gradient gel electrophoresis or high-resolution melt analysis. Therefore, the fluorescence values could be an expression of community diversity within a sample: if the values are low for the selected genes, then the number of microorganisms that metabolise via other chemical pathways could be greater, and the community more diverse. The technique does not allow quantification of fluorescence values in terms of gene concentration so this rationale can only be applied in comparing relative diversity in a qualitative manner. Confirmation of this hypothesis would require further investigation, though a study by Smith et al. (2019) indicated a parity between community diversity as determined using gene sequencing, and patterns of GeoChip data. Applying this reasoning, sample C 14c would appear to be the most diverse low tide level corrosion sample.

The fluorescence plot for marine sediment (Figure 6-5) also displayed significant concentrations of the fifteen target genes. As with the corrosion samples, there was signal variability between the samples: SED 01 had the lowest signal for all genes except for *soxB* and *assA*; SED 03 displayed the highest fluorescence for each gene apart from *nrfA*, *iro*, and *assA*. Like the corrosion samples, the *iro* gene fluorescence values were amongst the highest for these samples, and the sulfate-reducing gene and nitrate-reducing gene groups were present in approximately at the same intensities also.

The seawater samples (Figure 6-6) displayed variability in fluorescence between samples, though to a lesser degree compared with the corrosion and sediment samples: maximum variation between seawater sample signal was under 180 units, compared with 580 units and 660 units for the corrosion and sediment, respectively. The median signal per probe cluster was lower overall also, with only five gene passing 500 units. This contrasts with all fifteen genes in the sediment analysis surpassing this value. Of the seawater gene responses, the *iro* and *amoA* genes being the greatest.

Overall, it was observed that marine sediment samples had the greatest concentration of MIC-related genes relative to corrosion and seawater samples. The signal intensities for the corrosion samples were closer in overall fluorescence values to the sediment than to the seawater. This can be most clearly seen in Figure 6-7, which displays median responses of the three samples for each sample type. Additionally, the method of using averaged gene responses have not introduced an apparent bias. The fluorescence values

do not appear to have been influenced by the number of probe clusters present; the response of the sixteen *assA* gene probes returned similar values as those genes with several hundred probes.

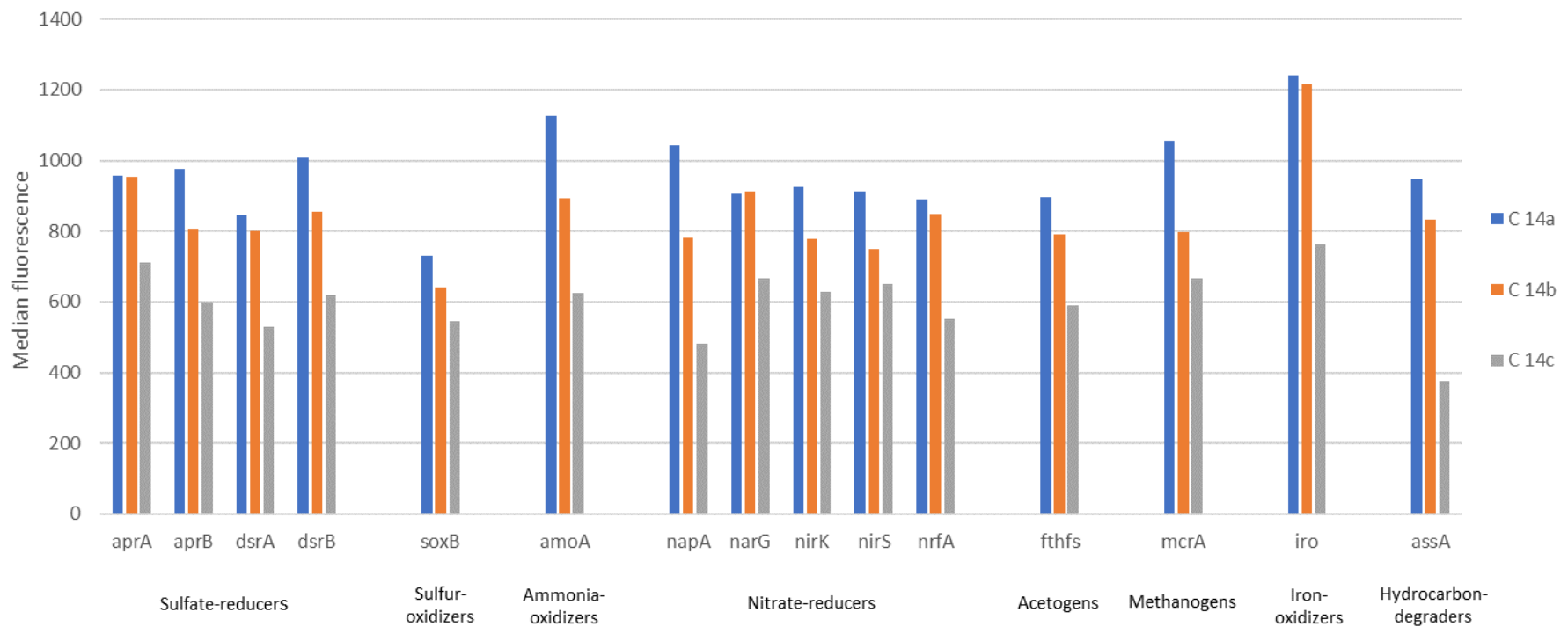


Figure 6-4 Median abundance of functional genes within microbial groups for corrosion samples C 14a, C 14b, and C 14c

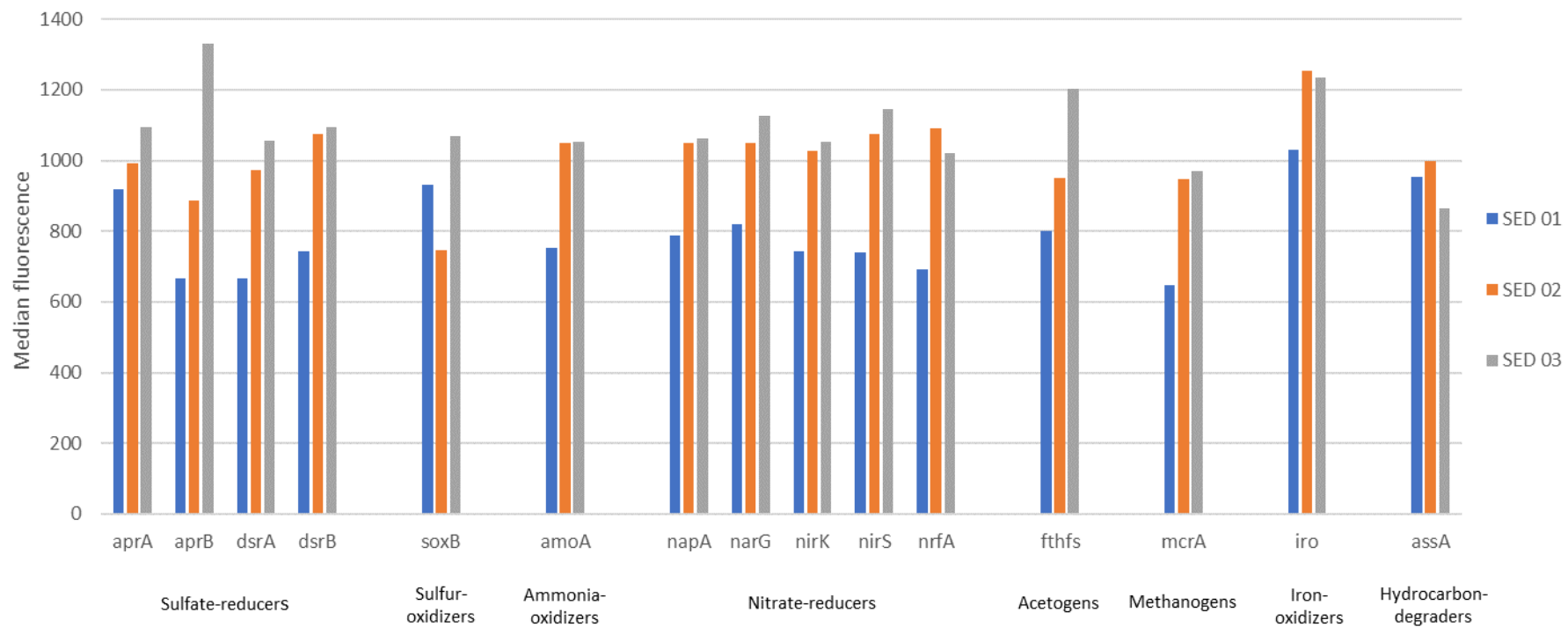


Figure 6-5 Median abundance of functional genes within microbial groups for marine sediment samples SED 01, SED 02, and SED 03

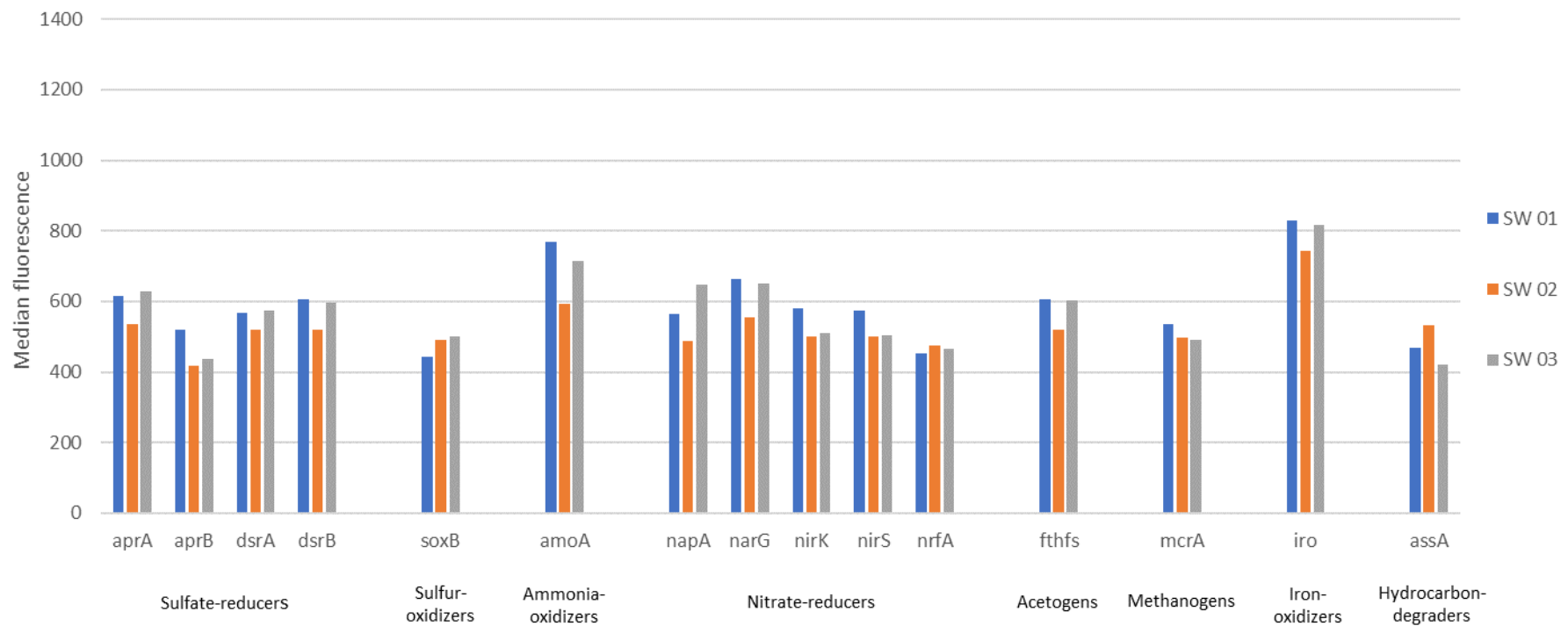


Figure 6-6 Median abundance of functional genes within microbial groups for seawater samples SW 01, SW 02, and SW 03

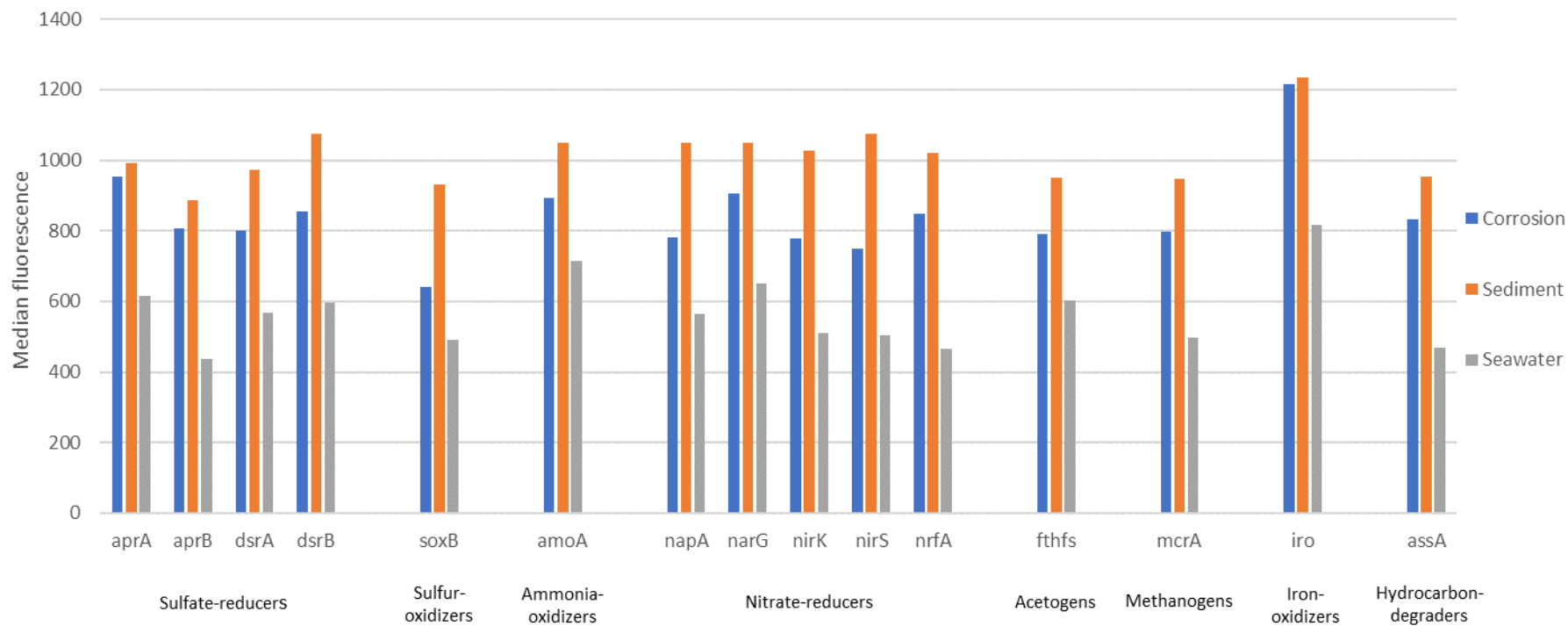


Figure 6-7 Median abundance of functional genes within microbial groups for corrosion, marine sediment, and seawater samples

6.3 Genetic similarity analysis of low tide zone corrosion, marine sediment, and seawater samples

The fluorescence data obtained from GeoChip analysis of low tide level corrosion (C 14a, 14b, and 14c), marine sediment (SED 01, 02, and 03), and seawater samples (SW 01, 02, and 03) were analysed for similarity within the gene types and dendrograms constructed, as described in Section 3.2.2.

6.3.1 *aprA* gene

The dendrogram derived from analysis of the *aprA* gene (Figure 6-8) indicated a 98.26% similarity between the sediment samples SED 01 and SED 03. The adjacent cluster comprised the sediment sample SED 02 and corrosion sample C 14b; these were found to be 96.90% similar. These two clusters possessed a 91.67% similarity. This grouping linked to the corrosion sample cluster comprising C 14a and C 14c (similarity of 87.77%) with a similarity of 80.64%. The seawater samples SW 02 and SW 03 formed a cluster with a 90.91% similarity; this then linked to the sediment/corrosion sample cluster with a 70.11% similarity. The final sample, SW 01, was found to bear a 67.22% linkage to the other eight samples.

6.3.2 *aprB* gene

Analysis of the fluorescence values for genera identified with the *aprB* gene (Figure 6-9) indicated the presence of two main clusters that bore an 85.32% similarity. The first cluster included two sediment and two corrosion samples: C 14C and SED 03 had an indicated similarity of 99.25%; SED 02 was found to cluster with these two samples (97.81% similarity); and C 14b completed the cluster with a 95.62% similarity. The second cluster comprised all three seawater samples (SW 01, 02, and 03) and the remaining corrosion and sediment samples. Samples SW 01 and SW 03 had a similarity of 99.39%, and sediment sample SED 01 linked to this group with a 97.67% similarity. Corrosion sample C 14b and seawater sample SW 02 had a 98.29% similarity; this pair linked to the rest of the cluster with a 93.95% similarity.

6.3.3 *dsrA* gene

The dendrogram for this gene (Figure 6-10) illustrates the closest correlation between samples occurred between the seawater samples SW 01 and SW 03; these had a similarity of 90.21%. This group linked with a sediment cluster comprising SED 01 and SED 02 (81.12% similarity) with a 71.06% correlation. The corrosion and remaining sediment and seawater samples formed a separate cluster (69.44% similarity to the first cluster). Within this grouping C 14c and SW 02 shared an 84.01% match in profile; the closest sample to this pair was C 14b (77.72% similarity). Samples C 14a and SED 03 were found to be 75.64% similar; the pair linked to the previous group with a 73.94% similarity.

6.3.4 *dsrB* gene

The corrosion samples formed a distinct cluster for this gene: as shown in Figure 6-11, C 14a and C 14c were found to have a 96.30% correlation; . Samples C 14b and SED 03 formed a pair (86.33% similarity) that had a 79.81% linkage to the first cluster. The remaining sediment samples (SED 01 and SED 02) were 93.11% similar and linked to the adjacent cluster with a correlation of 76.89%. The seawater samples SW 01 and SW 03 exhibited a similarity of 90.24%; the adjacent SW 02 sample linked to this pair with an 80.46% similarity. These three samples joined to the main corrosion and sediment samples with a 69.44% similarity.

6.3.5 *soxB* gene

Analysis of the *soxB* fluorescence values revealed two main clusters amongst the samples (Figure 6-12). The seawater samples along with one sediment sample formed a cluster within which SW 03 and SED 01 shared a 97.13% correlation. Seawater samples SW 01 and SW 02 also joined this grouping, with 93.35% and 90.74% correlation, respectively. The remaining samples formed a cluster which shared a 69.31% similarity with the seawater sample cluster. Corrosion samples C 14b and C 14c had an indicated similarity of 92.35%, which in turn were linked (84.24% correlation) to the next closest sample (C 14a). Samples SED 02 and SED 03 formed a pair with 84.21% correlation; this pair linked to the corrosion cluster with a 78.17% similarity.

6.3.6 *amoA* gene

Analysis of the *amoA* gene fluorescence data indicated a high degree (97.67%) of correlation between the sub-clusters present. Samples C 14a and SED 03 were the closest linked samples, possessing a similarity of 99.80%; this group was also linked subsequently to samples SED 02 and SW 01, with similarities of 99.53% and 99.00% respectively. Samples C 14c and SW 02 were 99.31% similar in composition and formed a three-sample cluster with SED 01 (99.03% correlation overall). This latter group subsequently linked to the first (98.46% similarity). The remaining corrosion sample C 14b and seawater sample SW 03 shared a similarity of 99.20%. This is illustrated in Figure 6-13.

6.3.7 *napA* gene

Three apparent clusters were revealed in this analysis (Figure 6-14). The closest was between the seawater samples: SW 02 and SW 03 were found to have a 99.09% similarity, both of which were then 95.99% correlated to SW 01. Corrosion samples C 14a and C 14b were paired with an 88.25% similarity and linked (76.66% correlation) to an 84.30% similar pairing of SED 01 and SED 02. These two clusters bore a 63.27% correlation. The final two samples (C 14c and SED 03) were found to be 68.66% similar and linked to the first two clusters with a 60.42% correlation.

6.3.8 *narG* gene

Figure 6-15 illustrates the sample similarities based on analysis of the *narG* gene. The closest correlation was between corrosion sample C 14a and seawater sample SW 03 (95.97% similarity). This pair has an 89.76% correlation with a nearby cluster comprising of C 14b, C 14c, and SED 01. The latter two samples are 94.92% similar in profile, and 92.54% linked to C 14c. Samples SED 02 and SED 03 demonstrate a 93.26% similarity, and link with SW 02 (88.63% correlation). This cluster links with the first with a 78.44% similarity. Sample SW 01 is not part of a cluster but correlates with the other sample groups with a similarity of 76.48%.

6.3.9 *nirK* gene

Analysis of this gene data (Figure 6-16) indicated the closest similarity occurred between corrosion sample C 14b and sediment sample SED 03 (99.56% correlation). The adjacent corrosion samples, C 14a and C 14c, were 99.56% similar in profile, and clustered with the first pair with a 99.05% similarity. Two sediment samples (SED 01 and SED 02) share a 99.04% correlation and are also linked to sample SW 02 with a 98.63% linkage. This group of three samples links to the first cluster with a 97.94% similarity. The remaining two seawater samples (SW 01 and SW 03) displayed a similarity of 96.41% and 96.02% respectively to the main cluster.

6.3.10 *nirS* gene

Figure 6-17 illustrate the linkages between the samples for the *nirS* gene. The corrosion samples C 14a and C 14b were found to be 93.53% similar in profile; the third corrosion sample C 14c was indicated to have an 87.97% similarity to this pair. Sediment samples SED 01 and SED 03 expand this cluster with pairings of 83.08% and 77.06%, respectively. Seawater samples SW 01 and SW 02 were found to have a 94.53% similarity; this pair joined the main cluster with a 74.06% linkage. The remaining two samples (SED 02 and SW 01) linked to the main cluster with 67.70% and 60.77% correlation, respectively.

6.3.11 *nrfA* gene

The dendrogram of the *nrfA* gene analysis (Figure 6-18) indicated a similarity of 98.59% between corrosion samples C 14b and C 14c; this pair also linked with sample C 14a (96.38% similarity). The sediment sample SED 02, and seawater sample SW03 also joined this cluster, with linkages of 88.51% and 70.53% respectively. Sediment samples SED 01 and SED 03 were linked with a 97.25% similarity; seawater samples SW 01 and SW 02 linked together with 98.67% similarity. These latter pairs connected with the main cluster with 65.75% and 62.62% similarities, respectively.

6.3.12 *fthfs* gene

For this gene, seawater and most of the sediment samples comprised the main cluster. Figure 6-19 showed a pairing of SW 01 with SW 03 (96.82% similarity), and C 14a

with C 14b (97.62% similarity); the latter were also linked to SW 02 (96.09% similarity). These two groups were found to be 82.98% similar. Corrosion sample C 14c then joined with cluster (65.73%). Samples SW 01 and SW 02 formed a pair with 73.63% linkage; they bear a 60.41% similarity to the main cluster. Sediment sample SED 03 also joins the main cluster with 52.65% similarity.

6.3.13 *mcrA* gene

The dendrogram for this gene (Figure 6-20) displayed the greatest correlation between the samples C 14a and C 14b. This pair was then linked to seawater sample SW 02 (96.28% similarity). Sample SW 03 joined this three-sample group, with a 94.08% similarity. Corrosion sample C 14c was found to be 93.65% to this. Sediment sample SED 01 linked to this subsequently with a similarity of 90.60%. The remaining samples joined the other samples singly (SW 01 with 75.90% linkage), and as a pair (SED 02 and SED 03 linked together with 62.57% similarity) with 57.76% similarity.

6.3.14 *iro* gene

Figure 6-21 displays the results of the analysis for the *iro* gene. All nine samples bore a greater than 98% similarity with each other. The seawater samples SW 02 and SW 03 were found to be linked with 99.86% similarity. Two sediment sample (SED 03 and SED 01) joined this pairing with 99.86% and 99.85% similarity, respectively. Sample SW 01 completed this cluster (99.75% similarity). The three corrosion samples formed were found to be grouped together: C 14a and C 14b were 99.81% correlated, and C 14c had a 99.77% correlation to this pair. These three samples were linked to the sediment and seawater cluster with 99.57% similarity. The final sample, SED 02, linked to the other samples with 98.96% similarity.

6.3.15 *assA* gene

The dendrogram for this gene (Figure 6-22) exhibited two distinct clusters, both of which contained samples from the three sample types. The larger cluster comprised five samples: C 14a and SED 01 (99.99% similarity) linked to C 14b and SED 03 (99.99% similarity) with a 99.62% correlation. Sample SED 02 linked to these four samples with a 98.92% similarity. The smaller cluster comprised of SW 01 and SW 02

(99.99% similarity) linked to C 14c (99.75% similarity) and SW 03 (99.37%). The two clusters were found to be 95.90% similar.

The first four functional genes analysed (*aprA*, *aprB*, *dsrA*, and *dsrB* genes) initially were indicative of sulfate-reducing prokaryotes (Section 2.3). The analysis revealed a high degree of diversity existed between the samples for each of the selected genes. The *aprA* gene analysis indicated that corrosion and marine sediment samples had a greater similarity in absolute fluorescence values for each of the identified microbial genera identified within the *aprA* probe set. The linkages to the seawater samples were the weakest. The related gene, *aprB*, did not show a similar pattern to this. The clusters for *aprB* possessed a broadly similar mix of corrosion, sediment, and seawater samples, though the degrees of similarity were overall higher suggesting that presence of the gene was more uniform amongst the samples that for the *aprA* analysis despite this. The *dsrA* gene analysis indicates a similarity in composition amongst the corrosion samples, which tended to group together, and between the sediment and seawater samples, which formed a separate cluster. The clustering of *dsrB* probe responses indicated a similar pattern to that for *dsrA*: corrosion samples formed a separate cluster, and sediment and seawater samples tended to cluster closely. The similarity between these clusters was also similar (between 67.04% versus 69.44%).

Analysis of the functional gene associated with sulfur-oxidizing bacteria (*soxB* gene) produced a dendrogram that also grouped corrosion samples together as a single cluster, whilst clustering sediment and seawater samples together. As with the *dsrA* and *dsrB* gene analysis the two main clusters displayed a similarity in the upper 60s percent (69.31%).

The *amoA* gene data, which is indicative of nitrite-oxidizing bacteria, produced a dendrogram with no clear pattern of sample correlation; like that obtained from analysis of the *aprB* data. Similarly, the dendrogram displayed a high overall correlation (97.67%) between all samples.

The next group of genes analysed were those associated with the presence of nitrate-reducing prokaryotes (*napA*, *narG*, *nirK*, *nirS*, and *nrfA* genes). The *napA* dendrogram clustered the seawater samples together closely and correlates the corrosion and sediment samples together albeit with lower degrees of similarity. The *narG* plot

displays a clustering of the corrosion samples together, whilst the sediment and seawater samples generally clustered together in a similar fashion to the *dsrA* and *dsrB* gene analysis. The *nirK* dendrogram also displayed a high degree of correlation between samples (minimum similarity of 96.02%), though unlike those for *aprB* and *amoA* genes some sample patterns were apparent: corrosion samples were clustered together, as were two of the sediment samples. Analysis of the *nirS* gene indicated a close clustering of corrosion samples also, with sediment and then seawater samples joining the grouping. Similarly, analysis of *nrfA* demonstrated a clustering together of corrosion samples, followed by individual or paired samples of sediment and seawater.

Analysis of the gene indicative of acetogenic prokaryotes (*fthfs* gene) revealed the greatest correlation occurred between sediment and seawater samples; the corrosion samples were more diverse and did not form a separate cluster. The *mcrA* gene analysis indicates that the fluorescence values of methanogenic archaea present in the samples correlated most closely between corrosion and seawater; the sediment generally displayed a significantly lower similarity. The *iro* gene data, which is indicative of iron-oxidizing bacteria, displayed an extremely high degree of correlation between all samples (greater than 98.96%) and featured a corrosion sample cluster adjacent to a cluster made up of only sediment and seawater. The functional gene indicative of hydrocarbon degrading bacteria (*assA* gene) similarly indicated a high degree of correlation between samples (greater than 95.90%). The clustering pattern also resembled that of the *aprB* gene analysis in that the corrosion, sediment, and seawater samples do not form sample type clusters, but assemble as mixed groupings.

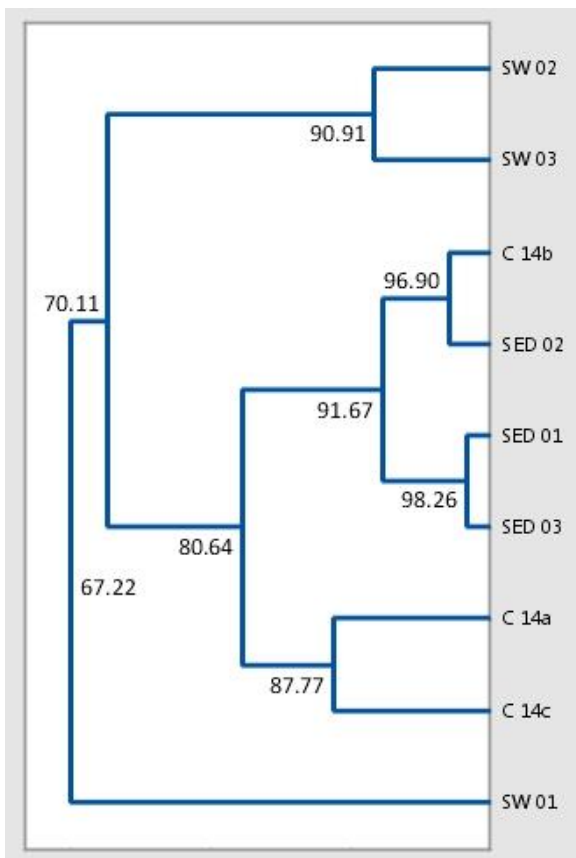


Figure 6-8 Similarity analysis of samples using *aprA* gene data

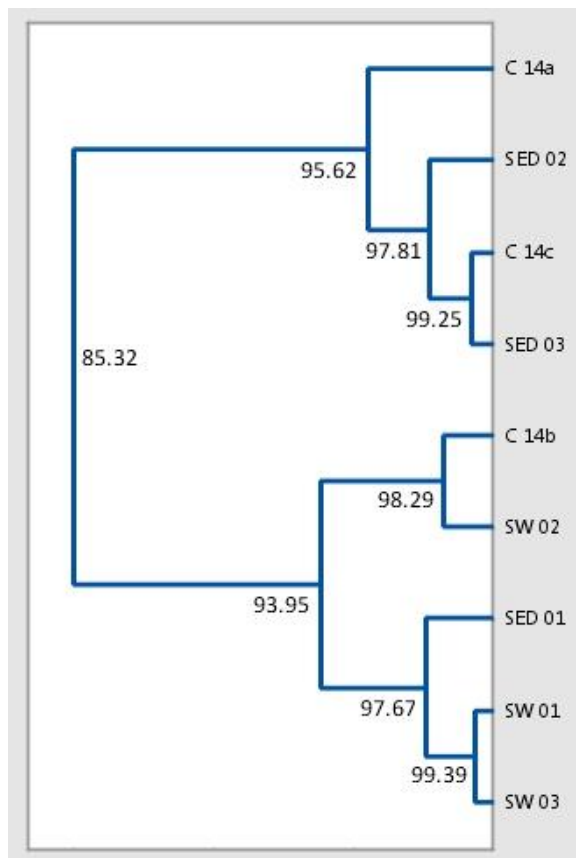


Figure 6-9 Similarity analysis of samples using *aprB* gene data

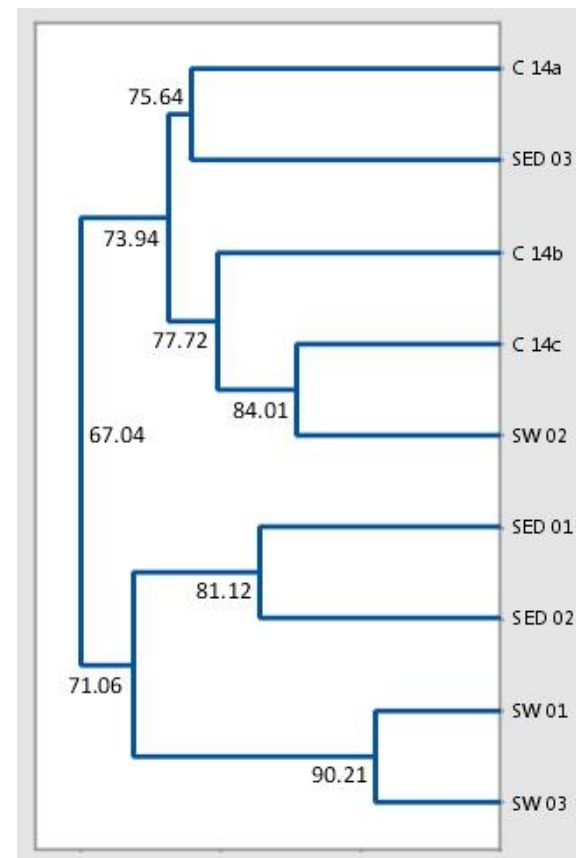


Figure 6-10 Similarity analysis of samples using *dsrA* gene data

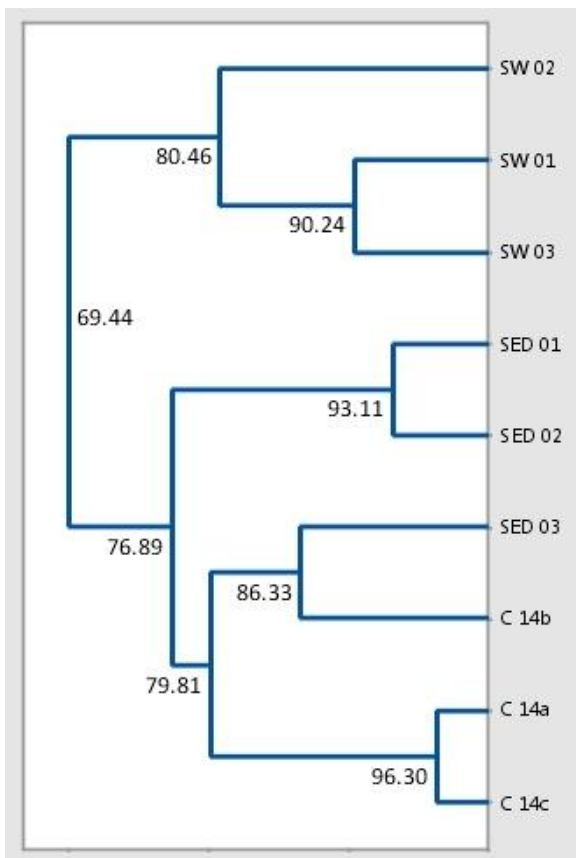


Figure 6-11 Similarity analysis of samples using *dsrB* gene data

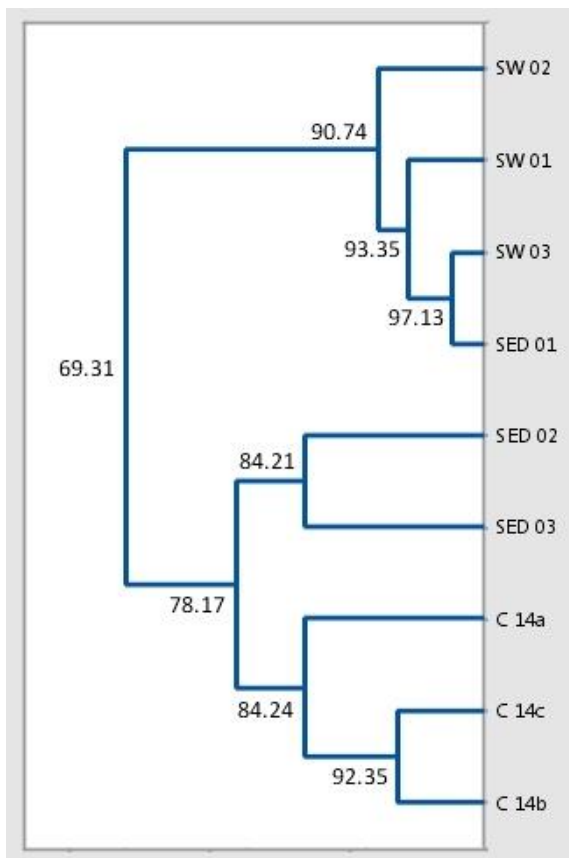


Figure 6-12 Similarity analysis of samples using *soxB* gene data

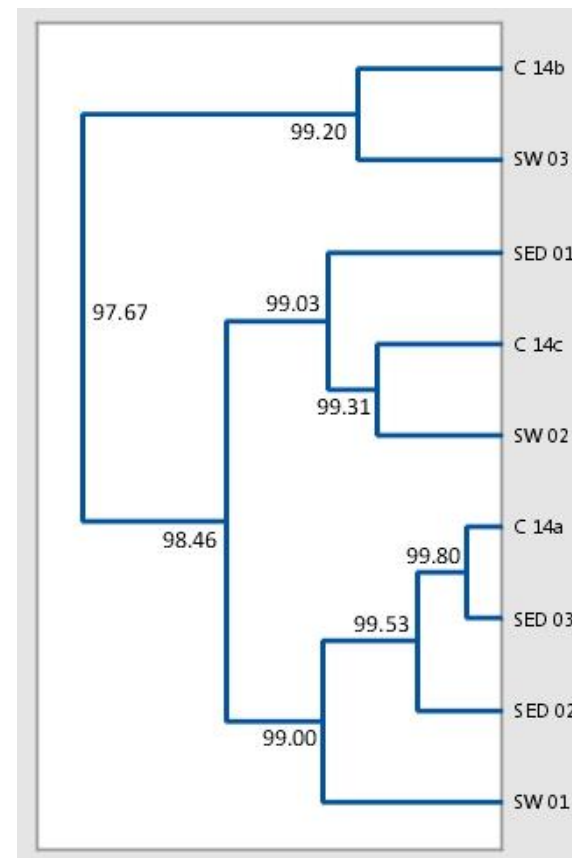


Figure 6-13 Similarity analysis of samples using *amoA* gene data

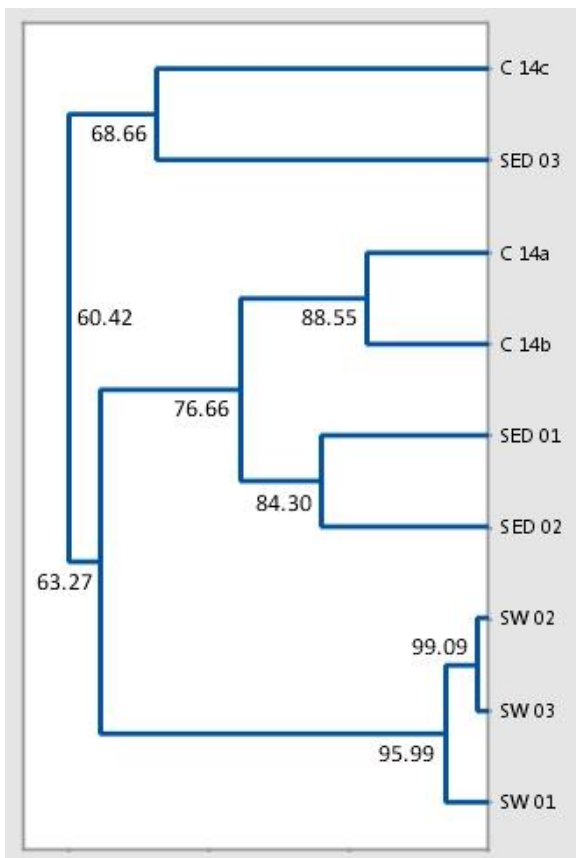


Figure 6-14 Similarity analysis of samples using *napA* gene data

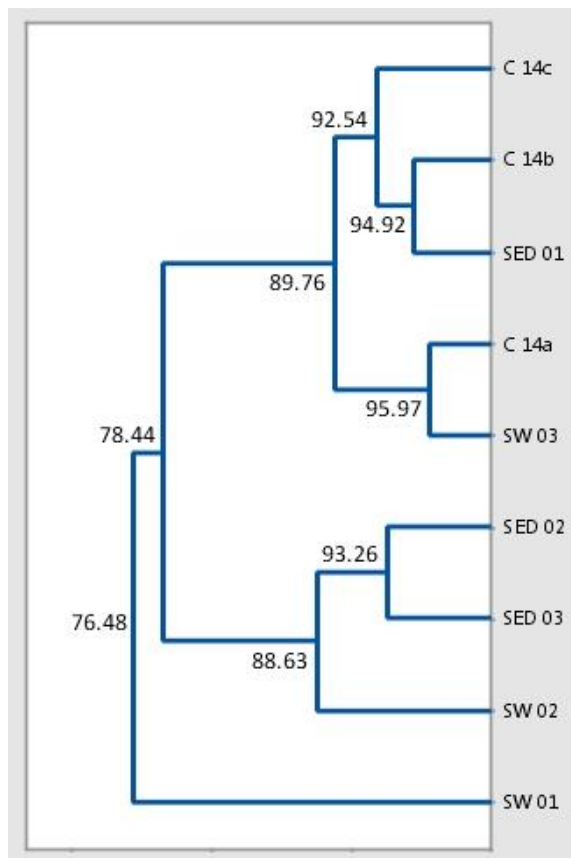


Figure 6-15 Similarity analysis of samples using *narG* gene data

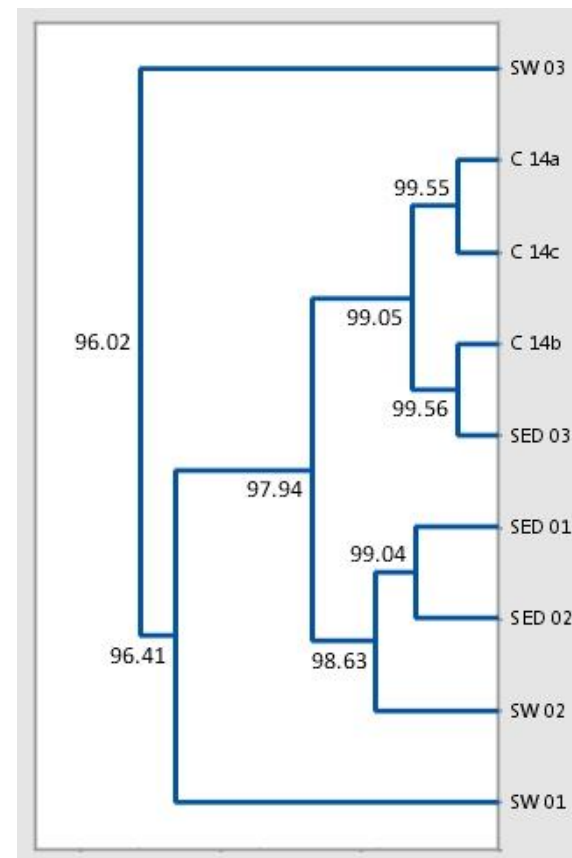


Figure 6-16 Similarity analysis of samples using *nirK* gene data

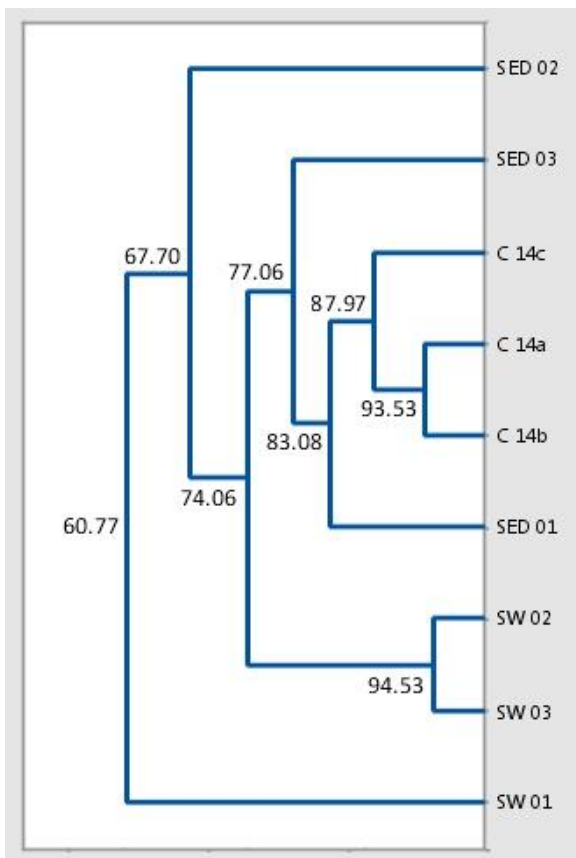


Figure 6-17 Similarity analysis of samples using *nirS* gene data

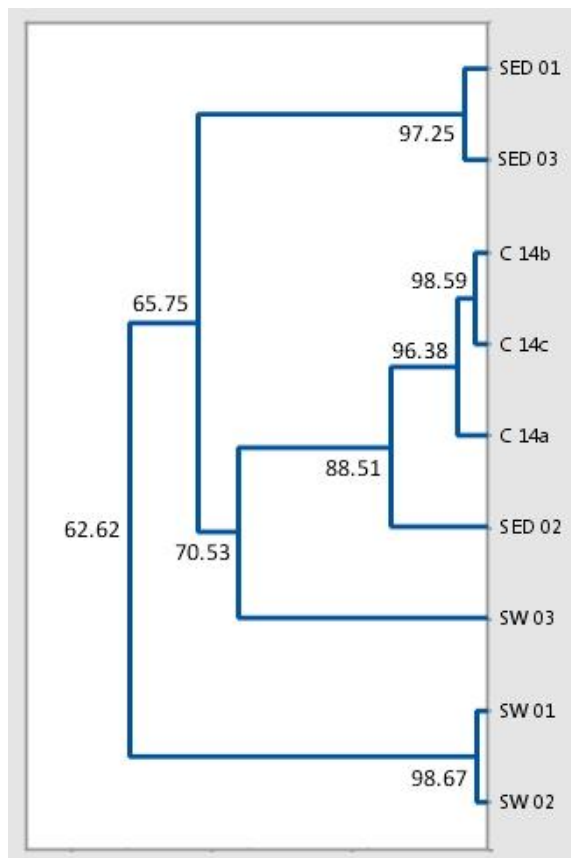


Figure 6-18 Similarity analysis of samples using *nrfA* gene data

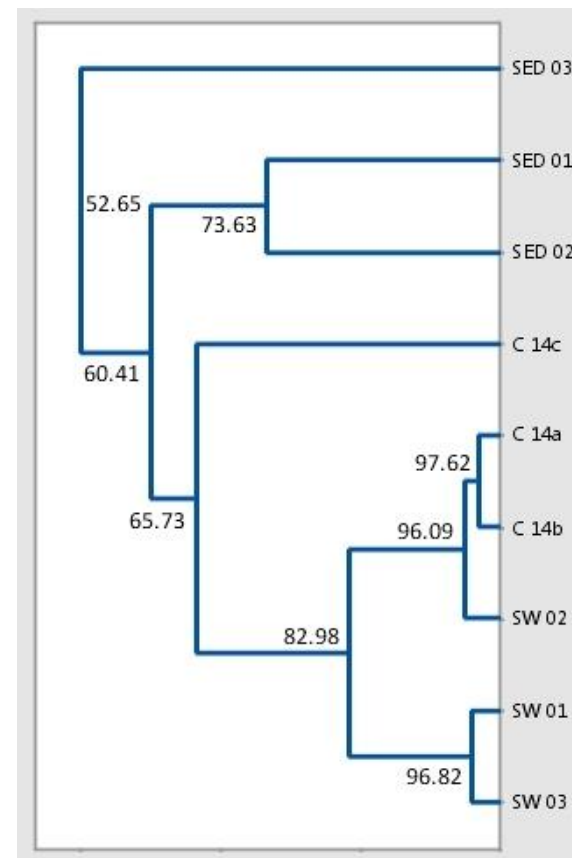


Figure 6-19 Similarity analysis of samples using *fthfs* gene data

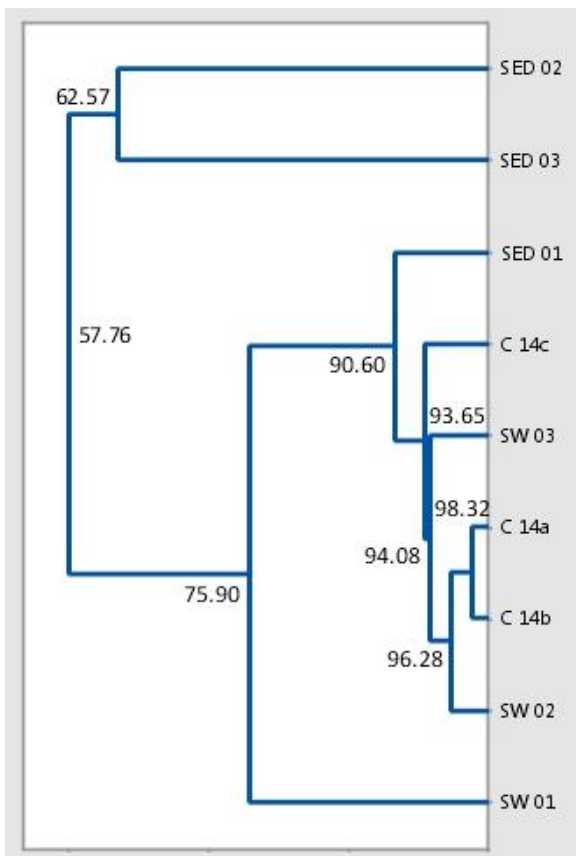


Figure 6-20 Similarity analysis of samples using *mcrA* gene data

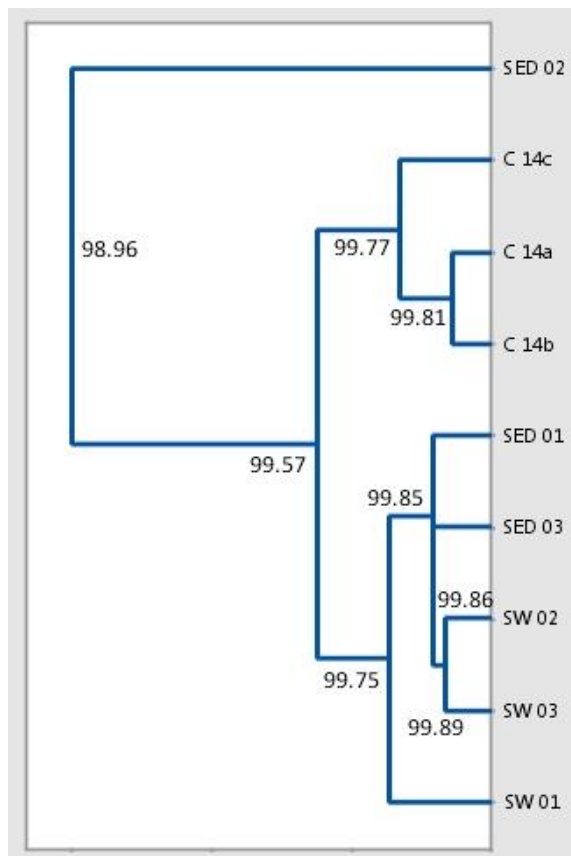


Figure 6-21 Similarity analysis of samples using *iro* gene data

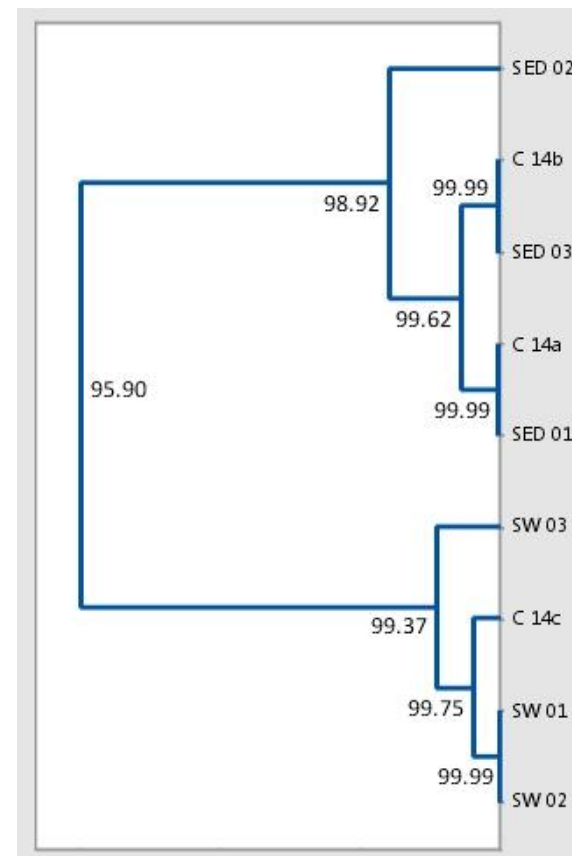


Figure 6-22 Similarity analysis of samples using *assA* gene data

6.4 Taxonomy of low tide zone corrosion

The data obtained from GeoChip analysis of three low tide zone corrosion samples (C 14a, 14b, and 14c) are displayed in Table 6-1 below. The table comprises a set of median responses from the three samples for MIC-related genes included on the GeoChip 5.0 microarray, and the taxonomy of corresponding microorganisms, from kingdom to genus.

Whilst analysing the raw data, it was found that a proportion of each set of probe clusters bore oligonucleotide probes derived from unidentified microorganisms; these amounted to 74% of the total probes present. As the intention was to characterise the microbial composition of the corrosion samples, the responses for unidentified microorganism, and identified microorganisms that had no detectable fluorescence across all genes have been excluded from Table 6-1. Where a probe cluster was present for a gene associated with a particular microorganism, but fluorescence values were below the detection threshold, the position is coloured according to the gene type, but without a numerical value.

The analysis identified the presence of two domains within the samples: bacteria and archaea. Of bacteria there were found to be 18 phyla, 30 classes, 66 orders, 121 families, and 281 genera; and of archaea, 2 phyla, 8 classes, 16 families, and 30 genera were identified.

A qualitative appraisal of the gene probe types versus microbial phyla present indicates that Acidobacteria, Actinobacteria, Aquificae, Bacterioidetes, Chloroflexi, Cyanobacteria, Deinococcus-Thermus, Fusobacteria, Lentisphaerae, Nitrospirae, Planctomycetes, and Proteobacteria of the Alpha-, Beta-, Epsilon-, and the majority of Gammaproteobacteria classes were indicated by nitrogen-cycling genes (*napA*, *narG*, *nirK*, *nirS*, and *nrfA*), the *fthfs* acetogenic gene, and to a lesser extent, the *iro* iron reducing gene. Proteobacteria of the class Deltaproteobacteria, along with *Chromatiales* and *Ectothiorhodospiraceae* families with the Gammaproteobacteria class were identified by mostly sulfur-cycling genes (*aprA*, *aprB*, *dsrA*, *dsrB*). Whereas members of the Spirochetes, Thermodesulfobacteria, and Verrucombia phyla were indicated by either sulfur-reduction or the acetogenic gene *fthfs*. The archaea were identified mostly by the presence of sulfate-reducing genes (Phylum Crenarchaeota), or sulfate-reducing genes and the

methanogenic gene *mcrA* (Five families within the phylum Euryarchaeota), or nitrate-reducing genes (Family *Halobacteriaceae* within the phylum Euryarchaeota). The Firmicutes mostly by activity of the *fthfs* acetogenic gene, and some sulfur-cycling genes.

For each gene, the highest signals were due to *Desulfocaldus* spp. (*aprA*); *Desulforudis* spp. (*aprB*); *Thermoproteus* spp. (*dsrA*); *Moorella* spp. (*dsrB*); *Thiobacillus* spp. (*soxB*); *Haemophilus* spp. (*napA*); *Selenomonas* spp. (*narG*); *Cardiobacterium* spp. (*nirK*); *Desulfurivibrio* spp. (*nrfA*); *Brevibacterium* spp. (*fthfs*); *Methanobrevibacterium* spp. (*mcrA*); and *Kokuria* spp. (*iro*). No fluorescence values were recorded for the hydrocarbon-degrading related *assA* gene.

Where they were present, the genes probes involved in sulfate reduction (*aprA*, *aprB*, *dsrA*, and *dsrB*) were positive for sulfate-reducing Deltaproteobacteria of the families *Desulfarculaceae*, *Desulfotobacteraceae*, *Desulfobulbaceae*, and *Syntrophobacteraceae*; for Gammaproteobacteria of family *Chromatiaceae* and *Ectothiorhodospiraceae*; for Chlorobia of the family *Chlorobiaceae*; and the Archaeal Class Thermoprotei and Family *Thermoproteaceae*. When comparing the microarray data with SRP genera implicated in MIC (Section 2.1 and 2.2), the majority are identified, with measurable levels of fluorescence. These comprise species of the genera *Chlorobaculum*, *Chlorobium*, *Desulfobacterium*, *Desulfobacula*, *Desulfobotulus*, *Desulfobulbus*, *Desulfocaldus*, *Desulfococcus*, *Desulfofaba*, *Desulfoglaeba*, *Desulfohalobium*, *Desulfomicrobium*, *Desulfonatronospira*, *Desulfonatronovibrio*, *Desulforudis*, *Desulfosporosinus*, *Desulfotalea*, *Desulfothermus*, *Desulfotomaculum*, *Desulfovibrio*, *Desulfurivibrio*, *Fibrobacter*, and *Halorhodospira*. Of the remainder, *Brevibacterium*, *Clavibacter*, *Corynebacterium*, *Desulfuromonas*, *Dethiosulfovibrio*, and *Kytococcus* were identified as being present within the microbial community via MIC-related genes other than *aprA*, *aprB*, *dsrA*, and *dsrB*; the microarray lacked SRP-related probe clusters for these genera. Similarly, the genera *Desulfitobacterium*, *Desulforhopalus*, *Desulfopila*, *Desulfobacter*, *Desulfocella* were detected by other probe clusters, whilst displaying fluorescence levels below detection thresholds for SRP-related gene probes. Species of *Desulfocapsa*, and *Desulfotignum*, were found to be present during the GeoChip analysis, but MIC-relevant probes were not present. Finally, the genera *Desulfonauticus*, *Desulfustis*, *Desulfotoregula*, *Desulfotobulbus*, and *Desulfosarina* were found to be entirely absent; no probes were present in the microarray.

Sulfate-reducing archaea were also identified within the corrosion samples. The genera *Caldivirga*, *Pyrobaculum*, *Thermoproteus*, and *Vulcanisaeta* within the phylum Crenarchaeota were identified by fluorescence of *aprAB* or *dsrAB* gene probes. Within the family Euryarchaeota, twelve SRP genera were similarly identified: *Archaeoglobus*; *Methanothermus*, *Methanotorris*, *Methanoculleus*, *Methanoplanus*, *Methanolinea*, *Methanosphaerula*, *Methanoregula*, *Methanococoides*, *Methanohalophilus*, *Methanosarcina*, and *Methanopyrus*. Both *Thermoproteus*, and *Vulcanisaeta* are of note as the genera are thermophiles, growing optimally above 40°C. *Vulcanisaeta* is also an acidophile, growing optimally below pH 4.5 (Madigan et al., 2009).

The gene involved with thiosulfate oxidation (*soxB*) was present in the Alpha, Beta, and Gammaproteobacteria classes mainly; and a single genus (*Chlorobaculum*) within Class Chlorobia. Six of the nine probe groups displayed a measurable level of fluorescence. These corresponded with: *Citreicella* spp. within the family *Rhodobacteraceae*; *Advenella* spp. within the family *Alcaligenaceae*; *Hydrogenophaga* spp. and *Ramlibacter* spp., both of family *Comamonadaceae*; *Thiobacillus* spp. belonging to family *Hydrogenophilaceae*; and *Congregibacter* spp. within the family *Xanthomonadaceae*. The number of gene clusters (21) present in the microarray was amongst the lowest number for the gene set selected. So, whilst the data has confirmed a significant level of activity for an important genus of SOB (*Thiobacillus*), and allowed identification of other genera, this technique was not able to provide a thorough investigation of the prevalence of sulfur oxidizing microorganisms in the corrosion samples. The SOB discussed previously in Section 2.2, *Halothiobacillus*, *Thiocapsa*, *Thiobacillus*, *Thiomonas*, and *Thioalkalivibrio* were all found to be present in the corrosion samples. Except for *Thiobacillus*, *soxB* gene probes were not present for these genera but instead they were identified by the presence of iron-reducing gene (*iro*), the sulfate-reducing genes, a nitrate-reducing gene (*narG*), and a gene involved in nitrite-reduction (*nrfA*). *Acidithiobacillus* spp. and *Acidiphilium* spp. were identified as present during the analysis, but without MIC-related gene probes. However, the two genes present (*sqr* and *cysJ*), whilst involved with sulfate-reduction, form part of the assimilatory pathways for this process. As indicated in Section 3.2.2, the microarray used did not possess probes for the nitrite oxidoreductase gene, *nxr*, therefore the analysis was not able to discern nitrite-oxidizing bacteria on this basis. However, the presence of *Nitrobacter* spp. was detected

based on measurable fluorescence of the *iro* gene, and *Nitrospira* spp. by activity of *fthfs* probes. *Nitrococcus* spp. was also detected albeit via two assimilatory sulfite-reductase genes (*sir* and *cysJ*). Probes for genes of the fourth genus, *Nitrospina*, were not present on the microarray. Other acid-producing bacteria implicated in MIC were also discerned: *Acetobacter* spp. and *Propionibacterium* spp., via the *dsrA*, and *narG* and *fthfs* genes, respectively.

Measurable fluorescence for the ammonia monooxygenase gene (*amoA*) was limited to AOB Betaproteobacteria of the family *Nitrosomonadaceae*, genera *Nitrosomonas*, and *Nitrospira*., and Gammaproteobacteria of the family Chromatiaceae and genus *Nitrosococcus*. As discussed in Section 3.2.2, the microarray included 146 probes for this gene, of which 86 displayed measurable fluorescence. However, 81 of these corresponded with unidentified microorganisms. Probes were present for species of genera *Pseudomonas* but displayed no measurable fluorescence.

The nitrate reductase gene *napA*, was observed in 37 genera, mainly within the phyla Bacteroidetes, Proteobacteria, and a single genera (*Haloferax*) within the Archaeal phylum Euryarchaeota. *Persephonella* spp. in the phylum Aquificae, *Cytophaga* spp. and *Zobellia* spp. of the phylum Bacteroidetes were discerned. Within the class Alphaproteobacteria, the genera *Bradyrhizobiaceae*, *Rhodopseudomonas*, *Dinoroseobacter*, *Paracoccus*, *Rhodobacter*, *Ruegaria*, *Azospirillum*, *Magnetospirillum*, and *Rhodospirillum* were identified. *Achromobacter* spp., *Bordetella* spp., *Cupriavidus* spp., *Chromobacterium* spp., and *Laribacter* spp. were identified from the class Betaproteobacteria. Two genera of the class Deltaproteobacteria were indicated: *Desulfovibrio* and *Sorangium*. The Gammaproteobacteria identified by this gene were: *Colwellia*, *Pectobacterium*, *Salmonella*, *Haemophilus*, and *Vibrio*.

The second nitrate reductase gene (*narG*) included in this study was present for species within nine genera of Actinobacteria: *Actinomyces*; *Mobiluncus*; *Gordonia*; *Microbacterium*; *Mycobacterium*; *Rhodococcus*; *Propionibacterium*; *Saccharopolyspora*; and *Streptomyces*. The gene was also detected in five genera of Firmicutes: *Geobacillus*; *Micrococcus*; *Staphylococcus*; *Lactobacillus*; and *Selenomonas*. Significant fluorescence levels were detected for genera within the Proteobacteria phylum also: *Phenylobacterium*; *Oligotrophpha*; *Pseudovibrio*; *Castellaniella*; *Cupriavidus*;

Lautropia; *Comamonas*; *Chromobacterium*; *Neisseria*; *Aromatoleum*; *Thauera*; *Escherichia*; *Pantoea*; *Shimwellia*; *Alcanivorax*; *Pseudomonas*; *Beggiatoa*; *Stenotrophomonas*; and *Methyloirabilis*. The gene is present for a single genera of nitrate-reducing archaea: *Haloferax*. Nitrate-reducing gene probes were absent for SRP of the genera *Marinobacter* and *Methyloversatilis*, but their presence was confirmed by fluorescence of the corresponding *fthfs* genes. *Microbacterium* had been found in waters surrounding MIC occurrence but had not been causally linked to its occurrence (Little et al., 2007). Bacteria of the genus *Actinomyces* are ubiquitous within the microbiota of animals and in soil but have not been associated with marine corrosion, though Laurent et al. (2000) note it has been observed in the presence of corrosion of nickel-chrome dental alloys. Similarly, *Mobiluncus* spp. have been commonly observed in animals, in cases of human urethritis (Fontaine et al., 1986), and not previously part of marine corrosion microbiota.

The nitrite-reducing genes, *nirK* and *nirS*, discern 16 genera which were identified by other genes; only two unique genera were identified by these genes alone: *Nisaea*, within the class Alphaproteobacteria, and *Natronomonas* within the Archaeal class Halobacteria. The third nitrate-reducing gene, *nrfA*, identified 14 genera of bacteria. Two were within the phylum Actinobacteria: genera *Mobilococcus* and *Eggerthella*, both commonly form part of the human microbiota, and have also been isolated from soil samples (Lau et al., 2004, Botero et al., 2015). A single genus was identified within each of the phyla Chloroflexi and Deinococcus-Thermus; these were *Anaerolinea* and *Meiothermus*, respectively. The former had previously been associated with damage to concrete sewers (Cai et al., 2017), while the latter has not been associated with MIC, it has been observed as a dominant component of biofilms in interim wet storage system for spent nuclear fuel (Masurat et al., 2005). Within the phylum Firmicutes, *Heliobacterium* spp. and *Carboxydotherrmus* spp. were identified. A single genus *Lentisphaera* was identified; this has been isolated from coastal marine sediment and has been found to be an early coloniser of biofilms (Jung et al., 2014, Rampadarath et al., 2017). From the phylum Planctomycetes, *Rhodopirellula* spp. were also identified. The *nrfA* probes indicated the presence of *Desulfuromonas* spp., previously implicated in MIC processes, which includes both sulfate-reducing and iron-reducing species according to Summer et al. (2014). Within the same order, Desulfuromonadales, the genera of iron-reducing bacteria

Pelobacter was also identified. Other proteobacteria identified were of genus: *Anaeromyxobacter*; and *Mannheimia*. A single genus of the phylum Verrucomicrobia, *Chthoniobacter* was indicated. This phylum is essentially ubiquitous in soil and marine sediments (Bergmann et al., 2011), but apparently not connected to occurrences of marine MIC. Of note is the nirK probes signal obtained for *Cardiobacterium* spp. within the class Gammaproteobacteria, and family *Cardiobacteriaceae*, which has the highest value for any of the probes in this analysis. This is a genera of fastidious bacilli that have been associated with human pathology (Wormser and Bottone, 1983) but also not apparently implicated in MIC processes.

The presence of acetogenic prokaryotes (AP) was indicated by the presence of *fthfs* probe activity. It was the third most numerous MIC-related probe in the GeoChip microarray, after *dsrA* and *narG* but had the greatest number of responsive probes clusters amongst the identified genera. Of the 123 genera identified using this gene, 69 genera corresponded with this gene alone. The identified genera were distributed widely amongst the various phyla, though only five of 34 genera within the class Betaproteobacteria had a corresponding probe set. Similarly, four of the 26 Archaea possessed *fthfs* probe clusters. From the list of acetogens identified previously in MIC processes *Bacillus* spp. were indicated by fluorescence of the *nrfA* probe cluster also; *Clostridium* spp. were confirmed by fluorescence of *dsrA* and *dsrB* genes in addition to *fthfs*, indicating that species within this genus may also be SRP. *Treponema* spp. was also indicated by fluorescence of the *fthfs* gene cluster, though the *dsrA* cluster also present indicated no measurable signal. *Acetobacterium* spp. were also indicated. However, an *fthfs* gene probe set was not present for this genera; its presence was indicated by activity in a *dsrA* probe cluster. Similarly, there were no *fthfs* probes present to identify *Desulfotomaculum* spp., *Eubacterium* spp. or *Moorella* spp. but these were identifiable instead via fluorescence of SRP-related genes. Gene probes corresponding with *Actogenium* spp. were present not in GeoChip, so its detection was not possible. Two genera of halophilic archaea were also indicated: *Haloarcula* and *Halorubrum*, along with two genera of the acidophilic archaeal class Thermoplasmata: *Ferroplasma* and *Aciduliprofundum*.

Gene probe groups indicative of methanogenic activity (*mcrA*) focused mainly on Archaea. All ten genera thus identified were part of the phylum Euryarchaeota. Of the genera previously implicated in occurrences of MIC, eight were identified by *mcrA*

fluorescence alone: *Methanobacterium*; *Methanofollis*; *Methanobrevibacter*; *Methanocorpusculum*; *Methanohalobium*; *Methanolobus*, *Methanothermobacter*, and *Methanosaeta*, of which the first two have previously been noted as contributing to MIC.

As previously discussed, no *feR* gene probes were present, so detection of IRB was limited. However, species of the genera *Acidobacterium* was identified by fluorescence of *fthfs* probe cluster (in Section 2.2). Similarly, the genus *Lactobacillus* was identified using this and the *narG* gene. Species of both these genera were part of the MIC implicated groups (Section 2.2).

The iron-oxidizing gene probe cluster (*iro*) was present for 69 genera of bacteria; no probes were present for the domain archaea. The analysis identified genera in the phyla: Actinobacteria; Bacteroidetes; Cyanobacteria; Firmicutes; and Proteobacteria. Unique identification of four genera was possible within the Actinobacteria: the SRP genus *Clavibacter*; *Liefsonia*; *Tsukamurella*; and *Kocuria*. The latter, as previously noted, possessed the highest fluorescence of the *iro* probe genera identified. The genus *Arthrobacter* includes acetogenic species that have been associated with MIC in copper (Swaroop et al., 2016); this analysis did not include copper oxidizing genes; the presence of *iro* gene suggests species within the genera are also capable utilising iron-oxidizing pathways. Amongst the Cyanobacteria, *Chloroflexus* and *Synechococcus* were indicated. Analysis of the *iro* gene fluorescence for Proteobacteria revealed the genus *Caulobacter* within the family *Caulobacteraceae*, which is an IRB that has been linked to MIC of copper also (Swaroop et al., 2016) and the genus *Rhodomicrobium*, within the family *Hyphomicrobiaceae*, previously linked to MIC in iron pipework (Section 2.2). In addition to these two Alphaproteobacteria, two genera of IOB were identified within the family *Sphingomonadaceae*: *Novosphingobium* and *Spingomonas*. The former having been isolated from biofilms in corroded concrete sewers (Satoh et al., 2009), and the latter having been associated with corrosion of stainless-steel welds (Takeuchi et al., 2001). Within the class Betaproteobacteria, eight genera were uniquely identified. Within the family *Burkholderiaceae* the genera *Limnobacter* and *Ralstonia* were indicated. Species of *Limnobacter* have been isolated that are capable of sulfur oxidation, and the genera has been linked to corrosion of cast iron pipework systems (Wang et al., 2012), whereas species of the genus *Ralstonia* have been observed to reduce corrosion (Section 2.2). The genus *Acidovorax*, within the family *Comamonas* has been associated with copper

corrosion and the formation of goethite (α -FeOOH) in steel pipework under simulated conditions (Beale et al., 2010, Sun et al., 2014). Within the same family, species of the genus *Delftia* have been shown to accelerate the deterioration of nickel-zinc alloy coatings (San et al., 2012), and *Variovorax* spp. have been indicated to contribute to MIC in water pipework (Beale et al., 2013). *Methylothera* spp. from the family *Methylophilaceae* was identified; this genus is apparently common in soil and ground water has been linked to degradation of machine oils that have a high metal content (Wang et al., 2019). This genus also includes species that reduce nitrate in the presence of zero valence iron (Zhang et al., 2019).

The *assA* gene was provided with the fewest number of probe clusters within the MIC-related gene group. Amongst the 21 probe clusters on the microarray, one genus has been identified: *Desulfoglaeba* in the family *Syntrophobacteraceae*. This genus was identified in Section 2.2 as a potential contributor to MIC. The *assA* probe cluster did not register fluorescence above detection threshold; identification was possible by fluorescence of the *dsrB* gene probe cluster, however.

The analysis of low tide zone corrosion samples allowed 311 genera of bacteria and archaea to be identified. Of these, 116 were either linked to previous corrosion studies in various environments or had not been previously connected with MIC occurrences. The remaining 195 genera were not checked for their involvement in MIC. Bacterial genera accounted for 281 of those identified; these were categorised as sulfate-reducing prokaryotes (SRP), sulfate-oxidizing bacteria (SOB), ammonia-oxidizing bacteria (AOB), nitrate-reducing prokaryotes (NRP), acetogenic prokaryotes (AP), methanogenic prokaryotes (MP), and iron-oxidizing bacteria (IRB). The remaining thirty genera belonged to the domain archaea; these were found to fall within the categories of SRP, NRP, AP, and MP. The use of GeoChip microarray technology allowed this identification to occur on a metagenomic basis, without the need to isolate and propagate individual genera. Limitations of the technique precluded identification of microorganisms not previously isolated via gene sequencing techniques and included relevant gene probes included in the microarray; several genera were identified using gene probes other than those associated with MIC-related chemical pathways, however. The gene linked to hydrocarbon-degradation (*assA*) was underrepresented in the microarray and consequently only identified a single genus, though the gene displayed fluorescence

below the measurable threshold, and thus the microbe had to be confirmed via other probes. Note that the fluorescence values for the *assA* gene in Section 6.1 were derived from all such gene probes, including those which were not identified or cultured. Fluorescence values were obtained for every other relevant probe, though the lack of a quantifiable standard by which to gauge the values precluded an assessment of concentration of each genera within the community. Maximum values for each gene were obtained; *nirK* and *fthfs* displayed genera of the highest fluorescence. Of note are the occurrences within the data set of uneven fluorescence values of probes within a group. For example, *Desulfarculus* spp. exhibited values of 322, 611, 618, and 1044 for the *aprA*, *aprB*, *dsrA*, and *dsrB* genes. The reason for this is unclear as these genes might be expected to be present in a ratio of 1:1:1:1 (Griswold, 2008) and so the anticipated fluorescence would be in the same proportions also. GeoChip identifies a single species for this genera only. It is possible that it is a limitation of the technology and the gene and gene probe affinity vary according to sequence; it is possible that a high A-T content could reduce hybridisation and lead to inaccurate fluorescence values. Alternatively, the imbalance may be due to hybridization of an unidentified species of *Desulfarculus* that has gene sequences close enough to allow a degree of hybridization, thus skewing the fluorescence values. As the GeoChip analysis utilised DNA samples instead of mRNA, the difference in fluorescence is not due to greater expression of certain genes over others. Further research would be necessary to explore this issue.

Though not directly related to this study, the identification of specific genera within MIC formations may have bearing on how the corrosion is controlled. As discussed in section 2.7 the methods commonly employed are currently of variable efficacy. Anodic and cathodic systems can be expensive to set up and have on-going costs; alternative materials are not always viable; and conventional biocides can be damaging to the environment. Much of recent research seems to focus on developing ecologically-friendly methods of destroying microbes, however as noted by Plaza and Achal (2020) and Rasheed et al. (2018), biocides are mostly ineffective against biofilms so their ability to neutralise the microbes within are limited. Currently biofilm focused approaches are being posited. As discussed in Section 2.4 quorum sensing is one of the key mechanisms by which the microbial community within biofilms maintain their protective environment. Wolska et al. (2016) illustrated this function in *Pseudomonas aeruginosa*, *Staphylococcus aureus*,

Salmonella enterica serovar Typhimurium, and Vibrio cholerae. As more microbes are identified within MIC-related biofilms, it will be possible to similarly discern how they communicate within the community, and to block this, leading to attenuated biofilm production that can be more easily removed with biocides, or its complete destruction.

Table 6-1 Results of GeoChip 5.0 analysis of samples C 14a, 14b, and 14c,
with median fluorescence values of MIC-related genes and corresponding microbial organisms

Kingdom / Phylum	Class	Order	Family	Genus	aprA	aprB	dsrA	dsrB	soxB	amoA	napA	narG	nirK	nirS	nrfA	ftfhs	mcrA	iro	assA			
Bacteria																						
Acidobacteria	Acidobacteriia	Acidobacteriales	Acidobacteriaceae	Acidobacterium spp.												437						
Actinobacteria	Actinobacteria	Actinomycetales	Actinomycetaceae	Actinomyces spp.							1260					889						
			Mobiluncus spp.									442										
			Brevibacteriaceae	Brevibacterium spp.														26791		821		
			Corynebacteriaceae	Corynebacterium spp.														627				
			Dermacoccaceae	Kytococcus spp.														2731				
			Mobilicoccus spp.														3418					
			Glycomycetaceae	Stackebrandtia spp.														784				
			Gordoniaceae	Gordonia spp.										670								
			Microbacteriaceae	Clavibacter spp.																	1802	
				Leifsonia spp.																	539	
				Microbacterium spp.										1958								
			Micrococcaceae	Arthrobacter spp.															583		770	
				Kocuria spp.																	10936	
				Renibacterium spp.															2398			
				Rothia spp.															534			
				Mycobacteriaceae	Mycobacterium spp.										745							
			Nocardiaceae	Rhodococcus spp.										1547								
			Propionibacteriaceae	Propionibacterium spp.										2419					732			
				Saccharomonospora spp.															1336			
				Saccharopolyspora spp.											497							
Streptomyces spp.												1111						1368				
Tsukamurellaceae	Tsukamurella spp.																350					
Bifidobacteriales	Bifidobacteriaceae	Bifidobacterium spp.														568						
Coriobacteriales	Coriobacteriaceae	Atopobium spp.														419						
		Collinsella spp.															438					
		Eggerthella spp.														312						
		Gordonibacter spp.						1124														
		Olsenella spp.															1667					
		Slackia spp.														776	404					
Rubrobacteriales	Rubrobacteraceae	Rubrobacter spp.													725							
Aquificae	Aquificae	Aquificales	Hydrogenothermaceae	Persophonella spp.							514											
Bacteroidetes	Bacteroidia	Bacteroidales	Bacteroidaceae	Bacteroides spp.												507	1220					
			Porphyromonadaceae	Dysgonomonas spp.													950					
			Prevotellaceae	Paraprevotella spp.														403				
			Prevotella spp.														749	1028				
	Cytophagia	Cytophagales	Cytophagaceae	Cytophaga spp.								334										
				Microscilla spp.												550		895				

Kingdom / Phylum	Class	Order	Family	Genus	aprA	aprB	dsrA	dsrB	soxB	amoA	napA	narG	nirK	nirS	nrfA	ftfhs	mcrA	iro	assA
Bacteria																			
Bacteroidetes	Flavobacteria	Flavobacteriales	Flavobacteriaceae	<i>Polaribacter</i> spp.												458			
				<i>Capnocytophaga</i> spp.												373		518	
				<i>Myroides</i> spp.												1802			
				<i>Zobellia</i> spp.							410								
Chlorobi	Chlorobia	Chlorobiales	Chlorobiaceae	<i>Chlorobaculum</i> spp.	647		721	1402											
				<i>Chlorobium</i> spp.			608												
				<i>Pelodictyon</i> spp.			737	855											
				<i>Prosthecochloris</i> spp.			2085												
Chloroflexi	Anaerolineae	Anaerolineales	Anaerolineaceae	<i>Anaerolinea</i> spp.											834				
	Chloroflexi	Chloroflexales	Chloroflexaceae	<i>Chloroflexus</i> spp.												1491			
Cyanobacteria	Cyanophyceae	Oscillatoriales	Cyanothecaceae	<i>Cyanotheca</i> spp.														867	
				<i>Synechococcus</i> spp.														3157	
Deinococcus-Thermus	Deinococci	Thermales	Thermaceae	<i>Meiothermus</i> spp.											563				
				<i>Thermus</i> spp.												615			
Fibrobacteres	Fibrobacteria	Fibrobacterales	Fibrobacteraceae	<i>Fibrobacter</i> spp.	806			805											
Firmicutes	Bacilli	Bacillales	Bacillaceae	<i>Bacillus</i> spp.											3015	640			
				<i>Geobacillus</i> spp.							813	1870							
				<i>Lysinibacillus</i> spp.															
				<i>Listeria</i> spp.												630			
				<i>Paenibacillaceae</i>												572			
				<i>Paenibacillus</i> spp.												575			
				<i>Planococcaceae</i>												4515			
				<i>Staphylococcaceae</i>															
				<i>Macrococcus</i> spp.							870								
				<i>Staphylococcus</i> spp.							289					396			
		Lactobacillales	<i>Aerococcaceae</i>	<i>Eremococcus</i> spp.												1545			
			<i>Enterococcaceae</i>	<i>Enterococcus</i> spp.												492			
			<i>Lactobacillaceae</i>	<i>Lactobacillus</i> spp.							705					1289			
				<i>Pediococcus</i> spp.												744			
			<i>Leuconostocaceae</i>	<i>Fructobacillus</i> spp.												853			
				<i>Leuconostoc</i> spp.												549			
				<i>Weissella</i> spp.												739			
			<i>Streptococcaceae</i>	<i>Streptococcus</i> spp.												509			
				<i>Alkaliphilus</i> spp.												536			
			<i>Clostridiaceae</i>	<i>Clostridium</i> spp.												686			
			<i>Clostridiales</i>	<i>Anaerococcus</i> spp.			1052	1023								954			
			<i>Eubacteriaceae</i>	<i>Acetobacterium</i> spp.			283												
				<i>Eubacterium</i> spp.			1144												
				<i>Pseudoramibacter</i> spp.												734			
			<i>Hellobacteriaceae</i>	<i>Hellobacterium</i> spp.											473				
			<i>Lachnospiraceae</i>	<i>Anaerostipes</i> spp.												380			
				<i>Blautia</i> spp.			277												
				<i>Catonella</i> spp.												391			
				<i>Oribacterium</i> spp.												480			
				<i>Shuttleworthia</i> spp.												731			
			<i>Oscillospiraceae</i>	<i>Oscillibacter</i> spp.												895			
			<i>Peptococcaceae</i>	<i>Desulfuridis</i> spp.			4882	984											
				<i>Desulfitobacterium</i> spp.											661				

Kingdom / Phylum	Class	Order	Family	Genus	aprA	aprB	dsrA	dsrB	soxB	amoA	napA	narG	nirK	nirS	nrfA	ftfhs	mcrA	iro	assA
Bacteria																			
Firmicutes	Clostridia	Clostridiales	Peptococcaceae	<i>Desulfosporosinus</i> spp.			1342									1211			
				<i>Desulfotomaculum</i> spp.	3085	1253	558	549											
				<i>Pelotomaculum</i> spp.												556			
				<i>Ruminococcus</i> spp.												6062			
				<i>Subdoligranulum</i> spp.			834												
			Syntrophomonadaceae	<i>Dethiobacter</i> spp.			739												
				<i>Syntrophothermus</i> spp.												1769			
				<i>Pseudoflavonifractor</i> spp.				518											
		Halanaerobiales	Halanaerobiaceae	<i>Halothermothrix</i> spp.	652														
		Thermoanaerobacterales	Thermoanaerobacteraceae	<i>Carboxydotherrmus</i> spp.											715				
				<i>Moorella</i> spp.			567	3102										478	
				<i>Caldicellulosiruptor</i> spp.												8475			
	Erysipelotrichia	Erysipelotrichales	Erysipelotrichaceae	<i>Holdemania</i> spp.			2267												
	Negativicutes	Selenomonadales	Veillonellaceae	<i>Acetoneia</i> spp.			760									704			
				<i>Centipeda</i> spp.												1164			
				<i>Megasphaera</i> spp.												538			
				<i>Selenomonas</i> spp.			696				4882				766	306			
				<i>Thermosinus</i> spp.											1046				
				<i>Veillonella</i> spp.												1456			
Fusobacteria	Fusobacteria	Fusobacteriales	Fusobacteriaceae	<i>Leptotrichia</i> spp.												486			
Lentisphaerae	Lentisphaeria	Lentisphaerales	Lentisphaeraceae	<i>Lentisphaera</i> spp.											335				
Nitrospirae	Nitrospira	Nitrospirales	Nitrospiraceae	<i>Leptospirillum</i> spp.		852										1945			
				<i>Nitrospira</i> spp.												345			
Planctomycetes	Planctomycetia	Candidatus Brocadiales	Candidatus Brocadaceae	<i>Candidatus Kueneria</i> spp.		691										631			
		Planctomycetales	Planctomycetaceae	<i>Isosphaera</i> spp.												711			
				<i>Planctomyces</i> spp.											517	38742			
				<i>Rhodopirellula</i> spp.											812				
				<i>Singulisphaera</i> spp.												689			
Proteobacteria	Alphaproteobacteria	Caulobacterales	Caulobacteraceae	<i>Brevundimonas</i> spp.												496		1262	
				<i>Caulobacter</i> spp.														869	
				<i>Phenylbacterium</i> spp.							906								
		Parvularculales	Parvularculaceae	<i>Parvularcula</i> spp.														1143	
		Rhizobiales	Beijerinckiaceae	<i>Beijerinckia</i> spp.												1036		1686	
			Bradyrhizobiaceae	<i>Bradyrhizobium</i> spp.						3281		728						6139	
				<i>Nitrobacter</i> spp.														583	
				<i>Oligotropha</i> spp.							343								
				<i>Rhodopseudomonas</i> spp.						636								566	
			Brucellaceae	<i>Ochrobactrum</i> spp.									1362						
			Hyphomicrobiaceae	<i>Hyphomicrobium</i> spp.												730			
				<i>Rhodomicrobium</i> spp.														617	
			Methylobacteriaceae	<i>Methylobacterium</i> spp.		7550										1227		667	
			Phyllobacteriaceae	<i>Chelativorans</i> spp.												293			
			Phyllobacteriaceae	<i>Mesorhizobium</i> spp.		1309													
			Rhizobiaceae	<i>Agrobacterium</i> spp.									8272			635			
				<i>Rhizobium</i> spp.									668						
				<i>Sinorhizobium</i> spp.												1062			

Kingdom / Phylum	Class	Order	Family	Genus	aprA	aprB	dsrA	dsrB	soxB	amoA	napA	narG	nirK	nirS	nrfA	ftfhs	mcrA	iro	assA		
Bacteria																					
Proteobacteria	Alphaproteobacteria	Rhizobiales	<i>Xanthobacteraceae</i>	<i>Azorhizobium</i> spp.												5736		1414			
		Rhodobacterales	<i>Rhodobacteraceae</i>	<i>Ahrensia</i> spp.													755				
						<i>Citricella</i> spp.				265							4870				
						<i>Dinoroseobacter</i> spp.						1122									
						<i>Labrenzia</i> spp.												604			
						<i>Oceanibulbus</i> spp.												964			
						<i>Paracoccus</i> spp.						387							1173		
						<i>Pseudovibrio</i> spp.							504					364			
						<i>Rhodobacter</i> spp.						459						615			
						<i>Roseibium</i> spp.												741			
						<i>Roseobacter</i> spp.												787			
						<i>Ruegeria</i> spp.						1044						1371			
						<i>Sagittula</i> spp.												463			
				Rhodospirillales	<i>Acetobacteraceae</i>	<i>Granulibacter</i> spp.												1264		1476	
						<i>Roseomonas</i> spp.												949			
					<i>Rhodospirillaceae</i>	<i>Azospirillum</i> spp.						850									
						<i>Magnetospirillum</i> spp.			551			487									
						<i>Nisaea</i> spp.									866						
						<i>Rhodospirillum</i> spp.						832									
				Sphingomonadales	<i>Sphingomonadaceae</i>	<i>Novosphingobium</i> spp.														513	
					<i>Sphingomonas</i> spp.														351		
	Betaproteobacteria	Burkholderiales	<i>Alcaligenaceae</i>		<i>Achromobacter</i> spp.							596									
					<i>Advenella</i> spp.				1020												
					<i>Bordetella</i> spp.								257								1477
					<i>Castellaniella</i> spp.									293							
					<i>Burkholderia</i> spp.	<i>Burkholderiaceae</i>															1261
					<i>Cupriavidus</i> spp.								681	362							1911
					<i>Lautropia</i> spp.									367	552				786		
					<i>Limnobacter</i> spp.																577
					<i>Ralstonia</i> spp.																1253
				<i>Comamonadaceae</i>		<i>Acidovorax</i> spp.														2311	
					<i>Comamonas</i> spp.								475						2621		
					<i>Delftia</i> spp.														656		
					<i>Diaphorobacter</i> spp.								3512								
					<i>Hydrogenophaga</i> spp.						1101										
					<i>Ramibacter</i> spp.						514										
					<i>Variovorax</i> spp.														960		
				<i>Oxalobacteraceae</i>		<i>Hermiminomonas</i> spp.													8300		
						<i>Janthinobacterium</i> spp.													837		
				<i>Sutterellaceae</i>		<i>Methylobium</i> spp.													941		
						<i>Thiomonas</i> spp.							911								
		Gallionellales	<i>Gallionellaceae</i>	<i>Sideroxydans</i> spp.		516															
		Hydrogenophilales	<i>Hydrogenophilaceae</i>	<i>Thiobacillus</i> spp.	827	869			2031									486			
		Methylophilales	<i>Methylophilaceae</i>	<i>Methylothena</i> spp.														278			
				<i>Methylovorus</i> spp.												488		751			
		Neisseriales	<i>Neisseriaceae</i>	<i>Chromobacterium</i> spp.							4890	606	573								

Kingdom / Phylum	Class	Order	Family	Genus	aprA	aprB	dsrA	dsrB	soxB	amoA	napA	narG	nirK	nirS	nrfA	ftfhs	mcrA	iro	assA				
Bacteria																							
Proteobacteria	Betaproteobacteria	Neisseriales	Neisseriaceae	<i>Eikenella</i> spp.												1058							
				<i>Laribacter</i> spp.								971											
				<i>Neisseria</i> spp.										3823	5823				673		1600		
		Nitrosomonadales	Nitrosomonadaceae	<i>Nitrosomonas</i> spp.								312			561								
				<i>Nitrospira</i> spp.								4526			626								
				<i>Aromatoleum</i> spp.										886									
		Rhodocyclales	Rhodocyclaceae	<i>Azoarcus</i> spp.																			
				<i>Methyloversatilis</i> spp.			1105												660				
				<i>Thauera</i> spp.										1237							1654		
				<i>Bdellovibrio</i> spp.														4172			361		
		Deltaproteobacteria	Bdellovibrionales	Bdellovibrionaceae	<i>Desulfarculus</i> spp.	322	611	618	1044												632		
					Desulfobacteriales	Desulfobacteraceae	<i>Desulfobacterium</i> spp.	796	332	498													
	<i>Desulfobacula</i> spp.								8785														
	<i>Desulfobotulus</i> spp.						913	542															
	<i>Desulfococcus</i> spp.		651						500														
	<i>Desulfofaba</i> spp.								3002														
	<i>Desulfofrigus</i> spp.		549																				
	<i>Desulforegula</i> spp.		815																				
	<i>Desulfospira</i> spp.		4067				635	2424															
	Desulfobulbaceae		<i>Desulfobulbus</i> spp.	550				784	646										583				
			<i>Desulfofustis</i> spp.				792																
			<i>Desulfotalea</i> spp.				403		727														
			<i>Desulfurivibrio</i> spp.																				
			<i>Desulfohalobium</i> spp.		486	504	1537																
			<i>Desulfonatronospira</i> spp.		257																		
			<i>Desulfonatronovibrio</i> spp.				509																
			<i>Desulfothermus</i> spp.	599																			
	Desulfovibrionales		Desulfomicrobiaceae	<i>Desulfomicrobium</i> spp.			848	320									610	1767					
				<i>Desulfonatronumaceae</i>	<i>Desulfonatronum</i> spp.				1234														
			Desulfovibrionaceae	<i>Bilophila</i> spp.			746																
				<i>Desulfovibrio</i> spp.	878	807	775	1391					426					4076	561				
	<i>Lawsonia</i> spp.																570						
	Desulfuromonadales		Desulfuromonadaceae	<i>Desulfuromonasspp.</i>														683					
<i>Geobacteraceae</i>				<i>Geobacter</i> spp.			624										637						
<i>Pelobacteraceae</i>			<i>Pelobacterspp.</i>													2715							
Myxococcales	<i>Myxococcaceae</i>		<i>Anaeromyxobacter</i> spp.													446							
	<i>Polyangiaceae</i>		<i>Sorangium</i> spp.								2170					779							
Syntrophobacterales	Syntrophaceae		<i>Desulfobacca</i> spp.														4979						
			<i>Desulfomonile</i> spp.	322																			
			<i>Syntrophus</i> spp.													530	703						
	Syntrophobacteraceae	<i>Desulfacinum</i> spp.			366	331																	
		<i>Desulfoglaeba</i> spp.				1477																	
		<i>Desulforhabdus</i> spp.			871	686																	
		<i>Syntrophobacter</i> spp.	5008		1066	828									1008								
<i>Thermodesulforhabdus</i> spp.			491																				
<i>Desulfocaldus</i> spp.	15361	368																					

Kingdom / Phylum	Class	Order	Family	Genus	aprA	aprB	dsrA	dsrB	soxB	amoA	napA	narG	nirK	nirS	nrfA	ftfhs	mcrA	iro	assA
Bacteria																			
Proteobacteria	Epsilonproteobacteria	Campylobacterales	Campylobacteraceae	Campylobacter spp.							916				1062				
			Helicobacteraceae	Helicobacter spp.							301				389				
	Gammaproteobacteria	Aeromonadales	Aeromonadaceae	Aeromonas spp.												1002		4554	
		Alteromonadales	Alteromonadaceae	Marinobacter spp.															
			Colwelliaceae	Colwellia spp.							1709								
			Ferrimonadaceae	Ferrimonas spp.											535	967			
			Shewanellaceae	Shewanella spp.											2324	701		452	
		Cardiobacteriales	Cardiobacteriaceae	Cardiobacterium spp.									63271			463			
		Chromatiales	Chromatiaceae	Halochromatium spp.				1658											
				Nitrosococcus spp.					487										
				Thiocapsa spp.	576			878											
				Thiorhodovibrio spp.	312	320		638											
		Chromatiales	Ectothiorhodospiraceae	Alkalicoccus spp.				636											
				Halorhodospira spp.				669	1842										
				Thioalkalivibrio spp.		908	1333	1637							9554				
			Halothiobacillaceae	Halothiobacillus spp.															736
		Enterobacteriales	Enterobacteriaceae	Citrobacter spp.											319				735
				Dickeya spp.															1557
				Enterobacter spp.															819
				Escherichia spp.							297								757
				Klebsiella spp.															3490
				Pantoea spp.								543							1344
				Pectobacterium spp.							630				1009				919
				Proteus spp.												7227			
				Salmonella spp.							1003								
				Serratia spp.															719
				Shimwellia spp.								835							
				Yersinia spp.											190	802			483
		Methylocoocales	Methylococcaceae	Methylococcus spp.															359
				Methylomicrobium spp.															423
		Oceanospirillales	Alcanivoracaceae	Alcanivorax spp.								314							579
			Halomonadaceae	Halomonas spp.												333			
		Pasteurellales	Pasteurellaceae	Aggregatibacter spp.											1146				1456
				Haemophilus spp.							14989		514		566				
				Mannheimia spp.											3609				
		Pseudomonadales	Moraxellaceae	Acinetobacter spp.															453
				Psychrobacter spp.												1695			919
			Pseudomonadaceae	Azotobacter spp.															779
				Pseudomonasspp.								2211	1365	1463					908
		Thiotrichales	Piscirickettsiaceae	Methylophaga spp.															573
			Thiotrichaceae	Beggiatoa spp.								658							
		Vibrionales	Vibrionaceae	Photobacterium spp.															616
				Vibrio spp.							460				565	1044			342
		Xanthomonadales	Xanthomonadaceae	Stenotrophomonas spp.								474							1106
				Candidatus Thiobios spp.	273														
				Congregibacter spp.					557										

Kingdom / Phylum	Class	Order	Family	Genus	aprA	aprB	dsrA	dsrB	soxB	amoA	napA	narG	nirK	nirS	nrfA	ftfhs	mcrA	iro	assA
Bacteria																			
		Xanthomonadales	Xanthomonadaceae	Magnetococcus spp.				575											
Spirochaetes	Spirochaetes	Spirochaetales	Spirochaetaceae	Treponema spp.															1936
				Sphaerochaeta spp.			935												385
	Synergistia	Synergistales	Synergistaceae	Aminomonas spp.															3718
				Dethiosulfovibrio spp.															507
				Jonquetella spp.															956
				Pyramidobacter spp.															572
				Synergistes spp.			1548												
Thermodesulfobacteria	Thermodesulfobacteria	Thermodesulfobacteriales	Thermodesulfobacteriaceae	Thermodesulfatator spp.				505											
				Thermodesulfobacterium spp.	6115		569												
Verrucomicrobia	Verrucomicrobiae	Verrucomicrobiales	Opitutaceae	Opitutus spp.												967			487
	Spartobacteria	Cthnionibacteriales	Cthnionibacteraceae	Cthnionibacter spp.												1973			
				Methylomirabilis spp.							514	864							
Archaea																			
Crenarchaeota	Thermoprotei	Thermoproteales	Thermoproteaceae	Caldivirga spp.			599												
				Pyrobaculum spp.	862	633	802	478											
				Thermoproteus spp.		492	9662												
				Vulcanisaeta spp.	1228			596											
Euryarchaeota	Archaeoglobi	Archaeoglobales	Archaeoglobaceae	Archaeoglobus spp.	968		593												
	Halobacteria	Halobacteriales	Halobacteriaceae	Haloarcula spp.															545
				Haloferax spp.						1430	2676	660							
				Halorubrum spp.															2355
				Natronomonas spp.									884						
	Methanobacteria	Methanobacteriales	Methanobacteriaceae	Methanobacterium spp.															601
				Methanobrevibacter spp.															6059
				Methanothermobacter spp.															514
			Methanothermaceae	Methanothermus spp.			363												
				Methanotorris spp.			549												
	Methanococci	Methanococcales																	
	Methanomicrobia	Methanomicrobiales	Methanocorpusculaceae	Methanocorpusculum spp.															1056
			Methanomicrobiaceae	Methanoculleus spp.			609												812
				Methanofollis spp.															666
				Methanoplanus spp.			293												
			Methanoregulaceae	Methanolinea spp.			897												
				Methanosphaerula spp.			990												884
			Methanosphaerula	Methanoregula spp.			990	528											
		Methanosarcinales	Methanosaetaceae	Methanosaeta spp.															1282
			Methanosarcinaceae	Methanococcoides spp.			407												
				Methanohalobium spp.															417
				Methanohalophilus spp.			257												
				Methanobolus spp.															1306
				Methanosarcina spp.			685												
	Methanopyri	Methanopyrales	Methanopyraceae	Methanopyrus spp.			506												
	Thermoplasmata	Thermoplasmatales	Ferropasmaceae	Ferroplasma spp.															1021
			Thermoplasmataceae	Aciduliprofundum spp.															1488

6.5 Summary

The techniques employed in this chapter allowed corrosion, marine sediment, and seawater samples to be analysed on a metagenomic basis. This approach allowed differences in community composition to be discerned within the context of functional genes significant to microbially influenced corrosion, and for the microbial composition of corrosion samples to be explored.

A comparison of the median fluorescence responses for MIC-related genes revealed variability in gene numbers between samples and between environments. The marine sediment exhibited the highest average fluorescence, whilst the seawater showed the lowest average response between genes. The corrosion samples demonstrated gene number closer to the sediment than to the seawater. There were also indications of a greater microbial diversity within the seawater samples.

The dendrograms for the fifteen genes demonstrated that the community similarities between corrosion, marine sediment, and seawater samples were more variable than apparent from total fluorescence values. Analysis showed significant clustering of corrosion samples separate from sediment and seawater for eight of the fifteen genes, for both anaerobic and aerobic metabolisms between sulfur, nitrogen, and iron-cycling. Corrosion closely clustered with sediment for four of the genes, and corrosion was closely clustered with seawater for a single gene. Sediment and seawater samples were found to more closely cluster for five genes. These data appear to undermine the earlier observations that corrosion samples more consistently correlate with sediment than with seawater. However, the nature of the data must be considered: both sets originate from the same GeoChip analysis, but whereas the results in Section 6.1 provide an indication of overall diversity between sample types based on total fluorescence, Section 6.3 analysed the fluorescence values of specific genera across each sample and provided a more detailed investigation into the similarities between samples based on identified members of the community.

The GeoChip data also revealed the presence of bacteria and archaea that have been previously linked to MIC of mild steel piling in the marine environment. The analysis

was conducted down to the genera level, and it was found that many of those identified were also implicated in MIC occurrences in other environments including oil and water pipeline systems, concrete sewers, suggesting a degree of commonality between MIC microbiota from different environments. Other genera, including some extremeophiles, not previously associated with MIC processes were also identified.

Chapter 7 Genetic diversity analysis using denaturing gradient gel electrophoresis and high-resolution melt

7.1 Denaturing gradient gel electrophoresis and high-resolution melt analysis of low tide zone corrosion, marine sediment, and seawater

The denaturing gradient gel electrophoresis (DGGE image) obtained of twelve PCR amplicons taken from environmental samples described is shown in Figure 7-1. The dendrogram obtained from analysis of the image band distribution is displayed in Figure 7-2. The comparison analysis indicates the data can be sectioned in to two main groups, with a 36.1% overall similarity. The first group comprises the four seawater samples and a single marine sediment sample. Seawater samples SW 04, 05, and 07 form a subgroup with 84.2% similarity in band location and number. Marine sediment sample SED 04 has a similarity to seawater sample SW 06 of 89.6%. Together, these subgroups bear a 71.3% similarity. The second main group comprises the four corrosion samples and remaining three sediment samples. The corrosion samples display the greatest degree of similarity (88.2% overall). Within this subgroup, corrosion samples C 14d and C 14e are indicated to be 94.7% similar, with C 14f being 89.7% similar in profile. Sediment samples SED 07, 05, and 06 do not form their own subgroup, but attach to the corrosion subgroup with 78.4%, 76.4%, and 75.1% similarity, respectively.

Figure 7-3 shows the melt-curve plot for the same twelve samples as analysed using DGGE. The corresponding dendrogram for this analysis is shown in Figure 7-4. The dendrogram indicates the presence of three groups. The first group comprises the seawater samples and one marine sediment sample, SED 04. Seawater samples SW 04 and SW 05 are most similar in melt profile, at 84.8%; SW 07 is grouped closely with these samples with an 83.8% similarity. Samples SW 06 and SED 04 are associated with this subgroup with 79.6% and 74.7% similarity, respectively. The remaining three sediment samples form a group which has an overall correlation of 79.1%, but a similarity between SED 06 and SED 07 of 87.6%. The four corrosion samples form a group comprised of two subgroups with 79.4% similarity between them; C 14d and C 14e have a 87.1% match in profile,

whereas C 14 f and C 14g bear a 86.8% similarity. The corrosion group is most closely matched with the three-sediment group, with the seawater and one sediment group being most dissimilar with a value of 30.5%.



Figure 7-1 DGGE gel image (*dsrB* PCR products from twelve environmental samples)

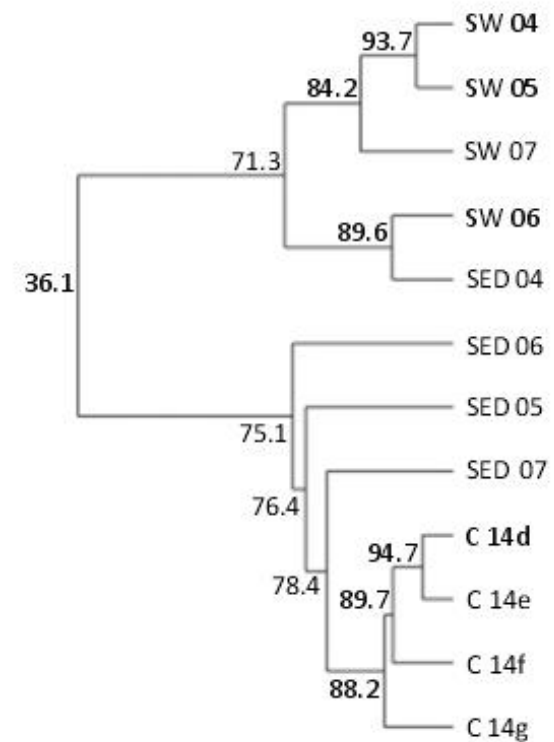


Figure 7-2 Similarity analysis of DGGE gel image (*dsrB* PCR products from twelve environmental samples)

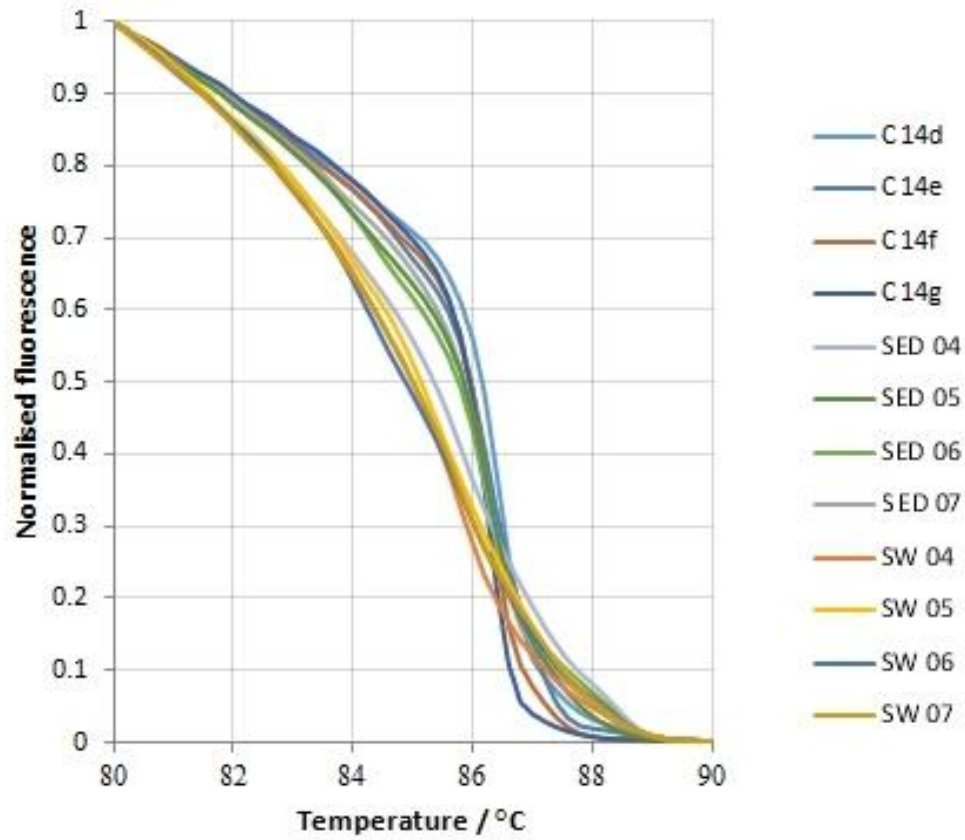


Figure 7-3 HRM curves (*dsrB* gene PCR products for twelve environmental samples)

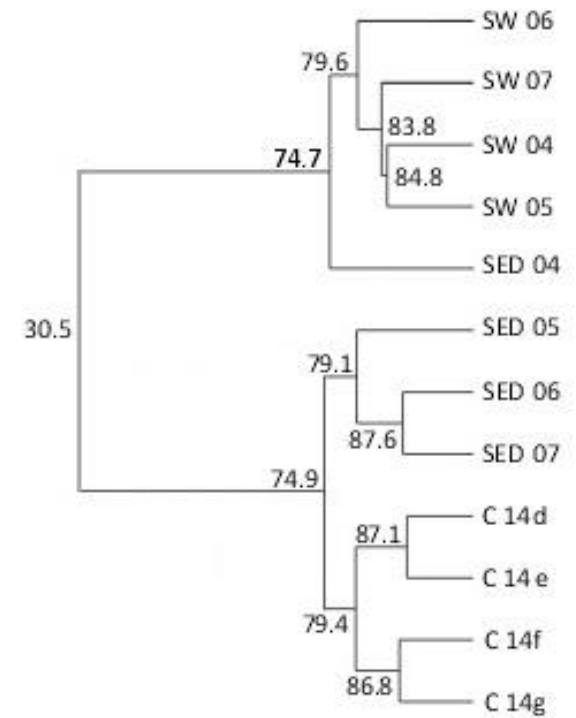


Figure 7-4 Similarity analysis of HRM data (*dsrB* gene PCR products for twelve environmental samples)

The results of the *dsrB* gene variations analysis using DGGE and HRM, displayed a high degree of sample type correlation. Both techniques produced corrosion and seawater sample clusters and indicated a higher similarity of three sediment samples to the corrosion cluster than that of the seawater.

However, comparing the *degree* of similarity between techniques for a sample type it was apparent that these did not have the same values. The DGGE dendrogram indicated a higher level of similarity between corrosion samples compared with that for HRM, both between adjacent samples and within the whole cluster. The seawater cluster showed a similar pattern, albeit to a lesser degree. Three sediment samples formed a group within the HRM dendrogram which attached to the corrosion cluster; the same three samples likewise attached to the DGGE corrosion cluster singly and with greater similarity values. This discrepancy can be reconciled, and thus the more accurate result determined, if the nature of the raw data obtained from each technique is considered. HRM melt curve data is a record of how sample fluorescence decreases with increasing temperatures; each sample is processed entirely within the qPCR/HRM thermocycler. DGGE analysis is based on the location of bands visible on a gel image, the position and resolution of which can be inadvertently affected by any of the procedures carried out post-PCR amplification, particularly gel gradient consistency, and gel staining and handling. If some sequences present in the gel are poorly resolved or are too weakly defined, inaccuracies will result. If the DGGE data above, has been affected thus, it would account for the overestimation of sample similarities. This seems more likely due to the single-step nature of HRM analysis and the concordant lesser probability of cumulative processing errors occurring with this technique. In addition, as each amplicon is analysed as a whole, there is a greater likelihood the results will more accurately reflect the composition of the entire sample, and therefore comparisons between sample profiles will be correspondingly more accurate.

An additional observation made during DGGE gel image and HRM curve observation concerns a qualitative similarity in profile. As discussed previously, amplicons would separate on a gel based on their G-C content. Therefore, a sample containing a higher proportion of A-T base-pairs would tend to form bands nearer the top of the gel, starting with the most A-T rich amplicons. The converse will apply for more G-C rich amplicons. As the temperature gradient of the HRM and denaturing gradient of a DGGE gel follow

this same trend, it would be anticipated that high A-T content samples would display an earlier decrease in fluorescence before those with higher G-C content. The seawater samples display a greater number of bands, the strongest of which tend towards the 30% denaturant end of the gel (left side of Figure 7-1), and the corrosion samples strongest bands lie to the right of these, indicating higher G-C content, and are fewer in number. This pattern is reflected in the HRM curve profiles. The four seawater samples each display a fluorescence profile that commences to decrease at a lower temperature than any of the other samples; the corrosion samples display the highest melt temperatures. The shape of the HRM curves also has a parallel in the number of bands visible in the DGGE image. The DGGE gel image displayed the greatest number of bands for the seawater samples (five to eight bands each) and sediment samples SED 01 and 03 (eight bands each); and the fewest amongst the corrosion samples (two to four bands each) and the two sediment samples most closely linked to them (SED 02 and 04), which possess three bands each. When comparing the number of DGGE bands present to the profile of the HRM curves, it is apparent that samples with fewer bands tend to display a shallower initial gradient that is followed by a sudden rapid steepening at their midpoint followed by a more pronounced flattening towards the end, whereas the more diverse samples display a melt curve that are more linear in profile, and lack the characteristic sharp fluorescence decrease and levelling off the less diverse samples possess. These observations provide a qualitative but independent verification of the similarities between the dendrograms and help in the interpretation of the HRM curves profiles with regard to community diversity (Figure 7-2 and Figure 7-4).

This section had utilised twelve samples, and one target gene to compare two genetic diversity analytical methods. While the findings were internally consistent, an expansion of the study to include a larger number of samples, a wider range of environments, as well as a greater number of genes would increase confidence in these findings and indicate the degree to which the compatibility of the techniques could be extended to other applications.

7.2 High-resolution melt analysis of vertical profile corrosion

As discussed in Chapter 3, the DNA from fifteen corrosion samples obtained from a vertical section of piling were subjected to analysis using HRM. The results of four rounds of the technique are shown in Figure 7-5 to Figure 7-12 below. For each of the four genes selected there are a plot of the melt curves obtained during the HRM processing, and a hierarchical clustering plot (dendrogram) of melt curve similarity between the fifteen corrosion samples.

Three of the four genes were selected from those involved in sulfur cycling as discussed in Section 2.3. These were: *aprA*, which codes for the AprA component of the dissimilatory adenosine 5' phosphosulfate (APS) reductase complex responsible for reducing APS to sulfite; *dsrB*, which codes for the DsrB component of the dissimilatory sulfite reductase complex; and *soxB* which codes for the SoxB component of the periplasmic thiosulfate complex (Table 2-2). These were chosen to elucidate the diversity of two ubiquitous microbial groups found within MIC formations: sulfate-reducing and sulfur-oxidizing prokaryotes (Sections 2.1 and 2.2.). The fourth gene selected for HRM analysis was the *16S* ribosomal RNA gene, which codes for the 16S rRNA component of the prokaryotic ribosomal subunit (30S sub-unit). This gene is highly conserved between species (Coenye and Vandamme, 2003) and is often used in phylogenetic studies (Weisburg et al., 1991), to detect pathogenic variations within a species (Sánchez et al., 2017, Liu et al., 2018), and to differentiate species within a genus (Robertson et al., 2009). As 16S rRNA is present in all prokaryotes, analysis provides data on diversity within the whole bacterial and archaeal community.

7.2.1 Melt-curve for *aprA* gene

According to the results obtained from the dendrogram for this gene (Figure 7-6) the closest match in melt profile was between samples C 12 and C 14 (86.04% similarity); the second closest match was between samples C 10 and C 11 (85.96% similarity); these two clusters shared a 76.68% similarity. Sample C 09 correlated subsequently with this four-sample cluster with a 68.69% similarity. C 07 and C 13 shared an 81.56% match in melt profile and the pair bears a 61.36% correlation with the C 09, C 10, C 11, C 12, C 14 cluster. Samples C 02 and C 04 from the upper section of piling were 77.26% similar

in profile, and clustered with the upper most sample C 01 with a value of 64.41%. This cluster of three samples was found to have a 55.53% similarity to the C 08 to C 14 group. The sample closest to the sediment bed (C 15) was found to have only a 40.23% melt curve similarity to this main cluster. The samples C 03, C 05, C 06, and C 08 a distinct cluster with an overall similarity of 60.52%, within which C 05 and C06 were most similar (83.38%). This four-sample cluster had only a 33.39% similarity to the main eleven-sample cluster.

Examination of the curve profiles reveals considerable variation between most of the samples. Applying the diversity observation based on curve profile that was posited previously, C 03, C06, and C 05 display a steep gradient followed by a levelling at approximately 85.5 °C, which could be indicative of diverse gene sequences of lower G- C content. Conversely, samples C 07 and C 13 display a profile like the corrosion samples in Figure 7-3, with more vertical profiles after 85 °C, which could be indicative of less diversity of the gene and a higher G-C content. The C 08-C 14 cluster have profiles that lie between these two groups; they display relatively straight melt curves, indicating a high degree of diversity, and gradual levelling off after 87 °C, which indicates a relatively high G-C content.

7.2.2 Melt curve for *dsrB* gene

Figure 7-8 indicates the degree of community similarity for the *dsrB* gene. Samples C 13 and C14 share an 89.72% similarity. The adjacent cluster of samples C 11, C 12, and C 13 bear a 75.13% to the C 13-C 14 group. Within this cluster the curves for C 11 and C 12 are 81.90% similar in profile; C 10 correlates to C 11 and C 12 to the extent of 77.79%. Sample C 08 is linked to this overall group with a similarity of 56.51%. A second main cluster comprising the balance of samples indicates the greatest similarity between C 01 and C 06 (an 82.69% match). This cluster correlates with the next significant sample, C 03, with a parity of 81.24%. The next two samples which form part of the second cluster are joined singly: C 02 is 69.92% similar; C 05 displays a 59.37% correlation. Samples C 07 and C 15 are clustered with a 71.92% match in profile and share a 58.31% correspondence with the second main cluster. Finally, C 04 and C 09 are grouped together at 68.36% match: this cluster links to the second main cluster with a 48.87% similarity.

The initial C 08, C 10 to C 14 cluster links to the C 01 to C 07, C 15 cluster with a parity of 40.64%.

The melt curves profiles show significant differences in profile. The cluster C 08-C 14, corresponding with positions 3.4 m to 1.0 m above sediment bed level, exhibited melt curve profiles with a gradual decrease followed by a steep drop in fluorescence between 84 °C and 86 °C. Similar profiles in Section 7.1 suggested lower diversity within the communities. Samples C 04 and C 09 possessed curves that show an early dip between 72 °C and 74 °C, followed by a steady decrease afterwards, which may be indicative of high level of community diversity and greater A-T content. Samples C01, C06, C 03, and C 02 display the straightest melt-curves being possibly indicative of the most diverse *dsrB* gene composition of the samples.

7.2.3 Melt curve for *soxB* gene

The degree of similarity between *soxB* genes in the communities comprising the fifteen samples is shown in Figure 7-10. The closest curve profiles belong to samples C 12 and C 13; these are 92.48% similar. Samples C 11 and C 10 link with this cluster with matches of 87.74% and 80.41% respectively. The next adjacent cluster is made up of C 01, C 08 (89.43% similarity), and C 02 which has a similarity to C 01, C 08 of 82.51%. These two clusters share a 64.52% match in melt-curve profile. A second large cluster contains samples C 04 and C 09 (88.93% match), and C 14 and C 15 (89.08% match) which are linked with an 83.53% correlation. This cluster of four links to samples C 05 and C 06 (correlation of 89.18%) with a similarity of 75.99%. The final two samples (C 07 and C 03) link individually with the cluster with parity of 68.18% and 61.23% respectively. The two main clusters display a 43.28% match.

Each of the *soxB* melt-curve profiles exhibit a smooth curves resembling those observed for the water samples in Section 7.1, indicating more diverse community compositions. This suggests that, while there are variations in the community composition between samples, the degree of diversity of the *soxB* gene was broadly similar at each position on the steel piling.

7.2.4 Melt curve for *16S* gene

Figure 7-12 indicates the degree of correlation found between the *16S* rRNA gene in the fifteen corrosion samples. The closest match in melt-curve profiles were between C 01 and C 10 (86.17% similarity). This cluster is grouped with samples C 09 and C 08 with a similarity of 74.96% and 64.33% respectively. Profiles for samples C13 and C 14 display a 79.78% match, and in turn share a 75.83% parity with C 12. This cluster of three samples links to the C 01, C 08-C 10 grouping (61.77% similarity). C 07 links to this cluster with a 57.61% similarity. Adjacent to this cluster is the grouping of C 11 and C 15 (58.82% correlation) which bears a 45.48% curve profile similarity. Distinct from this large cluster of ten samples lies a cluster of the remaining five. Samples C 03 and C 06 are most closely correlated (84.83% similarity). C 05 connects with these two samples with a 78.79% profile match. A cluster of two samples comprising C 02 and C 04 (74.78% correlation) is linked to the C 03, C 05-C 06 cluster with a parity of 67.52%. This five-sample cluster is linked with the ten-sample cluster with a similarity of 26.77%.

The *16S* melt curves fall into three distinct groups, that closely reflect the dendrogram clusters. The lower group comprises of samples C 02-C06, spanning heights above the sediment bed of 5.8 m to 4.2 m, which exhibit the greatest initial drop in fluorescence, possibly indicating a higher community A-T composition. The upper group consists of the samples C 12, C 13, and C 14. These three samples exhibit a lower fluorescence drop-off until approximately 83 °C when the curve steepness increases; this may be indicative of less diverse communities in the 1.8 m to 1.0 m region above the sediment bed.

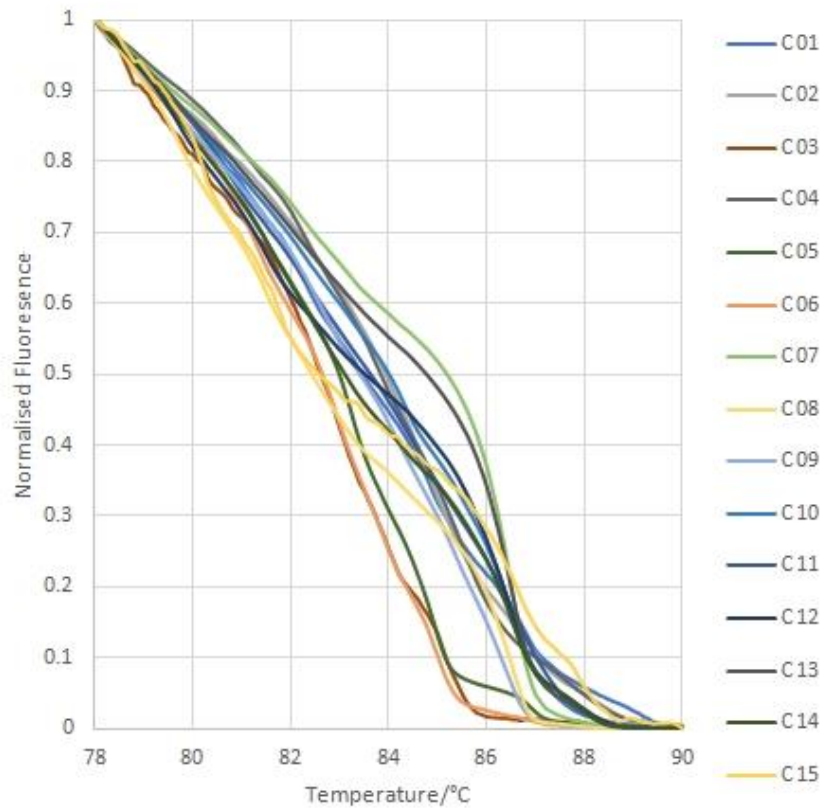


Figure 7-5 HRM curves for fifteen *aprA* amplicons

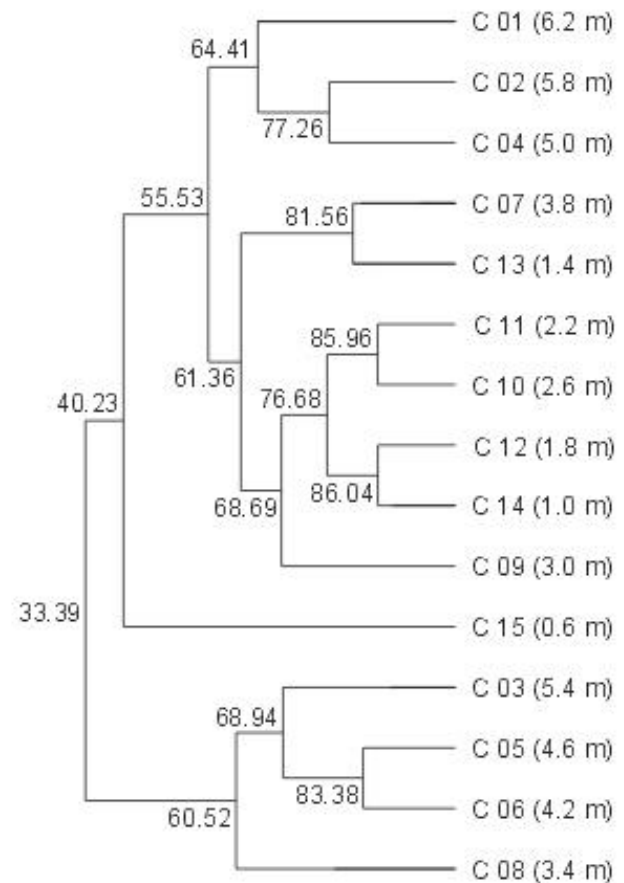


Figure 7-6 Similarity analysis of HRM curves for fifteen *aprA* amplicons

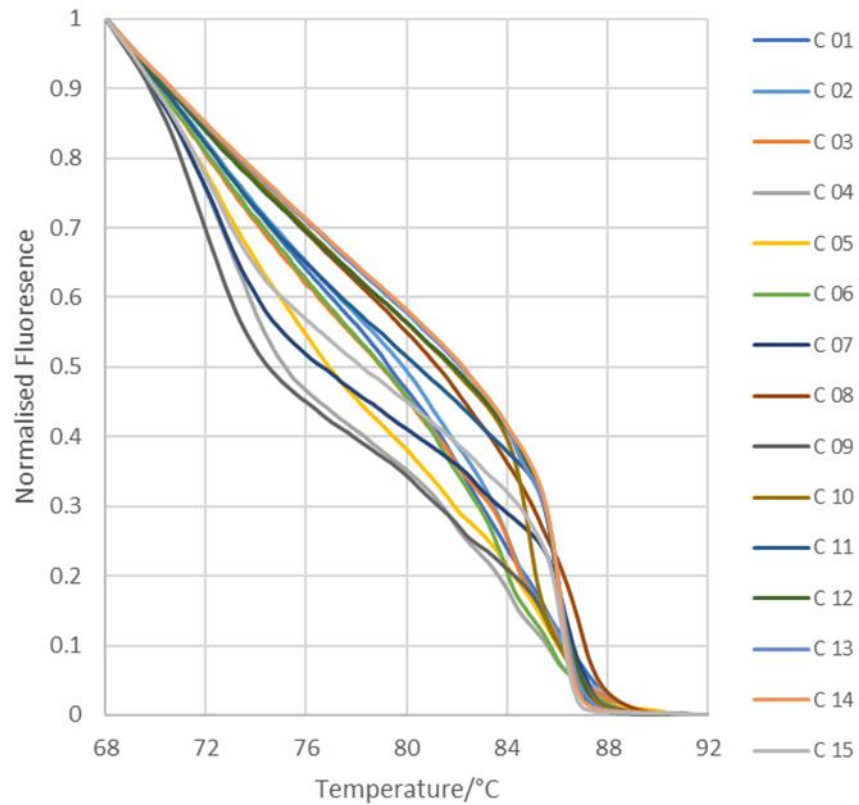


Figure 7-7 HRM curves for fifteen *dsrB* amplicons

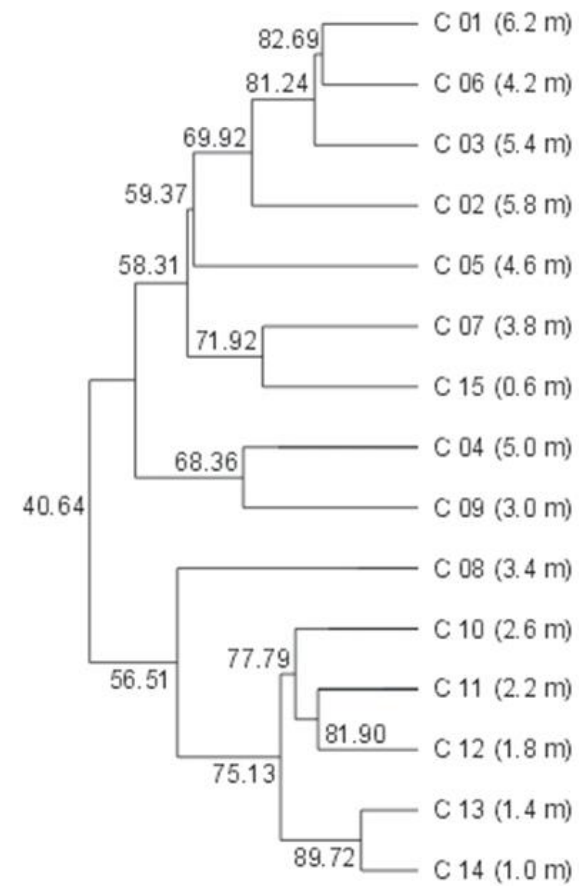


Figure 7-8 Similarity analysis of HRM curves for fifteen *dsrB* amplicons

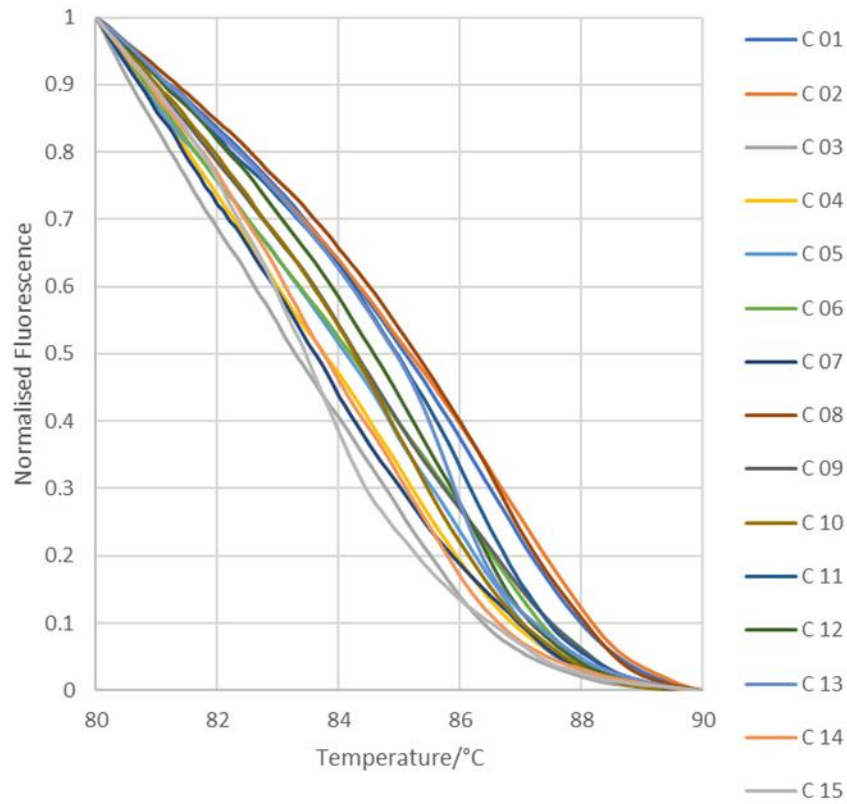


Figure 7-9 HRM curves for fifteen *soxB* amplicons

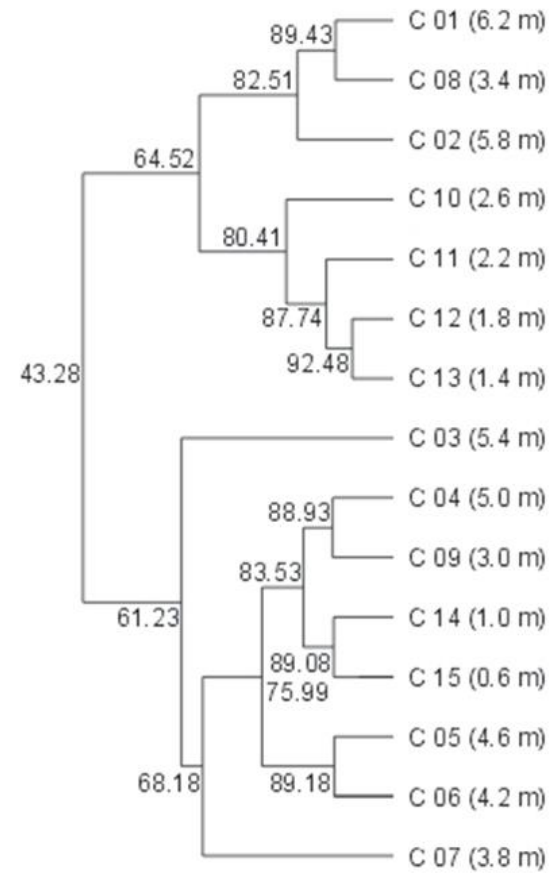


Figure 7-10 Similarity analysis of HRM curves for fifteen *soxB* amplicons

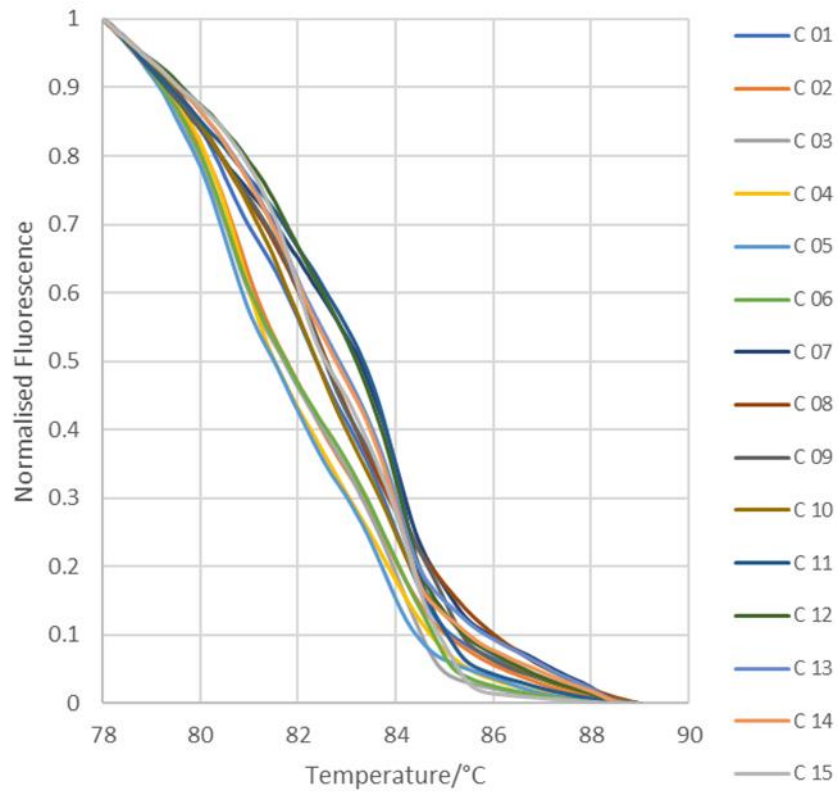


Figure 7-11 HRM curves for fifteen *16S* amplicons

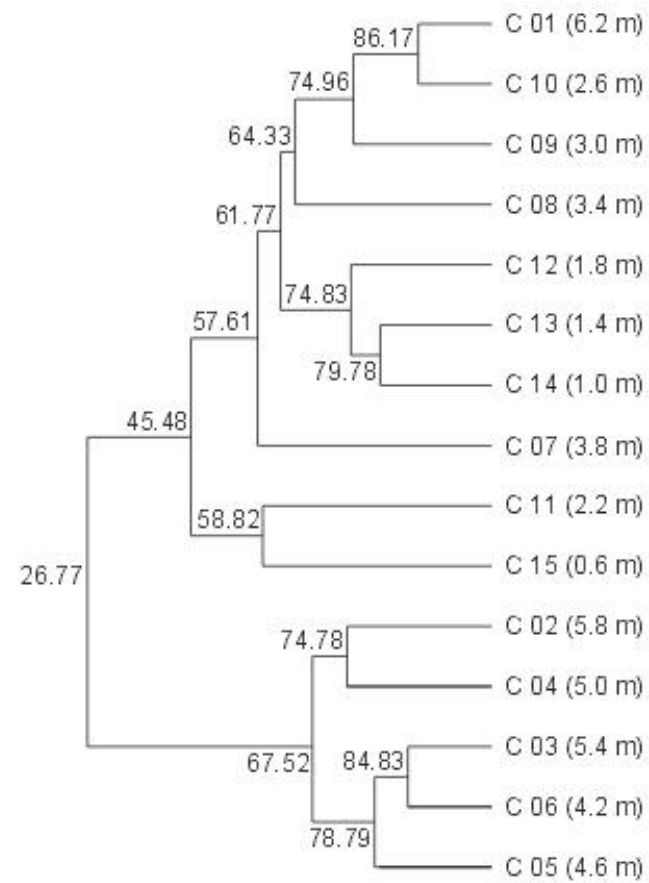


Figure 7-12 Similarity analysis of HRM curves for fifteen *16S* amplicons

7.3 Summary

The results of the DGGE and HRM analysis of twelve environmental samples indicated a degree of diversity of the *dsrB* gene between samples of the same type. The clustering pattern within the dendrogram shows that like sample types tend to be most similar, however. In both analyses the four corrosion samples formed a cluster, as did the seawater samples. The sub-surface sediment samples tended to cluster with the corrosion samples, whilst the surface sample reflected the diversity of the water samples more closely.

The two techniques were found to provide comparable degrees of differentiation when applied to the genetic variation of the community composition of the *dsrB* gene for the samples used. Of the two techniques, HRM required fewer pieces of apparatus, fewer experimental steps, it took significantly less time to set up and perform and provided a more credible assessment of gene diversity within the samples. However, DGGE has the advantage of allowing subsequent extraction of separated bands for further analysis, whereas all HRM amplicons remain mixed.

Additionally, by comparing the HRM curve profiles and distribution of DGGE bands, there was an apparent correlation between the straighter, gradual melt curves and the more diverse microbial communities as revealed by DGGE analysis, and between the less diverse communities and profiles displaying a steeper HRM profile and more defined melt temperature. This suggests that it may be possible to make quick assessments of relative community diversity based on the shape of HRM curves.

The HRM analysis of the vertical piling samples using *aprA*, *dsrB*, *soxB*, and *16S* primers revealed the presence of microbial organisms throughout the entire vertical profile of the marine piling that carried the targeted genes. This suggests that sulfur-reduction and sulfur-oxidation processes are occurring throughout the length of the piling. There were also observable patterns in diversity according to the vertical position on the piling the samples were extracted.

The dendrogram for each of the melt-patterns display variations between each gene; there is no single pattern that is entirely consistent between each gene. However, the plots do indicate that the closest correlation between community gene composition occurs between some adjacent samples. The samples C 10, C 11, C 12, and C 13 form part of the

same cluster for the *soxB* gene curve. These samples comprise all of those extracted between 2.6 m and 1.4 m above the sediment bed level. A similar cluster occurs between C 10, C 11, C 12, C 13, and C 14 for the *dsrB* gene dendrogram, which correspond with samples extracted between 2.6 m and 1.0 m above the sediment bed. The *aprA* dendrogram groups C 12 adjacent to C 14, with C 13 linked more distantly. However, when the cluster including C 13 is reviewed, the group comprises C07, C 08, C 09, C 10, C 12, C 13, and C 14 and covers vertical heights from 3.8 m to 2.6 m, and 1.8 m to 1.0 m above sediment bed level, though the similarity of this cluster is 61.36%. A similar group can be seen in the *I6S* dendrogram comprising C 07, C 08, C 09, C 10, C 12, C 13, C 14, and C 01. The C 02-C06 cluster in the *I6S* analysis may also be significant, indicating a region of community similarity towards the top of the piling. Of note in each of the plots is sample C 15, as it does not link closely with any of the previous sequences. In the *soxB* plot it pairs with C 14 and forms a cluster with samples C 03 to C 07, and C 09. For the *dsrB* dendrogram it clusters with C 01 to C 03, and C 05 to C 07. Similarly, C 15 correlates less well to the previously mentioned cluster adjacent than to samples that are not contiguous with it (C 01, C02, and C 04). The *I6S* melt-curve plot pairs C 15 with C 11, and only then links the samples to the main cluster.

Chapter 8 Spectroscopic analysis of corrosion samples using X-ray powder diffraction

8.1 Low tide zone corrosion

The data obtained from XRD analysis (section 3.2.5) of three low tide zone corrosion samples (C 14a, C 14b, and C 14c), extracted from 1.0 m above the sediment bed, are displayed as a combined diffractogram in Figure 8-1. The three samples were plotted with an arbitrary vertical offset for the sake of clarity. Analysis revealed a high degree of correspondence between the three samples: a total of twenty-one common peaks were identified as significant for each sample; each peak corresponded to one or more minerals or compounds (section 3.2.5) as summarised in Table 8-1 and Table 8-2. The diffractograms obtained displayed relatively large amounts of background noise with reduced identifiable peak intensities despite measures taken to reduce iron fluorescence (Section 3.2.5). Consequently, identification was focused on a reduced array of the most significant peaks attributed to each mineral. Several minerals considered possess diffractogram profiles that overlap by one peak or more with other minerals in the analysis. This has produced some uncertainty as to some mineral's presence. Where a peak corresponds with a single mineral or chemical compound, this has been taken as an indicator of occurrence within a sample.

Analysis identified several corrosion products in each sample. Goethite (α -FeOOH) was indicated by uniquely designated peaks at 24.5° (Peak j) and 43° (Peak w), and a peak at 62.5° which was shared with three other minerals. Similarly, lepidocrocite (γ -FeOOH) was also indicated by unique peaks at 14° (Peak f) and 47° (Peak y), and shared peaks at 26.5° (Peak k) and 36.5° (Peak v). The presence of magnetite (Fe₃O₄) in each sample was consistent with observed peaks at 35°, 36.5°, and 62.5° (Peak ad) though each of these peaks were also consistent with other minerals observed. Therefore, though it is consistent with observations, magnetite could not be confirmed by this analysis. This also applies to ferrous hydroxide (Fe(OH)₂), which has a single identifiable peak at 27° (Peak l) shared with akaganeite (β -FeOOH) and silica (SiO₂). Akaganeite was not indicated despite shared peaks at 27° and 35°, as its unique peak at 12° (Peak d) is absent. Similarly, a peak at 32.5° (Peak q) common to both hematite (α -Fe₂O₃) and siderite (FeCO₃) is absent

suggesting these two minerals were also not present. Maghemite ($\gamma\text{-Fe}_2\text{O}_3$) shares a resolvable peak at 30° (Peak n) with three iron sulfide minerals: greigite (Fe_3S_4); smythite (Fe_9S_{11}); and pyrrhotite (Fe_7S_8), and at 35.5° (Peak u) that it shares with feroxyhyte ($\delta\text{-FeOOH}$) and ferrihydrite ($\text{Fe}_5\text{HO}_6\cdot 4\text{H}_2\text{O}$). The X-ray diffraction patterns of greigite and smythite share a peak at 52° (Peak aa), whilst pyrrhotite possesses unique peaks at 44° (Peak x) and 53.5° (Peak ab). These peaks were not observed, indicating that the minerals were absent from the samples. The peak found at 30° in each sample could therefore be attributed to maghemite, thus strongly indicating this mineral's presence. Feroxyhyte and ferrihydrite also share an indicated peak at 62.5° so are unverifiable in this analysis. Identifying peaks for chloride green rust ($\text{GR}(\text{Cl}^-)$) at 5° and 10.5° , and carbonate green rust ($\text{GR}(\text{CO}_3^{2-})$) at 13.5° are absent. As chloride green rusts forms prior to akaganeite its absence supports the observations made above regarding the latter mineral. Ferrihydrite forms from ferrous hydroxide via the carbonate green rust pathway, but also directly from oxidation of ferrous hydroxide in the presence of certain metal ions (Section 2.5.3). The absence of carbonate green rust does not therefore preclude ferrihydrite from the three samples. Sulfate green rust ($\text{GR}(\text{SO}_4^{2-})$) is indicated due to two peaks at 11° (Peak c) and 21° (Peak i). These are unique to sulfate green rust in this analysis and occur in the diffractograms for each of the three corrosion samples.

Other iron sulfide minerals associated with MIC (Section 2.5.6) were also reviewed against the sample diffractograms. Pyrite (FeS_2) possessed an identifying peak at 56° (Peak ac) that was common to each sample along with a shared peak at 33° (Peak r), indicating its presence. Mackinawite (FeS_{1-x}) associated peaks at 18° (Peak g) and 51° (Peak z) were absent from the three samples. Due to having a chemical formula identical to pyrite, marcasite (FeS_2) is denoted as $\text{FeS}_2(\text{M})$ in Table 8-1 and Table 8-2. This mineral shares a peak with pyrite at 33° , and with greigite and smythite at 52° . As indicated previously all three samples display a peak at 33° , but peaks at 52° are absent indicating marcasite is not present.

Halite (NaCl) and calcite (CaCO_3) were indicated in each sample due to unique peaks at 32° (Peak p), and 29.5° (Peak m) respectively. Nahcolite (NaCO_3) was indicated by peaks at both 30.5° (Peak o) and 34.5° (Peak s). Peaks at 20° (Peak h), 26.5° , and 35° imply the presence of illite in each of the samples also. Kaolinite possesses a single discernible peak at 26.5° shared with lepidocrocite and illite, so was not verifiable during this analysis.

Similarly, silica (SiO_2) was implied in each sample due to a shared peak at 27° but was not separately confirmed.

As has been previously discussed, most MIC studies of marine steel piling have concentrated on low tide zone formations and single samples from various environments. The extraction and analysis of three samples from the same location and height on the piling was intended to provide a greater degree of confidence about variability in mineral composition of the corrosion at this position.

The XRD profiles for the three samples were closely matched and the analysis revealed the same significant peaks, indicating a similar mineralogy between all. Multiple minerals previously identified as common to MIC were identified (ferrous hydroxide, sulfate green rust, ferrihydrite, lepidocrocite, goethite, and maghemite); magnetite could not be unambiguously identified, however. The analysis was also able to discern pyrite (FeS_2). The occurrence of this mineral is consistent with metabolic activity of sulfate-reducing microorganisms, which produce hydrogen sulfide. Other iron sulfides were searched for but corresponding peaks were not observed. A lack of signal for these may be explained by low concentrations due to rapid oxidation of these sulfides by elemental sulfur, hydrogen sulfide, or hydrogen ions (Jørgensen and Kasten, 2006) or by their absence, with pyrite forming by direct precipitation (Section 2.5.6). Calcite and two clay minerals were indicated as were halite and nahcolite. These imply the percolation of seawater into the corrosion formation. Non-MIC related minerals were absent: neither chloride green rust, carbonate green rust, siderite, akaganeite, nor hematite were indicated in any of the samples.

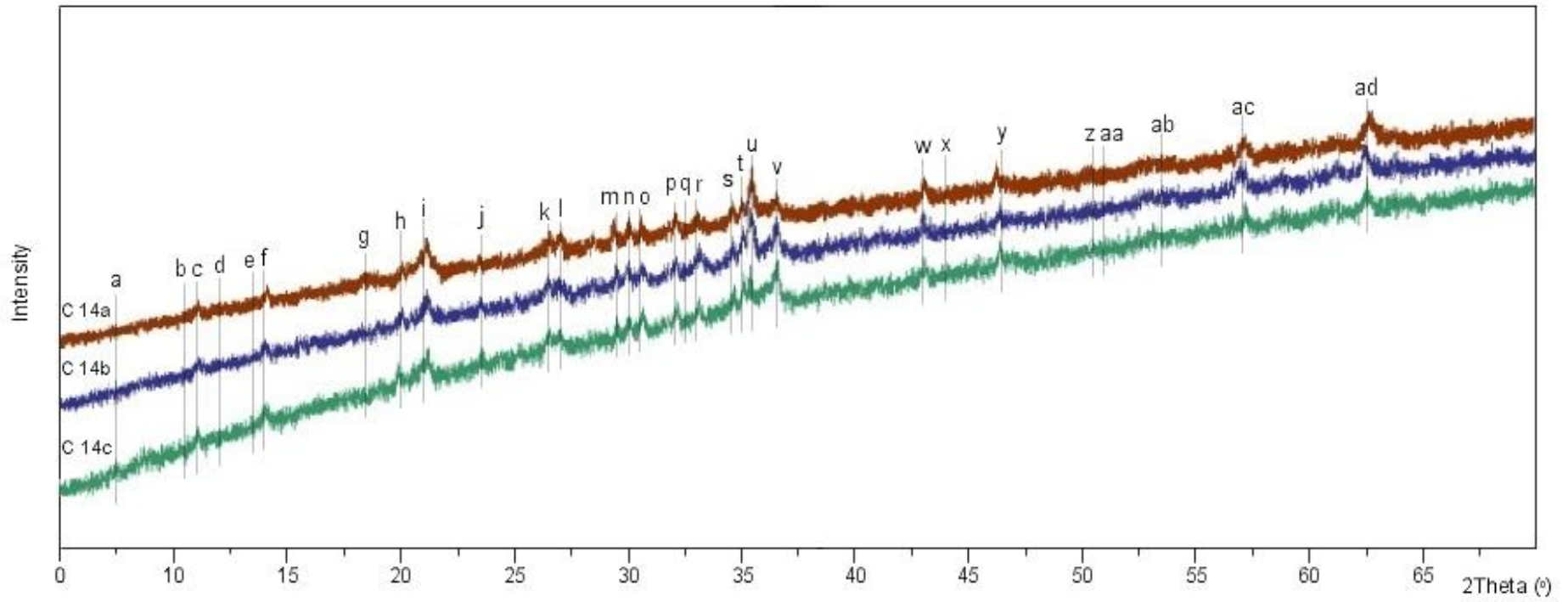


Figure 8-1 XRD diffractogram with identified peaks for corrosion samples C 14a, C 14b, and C 14c

Table 8-1 XRD peaks (a to o) with corresponding minerals and chemical compounds
for corrosion samples C 14a, C 14b, and C 14c

Peak reference		a	b	c	d	e	f	g	h	i	j	k	l	m	n	o
2Theta (°)		5	10.5	11	12	13.5	14	18	20	21	24.5	26.5	27	29.5	30	30.5
Mineral/compound		GR(Cl)	GR(Cl)	GR(SO ₄ ²⁻)	β-FeOOH	GR(CO ₃ ²⁻)	γ-FeOOH	FeS _{1-x}	Illite	GR(SO ₄ ²⁻)	α-FeOOH	γ-FeOOH Illite Kaolinite	β-FeOOH Fe(OH) ₂ SiO ₂	CaCO ₃	γ-Fe ₂ O ₃ Fe ₃ S ₄ Fe ₉ S ₁₁ Fe ₇ S ₈	NaHCO ₃
Sample reference	Height above sediment bed															
C 14a	1.0 m	X	X	✓	X	X	✓	X	✓	✓	✓	✓	✓	✓	✓	✓
C 14b		X	X	✓	X	X	✓	X	✓	✓	✓	✓	✓	✓	✓	✓
C 14c		X	X	✓	X	X	✓	X	✓	✓	✓	✓	✓	✓	✓	✓

✓ = peak observed; x = peak not observed

Table 8-2 XRD peaks (p to ad) with corresponding minerals and chemical
compounds for corrosion samples C 14a, C 14b, and C 14c

Peak reference		p	q	r	s	t	u	v	w	x	y	z	aa	ab	ac	ad
2Theta (°)		32	32.5	33	34.5	35	35.5	36.5	43	44	47	51	52	53.5	56	62.5
Mineral/compound		NaCl	α-Fe ₂ O ₃ FeCO ₃	FeS ₂ FeS ₂ (M)	NaHCO ₃	Fe ₃ O ₄ α-Fe ₂ O ₃ β-FeOOH Illite	γ-Fe ₂ O ₃ δ-FeOOH Fe ₅ HO ₆ .4H ₂ O	Fe ₃ O ₄ γ-FeOOH	α-FeOOH	Fe ₇ S ₈	γ-FeOOH	FeS _{1-x}	Fe ₃ S ₄ FeS ₂ (M) Fe ₉ S ₁₁	Fe ₇ S ₈	FeS ₂	Fe ₃ O ₄ α-FeOOH δ-FeOOH Fe ₅ HO ₆ .4H ₂ O
Sample reference	Height above sediment bed															
C 14a	1.0 m	✓	X	✓	✓	✓	✓	✓	✓	X	✓	X	X	X	✓	✓
C 14b		✓	X	✓	✓	✓	✓	✓	✓	X	✓	X	X	X	✓	✓
C 14c		✓	X	✓	✓	✓	✓	✓	✓	X	✓	X	X	X	✓	✓

✓ = peak observed; x = peak not observed

8.2 Vertical profile corrosion

The results of XRD analysis (section 3.2.5) of corrosion samples C 01 to C 15, from positions between 6.2 m and 0.6 m above the sediment bed, are shown in Figure 8-2 as a combined diffractogram. For clarity, each diffractogram has been plotted vertically offset from its adjacent sample. A total of twenty-six peaks were identified between the samples; the array of minerals for each sample is summarised in Table 8-3 and Table 8-4. As discussed in Section 8.1, the diffractograms obtained for these samples displayed relatively large amounts of background noise with reduced identifiable peak intensities despite measures taken to reduce iron fluorescence.

Analysis indicated several minerals that were common to all samples: the defining peaks of goethite (α -FeOOH) were present at 24.5° (Peak j) and 43° (Peak w); lepidocrocite (γ -FeOOH) peaks at 14° (Peak f) and 47° (Peak y) were observed; unambiguous halite (NaCl) and calcite (CaCO₃) peaks at 32° (Peak p) and 29.5 (Peak m) were also resolved. Nahcolite (NaHCO₃) was also indicated in each sample by peaks at 30.5° (Peak o) and 34.5° (Peak s), as was illite (Peak h at 20°).

Peaks consistent with magnetite were observed at 35° (Peak t), 36.5° (Peak v), and 62.5° (Peak ad) for each of the samples. As discussed in Section 8.1, these peaks were also applicable to other minerals, so the presence of magnetite could not be confirmed. This is also true of ferrous hydroxide (Fe(OH)₂) and silica (SiO₂), which possess a single peak shared with akaganeite at 27° (Peak l), and kaolinite, which has a shared peak at 26.5°. Identification of akaganeite (β -FeOOH) in the samples was determined by Peak d (12°) due to its correlation with this mineral only. The analysis indicated akaganeite was present in samples C 01 to C 08 but absent from samples C 09 to C 15. Shared peaks for akaganeite at 27° and 35° (Peak t) also supported this.

Siderite (FeCO₃) displayed a single peak at 32.5° (Peak q) that is shared with hematite (α -Fe₂O₃). The occurrence of this peak in the diffractogram indicates one or both minerals are present in samples C 01 to C 08 are both are missing from samples C 09 to C 15. Hematite also shares a peak at 35° that is present in all fifteen corrosion samples. This confirms that peaks recorded at 32.5° must include hematite, and that the mineral was only observed in samples at the height of C08 and above. Maghemite (γ -Fe₂O₃) displays two peaks in this analysis: 30° (Peak n), which is shared with greigite (Fe₃S₄), smythite

(Fe₉S₁₁), and pyrrhotite (Fe₇S₈); and 35.5° (Peak u). The latter peak corresponds with feroxyhyte (δ-FeOOH) and ferrihydrite (Fe₅OH₆·4H₂O) also. Peaks at 30° were observed for samples C 07 to C 15, which indicates maghemite and the iron sulfide minerals were absent from samples C 01 to C 06. Greigite and smythite possess a diffraction peak at 52°, and pyrrhotite has a unique peak at 53.5°. These correspond with Peaks aa and ab in Table 8-4, which are not resolved in the diffractogram (Figure 8-2) indicating an absence of these minerals. This suggests that the peak observed at 30° was due to maghemite only. The full complement of observed peaks at 62.5° (Peak ad) suggests feroxyhyte and ferrihydrite could be present in any or all the samples; the response at Peak r limits this to sample C 07 to C 15 in line with the occurrence of maghemite, however. Unlike maghemite, these two minerals were not verified during this analysis.

Pyrite (FeS₂) has resolvable peaks at 33° (Peak r) along with marcasite (FeS₂) (denoted as FeS₂(M) for clarity in Table 8-4), and at 56° (Peak ac). Analysis of the samples indicates these minerals are only consistent with samples C 08 to C 15. Furthermore, no peaks at 52° were observed for these samples, and therefore the peaks were due to pyrite only. Mackinawite (FeS_{1-x}) displays peaks at 18° (Peak g) and 51° (Peak z). No peaks were visible at these positions throughout the fifteen samples.

The presence of chloride green rust (GR(Cl⁻)) was determined by peaks at 5° (Peak a) and 10.5° (Peak b). Sample C 01 was found to lack these peaks, but they were observed in the following six samples (C 02 to C 07). Samples C 08 to C 15 did not display these peaks. Carbonate green rust (GR(CO₃²⁻)) was assessed by a single peak at 13.5° (Peak e); none of the samples had a discernible peak at this location. Sulfate green rust (GR(SO₄²⁻)) was identified by peaks at 11° (Peak c) and 21° (Peak i). Three samples (C 01, C 02, and C 06) had no resolvable peaks at these positions; the remaining twelve samples all displayed peaks at these locations.

The XRD analysis therefore revealed that significant mineralogical differences were present in the samples collected. The samples could be broadly divided into three groups: those with typically MIC mineralogy; those that reflected NWC corrosion composition; and an intermediate groups with a mixed mineralogy. The upper six samples (C 01 to C 06) spanned above sediment bed heights of 6.2 m to 4.2 m. These were characterised by the presence of akaganeite, and hematite/siderite. Within this group, C 01 is of note as it

lacked peaks corresponding with either chloride green rust or sulfate green rust, whereas C 02 to C 06 all had chloride green rust peaks. The lower six samples (C10 to C 15) exhibited MIC mineralogy. Located at heights of 2.6 m to 0.6 m above the sediment bed; these were distinguished by the presence of maghemite and pyrite. The remaining samples (C 07, C 08, and C 09) formed a transitional band between the upper and lower group. All three of these samples displayed peaks for akaganeite, whilst C 07 and C 08 showed peaks corresponding with hematite/siderite. Only C 07 exhibited chloride green rust peaks. All three showed peaks for maghemite; pyrite peaks were visible in the diffractograms for C 08 and C 09 only. As noted above, the minerals goethite and lepidocrocite were common to all samples, as were halite, nahcolite, and the clays illite and kaolinite.

The observation that akaganeite and hematite/siderite were common to the high-level 'NWC' samples, and that maghemite and pyrite in the low-level 'MIC' samples suggests that XRD could be utilised as a fast-analytical technique in MIC detection. Further sampling would be necessary to verify the mineralogical pattern however, and to explore the intermediate zone between the upper and lower groups more fully.

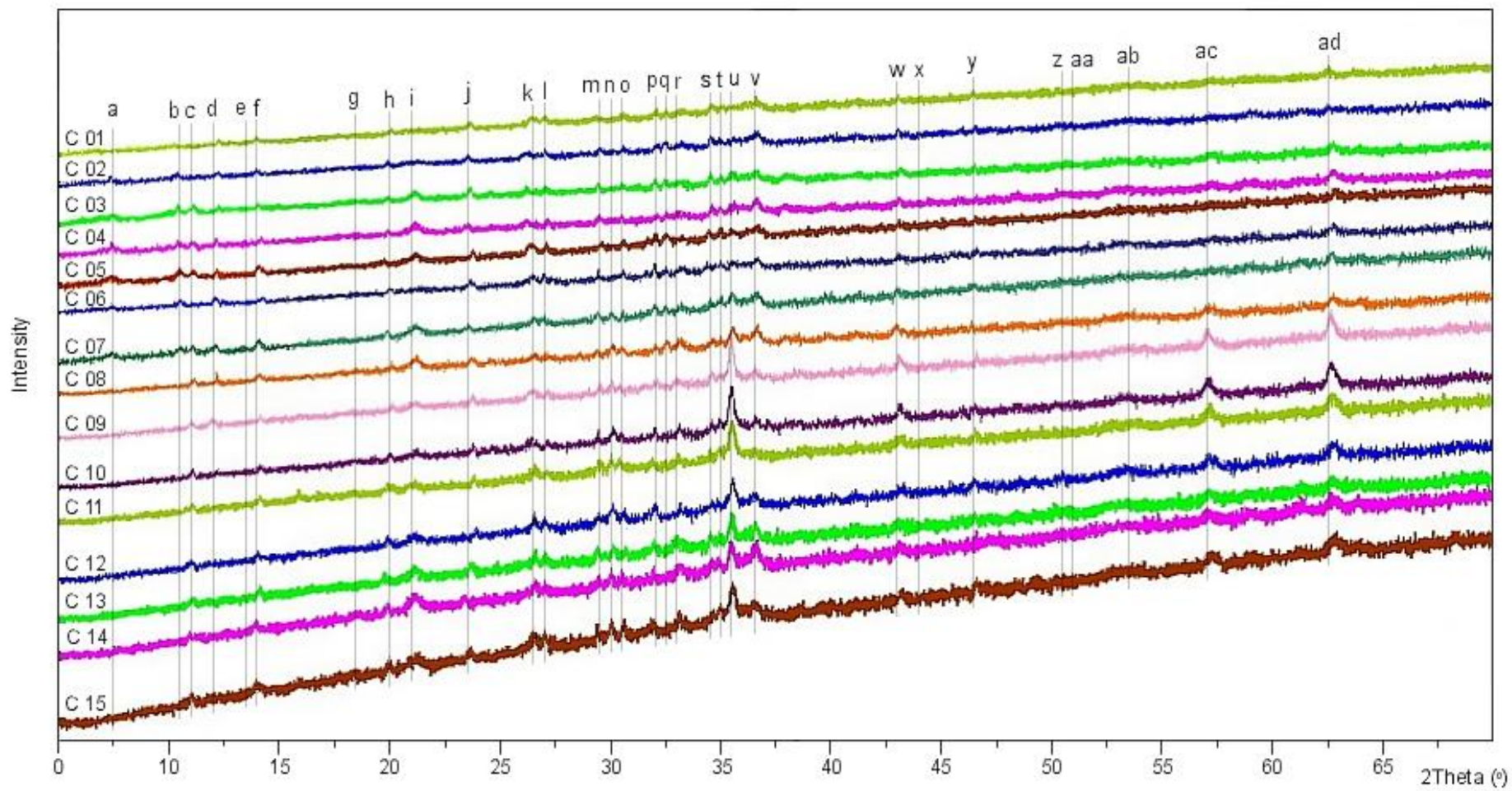


Figure 8-2 XRD diffractogram with identified peaks for corrosion samples C 01 to C 15

Table 8-3 XRD peaks (a to o) with corresponding minerals and chemical compounds
for corrosion samples C 01 to C 15

Peak reference		a	b	c	d	e	f	g	h	i	j	k	l	m	n	o
2Theta (°)		5	10.5	11	12	13.5	14	18	20	21	24.5	26.5	27	29.5	30	30.5
Mineral/compound		GR(Cl ⁻)	GR(Cl ⁻)	GR(SO ₄ ²⁻)	β-FeOOH	GR(CO ₃ ²⁻)	γ-FeOOH	FeS _{1-x}	Illite	GR(SO ₄ ²⁻)	α-FeOOH	γ-FeOOH Illite Kaolinite	β-FeOOH Fe(OH) ₂ SiO ₂	CaCO ₃	γ-Fe ₂ O ₃ Fe ₃ S ₄ Fe ₉ S ₁₁ Fe ₇ S ₈	NaHCO ₃
Sample reference	Height above sediment bed															
C 01	6.2 m	X	X	X	✓	X	✓	X	✓	X	✓	✓	✓	✓	X	✓
C 02	5.8 m	✓	✓	X	✓	X	✓	X	✓	X	✓	✓	✓	✓	X	✓
C 03	5.4 m	✓	✓	✓	✓	X	✓	X	✓	✓	✓	✓	✓	✓	X	✓
C 04	5.0 m	✓	✓	✓	✓	X	✓	X	✓	✓	✓	✓	✓	✓	X	✓
C 05	4.6 m	✓	✓	✓	✓	X	✓	X	✓	✓	✓	✓	✓	✓	X	✓
C 06	4.2 m	✓	✓	X	✓	X	✓	X	✓	X	✓	✓	✓	✓	X	✓
C 07	3.8 m	✓	✓	✓	✓	X	✓	X	✓	✓	✓	✓	✓	✓	✓	✓
C 08	3.4 m	X	X	✓	✓	X	✓	X	✓	✓	✓	✓	✓	✓	✓	✓
C 09	3.0 m	X	X	✓	✓	X	✓	X	✓	✓	✓	✓	✓	✓	✓	✓
C 10	2.6 m	X	X	✓	X	X	✓	X	✓	✓	✓	✓	✓	✓	✓	✓
C 11	2.2 m	X	X	✓	X	X	✓	X	✓	✓	✓	✓	✓	✓	✓	✓
C 12	1.8 m	X	X	✓	X	X	✓	X	✓	✓	✓	✓	✓	✓	✓	✓
C 13	1.4 m	X	X	✓	X	X	✓	X	✓	✓	✓	✓	✓	✓	✓	✓
C 14	1.0 m	X	X	✓	X	X	✓	X	✓	✓	✓	✓	✓	✓	✓	✓
C 15	0.6 m	X	X	✓	X	X	✓	X	✓	✓	✓	✓	✓	✓	✓	✓

✓ = peak observed; x = peak not observed

Table 8-4 XRD peaks (p to ad) with corresponding minerals and chemical compounds
for corrosion samples C 01 to C 15

Peak reference		p	q	r	s	t	u	v	w	x	y	z	aa	ab	ac	ad
2Theta (°)		32	32.5	33	34.5	35	35.5	36.5	43	44	47	51	52	53.5	56	62.5
Mineral/compound		NaCl	α -Fe ₂ O ₃ FeCO ₃	FeS ₂ FeS ₂ (M)	NaHCO ₃	Fe ₃ O ₄ α -Fe ₂ O ₃ β -FeOOH Illite	γ -Fe ₂ O ₃ δ -FeOOH Fe ₅ HO ₆ .4H ₂ O	Fe ₃ O ₄ γ -FeOOH	α -FeOOH	Fe ₇ S ₈	γ -FeOOH	FeS _{1-x}	Fe ₃ S ₄ FeS ₂ (M) Fe ₉ S ₁₁	Fe ₇ S ₈	FeS ₂	Fe ₃ O ₄ α -FeOOH δ -FeOOH Fe ₅ HO ₆ .4H ₂ O
Sample reference	Height above sediment bed															
C01	6.2 m	✓	✓	X	✓	✓	X	✓	✓	X	✓	X	X	X	X	✓
C02	5.8 m	✓	✓	X	✓	✓	X	✓	✓	X	✓	X	X	X	X	✓
C03	5.4 m	✓	✓	X	✓	✓	X	✓	✓	X	✓	X	X	X	X	✓
C04	5.0 m	✓	✓	X	✓	✓	X	✓	✓	X	✓	X	X	X	X	✓
C05	4.6 m	✓	✓	X	✓	✓	X	✓	✓	X	✓	X	X	X	X	✓
C06	4.2 m	✓	✓	X	✓	✓	X	✓	✓	X	✓	X	X	X	X	✓
C07	3.8 m	✓	✓	X	✓	✓	✓	✓	✓	X	✓	X	X	X	X	✓
C08	3.4 m	✓	✓	✓	✓	✓	✓	✓	✓	X	✓	X	X	X	✓	✓
C09	3.0 m	✓	X	✓	✓	✓	✓	✓	✓	X	✓	X	X	X	✓	✓
C10	2.6 m	✓	X	✓	✓	✓	✓	✓	✓	X	✓	X	X	X	✓	✓
C11	2.2 m	✓	X	✓	✓	✓	✓	✓	✓	X	✓	X	X	X	✓	✓
C12	1.8 m	✓	X	✓	✓	✓	✓	✓	✓	X	✓	X	X	X	✓	✓
C13	1.4 m	✓	X	✓	✓	✓	✓	✓	✓	X	✓	X	X	X	✓	✓
C14	1.0 m	✓	X	✓	✓	✓	✓	✓	✓	X	✓	X	X	X	✓	✓
C15	0.6 m	✓	X	✓	✓	✓	✓	✓	✓	X	✓	X	X	X	✓	✓

✓ = peak observed; x = peak not observed

8.3 Summary

The results of the XRD analysis of corrosion samples indicated compositions that were consistent with previous corrosion studies; iron oxides, oxyhydroxides, and green rusts were indicated. However, the samples also could be divided between three contiguous corrosion groups, each of which possessed unique combinations of minerals in addition to goethite and lepidocrocite observed at all positions on the piling analysed. The group with mineralogy closest to normal water corrosion was found at the top of the piling, whereas the corrosion nearest to the sediment bed possessed a mineralogy of that observed in microbially influenced corrosion. Identification of the unique mineral combinations in each group may provide a method of classifying the type of corrosion and to provide a guide as to anticipated rates of corrosion.

Chapter 9 Spectroscopic analysis of corrosion samples using Fourier-transform infrared spectroscopy

9.1 Low tide zone corrosion

The spectra obtained from FTIR analysis (section 3.2.6) of three low tide zone corrosion samples taken from 1.0 m above sediment bed level (C 14a, C 14b, and C 14c) are displayed along with corresponding deconvoluted peaks in Figure 9-1. Deconvolution using PeakFit software achieved a coefficient of determination of $R^2 > 0.99$ for each spectrum. The correlation of identified peaks with minerals, compounds, and chemical species (Appendix H) are summarised in Table 9-1 and Table 9-2. Analysis revealed a composition consistent with eighteen minerals, five chemical compounds, and three chemical species, according to the positions of the deconvoluted peaks.

As described in Section 8.1, where a single type of mineral or compound corresponds with a peak this has been taken as confirmation of its presence within the sample. This applies to surface adsorbed water molecules (Peak A), nahcolite (Peak C), calcite (Peak D), sulfate ions (Peak G), sulfite (Peak H), lepidocrocite (Peak J), sulfate green rust (Peak K), magnetite (Peak AE), and maghemite (Peak AG).

The FTIR analysis of C 14a, C 14b, and C14c display peaks corresponding to all references A through to AF for each of the three samples. Only C 14a displays a peak consistent with AG (maghemite), however. Determining mineral and chemical species within each sample is less certain due to the presence of shared peaks, apart from those minerals noted in the previous paragraph. Based on minerals and compounds common to both normal-water corrosion (NWC) (Section 2.5.3) and microbially influenced corrosion (MIC) (Section 2.5.6) it would be anticipated that in this environment, the following would be present: magnetite, maghemite, goethite, lepidocrocite, ferrihydrite, ferrous hydroxide, and sulfate green rust, however.

Where magnetite is indicated, it shares peaks with maghemite, akaganeite, and chloride green rust (Peak AA); goethite (Peak AC); and occurs on its own (Peak AE). If the corrosion samples possess compositional properties of normal water corrosion, all these corresponding minerals and ions could be present and contributing to these FTIR peaks.

As noted in Section 2.5.6, the core region of MIC formations would not be anticipated to include either chloride green rust due to the preferential formation of sulfate green rust, but maghemite, goethite, and ferrihydrite would be consistent.

As noted above maghemite is indicated in sample C 14a (Peak AG) and implied by its correlation with Peak AA. The lack of a peak at 560 to 550 cm^{-1} for C 14b and C 14c indicates this mineral is not present. However, this wavenumber range is close to the minimum wavenumber measurable with the equipment used (550 cm^{-1}), and vibrational modes display a range of values between samples, so it is possible that Fe-O vibrations representative of maghemite were present for sample C 14b and C 14c immediately below 550 cm^{-1} and therefore not resolvable.

Vibrational modes attributed to goethite occur within Peaks E, U, W, and AC. Peak E includes akaganeite, carbonate green rust and siderite; Peak U includes sulfate green rust and calcite; Peak W also corresponds with chloride green rust, silica, and illite; and Peak AC is as discussed in the previous paragraph. As covered in Sections 2.5.3 and 2.5.6, akaganeite, carbonate and chloride green rusts and are commonly found in NWC but are not discerned in MIC core regions due to unfavourable conditions. Calcite, silica, and illite are not corrosion product, but their presence is consistent with interaction of suspended particles in seawater with the corrosion formation; either via percolation into the corrosion followed by deposition and/or surface capture and assimilation as the corrosion formation developed. Seawater percolation with subsequent precipitation upon sample drying would also explain the detection of nahcolite in the samples (Music et al., 2004). The presence of halite would confirm the inundation of the inner corrosion layers by seawater, but as the mineral displays no absorption peaks under infrared light (Addala et al., 2013, Rruff Project, 2020), it was not possible to verify using this technique.

The presence of lepidocrocite is indicated by its unique correlation with Peak J. Its other modes are consistent with Peaks P, Y, and AD. Peak P is occurs shared with nahcolite and sulfite. Both also occur as single correlations with a peak (C and H respectively) and are thus contributing to the intensity of this peak for each of the samples. Likewise, lepidocrocite shares Peak AD with akaganeite, and sulfate which is also a separately verified mineral. Peak Y includes two clay minerals, illite and kaolinite, the presence of which are consistent with interactions between the corrosion and suspended sediment in

the water column as noted previously. However, as vibrational modes for illite and kaolinite coincide with common corrosion products their occurrence in the samples requires verification using other experimental techniques.

Ferrihydrite has been observed in both NWC and MIC. Its vibrational modes between 1650 cm^{-1} and 550 cm^{-1} correspond with Peaks N, Z, and AF. Peak N is shared with ferrous hydroxide and sulfate. Ferrous hydroxide is a precursor to many minerals in abiotic steel corrosion (Figure 2-5) and its occurrence would therefore be predicted in both NWC and MIC. As previously noted, sulfate is a verified chemical species in this analysis and would be expected to contribute to the peak intensity at these wavenumbers. Peak Z encompasses siderite, calcite, illite, and kaolinite also. As described before siderite is common in NWC but would not be expected to form in MIC core regions. The presence of calcite, illite, and kaolinite are possible as described in the previous paragraph. As well as ferrihydrite, Peak AF includes the wavenumbers associated with a stretching mode in hematite, a mineral common to NWC but not associated with MIC (Sections 2.5.3 and 2.5.6 respectively). Vibrational modes of ferrous hydroxide also correspond with Peaks F (with carbonate green rust and nahcolite), R (with feroxyhyte), S, and V (with akaganeite, carbonate green rust, and siderite). Peak S includes the important species thiosulfate, which is source of electrons for sulfur-oxidizing bacteria (Madigan et al., 2009). It is produced mainly in abiotic reactions between elemental sulfur and sulfite. Sulfate-reducing prokaryotes have been associated with production of these reagents, though the SRP are not causally linked with catalysing the subsequent reaction (Kletzin, 1988). The reaction also produces hydrogen ions, and so is also a potential contributor to corrosion. Thiosulfate is also indicated at Peaks L and Q, each of which also include kaolinite. The NWC minerals akaganeite and feroxyhyte correspond with Peak L, and Peak Q includes the confirmed species sulfate.

Sulfite is indicated by Peaks H, M, O, P, and T. Sulfite forms as an intermediate species between sulfate and sulfide during the dissimilatory reduction pathway driven by sulfate-reducing prokaryotes (SRP) and so its presence in these samples could be indicative of microbial activity. Sulfide was not observed using the equipment available as iron-sulfur and sulfur-sulfur vibrational modes lying below 550 cm^{-1} (Weerasooriya et al., 2010, Oliveira et al., 2016).

As discussed above sulfate green rust is confirmed by Peaks K and AB. It also occurs in Peaks B, I, M, and X. It shares peak B with carbonate green rust and chloride rust. The abiotic formation of these minerals is outlined in Section 2.5.3 and their occurrence in MIC is discussed in Section 2.5.6.

Aragonite (CaCO_3) and brucite ($\text{Mg}(\text{OH})_2$) can be formed by the reaction of hydroxide ions with metal ions in seawater (Section 2.5.3), and both have FTIR profiles that correspond with peaks observed during the analysis. Aragonite shared peaks with other carbonate minerals in the analysis: calcite (Peaks D and Z); siderite and carbonate green rust (Peak V). It also displayed a peak between 1090 cm^{-1} and 1080 cm^{-1} along with silica and several sulfur species (Peak M). Brucite displayed two peak within the wavenumber range analysed. The region occupied by the first was 1402 and 1386 wavenumbers and was shared with M-O-H bending modes of goethite and akaganeite, and O-C-O stretching modes of calcite, carbonate green rust and siderite.

As previously discussed in Section 8.1, the intention of analysing three corrosion samples was to provide preliminary indications of any variability in composition between low water level corrosion in a specific location. The analysis indicated a high degree of similarity between the three samples, both in their FTIR spectra and the minerals and compounds these correspond with.

The main difficulty in interpreting the spectra were the number of possible candidates that are applicable to certain wavenumber regions. This is illustrated most clearly in the 1461 cm^{-1} to 1443 cm^{-1} region (Peak E) and 711 cm^{-1} to 728 cm^{-1} region (Peak Z), both of which have six corresponding minerals consistent with their position. The data is consistent with what has been isolated from MIC samples in other studies (Section 2.5.6): ferrous hydroxide, sulfate green rust, ferrihydrite, lepidocrocite, goethite, maghemite, and magnetite are all indicated. However, many minerals associated with normal water corrosion are also consistent with the results. Both carbonate and chloride green rusts, brucite, siderite, akaganeite, and hematite are also indicated. Therefore, despite being positioned within the low tide zone within a region with recorded incidence of MIC, these three samples cannot be designated as typical of MIC by this technique alone. Minerals not related to corrosion are also indicated. The presence of calcite suggests assimilation of marine barnacles as the corrosion developed (Section 2.5.6), or the presence of forams

or coccolithophores carried into the formation by percolating seawater. The indications of the clay minerals observed is similarly explained (See above).

The most unambiguous feature of the analysis was the identification of various sulfur species (sulfate, sulfite, and thiosulfate). Sulfate is found in relatively high concentration in seawater, but reduced sulfur species quickly become oxidized in the environment. Sulfate-reducing prokaryotes utilize sulfate during anaerobic respiration producing these reduced species (Section 2.2). Their presence is therefore a strong indication of anaerobic microbial activity within the corrosion.

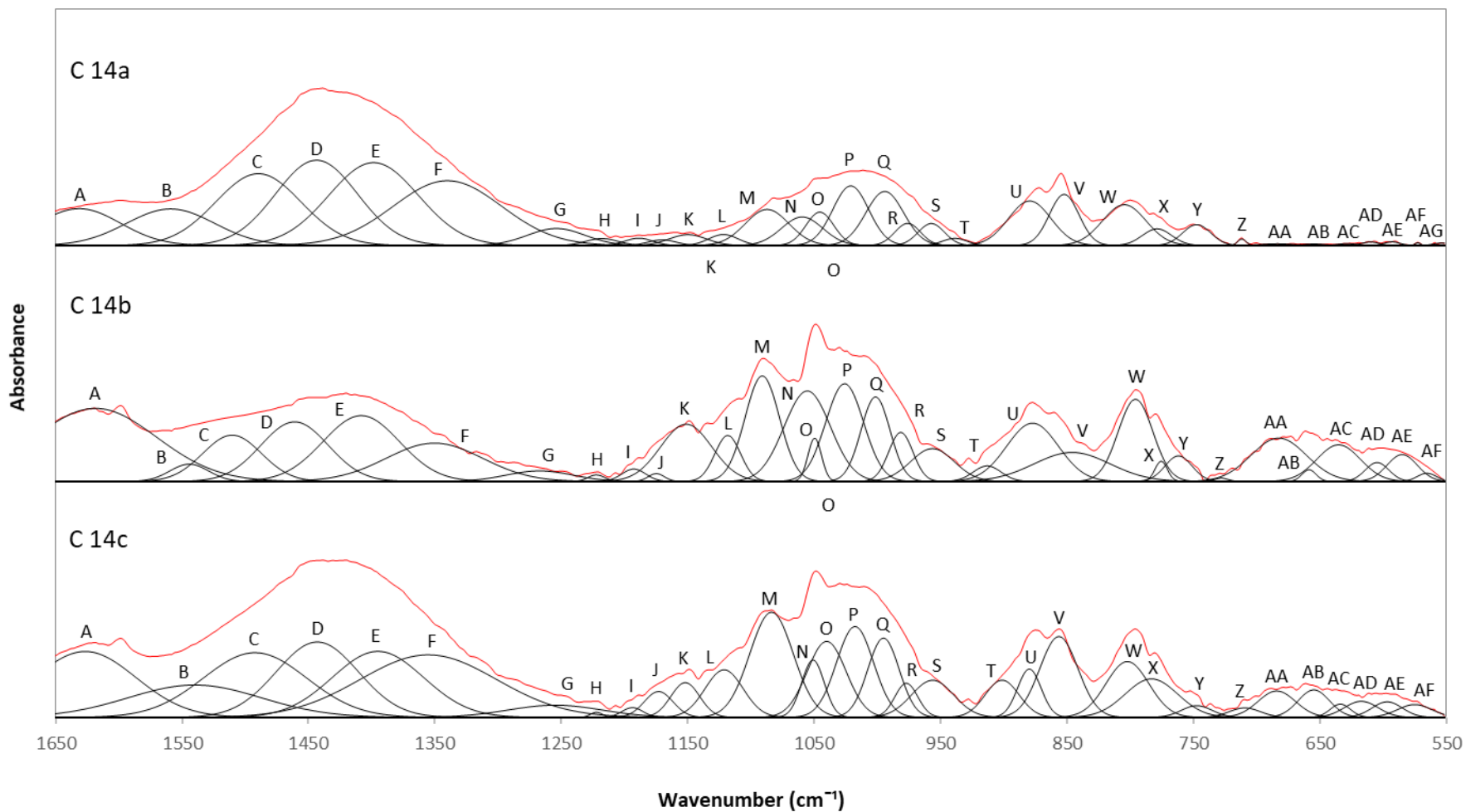


Figure 9-1 FTIR spectra and deconvoluted peaks for corrosion samples C 14a, C 14b, and C 14c

Table 9-1 Deconvoluted FTIR peaks (A to O) with wavenumbers and corresponding minerals, compounds, and chemical species for corrosion samples C 14a, C 14b, and C 14c

Peak reference		A	B	C	D	E	F	G	H	I	J	K	L	M	N	O	P	Q
Mineral/ compound / chemical species		H ₂ O	GR(SO ₄ ²⁻) GR(CO ₃ ²⁻) GR(Cl ⁻)	NaHCO ₃	Calcite Aragonite	α-FeOOH β-FeOOH GR(CO ₃ ²⁻) FeCO ₃ Calcite Mg(OH) ₂	Fe(OH) ₂ GR(CO ₃ ²⁻) NaHCO ₂	SO ₄ ²⁻	SO ₃ ²⁻	GR(SO ₄ ²⁻) SO ₄ ²⁻	γ-FeOOH	GR(SO ₄ ²⁻)	β-FeOOH δ-FeOOH S ₂ O ₃ ²⁻ Kaolinite	GR(SO ₄ ²⁻) SO ₄ ²⁻ SO ₃ ²⁻ SiO ₂ Aragonite	Fe(OH) ₂ SO ₄ ²⁻ Fe ₅ HO ₆ .4H ₂ O SiO ₂	SO ₃ ²⁻ Kaolinite	γ-FeOOH SO ₃ ²⁻ NaHCO ₃	SO ₄ ²⁻ S ₂ O ₃ ²⁻ Kaolinite
Sample reference	Height above sediment bed																	
C 14a	1.0 m	1631	1559	1489	1443	1398	1340	1254	1217	1188	1170	1150	1121	1087	1059	1045	1021	994
C 14b		1618	1544	1510	1461	1408	1350	1267	1222	1192	1174	1151	1118	1091	1055	1049	1026	1001
C 14c		1626	1540	1492	1443	1395	1355	1255	1222	1193	1173	1152	1121	1083	1051	1040	1017	995

Table 9-2 Deconvoluted FTIR peaks (P to AD) with wavenumbers and corresponding minerals, compounds, and chemical species for corrosion samples C 14a, C 14b, and C 14c

Peak reference		R	S	T	U	V	W	X	Y	Z	AA	AB	AC	AD	AE	AF	AG
Mineral/ compound / chemical species		δ-FeOOH Fe(OH) ₂	Fe(OH) ₂ S ₂ O ₃ ²⁻ Kaolinite	SO ₃ ²⁻ Illite Kaolinite	α-FeOOH GR(SO ₄ ²⁻) Calcite	β-FeOOH Fe(OH) ₂ GR(CO ₃ ²⁻) FeCO ₃ Aragonite	α-FeOOH GR(Cl ⁻) SiO ₂ Illite	GR(SO ₄ ²⁻) GR(CO ₃ ²⁻) SiO ₂ Kaolinite	γ-FeOOH Illite Kaolinite	Fe ₅ HO ₆ .4H ₂ O FeCO ₃ Calcite Aragonite Illite Kaolinite	Fe ₃ O ₄ γ-Fe ₂ O ₃ β-FeOOH GR(Cl ⁻)	GR(SO ₄ ²⁻)	Fe ₃ O ₄ α-FeOOH	α-FeOOH γ-FeOOH GR(SO ₄ ²⁻)	Fe ₃ O ₄	α-Fe ₂ O ₃ Fe ₅ HO ₆ .4H ₂ O Mg(OH) ₂	γ-Fe ₂ O ₃
Sample reference	Height above sediment bed																
C 14a	1.0 m	976	957	938	879	852	804	778	747	711	683	654	628	610	593	572	553
C 14b		981	956	913	877	846	795	775	761	728	682	658	635	604	585	565	
C 14c		977	956	901	879	856	802	783	747	709	684	654	633	617	596	575	

9.2 Vertical profile corrosion

The spectra obtained from Fourier-transform infrared (FTIR) analysis (section 3.2.6) of fifteen corrosion samples (C 01 to C 15), from positions between 6.2 m and 0.6 m above the sediment bed, are displayed along with corresponding deconvoluted peaks as combined plots in Figure 9-3 to Figure 9-6. Deconvolution using PeakFit software achieved a coefficient of determination of $R^2 > 0.99$ for each spectrum. The correlation of identified peaks with minerals, compounds, and chemical species (Appendix H) are summarised in Table 9-3 and Table 9-4, and the modes associated with each are described in Section 9.1.

Analysis indicated that several peaks were common to all samples. These were Peaks A, C, D, F, P, U, V, W, X, Y, AC, AD, and AE. Three of these correspond with a single mineral or chemical compound: Peak A corresponds with surface adsorbed water; Peak C is consistent with nahcolite (NaHCO_3). Peak D corresponds with two minerals of calcium carbonate: calcite and aragonite.

The FTIR analysis of C 01 indicates that corrosion products present are goethite (α - FeOOH), lepidocrocite (γ - FeOOH), magnetite (Fe_3O_4), with hematite (Fe_2O_3). Goethite vibrational modes are visible at 1386 cm^{-1} (Peak E), 882 cm^{-1} (Peak U), 803 cm^{-1} (Peak W), 631 cm^{-1} (Peak AC), and 617 cm^{-1} (Peak AD). Magnetite is indicated by peaks at 631 cm^{-1} (Peak AC), 592 cm^{-1} (Peak AE), and 690 cm^{-1} (Peak AA). The lack of a peak around 1170 cm^{-1} (Peak J) suggest that lepidocrocite is not present, though other modes for this mineral are consistent with Peaks P (1026 cm^{-1}), Y (748 cm^{-1}), and AD (617 cm^{-1}). Due to the relatively low intensity for the 1170 cm^{-1} peak compared with the mineral's characteristic peak around 1020 cm^{-1} (Cui et al., 2013) and the significant width of Peak L for this sample, the Fe-O-H bending mode is probably present but not resolved in this analysis. Ferrihydrite is indicated alongside silica at 1118 cm^{-1} , at 573 cm^{-1} (Peak AF) with hematite, and 708 cm^{-1} (Peak Z). Peaks consistent with akaganeite occur at 1386 cm^{-1} (Peak E), 1118 cm^{-1} (Peak L), 837 cm^{-1} (Peak V) and 690 cm^{-1} (Peak AA); however, one Fe-O stretching mode for this mineral are not resolved. A visual examination of the plot indicates that the expected wavenumbers for this mode are included within a broad adjacent peak (Peak AC). The clays illite and kaolinite are indicated by Peaks L, Q, W,

X, Y, and Z. The characteristic peak for green rusts is not discerned at 1560 to 1540 cm^{-1} indicating an absence of the three types of green rust reviewed. The uncertainty associated with akaganeite in this sample is increased by the absence of chloride green rust as this is a precursor mineral to the oxyhydroxide (Figure 2-5). Alternatively, if akaganeite is present and chloride green rust is found to be absent, a fast oxidation pathway from ferrous hydroxide to akaganeite is implied. Lepidocrocite can be formed directly from ferrous hydroxide or via the sulfate green rust route (Section 2.5.3) therefore the lack of this latter mineral does not conflict with the presence of the sulfate green rust. Similarly, the absence of carbonate green rust also does not preclude the formation of ferrihydrite which can form via an oxidation pathways from ferrous hydroxide in the presence of silicon, chromium, or calcium. According to the corrosion model discussed previously, ferrous hydroxide is the first corrosion product formed. Peaks F, N, and V are consistent with its presence, but concordant peaks between 980 cm^{-1} and 955 cm^{-1} are absent. Applying the same visual approach to the spectrum as used for akaganeite, a variation can be observed in this region which could be interpreted as a relevant peak, though this would require further verification. The defining peaks for sulfate and sulfite (G and H) was not discerned during the analysis. The region of the spectrum corresponding with these peaks is between the A to F peak and L to Q clusters. As discussed above the width of Peak L could be masking certain modes. Thiosulfate ions are indicated by Peaks L, Q, but as it forms from reduced sulfur species and oxidizes to form sulfate, confidence of its occurrence in this sample is dependent upon the presence of sulfate.

Sample C 02 exhibits peaks consistent with magnetite (Peak AC and AE), hematite (Peak AF), goethite (Peaks E, U, W, and AC), feroxyhyte (Peaks L and R), akaganeite (Peaks E, L, V, AA, and AB), ferrihydrite (Peaks N, Z, and AF), ferrous hydroxide (Peaks F, N, R, S, and V), siderite (Peaks E, V, and Z), silica, illite, and kaolinite, in addition to calcite, nahcolite, and adsorbed water molecules, found in all fifteen samples. The absence of a peak around 560 cm^{-1} indicating maghemite is discussed in Section 9.1. Lepidocrocite is indicated by Peaks P, Y, and AD. As with sample C 01 a peak at 1170 cm^{-1} was not recognised during the analysis; however, a visual examination of the spectrum indicates a fluctuation at approximately this value. This minor peak is separate from the adjacent peak L and could be indicative of the absent mode. Three types of green rusts are indicated by the peak at 1550 cm^{-1} . Peaks I and K were not resolved, indicating the absence of

sulfate green rust. The spectrum is consistent with both chloride and carbonate forms of this mineral. The occurrence of ferrihydrite and akaganeite would be consistent with the presence of these forms of green rust, respectively. No peaks were identified between 1260 cm^{-1} and 1180 cm^{-1} , indicating that sulfate and sulfite ions were not present in detectable concentrations.

Sample C 03 correlates closely with C 02, possessing peaks that correspond to hematite, goethite, ferrosulfate, akaganeite, ferrihydrite, ferrous hydroxide, and siderite. Peak J (1172 cm^{-1}) is discerned and so the presence of lepidocrocite is indicated. Peaks indicating non-sulfate ions and sulfite ions are missing from the region between 1260 cm^{-1} and 1180 cm^{-1} . The peak pattern for sulfate green rust is uncertain for this sample as a S-O stretching mode should be evident at approximately 1185 cm^{-1} but is absent. The spectrum does possess a unique $\text{GR}(\text{SO}_4^{2-})$ peak at 1148 cm^{-1} and all other peaks that correspond with this mineral are present, however. As discussed previously, Peak I could be masked due to the width of the adjacent peak (Peak J) and the low level of absorbance at this location.

Analysis of the fourth samples spectrum (Sample C 04) matches that of C 03, except that unique and shared peaks for both non-green rust sulfate and sulfate green rust are present. Peaks corresponding with sulfite (1210 cm^{-1} and 910 cm^{-1}) are absent, however.

The FTIR spectrum for sample C 05 displays a full set of peaks apart from Peaks S and AG. All corrosion products common to NWC and MIC, apart from ferrous hydroxide, and maghemite (Peak AG), are consistent with the results obtained. The absence of a peak at approximately 950 cm^{-1} indicated that Fe-O-H bending modes assigned to ferrous hydroxide was not detected. In addition, this suggests modes associated with thiosulfate and kaolinite were also absent. Each of the three green rusts considered previously are indicated, as are non-green rust sulfate ions.

The profile of the FTIR spectrum for Sample C 06 deviates from previous samples considerably. The region mainly associated with metal-oxygen-hydrogen bending and carbon-oxygen stretching modes (Section 9.1), between 950 cm^{-1} and 700 cm^{-1} , dominate the plot. This suggests the presence of metal oxyhydroxides, green rusts, illite and kaolinite clays. The iron-oxygen stretch region (approximately 700 to 550 cm^{-1}) is also well-developed suggesting magnetite, hematite, goethite, akaganeite, lepidocrocite,

ferrihydrate, and chloride green rust. The region associated with oxygen-sulfur-oxygen stretches (between approximately 1250 cm^{-1} and 950 cm^{-1}) is mostly absent, with only Peak O and P being resolved. As modes associated with sulfate, sulfite, and thiosulfate are not resolved, these species are low in concentration or absent from this sample. The absence of higher energy O-H bending modes of goethite, akaganeite, lepidocrocite, and ferrihydrate in this region, despite consistent peaks between 950 cm^{-1} and 550 cm^{-1} suggest these former modes are less significant in determining the presence of these oxyhydroxides.

Sample C 07 is notable as it is the first to exhibit a peak that corresponds with maghemite. All other corrosion iron oxide, hydroxide, and oxyhydroxide compound and minerals are indicated. Peak J is broad and is centred at 1163 cm^{-1} , which is the lowest wavenumber for this peak amongst these samples. It is possible therefore that Peak J is obscuring the unique sulfate green rust peak (K). Also, examination of the spectrum reveals an apparent minor peak at 1110 cm^{-1} that was not resolved during the PeakFit analysis. A peak at this location would account for missing modes of akaganeite, ferrihydrite, thiosulfate, and kaolinite.

Analysis of sample C 08 indicates peaks consistent with minerals and compounds found in both NWC and MIC. Peaks AG (Fe-O stretch mode of maghemite), O and T (stretching modes of sulfite ions and kaolinite) are not present, each indicating the absence of the respective mineral or chemical species. The proximity of Peak AG to the lower wavenumber boundary and the likelihood of this stretching mode occurring outside the range of the equipment used has been discussed previously.

Corrosion samples C 09, C 10, and C 14 display an identical array of peaks. Each spectrum is consistent with NWC and MIC-related iron minerals and compounds, except for maghemite (Peak AG). The peaks also support the occurrence of illite and kaolinite clays, as well as sulfate and more reduced sulfur species. Similarly, analysis of sample C 11 indicates all sulfur species considered could be present. Peaks U, V, W, and X are prominent features that correlate with vibrational modes of green rusts, clays, and Fe-O-H bending modes of iron oxyhydroxides, whereas, the Fe-O stretch region (700 to 550 cm^{-1}) displays low absorbance throughout, and Peaks AB and AF are not resolved. The peak intensities in this latter region may suggest low concentrations of iron oxide and

oxyhydroxide minerals, and that the region between 900 cm^{-1} and 750 cm^{-1} is dominated by green rust and clay minerals.

PeakFit analysis of samples C 12 and C 13, identifies peaks corresponding with all specified minerals and compounds, including maghemite (Peak AG), as well as sulfate, sulfite, and thiosulfate. Sample C15 has a pattern of deconvoluted peaks that run in a continuous sequence up to Peak AE. The spectrum is apparently flat after this, indicating that Fe-O stretching modes of hematite, maghemite, and ferrihydrite are absent.

The FTIR analysis of the fifteen samples indicated the composition of the corrosion varied with vertical location. The patterns were complex however, and as described in the previous section; multiple assignments could be made for many of the peaks. The most consistent patterns emerged between 3.4 m and 0.6 m from the sediment bed (C 08 to C 15) where almost all peaks were observed. The missing peaks mostly occurred towards the lowest measurable value for the apparatus (550 cm^{-1}), which as discussed previously tended to suffer from data clipping. These eight samples matched the results obtained from three low tide samples analysed in Section 9.1 closely, and displayed peaks corresponding with minerals common to both MIC and NWC: ferrous hydroxide, sulfate green rust, ferrihydrite, lepidocrocite, goethite, maghemite, and magnetite. These samples contrasted with those from 6.2 m to 3.8 m (C 01 to C 07), which generally displayed fewer peaks, especially those corresponding with sulfur species. This suggests conditions were either unsuitable for sulfur-reducing prokaryotes or their activity was too low to allow accumulation of measurable levels of reduced-sulfur species. Green rusts were indicated in six of the seven of these samples, but as the peaks for sulfate green rust were not present in three of these it suggests that chloride green rust or carbonate green rust are the most dominant form at the higher positions. Samples C 01 (6.2 m) and C 06 (4.2 m) both displayed the fewest peaks, though their profiles were still largely consistent with corrosion minerals listed above. Neither possessed peaks unique to sulfate green rust, indeed sample C 01 lacked all green rust peaks, and main ferrous hydroxide peaks were also absent. Sample C 06 lies appears to be anomalous as it was extracted towards the centre of the samples, but its FTIR profile most closely reflects that of the sample taken from the top of the piling. The structure of these two samples may be explainable once their position on the piling is understood relative to the tidal cycle of the immediate marine environment.

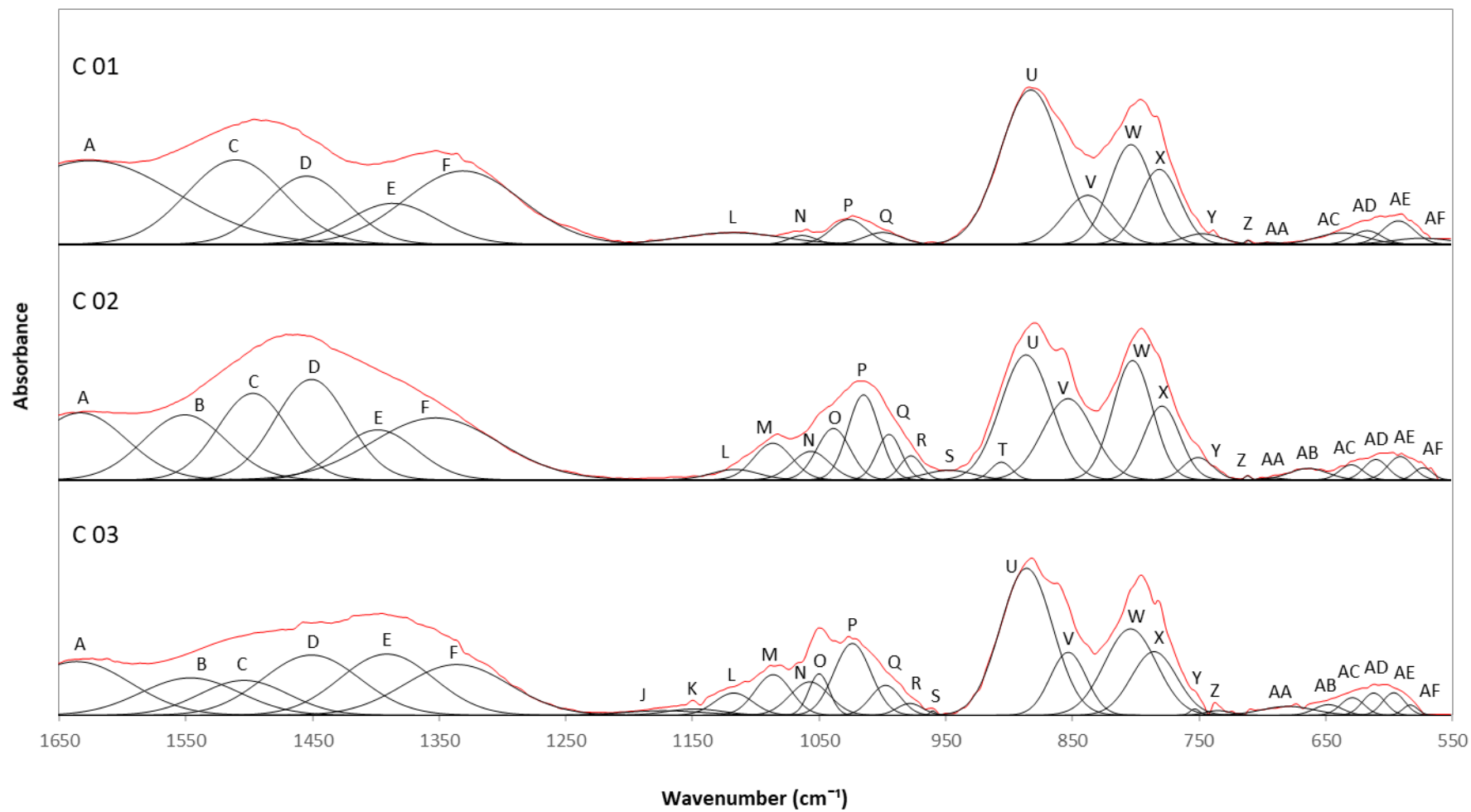


Figure 9-2 FTIR spectra and deconvoluted peaks for corrosion samples C 01, C 02, and C 03

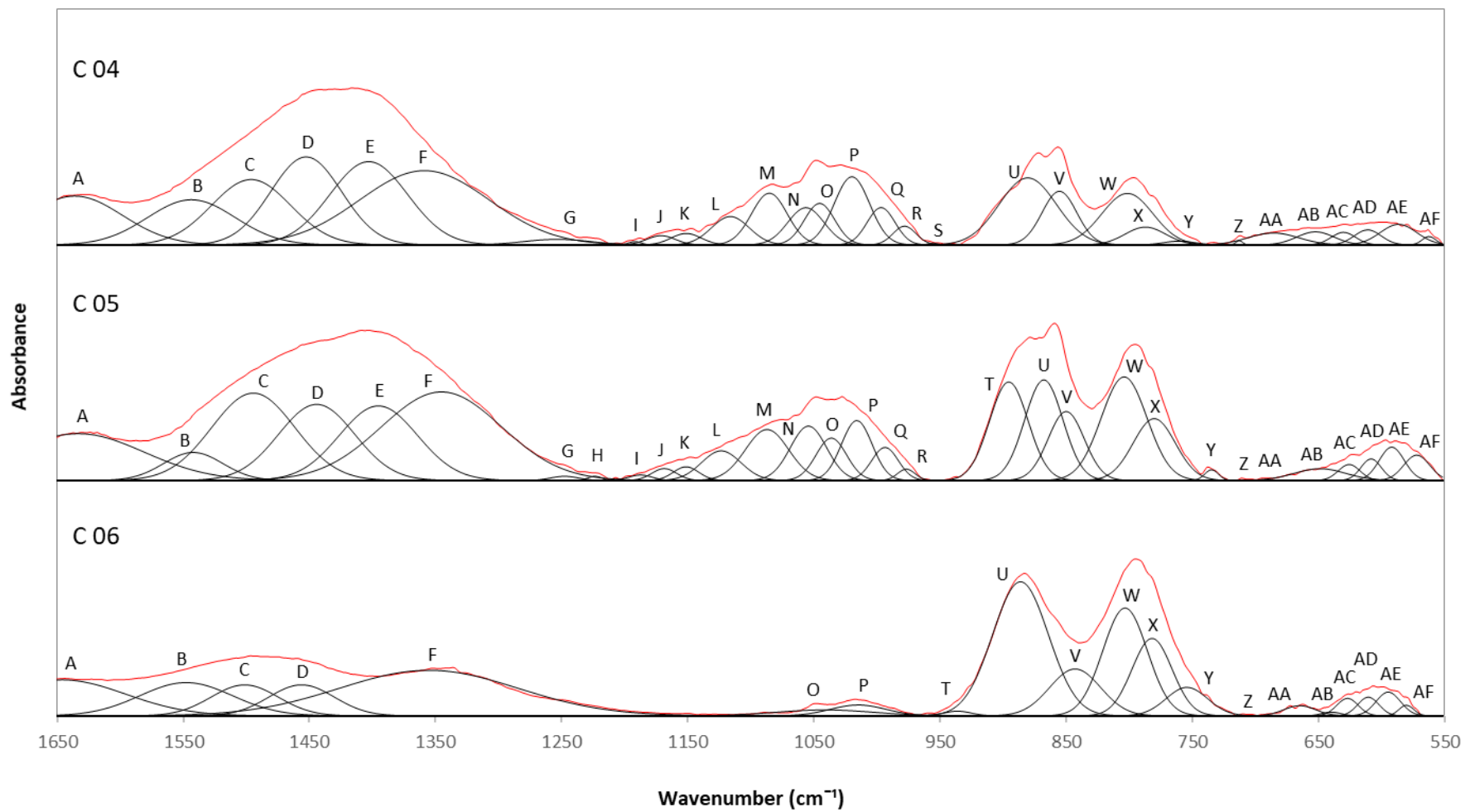


Figure 9-3 FTIR spectra and deconvoluted peaks for corrosion samples C 04, C 05, and C 06

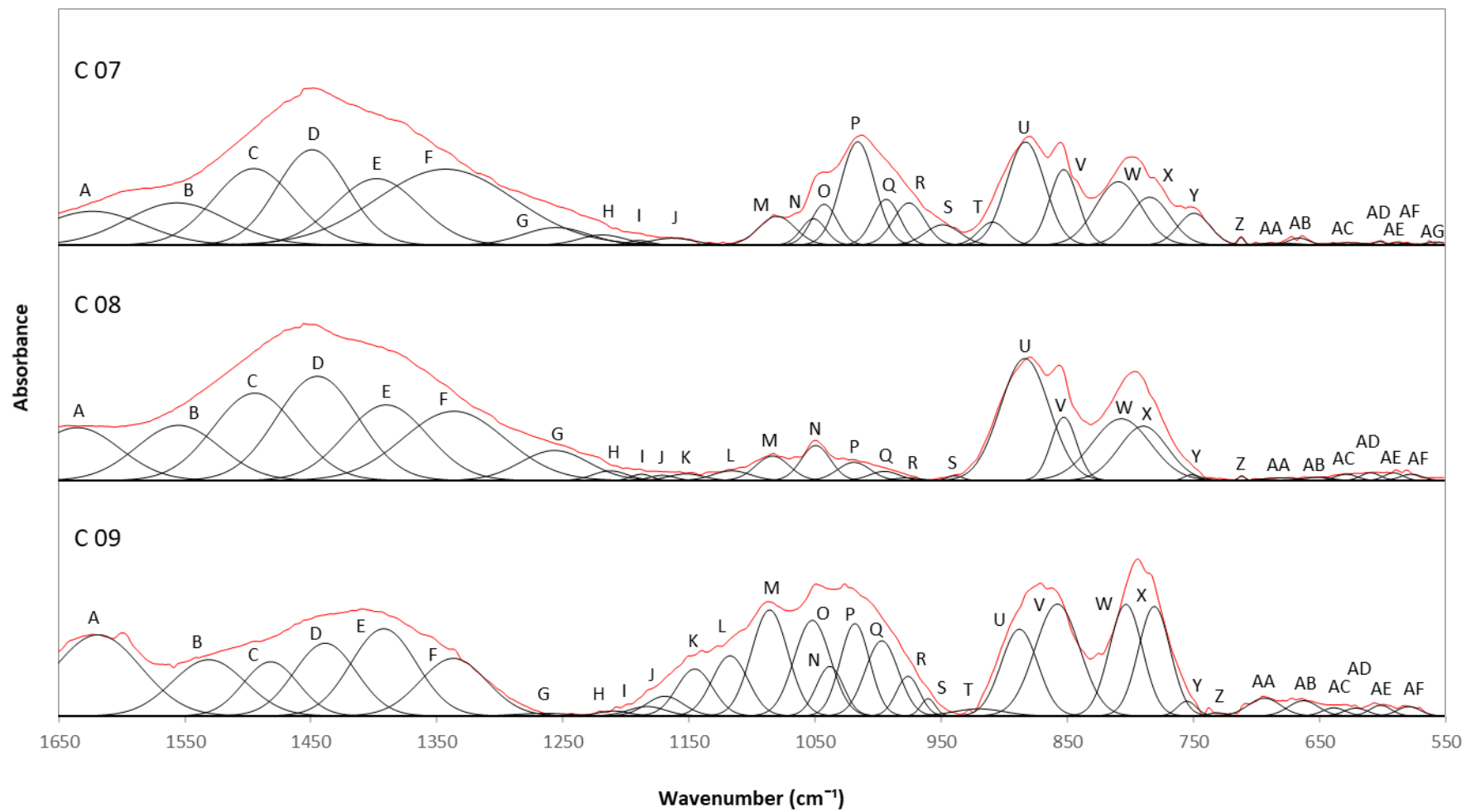


Figure 9-4 FTIR spectra and deconvoluted peaks for corrosion samples C 07, C 08, and C 09

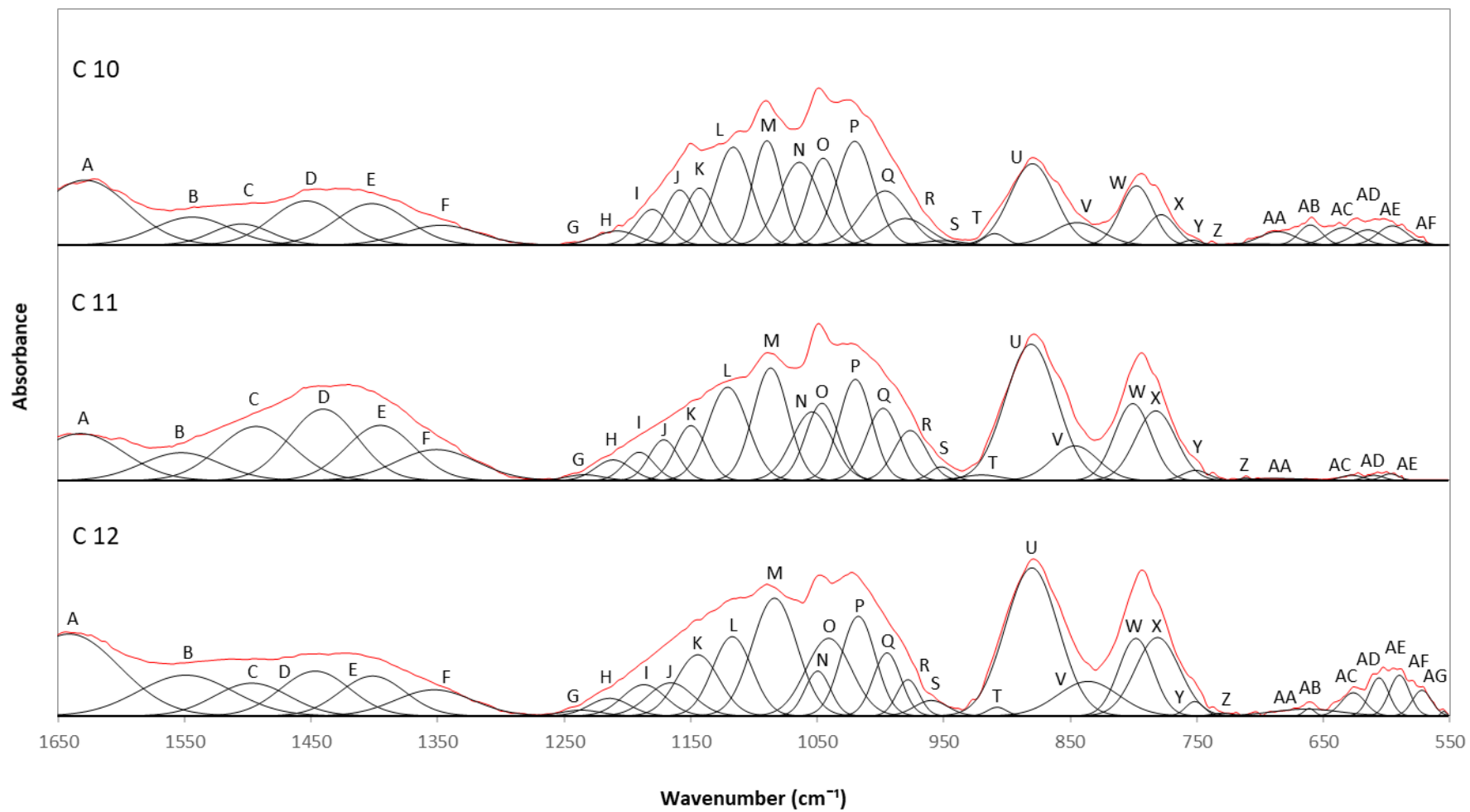


Figure 9-5 FTIR spectra and deconvoluted peaks for corrosion samples C 10, C 11, and C 12

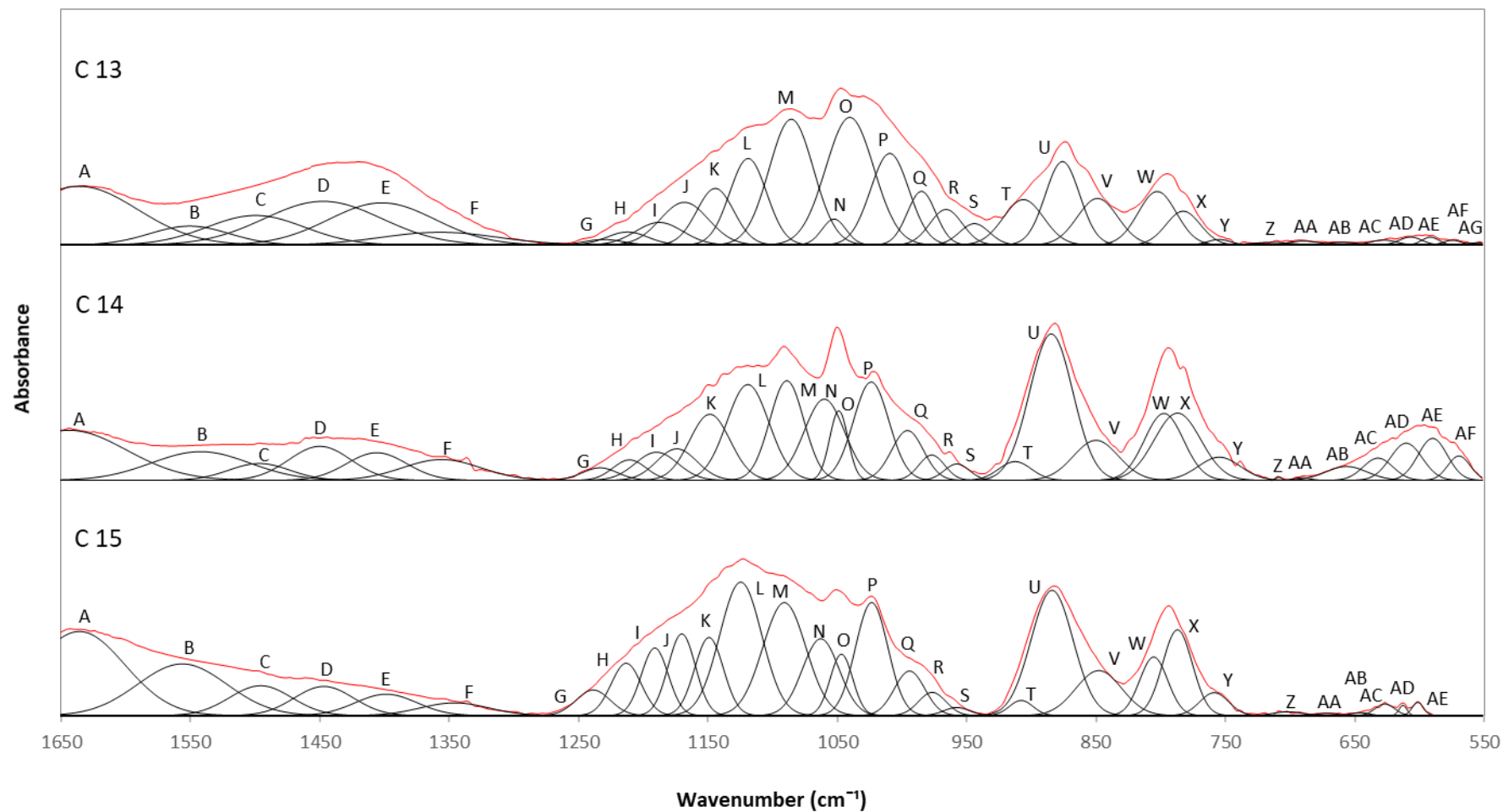


Figure 9-6 FTIR spectra and deconvoluted peaks for corrosion samples C 13, C 14, and C 15

Table 9-3 Deconvoluted FTIR peaks (A to O) with wavenumbers and corresponding minerals, compounds, and chemical species for corrosion samples C 01 to C 15

Peak reference		A	B	C	D	E	F	G	H	I	J	K	L	M	N	O	P	Q
Sample reference	Height above sediment bed	Mineral/compound / chemical species																
		H ₂ O	GR(SO ₄ ²⁻) GR(CO ₃ ²⁻) GR(Cl)	NaHCO ₃	Calcite Aragonite	α-FeOOH β-FeOOH GR(CO ₃ ²⁻) FeCO ₃ Calcite Mg(OH) ₂	Fe(OH) ₂ GR(CO ₃ ²⁻) NaHCO ₂	SO ₄ ²⁻	SO ₃ ²⁻	GR(SO ₄ ²⁻) SO ₄ ²⁻	γ-FeOOH	GR(SO ₄ ²⁻)	β-FeOOH δ-FeOOH S ₂ O ₃ ²⁻ Kaolinite	GR(SO ₄ ²⁻) SO ₄ ²⁻ SO ₃ ²⁻ SiO ₂ Aragonite	Fe(OH) ₂ SO ₄ ²⁻ Fe ₅ HO ₆ ·4H ₂ O SiO ₂	SO ₃ ²⁻ Kaolinite	γ-FeOOH SO ₃ ²⁻ NaHCO ₃	SO ₄ ²⁻ S ₂ O ₃ ²⁻ Kaolinite
C 01	6.2 m	1625		1510	1454	1386	1331						1118		1063		1026	999
C 02	5.8 m	1633	1550	1497	1450	1398	1353						1116	1086	1056	1038	1014	994
C 03	5.4 m	1636	1546	1504	1450	1391	1336				1172	1148	1117	1086	1057	1050	1023	997
C 04	5.0 m	1636	1543	1496	1452	1403	1358	1253		1191	1171	1151	1116	1085	1056	1045	1019	996
C 05	4.6 m	1633	1540	1494	1444	1395	1345	1247	1230	1187	1168	1151	1123	1087	1054	1036	1016	993
C 06	4.2 m	1646	1547	1501	1456		1355									1041	1014	
C 07	3.8 m	1623	1556	1495	1449	1398	1343	1255	1218	1189	1163			1080	1051	1043	1016	993
C 08	3.4 m	1635	1555	1494	1444	1390	1336	1256	1212	1187	1171	1152	1116	1083	1052		1019	995
C 09	3.0 m	1618	1531	1481	1438	1392	1337	1255	1209	1183	1169	1143	1117	1086	1052	1038	1018	997
C 10	2.6 m	1628	1544	1505	1453	1402	1347	1243	1208	1180	1158	1142	1116	1089	1064	1045	1020	996
C 11	2.2 m	1632	1552	1493	1440	1395	1351	1233	1211	1190	1171	1149	1120	1086	1054	1046	1019	998
C 12	1.8 m	1641	1549	1496	1446	1401	1352	1236	1214	1187	1165	1144	1117	1083	1049	1041	1017	994
C 13	1.4 m	1636	1550	1499	1447	1401	1357	1230	1212	1187	1168	1144	1118	1085	1052	1040	1009	984
C 14	1.0 m	1643	1542	1496	1449	1405	1355	1233	1210	1189	1174	1148	1119	1089	1060	1048	1023	995
C 15	0.6 m	1635	1556	1495	1446	1398	1345	1238	1213	1191	1170	1149	1124	1090	1062	1046	1023	994

Table 9-4 Deconvoluted FTIR peaks (P to AD) with wavenumbers and corresponding minerals, compounds, and chemical species for corrosion samples C 01 to C 15

Peak reference		R	S	T	U	V	W	X	Y	Z	AA	AB	AC	AD	AE	AF	AG
Sample reference	Height above sediment bed	δ-FeOOH Fe(OH) ₂	Fe(OH) ₂ S ₂ O ₃ ²⁻ Kaolinite	SO ₃ ²⁻ Illite Kaolinite	α-FeOOH GR(SO ₄ ²⁻) Calcite	β-FeOOH Fe(OH) ₂ GR(CO ₃ ²⁻) FeCO ₃ Aragonite	α-FeOOH GR(Cl) SiO ₂ Illite	GR(SO ₄ ²⁻) GR(CO ₃ ²⁻) SiO ₂ Kaolinite	γ-FeOOH Illite Kaolinite	Fe ₅ HO ₆ .4H ₂ O FeCO ₃ Calcite Aragonite Illite Kaolinite	Fe ₃ O ₄ γ-Fe ₂ O ₃ β-FeOOH GR(Cl)	GR(SO ₄ ²⁻) Fe ₃ O ₄ α-FeOOH	Fe ₃ O ₄ α-FeOOH	α-FeOOH γ-FeOOH GR(SO ₄ ²⁻)	Fe ₃ O ₄	α-Fe ₂ O ₃ Fe ₅ HO ₆ .4H ₂ O Mg(OH) ₂	γ-Fe ₂ O ₃
		C 01	6.2 m				882	837	803	781	748	708	690		631	617	592
C 02	5.8 m	977	947	906	886	853	802	779	750	711	692	663	629	610	591	573	
C 03	5.4 m	978	960		886	853	804	785	753	735	679	647	629	612	596	583	
C 04	5.0 m	978	955		880	855	801	787	760	712	685	652	630	611	586	562	
C 05	4.6 m	976		895	867	850	804	780	734	703	684	648	625	608	591	572	
C 06	4.2 m			936	886	843	803	782	754	702	664	639	627	610	594	580	
C 07	3.8 m	975	948	909	883	852	809	784	749	712	683	666	627	602	588	581	558
C 08	3.4 m	976	939		883	852	807	789	751	711	681	651	628	609	591	577	
C 09	3.0 m	976	960	919	888	857	803	781	755	731	693	652	638	621	601	579	
C 10	2.6 m	980	950	909	888	844	797	778	753	706	686	660	634	615	595	577	
C 11	2.2 m	976	952	920	881	846	800	782	751	711	685		628	610	597		
C 12	1.8 m	978	960	907	880	836	798	781	751	730	674	661	626	606	590	572	555
C 13	1.4 m	965	943	906	875	848	802	782	754	714	689	658	627	606	591	574	552
C 14	1.0 m	976	957	912	884	850	797	787	754	708	690	656	632	610	589	569	
C 15	0.6 m	976	957	980	884	847	805	787	758	701	651	645	626	612	601		

9.3 Summary

Fourier-transform infrared analysis allowed identification of several corrosion products within the samples. These were consistent with previous findings in microbially influenced corrosion and normal water corrosion formations. The assignment of several peaks to multiple minerals prevented unambiguous identification of many of those present, and the technique mostly provided a series of possible compositions especially in the lower-level samples. The technique allowed sulfate and two reduced sulfur species to be identified, mainly in lower-level samples, and suggested a change in corrosion composition occurred from approximately 3.4 m above the sediment bed level downwards. To explore the significance of this and to reduce ambiguities in the interpretation of minerals present, these data need to be cross referenced with other data analysed in this study (cf. Chapter 4 and Chapter 8). It is of note also, that the presence of magnetite (Fe_3O_4) was unambiguously determined using this technique; this contrasts with XRD analysis (Section 8.2). The analysis also revealed the presence of seawater infiltration and evidence of clay mineral deposition within the corrosion formations.

Chapter 10 Project synthesis

The synthesis of the various findings of this project falls into two sections. The first is the relationship between marine sediment, seawater, and corrosion of carbon steel piling; the second is the relationship between the corrosion mineralogy and microbial diversity relative to vertical location on steel piling.

10.1 Model for colonisation of carbon steel piling by microorganisms

This section outlines a conceptual model for the colonisation of the carbon steel piling at the Dredger Berth in Shoreham Port by microbial life forms that are responsible for driving microbially influenced corrosion. The model was based on comparative analyses of low tide corrosion, marine sediment, and seawater samples, and local seawater conditions.

The first data relevant to the model was the correlation of specific sample types into groups based on microbial community diversity. The result of the diversity analysis (Section 6.1) carried out on nine samples are summarised in Figure 10-1. The samples comprised three low tide level corrosion samples (C 14a, 14b, and 14c); three marine sediment samples (SED 01, 02, and 03); and three seawater samples (SW 01, 02, and 03). As described previously, three widely utilised measures of diversity were adopted: Simpson Index (1-D); Shannon-Wiener Index; and Shannon evenness. These were applied to the fluorescence data obtained from GeoChip analysis of environmental samples. A fourth measure of diversity derived from fluorescence levels of MIC-related functional gene probes obtained through GeoChip microarray analysis (Section 6.2) was also posited; to allow comparison with the former three techniques, these data were condensed to provide a single median fluorescence value for each sample.

As discussed in Section 6.1, the Simpson Index, Shannon-Wiener, and Shannon evenness analyses indicate a common pattern exists between the environmental samples. The condensed Geochip microarray data supported the observed trend also (Section 6.2). Microbial communities isolated from seawater samples were consistently the most diverse environmental group, with corrosion and sediment samples forming mixed

clusters of lower diversity. The lower diversity of these types of samples and the variability of the diversity order between corrosion and marine sediment suggested a more specialised microbiota within these environments as well as a closer link in the composition of the microbial communities (Morris et al., 2014, Liduino et al., 2019). This is consistent with diversity analysis of MIC-associated microbiota carried out by Liduino et al. (2019) in which communities in freely-mixing marine environments displayed greater diversity than more enclosed MIC biofilms. This contrasts however, with estimates of microbial diversity carried out by Zhang et al. (2019) in which seawater samples and marine biofilms were compared. Their findings indicated a greater microbial biodiversity existed in attached biofilms compared to adjacent seawater; the biofilms investigated were not derived from MIC formations however, so their findings do not contradict the diversity sequence produced by this study. Walsh et al. (2016) noted the consistently greater bacterial diversity in seawater compared with marine sediment, and demonstrated the lowest microbial richness and evenness occurred in environments of low oxygen concentration. This same reduction in microbial diversity with depth was also noted by Varliero et al. (2019). This latter point is consistent with the marine sediment analysis detailed in Chapter 5, wherein increasingly anoxic conditions were observed below the surface layer, and the correspondingly lower marine sediment diversities observed in Figure 10-1.

	Simpson Index (1-D)	Shannon-Wiener Index (H)	Shannon evenness (J)	Functional gene fluorescence
Increasing diversity ↑	SW 03	SW 01	SED 02	SW 02
	SW 01	SW 03	SW 01	SW 03
	SED 02	SW 02	SW 02	SW 01
	SW 02	SED 03	SED 03	C 14c
	SED 03	SED 02	SW 03	SED 01
	C 14a	C 14c	C 14c	C 14b
	C 14c	C 14a	SED 01	C 14a
	C 14b	C 14b	C 14b	SED 02
	SED 01	SED 01	C 14a	SED 03

Figure 10-1 Diversity analysis summary for nine environmental samples ordered by decreasing diversity

The second data used to support the colonisation model were the gene composition similarity data detailed in Section 6.3, which cover fifteen functional genes linked to activity of MIC-related microbiota (Section 2.3). The same samples used for the nine samples used for the diversity analysis (C 14a, SED 01, SW 01 etc.) were utilised for this section also. The dendrogram data from Section 6.3 were condensed to clusters of 75% and above to highlight major trends and plotted as a table in Figure 10-2. Nb. Each letter and number combination denoted a particular gene and 75%+ cluster and had no significance other than to provide clarity in interpreting the Figure. Six of the analysed genes were unable to provide meaningful data for this analysis due to all samples displaying a similarity of greater than 85%; these were *aprA*; *amoA*; *narG*, *nirK*, *iro*, and *assa*. The reason for the high degree of similarity for these genes was uncertain and may have been indicative of either an environmental homogeneity, or a limitation of GeoChip: *aprA*, *soxB*, and *assa* gene probe clusters numbered 52, 21, and 16 respectively but *narG*, *nirK*, and *iro* possessed probe clusters similar in number to those genes that differentiated corrosion, sediment, and seawater. As *aprA* and *aprB* genes work in unison to produce the *aprA* and *aprB* subunits of the adenosine 5'phosphosulfate reductase complex respectively (Barton and Hamilton, 2007, Dong et al., 2017) the genetic similarity of the sulfide reducing community within the samples could still be correlated. Similarly, *narG* and *nirK* function in unison with *napA* and *nirS* genes respectively (Smith et al., 2007, Reji et al., 2019) so the corresponding nitrate and nitrite reductase community correlation could be intimated. The *amoA*, *iro*, and *assa* genes have no similar analogue, however, so could not be clearly correlated.

The clustering patterns of genes associated with sulfate-reducing prokaryotes (SRP) (*aprA*, *dsrA*, and *dsrB*) displayed a linkage between corrosion and marine sediment; this microbial group were anticipated due to the increasingly anoxic conditions revealed during sediment bed analysis (Section 5.1). The sulfur-oxidizing gene (*soxB*) for the sediment samples displayed an almost equal split between corrosion and seawater, but no correlation between seawater and corrosion. This is indicative of a more diverse SOB community with the possibility of specific genera favouring conditions within MIC formations (Jørgensen et al., 2019). Nitrate-reducers, represented by *napA*, *nirS*, and *nrfA* genes, also displayed a clear correlation between corrosion and sediment; the seawater samples forming separate clusters. The clustering for the *fhfs* gene, associated with

acetogens, displayed a significant pattern different from trends observed to this point: strong linkages with corrosion and seawater but no strong correlation with sediment samples. Similarly, the methanogenic community (*mcrA*) within the samples show no strong linkage between corrosion and sediment. This suggests that the main vector for inoculation of MIC formations by acetogenic prokaryotes and methanogenic archaea is the seawater column. This result was consistent with observations of transportation of these types of microbes on suspended solids within the water column (Marty, 1993, van der Maarel et al., 1999).

In addition to the above, the microbiological study of low tide level corrosion, marine sediment, and seawater were further investigated in Section 7.16.1 of Chapter 7. The study was primarily intended to compare the efficacy of high-resolution melt (HRM) compared with the more established technique of denaturing gradient gel electrophoresis (DGGE) when assessing environmental samples. The chapter focused on the diversity of the *dsrB* gene, the data was therefore in line with that obtained from similarity analysis of the GeoChip data (Figure 10-2) and can therefore be plotted in the same summarised format; as shown in Figure 10-3. The samples used were unique to these sections and comprised four low tide level corrosion samples (C 14d, 14e, 14f, and 14g); four marine sediment samples (SED 04, 05, 06, and 07); and four seawater samples (SW 04, 05, 06, and 07). The results further strengthened the correlation of corrosion samples as possessing a unique microbiota with links to the adjacent marine sediment, and the separation of seawater samples into a distinct group. The correlation of a single gene (*dsrB*) did not provide the depth of analysis obtained from GeoChip microarray data, though the same overall trends was observed from the samples. However, this technique is far less expensive than GeoChip and, as discussed in Section 7.1, has the potential to be a valuable a high throughput technique for gene diversity analysis. In addition, the use of single genes such as *dsrB* as MIC activity indicators has been explored in studies (Jørgensen et al., 2019), and HRM investigations have the advantage of being only gene primer limited rather than being restricted to the gene probes present on a microarray.

	<i>aprA</i>	<i>aprB</i>	<i>dsrA</i>	<i>dsrB</i>	<i>soxB</i>	<i>amoA</i>	<i>napA</i>	<i>narG</i>	<i>nirK</i>	<i>nirS</i>	<i>nrfA</i>	<i>fthfs</i>	<i>mcrA</i>	<i>iro</i>	<i>assA</i>
C 14a	a1	b	c1	d1	e1	f	g1	h	i	j1	k1	l	m	n	o
C 14b			c2												
C 14c			c3												
SED 01			e2												
SED 02	c1	e1													
SED 03			c4	d2	e2	g2				j1	k2	l	m		
SW 01															
SW 02	a2	c2													
SW 03			c4							j2	k2				

Figure 10-2 Similarity analysis summary for nine environmental samples and fifteen functional genes with cluster references, based on dendrogram cluster data (75%+ similarity)

	DGGE <i>dsrB</i>	HRM <i>dsrB</i>
C 14d	p1	q1
C 14e		
C 14f		
C 14g		
SED 04	p2	q2
SED 05	p1	q1
SED 06		
SED 07		
SW 04	p3	q2
SW 05		
SW 06	p2	
SW 07	p3	

Figure 10-3 Similarity analysis summary for twelve environmental samples for *dsrB* gene, based on dendrogram cluster data (75%+ similarity)

Tidal data collected using a sonde monitoring device determined tidal variability and showed periodic turbidity events at the Dredger Berth (Chapter 4), providing evidence of resuspension of local marine sediment and mixing of suspended sediment transported by seawater. Both phenomena were previously reported during turbidity events in similar coastal environments (Lawler et al., 2006, Vangriesheim et al., 2009, Valipour et al., 2017).

Analysis of sediment pore water and solid-phase chemistry (Chapter 5) revealed the oxic region in the sediment extended to a depth of only 50 mm, below which anoxic conditions were quickly established (Broman et al., 2017). The oxic surface region would be a suitable environment for aerobic sulfate-oxidizing, ammonia-oxidizing, nitrite-oxidizing, and iron-oxidizing bacteria as described in Section 2.2 of Chapter 2. The anoxic region below providing an environment favourable to sulfate-reducing, nitrate-reducing and iron-reducing anaerobes along with acetogenic and methogenic prokaryotes, fermentative bacteria, and hydrocarbon-degrading bacteria (Huerta-Diaz and Morse, 1992, Mortimer et al., 2004).

Functional gene analysis using GeoChip microarray (Chapter 6) showed that, with the exception of nitrite-oxidizing, iron-reducing and fermentative bacteria these microbial groups were present in all corrosion, marine sediment, and seawater samples. This metagenomic technique also showed that, for the majority of the functional genes analysed, corrosion and marine sediment shared a closer degree of community similarity than to the seawater. Of note were the occurrences of both aerobic and anaerobic genera linked to MIC processes (Section 6.4) within each environment. As discussed in Section 2.8.1, the GeoChip data provided measurements of functional gene concentration, so could not be used as a gauge of gene activity, and therefore the active microbial processes, within each environment were not directly determined. Nevertheless, the consistent pattern of composition that emerged supported the existence of complex biofilm-bound communities supporting both aerobic and anaerobic activity within each environment, as by Melchers and Jeffery (2008), Jia et al. (2019) and Zhang and Fang (2001). The methodologies applied to the GeoChip data also provided complementary support to the model. The use of three common gauges of community diversity (Simpson Index, Shannon-Wiener, and Shannon evenness) and a simple comparison of GeoChip fluorescence values, produced results that closely corresponded with those obtained from cluster analysis of the same data set (Section 3.2.2) despite being significantly different in execution. The hierarchy of sample diversity was produced from diversity values derived from each sample independently, whereas the cluster analysis considered all samples during data processing and applied the simple agglomerative UPGMA method. Nevertheless, the results indicated the same overall trend: a strong connection between microbial communities in corrosion and marine sediment, with a lesser influence of

seawater. Complementary to this, cluster analysis of HRM and DGGE data showed this trend also.

Spectroscopic analysis using X-ray powder diffraction (XRD), detailed in Chapter 8, and Fourier-transform infrared spectroscopy (FTIR), in Chapter 9, confirmed the mineralogy and chemical composition of corrosion included reduced sulfur species consistent with metabolic processes of sulfate-reducing prokaryote. These techniques also showed the presence of illite and clay mineral particles within the layers of corrosion close to the steel piling surface; halite and nahcolite minerals confirmed the seawater infiltration amongst the corrosion formations. The XRD and FTIR were complementary techniques that provided significant amounts of mutually consistent data. As discussed in their respective chapters, samples of complex chemical composition tended to produce peaks in XRD and FTIR patterns that correspond with multiple minerals or chemical compounds, and subsequently identification was uncertain. However, correlation of the two sets of data significantly reduced assignment ambiguity, greatly increasing the number of the positively identified components. Whilst XRD was primarily employed to determine mineral composition of the corrosion samples, FTIR also identified several minerals present and were similarly able to differentiate several polymorphs of iron corrosion products. The most significant difference between the two techniques, with respect to this project, was the inability of FTIR to resolve iron-sulfide modes, and thus one of the anticipated products of SRP metabolism, pyrite, was not independently verified by this technique. However, as FTIR could analyse amorphous solids, it was able to discern several chemical species not available to XRD, notably several reduced sulfur species.

As reduced sulfur species rapidly oxidize to sulfate in the environment, these chemical species, along with the pyrite detected by XRD, suggested the active presence of sulfate-reducing microbes within the corrosion. The GeoChip, HRM, and DGGE analysis of the same samples provided a microbiological link to these observations: the presence of functional genes, including those involved in sulfur cycling, were verified further supporting the evidence of microbial involvement in the corrosion processes. These findings agreed with studies previously discussed in Chapter 2 despite there being an emphasis on crude oil processing and transportation in these papers. The similarity in these findings indicates the phenomenon along with methods of its diagnosis are comparable despite the different environments in which they occur.

The results allowed the construction of a Source-pathway-receptor model for the initial stages of colonisation of the piling surface (Figure 10-4). The model consists of six main stages:

1. Disturbance of sediment layers within the Dredger Berth by motor vessels or weather events resuspend oxic and anoxic marine sediment layers. Evidenced by turbidity events recorded in local marine sediment (Section 4.2).
2. Sediment carries with it aerobic and anaerobic microorganisms. Indicated by GeoChip, HRM, and DGGE analysis of marine sediment, which demonstrated the presence of sulfur and nitrogen cycling and other classes of microorganisms in marine sediment (Sections 6.1, 6.2, 6.3, and 7.1).
3. Planktonic and sessile microorganisms in suspended sediment are brought into the Dredger Berth during the tidal cycle. Indicated by acetogenic and methanogenic microbial gene composition similarities between corrosion and seawater (Sections 6.1, 6.2, and 6.3).
4. Seawater enters corrosion layers during flood tide conditions; suspended sediment and microorganisms are transported into the corrosion via cracks and lesions in the corrosion surface. Verified by deposition of clay minerals and precipitation of soluble compounds within corrosion formation (Chapter 8 and Chapter 9).
5. Seawater, sediment, and microorganisms percolate throughout structure of corrosion crust. Indicated by saturated state of inner corrosion layers (Section 3.1.3) and reported morphology of MIC formations (Section 2.5.6)
6. Bacteria and archaea colonise inner layers of corrosion and establish communities of diverse anaerobic and aerobic genera, moderated by extensive biofilms produced and maintained by its constituents. Where communities form at the steel-corrosion interface, MIC can result. Evidenced by GeoChip isolation of 115+ bacterial and archaeal genera linked with MIC, from inner layers of corrosion samples (Section 6.4) and observed MIC-related biofilm characteristics (Section 2.4).

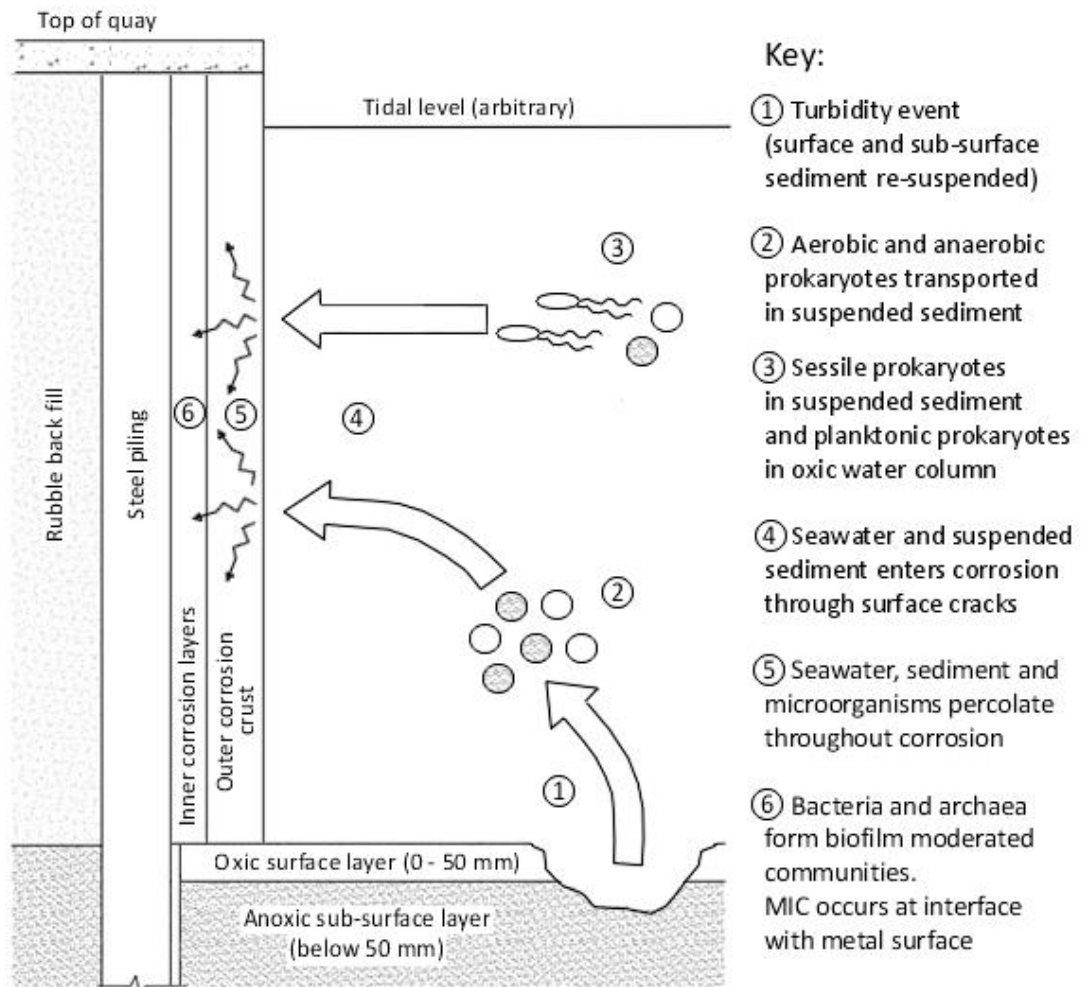


Figure 10-4 Source-pathway-receptor model for colonisation of corrosion on steel piling face at the Dredger Berth, Shoreham Port

10.2 Mineralogy and microbial diversity of vertical piling

Chapter 3 detailed how corrosion samples were extracted from vertical location on a section of piling. These samples were analysed using various techniques: high-resolution melt analysis (HRM) was used to detect variations in specific genes within the microbial communities present (Section 7.2 of Chapter 7); X-ray powder diffraction (Section 8.2 of Chapter 8) and Fourier-transform infrared spectrometry (Section 9.2 of Chapter 9) were used to determine the mineral composition of the samples. Combining these data with that obtained from measurement of the tidal range places the findings within an environmental context.

The results of the genetic diversity analysis using high-resolution melt (HRM) (Section 7.2 of Chapter 7) are displayed along with the corrosion location and tidal zones in Figure 10-5. This figure includes data from the four genes investigated using this technique (*aprA*, *dsrB*, *soxB*, and *16S*); the dendrograms from Section 7.2 have been condensed to highlight clusters of samples with 75% and greater similarity, and the data compiled as a matrix diagram. All samples sharing a reference number (and shading) were from the same 75%+ similarity cluster; those without shading or reference number were either singly linked or formed part of a cluster, with less than 75% similarity. The first important observation is that the target genes were observed at all locations sampled indicating a microbial presence in every location of the steel piling regardless of corrosion mineralogy or exposure to the atmosphere or seawater. Assessing the distribution of clusters, *dsrB* and *soxB* genes display a high degree of similarity (and therefore low diversity) from C 10 to C 14, and C 10 to C 13, respectively. Both groups are positioned downwards from the approximate level of mean tide (3.3 m). The *dsrB* data also indicate a widely spread cluster of three samples above (C 01, C 03, and C 06) whilst a second *soxB* cluster straddles the C 10 to C 13 group and includes C 04, C 05, and C 06. The plot of *aprA* similarity also suggests a higher-level cluster between C 02 and C 04, another between C 05 and C 06, and a third cluster between C 07 and C 13. The fourth cluster of the *aprA* gene also show a similar trend in low-level cluster position with four samples (C 09, C 10, C 12, and C 14) in only three samples are contiguous and straddle the mean tide line (3.3 m). The *16S* analysis indicates a 75%+ similarity cluster comprising C 01, C 09, and C 10; another comprising C 02 and C 04; a third of C 03, C 05, and C 06; and a fourth composed of samples C 12, C 13, and C 14. The overall pattern for *aprA*, *dsrB*, *soxB*, and *16S* suggests the diversity of microorganisms possessing these genes can be broadly grouped into samples taken from 3.0 m and above the sediment bed and those taken from below this. In terms of the tidal cycle, this border is midpoint between minimum high tide and mean tide level. This differentiation was not absolute however, as the 75% threshold is an arbitrary assignment and there are samples within some clusters that are above and below this border.

It should be noted that a strong similarity in diversity between samples does not indicate how diverse the community is in that cluster. As discussed in Section 10.1 the similarity is based on relative similarity between samples; diversity must be conducted using sample

independent measures such as those used in the previous section. Nevertheless, the results of DGGE/HRM *dsrB* analysis of corrosion samples (Section 7.1 of Chapter 7) suggested a relatively low microbial diversity in samples taken from 1.0 m above sediment bed level (C 14d, e, f, and g). As these four corrosion samples formed a cluster (88.2% similarity DGGE/78.1% and 76.8% HRM) samples extracted from the same height could be assumed to have similar level of community diversity. Therefore, the *dsrB* cluster between C10 and C 14 would be anticipated to share a lower level of diversity within the SRP section of the community. The SOB indicated by the *soxB* gene may follow a similar trend, but as there was no exploration of community members from this microbial group this was not determined in this study. This also applied to the HRM *16S* analysis of the community as a whole; three main clusters were defined and their positions on the piling determined, but their relative diversity is currently unknown for this same reason. Community diversity for *aprA* and *dsrB* genes would be anticipated to correlate closely due to both their involvement in the dissimilatory sulfate reductase pathway. However, though the pattern for samples at 2.6 m and below are similar for each, the higher-level samples do not form comparable clusters. This is possibly explained by the highly conserved nature of the *aprA* and *aprB* genes relative to *dsrA* and *dsrB* (Friedrich, 2002, Szttyler, 2014); the greater variability of the latter gene resulting in greater diversity. It is interesting to note a correlation between the mineralogy of sample C 10 to C 15 (Figure 10-6) and most of the same samples in Figure 10-5. This suggest the regions on the piling where Type C corrosion was analysed possesses a common microbiota; previous evidence indicate that the region where maghemite and reduced sulfur species are present has a less diverse composition than that of the adjacent marine sediment and surrounding seawater.

As discussed in Section 8.2 and Section 9.2, some corrosion products were common to all corrosion samples. This was first observed during XRD and FTIR analysis of low tide level corrosion samples; extending the scope of the analysis reveal this trend extended to other samples also. The common products were magnetite (Fe_3O_4), goethite ($\alpha\text{-FeOOH}$), and lepidocrocite ($\gamma\text{-FeOOH}$). The presence of other minerals, corrosion products and chemical species identified using XRD and FTIR were found to vary significantly between samples. However, when compared with their vertical locations on the piling it was found that samples of similar composition tended to form contiguous groups; four

groups were thus discerned. Figure 10-6 illustrates these relative to the position of the groups on the piling along with tidal zones. The groups were designated Type A1, A2, B, and C depending upon their location on the piling. N.B.: The area of piling above C 01 and below C 15 were not sampled; the diagram speculatively extends the nearest corrosion type to these adjacent regions.

The uppermost type of corrosion (Type A1) was found to lie above the maximum high tide level (Section 4.1), in a region commonly referred to as the atmospheric zone (Section 2.5.4) that generally only interacts with seawater via the spray raised during harsh weather conditions. A single sample (C 01), 6.2 m above the sediment bed, fell within this region; it was characterised by the occurrence of akaganeite (β -FeOOH) and hematite (α -Fe₂O₃) in addition to the common mineral above; the three common forms of green rust were found to be absent. Type A2 corrosion was characterised similarly to Type A1, except it also included chloride green rust (GR(Cl⁻)). Samples C 02 to C 06 (5.8 m to 4.2 m above bed level) fell within this corrosion type. Samples C 02, C 03, and C 04 were located above the mean high tide level (4.8 m), so were categorised as being within the splash zone. Samples C 05 and C 06 were below these and occupied the top of the intertidal zone.

Corrosion products classified as Type C were found in the samples extracted from the lower part of the piling. These were C 10 to C 15, which spanned the heights of 2.6 m to 0.6 m above the sediment bed. The mineralogy of this type was distinct from Type A2; they lacked the akaganeite, hematite, and chloride green rust previously observed, but were instead characterised by maghemite (γ -Fe₂O₃), pyrite (FeS₂), and the sulfur species: sulfate (SO₄²⁻), sulfite (SO₃²⁻), and thiosulfate (S₂O₃²⁻). Sample C 10 (2.6 m above bed) was located just above the mean high tide level (2.4 m); whereas C 11 and C 12 were above maximum low tide level (1.6 m). Samples C 13, C 14, and C 15 were situated below maximum high tide level but were still within the intertidal zone as defined in Section 2.5.4. As discussed in Section 4.1 the mean and minimum low tide levels were not measurable. Reference to low tide level samples has been retained in previous chapters due to the position of samples C 14a, b, and c below the maximum high tide, despite being within the tidal zone according to this new analysis of their location.

Between the Type A2 and Type C corrosion samples lay a series of samples that possessed a mineralogy with characteristics of both. Samples C 07, C 09 and C 09 were positioned

approximately astride the minimum high tide level (3.3 m). The upper sample (C 07) was found to include chloride green rust, hematite and akaganeite as well as maghemite, though no pyrite was observed despite indications of reduced sulfur species sulfite and thiosulfate. Sample C 08 had a mineralogy more characteristic of Type C corrosion than those above, having no chloride green rust and possessing pyrite and sulfate, sulfite, and thiosulfate, though analysis also revealed the presence of hematite and akaganeite. The third sample, C 09, was from 3.0 m above the sediment bed; this had Type C mineralogy but with the addition of akaganeite.

In comparing the mineralogy of the samples with the vertical locations a link between tidal cycle of the adjacent seawater was apparent. The entire visible face of the piling possessed extensive corrosion layers, but analysis indicated that corrosion composition was not homogenous but rather linked to the microbial activity occurring within it. The microbial communities within the corrosion also varied according to their position on the piling, with genetically similar communities being associated with specific forms of corrosion composition. As previously discussed, the *dsrB* gene has commonly been used as a primary indicator of MIC activity (Jørgensen et al., 2019) and is apparent from Figure 10-5 and Figure 10-6 that vertical locations on the piling bearing MIC mineralogy are also associated with a particular genetic composition. GeoChip analysis of low tide corrosion samples had provided a detailed assessment of the genera present as well as relative abundance values of the gene, but without similar data from locations on the piling associated with other forms of mineralogy, it is not possible to definitively state how the similarity in the overall *dsrB* gene relates to MIC activity. The same applied to the *aprA*, and *soxB* genes, both of which were investigated using GeoChip, and displayed similar clustering pattern to *dsrB*. Analysis of *16S* gene also displayed clustering within the MIC region, but to a lesser extent and overall, the gene displayed smaller groups of widely spread samples; GeoChip analysis did not include this gene so further investigation would have to be by other means such as next generation gene sequencing outlined in Section 2.8.2. Analysis of MIC-related communities by Cai et al. (2017) indicated that the microbiota diversity was highly susceptible to changes in nutrient levels. Diversity analysis of the low tide level corrosion samples (Section 6.1 and Section 10.1) revealed these were less diverse than seawater and generally below that of marine sediment also, suggesting that the microbiota within the MIC region (C 10 to C14) were

occupying a nutrient limited environment. As discussed previously this lower diversity in the MIC region may explain the clustering of genes observed. Sampling was conducted during a single month, and seawater nutrient levels not quantified, so it was not possible to investigate this further.

Also significant to the study of the MIC are the observations made regarding the position of MIC-related mineralogy. Research into MIC within the marine environment has focussed on the low tide zone, hence the widely used term ‘accelerated low water corrosion’ (Beech and Gaylarde, 1999, Melchers, 2013). The data presented here shows that the conditions favourable to the activity of sulfate-reducing prokaryotes is not limited to the low tide zone only. Microbial community and mineralogical analysis in this study has revealed that the phenomena identified as ALWC can also occupy contiguous regions from sediment bed level up to minimum high tide level.

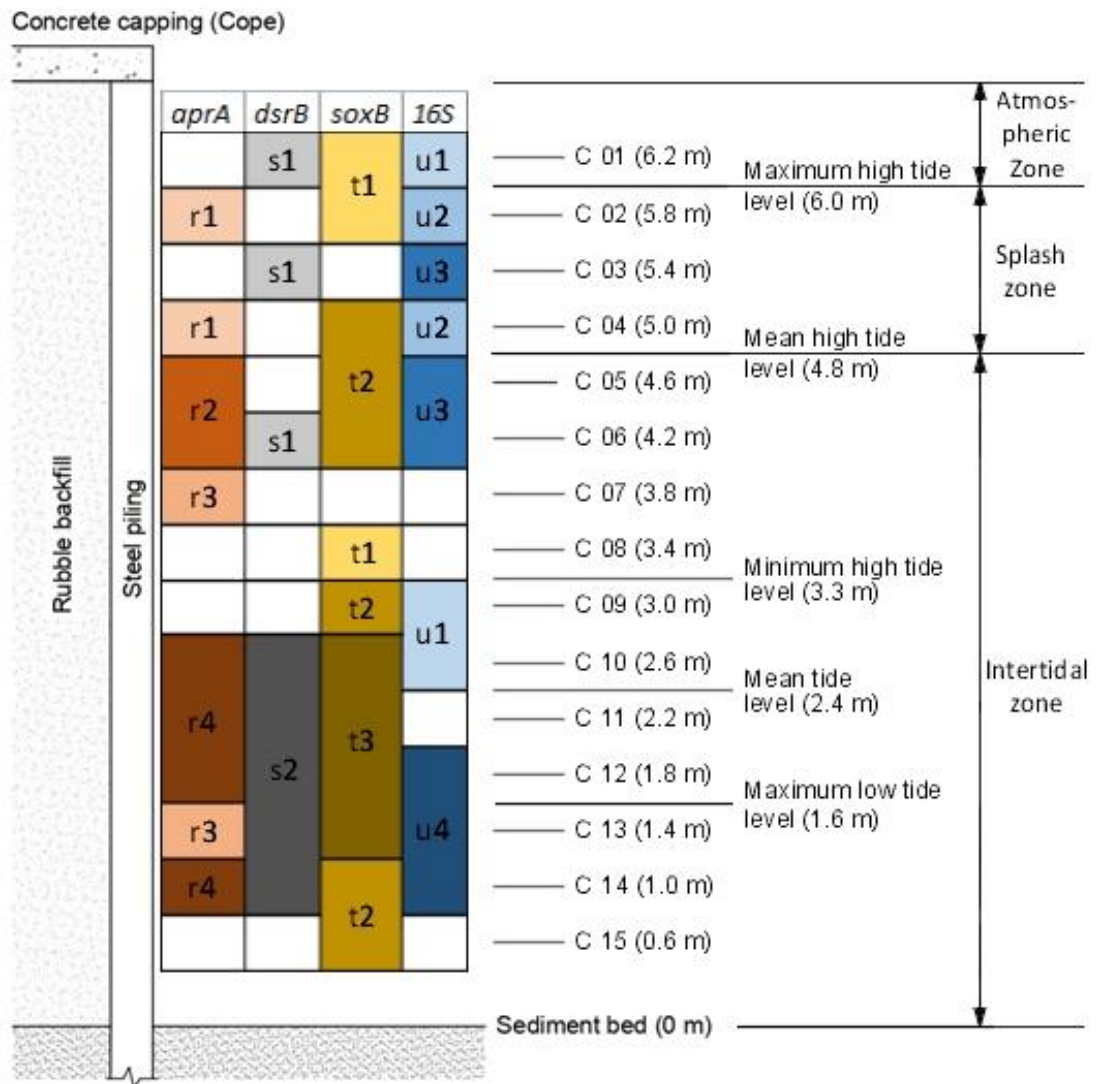


Figure 10-5 Schematic diagram of steel piling at the Dredger Berth with vertical positions of corrosion samples, tidal zones, and HRM dendrogram cluster data (75%+ similarity) for *aprA*, *dsrB*, *soxB*, and *16S* genes with cluster references

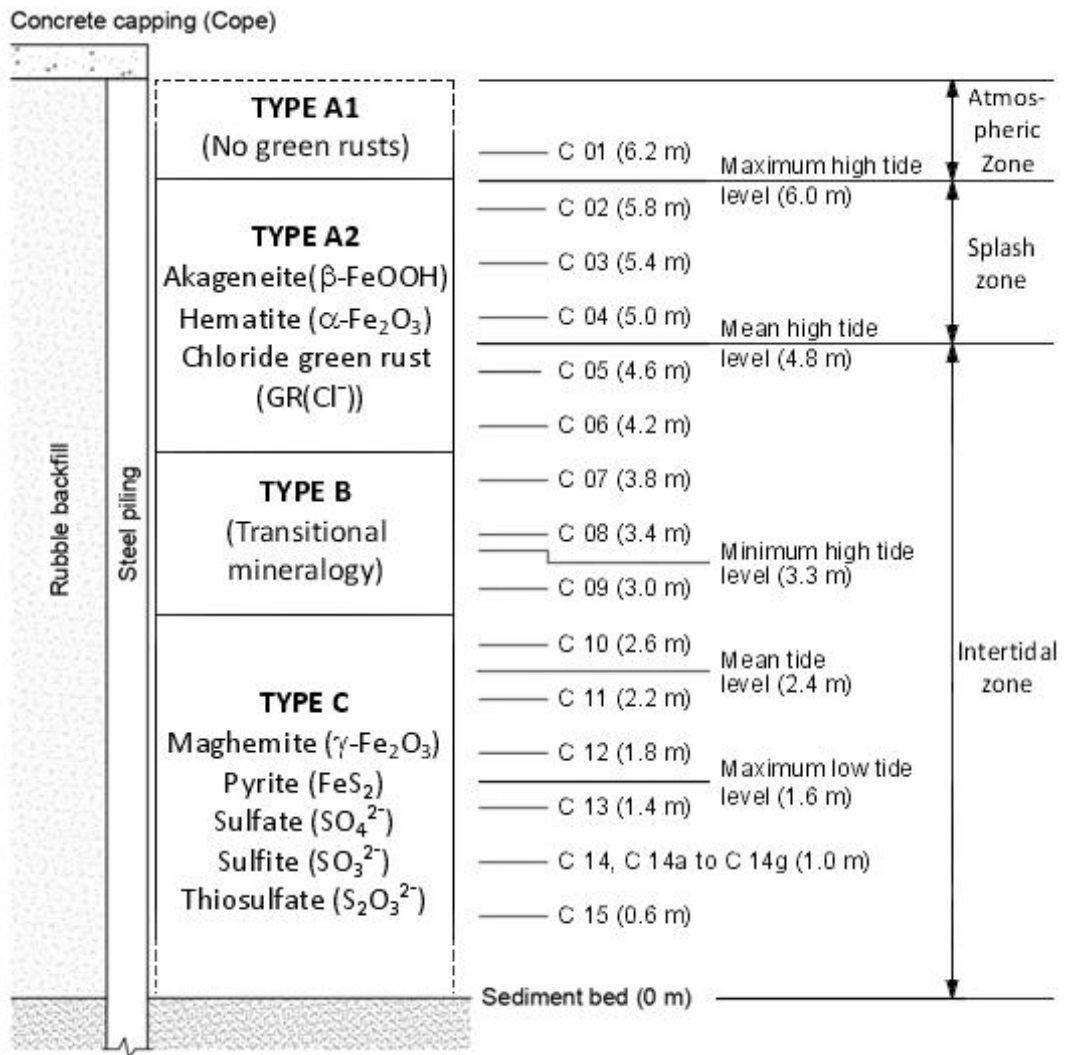


Figure 10-6 Schematic diagram of steel piling at the Dredger Berth with vertical positions of all corrosion samples, tidal zones, and characteristic minerals and chemical species, as determined by XRD and FTIR analysis

Chapter 11 Conclusions and further work

The microbially influenced corrosion of carbon steel piling in the marine environment has been a poorly understood and under-researched field of study. Where MIC studies have been carried out, oil field infrastructure have been the primary focus. However, it has also been observed within ports and harbours globally, and its ability to damage quaysides and moorings is well recorded.

MIC research in this environment have concentrated on corrosion observed in the region where the greatest rates of corrosion have been recorded: within the low tide zone. From this the term ‘accelerated low water corrosion’ (ALWC) has been coined and has led to an apparent assumption that all marine MIC occurs at or around the low water mark. Some studies have concentrated on isolating specific microbes that have been linked to MIC, and a very few have investigated links between the local marine environment. This study built on such work and widened the scope beyond the low water zone to include analysis of the microbiology and mineralogy of corrosion samples taken from several locations on an exposed vertical section of carbon steel piling as well as the adjacent marine sediment and seawater.

For the research aim of determining how the adjacent marine environment had microbial links to that of the MIC, low water level corrosion, marine sediment, and seawater samples were analysed for community diversity using Simpson Index, Shannon-Wiener, and Shannon evenness techniques and for similarities in their community *dsrB* gene composition using UPGMA clustering. These samples were also analysed using GeoChip microarray-derived data to determine similarities in fifteen functional genes and to provide additional data on community diversity. Seawater turbidity data obtained from site-based monitoring equipment showed that the sediment bed at the sampling location was subject to period resuspension, and XRD/FTIR analysis demonstrated that a portion of this sediment was assimilated into the structure of the corrosion. ICP-OES analysis of marine sediment determined oxic and anoxic regions depth in the column and indicated regions of reduced sulfur species; this was confirmed by XRD analysis of the marine sediment. From this data a source-pathway-receptor model was constructed for the microbial interaction between the marine sediment, seawater, and corrosion. The model

indicates the influence of local marine sediment upon the microbial composition of the MIC formations as well as the lesser influence of the microbiota transported by seawater.

For the research aim of characterising corrosion formations, several techniques were employed. Microarray analysis of low water level corrosion confirmed the presence of a complex microbiota that comprised many significant genera, within eight metabolic groups, observed in other MIC studies, as well as several genera that had previously been linked to MIC in other environments, and a number not previously identified within MIC formations. High-resolution melt (HRM) analysis of samples taken from several vertical position on a length of piling targeted three genes (*aprA*, *dsrB*, and *soxB*) utilised to indicate sulfur-cycling microbes, and the *16S* gene. A pattern of community diversity was observed for each gene indicating a more specialised microbiota existed at a specific height on the piling down to the level of the marine sediment bed. The mineralogical composition of these same samples was examined using X-ray powder diffraction (XRD) and Fourier-transform infrared (FTIR) analysis. Contiguous regions of similar mineralogy were revealed, forming three main regions. The location of the lower mineralogical region also corresponded with the low microbial diversity region noted in the HRM results above. Tidal data was also compared with these microbial and mineralogical trends; it was found that they only occurred at or below the mean tide level. Coupled to the microarray analysis of the low water level corrosion, XRD and FTIR were applied to confirm that a typical mineralogy for this location on the piling was present. It also increased certainty that the mineralogy of samples taken from higher on the piling was typical.

These finding constitute a considerable expansion to the understanding of microbially influenced corrosion of carbon steel piling in the marine environment and lay the foundations for further research. The study has intentionally excluded descriptions of the corrosion morphology outlined in Section 2.5, instead it has assessed samples according to the mineralogical and microbiological techniques used. Time constraints limited the number of microbial genera identified by the microarray analysis of corrosion; only 115 of 311 identified were correlated with MIC studies.

GeoChip has proven its value in identifying the presence of MIC-related prokaryotes in the corrosion. A logical extension of this analysis would be to include marine sediment

and seawater samples. This would allow verification of the community similarities observed by HRM and DGGE analysis. As regions of specific mineralogy have now been defined, this technique could also be used to analyse how the community structure varies amongst these different types of corrosion.

A further significant step in community analysis would be the use of mRNA instead of DNA for GeoChip analysis; this would allow the degree of gene expression to be assessed. As previously discussed, the use of DNA only indicates the presence of a gene within a community but does not indicate if the associated microorganisms are active, dormant, or dead.

Consideration should also be made of the value of a custom microarray. The GeoChip microarray utilised was a standard version offered by the supplier and was chosen due to its economy and its extensive coverage of sulfur and nitrogen-cycling probe sets. A custom microarray would allow more extensive investigation of the less extensively covered genes such as the methanogenic indicator (*mcrA*) gene, to explore the influence of archaea more fully; or the hydrocarbon-degrading microorganism indicator *assA* gene which only possessed 16 probe clusters.

Additionally, next generation sequencing techniques are becoming increasingly viable due to ever decreasing costs and the breadth of data obtainable; further studies would greatly benefit from these, either alongside or in place of other techniques employed in this study (e.g., DGGE).

Though this study primarily focused on characterisation of corrosion and aspects of the surrounding environment, if corrosion rates had been measurable during the study, it would have been able to see if corrosion rates at various vertical locations accorded with published literature, and if variations occurred within the Type C corrosion region, especially in the location typically assigned to ALWC. Similarly, this study extracted and analysed environmental samples from a single month of one year. As mentioned previously a greater understanding of the characteristics of MIC-related microbiota and corrosion product variability could potentially be obtained if seasonal sampling were carried out.

References

- Abdolahi, A., Hamzah, E., Ibrahim, Z. and Hashim, S. (2014). "Application of Environmentally-Friendly Coatings Toward Inhibiting the Microbially Influenced Corrosion (MIC) of Steel: A Review." Polymer Reviews **54**: 702–745.
- Addala, S., Bouhdjer, L., Chala, A., Bouhdjar, A., Halimi, O., Boudine, B. and M., S. (2013). "Structural and optical properties of a NaCl single crystal doped with CuO nanocrystals." Chinese Physics B **22**(9): 1-5.
- Akpa, J. (2013). "Modeling of the Corrosion rate of Stainless Steel in Marine oil Environment." ARPN Journal of Engineering and Applied Sciences **8**(8): 656-662.
- Al-Jaroudi, S. S., Ul-Hamid, A. and Al-Gahtani, M. M. (2011). "Failure of crude oil pipeline due to microbiologically induced corrosion." Corrosion Engineering, Science and Technology **46**(4): 568-579.
- AlAbbas, F. M., Williamson, C., Bholra, S. M., Spear, J. R., Olson, D. L., Mishra, B. and Kakpovbia, A. E. (2013). "Influence of sulfate reducing bacterial biofilm on corrosion behavior of low-alloy, high-strength steel (API-5L X80)." International Biodeterioration and Biodegradation **78**: 34-42.
- Alcantara, J., Chico, B., Diaz, I., de la Fuente, M. and Morcillo, M. (2015). "Airborne chloride deposit and its effect on marine atmospheric corrosion of mild steel." Corrosion Science **97**: 74-88.
- Alcántara, J., de la Fuente, D., Chico, B., Simancas, J., Díaz, I. and Morcillo, M. (2017). "Marine Atmospheric Corrosion of Carbon Steel: A Review." Materials **10**(406): 1-67.
- Amann, R. I., Stromley, J., Devereux, R., Key, R. and Stahl, D. A. (1991). "Molecular and Microscopic Identification of Sulfate-Reducing Bacteria in Multispecies Biofilms." Applied and Environmental Microbiology **58**(2): 614-623.
- An, D., Dong, X., An, A., Park, H. S., Stous, M. and Voordouw, G. (2016). "Metagenomic Analysis Indicates Epsilonproteobacteria as a Potential Cause of Microbial Corrosion in Pipelines Injected with Bisulfite." Frontiers in Microbiology **7**(28).
- Anandham, R., Indiragandhi, P., Madhaiyan, M., Ryu, K. Y., Jee, H. and Sa, T. M. (2008). "Chemolithoautotrophic oxidation of thiosulfate and phylogenetic distribution of sulfur oxidation gene (soxB) in rhizobacteria isolated from crop plants." Research in Microbiology **159**(9-10): 579-589.

- Andrews, J. T., Eberl, D. D. and Kristjansdottir, G. B. (2006). "An exploratory method to detect tephra from quantitative XRD scans: examples from Iceland and east Greenland marine sediments." The Holocene **16**(8): 1035-1042.
- Angell, P. (1999). "Understanding microbially influenced corrosion as biofilm mediated changes in surface chemistry." Current opinion in Biotechnology **10**: 269-272.
- Antunes, R. A., Ichikawa, R. U., Martinez, L. G. and Costa, I. (2014). "Characterization of Corrosion Products on Carbon Steel Exposed to Natural Weathering and to Accelerated Corrosion Tests." International Journal of Corrosion **2014**: 1-9.
- ArcelorMittal Commercial RPS S.à r.l. (2008). Piling Handbook. Luxembourg.
- ArcelorMittal Commercial RPS S.à r.l. (2011). AMLoCor Sheet Piling. Luxembourg.
- Arroyave, C. and Morcillo, M. (1997). "Atmospheric corrosion products in iron and steels." Trends Corros **2**: 1-16.
- Ashassi-Sorkhabi, H., Zarrini, G., Moradi-Haghighi, M. and Javaherdashti, R. (2012). "Corrosion behavior of carbon steel in the presence of two novel iron-oxidizing bacteria isolated from sewage treatment plants." Biodegradation **23**: 69–79.
- Atkins, P. W. (2006). Physical Chemistry. India, OUP Oxford.
- Atlas, R. M. and Bartha, R. (1998). Microbial Ecology: fundamentals and applications. California, USA, Benjamin/Cummings Science Publishing.
- Aydin, S., Shahi, A., Ozbayrama, E. G., Ince, B. and Ince, O. (2015). "Use of PCR-DGGE based molecular methods to assessment of microbial diversity during anaerobic treatment of antibiotic combinations." Bioresource Technology **192**: 735–740.
- Babu, B. R., Maruthamuthu, S., Rajasekar, A., Muthukumar, N. and Palaniswamy, N. (2006). "Microbiologically influenced corrosion in dairy effluent." Int. J. Environ. Sci. Tech. **3**(2): 159-166.
- Badamchi, A., Masoumi, H., Javadinia, S., Asgarian, R. and Tabatabaee, A. (2017). "Molecular detection of six virulence genes in *Pseudomonas aeruginosa* isolates detected in children with urinary tract infection." Microbial Pathogenesis **107**: 44-47.
- Balasubramaniam, R. and Kumar, A. V. R. (2000). "Characterisation of Delhi iron pillar rust by X-ray diffraction, Fourier-transform infrared spectroscopy and Mossbauer Spectroscopy." Corrosion Science **42**: 2085-2101.
- Balasubramaniam, R., Ramesh Kumar, A. V. and Dillmann, P. (2003). "Characterization of rust on ancient Indian iron." Current Science **85**(11): 1546-1555.

Barton, L. L. and Hamilton, W. A. (2007). Sulfate-reducing Bacteria. The Edinburgh Building, Cambridge CB2 8RU, UK, Cambridge University Press.

Beale, D. J., Dunn, M. S. and Marney, D. (2010). "Application of GC–MS metabolic profiling to 'blue-green water' from microbial influenced corrosion in copper pipes." Corrosion Science **52**: 3140–3145.

Beale, D. J., Palombo, E. A., Morrison, P. D. and Key, C. (2013). "Metabolic profiling of biofilm bacteria known to cause microbial influenced corrosion." Water science and technology **69**(1): 1-8.

Beck, T. F., Mullikin, J. C. and Biesecker, L. G. (2016). "Systematic Evaluation of Sanger Validation of NextGen Sequencing Variants." Clin Chem. **62**(4): 647–654.

Beech, I. B. and Campbell, S. A. (2008). "Accelerated low water corrosion of carbon steel in the presence of a biofilm harbouring sulphate-reducing and sulphur-oxidizing bacteria recovered from a marine sediment." Electrochimica Acta **54**: 14-21.

Beech, I. B. and Gaylarde, C. C. (1999). "Recent advances in the study of biocorrosion - An overview." Revista de Microbiologia **30**: 177-190.

Beech, I. B. and Sunner, J. (2004). "Biocorrosion: towards understanding interactions between biofilms and metals." Current Opinion in Biotechnology **15**: 181-186.

Behjati, S. and Tarpey, P. S. (2013). "What is next generation sequencing?" Arch Dis Child Educ Pract Ed **98**.

Behrendt, L., Larkum, A. W. D., Trampe, E., Norman, A., Sørensen, S. J. and Kuhl, M. (2012). "Microbial diversity of biofilm communities in microniches associated with the didemnid ascidian *Lissoclinum patella*." The ISME Journal **6**: 1222–1237.

Ben Abdallah, M., Karray, F., Kallel, N., Armougom, F., Mhiri, N., Quéméneur, M., Cayol, J. L., Erauso, G. and Sayadi, S. (2018). "Abundance and diversity of prokaryotes in ephemeral hypersaline lake Chott El Jerid using Illumina Miseq sequencing, DGGE and qPCR assays." Extremophiles **22**(5): 811–823

Bergmann, G. T., Bates, S. T., Eilers, K. G., Lauber, C. L., Caporaso, J. G., Walters, W. A., Knight, R. and Fierer, N. (2011). "The under-recognized dominance of Verrucomicrobia in soil bacterial communities." Soil Biol Biochem. **43**(7): 450–1455.

Bermont-Bouis, D., Janvier, M., Grimont, P. A., D. , Dupont, I. and Vallaey, T. (2007). "Both sulfate-reducing bacteria and Enterobacteriaceae take part in marine biocorrosion of carbon steel." Journal of Applied Microbiology **102**: 161-168.

Besaury, L., Ouddaneb, B., Pavissich, J. P., Dubrulle-Brunaud, C., González, B. and Quillet, L. (2012). "Impact of copper on the abundance and diversity of sulfate-reducing

prokaryotes in two chilean marine sediments." Marine Pollution Bulletin **64**: 2135-2145.

Bhola, S. M., AlAbbas, F. M., Bhola, R., Spear, J. R., Mishra, B., Olson, D. L. and Kakpovbia, A. E. (2013). "Neem extract as an inhibitor for biocorrosion influenced by sulfate-reducing bacteria: A preliminary investigation." Engineering Failure Analysis **36**: 92-103.

Bielefeldt, A., Gutierrez-Padilla, M. G. D., Ovtchinnikov, S., Silverstein, J. and Hernandez, M. (2010). "Bacterial Kinetics Of Sulfur Oxidizing Bacteria And Their Biodeterioration Rates Of Concrete Sewer Pipe Samples." Journal Of Environmental Engineering **136**(7): 731-738.

Blazejak, A., Erseus, C., Amann, R. and Dubilier, N. (2005). "Coexistence of Bacterial Sulfide Oxidizers, Sulfate Reducers, and Spirochetes in a Gutless Worm (Oligochaeta) from the Peru Margin." Applied and Environmental Microbiology **71**(3): 1553-1561.

Bock, E., Sand, W., Meincke, M., Wolters, B., Ahlers, B., Meyer, C. and Sameluck, F. (1988). Biologically induced corrosion of natural stones - strong contamination of monuments with nitrifying organisms. Biodeterioration **7**. D. R. Houghton, R. N. Smith and H. O. W. Eggins. Dordrecht, Springer.

Boddicker, A. M. and Mosier, A. C. (2018). "Unexpected versatility in the metabolism and ecophysiology of globally relevant nitrite-oxidizing Nitrotoga bacteria." The ISME Journal **112**(36): 11371–11376.

Bodtker, G., Thorstenson, T., Lillebø, B. P., Thorbjørnsen, B. E., Ulvøen, R. H., Sunde, E. and Torsvik, T. (2008). "The effect of long-term nitrate treatment on SRB activity, corrosion rate and bacterial community composition in offshore water injection systems." Biotechnol **35**: 1625–1636.

Boev, B., Jovanovski, G. and Makreski, P. (2009). "Minerals from Macedonia. XX. Geological Setting, Lithologies, and Identification of the Minerals from Ržanovo Fe-Ni Deposit." Turkish Journal of Earth Sciences **18**: 631–652.

Bolton, K. (2002). Corrosion. Milton Keynes, United Kingdom, The Open University.

Bonifay, V., Wawrik, B., Sunner, J., Aydin, E., Callaghan, A. V., Duncan, K. E., Snodgrass, E. C., Oldham, A., TLiengen, T. and Beech, I. (2017). "Metabolomic and Metagenomic Analysis of Two Crude Oil Production Pipelines Experiencing Differential Rates of Corrosion." Frontiers in Microbiology **8**(99): 1-17.

Borda, M. J., Strongin, D. R. and Schoonen, M. A. (2003). "A vibrational spectroscopic study of the oxidation of pyrite by molecular oxygen." Geochimica et Cosmochimica Acta **68**(8): 1807-1813.

- Botero, L. E., Delgado-Serrano, L., Hernández, M. L. C., Del Portillo Obando, P. and Zambrano Eder, M. M. (2015). "The Human Microbiota: The Role Of Microbial Communities In Health And Disease." Acta Biológica Colombiana **21**(1): 5-15.
- Botha, C. (2000). "Cathodic Protection For Ships." Mechanical Technology **May 2000**: 31-35.
- Boyatzis, S. C., Velivasaki, G. and Malea, E. (2016). "A study of the deterioration of aged parchment marked with laboratory iron gall inks using FTIR-ATR spectroscopy and micro hot table." Heritage Science **4**(13): 1-17.
- Briggs, W. F., Stanley, H. O., Okpokwasili, G. C., Immanuel, O. M. and Ugboma, C. J. (2019). "Isolation and Molecular Characterization of Acid Producing Bacteria from Selected Oilfield Environments within the Niger Delta." Journal of Advances in Microbiology **17**(3): 1-9.
- British Standards Institute (2000). BS6349-1 2000 Maritime Structures Part 1 – Code of general criteria. United Kingdom, BSI: 212-213.
- Broman, E., Sjöstedt, J., Pinhassi, J. and Dopson, M. (2017). "Shifts in coastal sediment oxygenation cause pronounced changes in microbial community composition and associated metabolism." Microbiome **5**(96): 1-18.
- Bryant, M. P., Campbell, L. L., Reddy, C. A. and Crabill, M. R. (1977). "Growth of *Desulfovibrio* in Lactate or Ethanol Media Low in Sulfate in Association with H₂-Utilizing Methanogenic Bacteria." Applied And Environmental Microbiology **33**(5): 1162-1169.
- Buccolieri, A., Buccolieri, G., Cardellicchio, N., Dell'Atti, A., Di Leo, A. and Maci, A. "Heavy Metals in Marine Sediment off Taranto Gulf." Marine Chemistry **99**: 227-235.
- Cai, W., Li, Y., Niu, L., Zhang, W., Wang, C., Wang, P. and Meng, F. (2017). "New insights into the spatial variability of biofilm communities and potentially negative bacterial groups in hydraulic concrete structures." Water Research **123**: 495-504.
- Cannon, J., Sanford, R. A., Connor, L., Yang, W. H. and Chee-Sanford, J. (2019). "Optimization of PCR primers to detect phylogenetically diverse *nrfA* genes associated with nitrite ammonification." Journal of Microbiological Methods **160**: 49–59.
- Cetin, D. and Aksu, M. L. (2009). "Corrosion behaviour of low-alloy steel in the presence of *Desulfotomaculum* sp." Corrosion Science **51**: 1584-1588.
- Chaban, B., Ng, S. Y. M. and Jarrell, K. F. (2006). "Archaeal habitats — from the extreme to the ordinary." Can. J. Microbiol. **52**: 73-116.

Chae, S. R., Ahn, Y. T. and Suh, C. W. (2006). Trends in Biotechnology Research. New York, Nova Science

Chaki, S. H., Malek, T. J., Chaudhary, M. D., Tailor, J. P. and Deshpande, M. P. (2015). "Magnetite Fe₃O₄ nanoparticles synthesis by wet chemical reduction and their characterization." Advances in Natural Sciences: Nanoscience and Nanotechnology **6**(3): 1-6.

Chakrabarty, D. and Mahapatra, S. (1999). "Aragonite crystals with unconventional morphologies." Journal of Materials Chemistry **9**: 2953-2957.

Chand, V. and Prasad, S. (2013). "ICP-OES assessment of heavy metal contamination in tropical marine sediments: A comparative study of two digestion techniques." Microchemical Journal **11**: 53–61.

Chang, Y., Chang, Y., Hung, C., Lee, J., Liao, H. and Chou, H. (2014). "Microbial community analysis of anaerobic bio-corrosion in different ORP profile." International Biodeterioration & Biodegradation **95**: 93-101.

Chauhan, R. P., Mathur, R., Singh, G., Kaul, A., Bag, N., Singh, S., Kumar, H., Patra, M. and Mishra, A. K. (2013). "Evaluation of Folate Conjugated Superparamagnetic Iron Oxide Nanoparticles for Scintigraphic/Magnetic Resonance Imaging." Journal of Biomedical Nanotechnology **9**: 323–334.

Chernyshova, I. V. (2003). "An in situ FTIR study of galena and pyrite oxidation in aqueous solution." Journal of Electroanalytical Chemistry **558**: 83-98.

Cheung, C. W. S., Walsh, F. C., Campbell, S. A., Chao, W. T. and Beech, I. B. (1994). "Microbial Contributions to the Marine Corrosion of Steel Piling." International Biodeterioration and Biodegradation: 259-274.

Christiaen, B., McDonald, A., Cebrian, J. and Ortmann, A. C. (2013). "Response of the microbial community to environmental change during seagrass transplantation." Aquatic Botany **109**: 31-38.

Chu, H., Wang, S., Yue, H., Lin, Q., Hu, Y., Li, X., Zhou, J. and Yang, Y. (2014). "Contrasting soil microbial community functional structures in two major landscapes of the Tibetan alpine meadow." MicrobiologyOpen **3**(5): 585–594.

Chukhrov, F. V., Zvyagin, B. B., Gorshkov, A. I., Yermilova, L. P., Korovushkin, V. V., Rudnitskaya, Y. S. and Yakubovskaya, N. Y. (1977). "Feroxyhyte, a new modification of FeOOH." International Geology Review **19**(8): 873-890.

Cieslak, L. A. (2012). The use of molecular techniques to study biofilm-influenced corrosion of CuNi alloys in marine environments. Master of Science, Technical Institute of Lodz.

- Coenye, T. and Vandamme, P. (2003). "Intragenomic heterogeneity between multiple 16S ribosomal RNA operons in sequenced bacterial genomes." FEMS Microbiology Letters **228**: 45-49.
- Colosi, J. C. and Schaall, B. A. (1993). "Tissue grinding with ball bearings and vortex mixer for DNA extraction." Nucleic Acids Research **21**(4): 1051-1052.
- Comensoli, L., Albini, M., Kooli, W., Maillard, J., Lombardo, T., Junier, P. and Joseph, E. (2020). "Investigation of Biogenic Passivating Layers on Corroded Iron." Materials **13**(1176): 1-13.
- Cong, J., Liu, X., Lu, H., Xu, H., Li, Y., Deng, Y., Li, D. and Zhang, Y. (2015). "Analyses of the influencing factors of soil microbial functional gene diversity in tropical rainforest based on GeoChip 5.0." Genomics Data **5**: 397–398.
- Conlette, O. C. (2016). "Microbial communities of light crude from Nigeria and potential for in situ biodegradation, souring, and corrosion." Petroleum Science and Technology **34**(1): 71–77.
- Cook, D. C., Oh, S. J., Balasubramaniam, R. and Yamashita, M. (1999). "The role of goethite in the formation of protective corrosion layers in steel." Hyperfien Interactions **122**: 59-70.
- Cornell, R. M. and Schwertmann, U. (2003). The Iron Oxides: Structure, Properties, Reactions, Occurrences, and Uses. Darmstadt, Wiley-VCH.
- Costerton, J. W., Geesey, G. G. and Cheng, K. J. (1978). "How Bacteria Stick." Scientific American **238**(1): 86-95.
- Cui, H., Ren, W., Lin, P. and Liu, Y. (2013). "Structure control synthesis of iron oxide polymorph nanoparticles through an epoxide precipitation route." Experimental Nanoscience **8**(7): 869-875.
- Daniels, L., Belay, N., Rajagopal, B. S. and Weimer, P. J. (1987). "Bacterial Methanogenesis and Growth from CO₂ with Elemental Iron as the Sole Source of Electrons." Science **237**(4814): 509-511.
- Das, S., Sarker, S., Ghorashi, S. A., Forwood, J. K. and Raidal, S. R. (2016). "A comparison of PCR assays for beak and feather disease virus and high resolution melt (HRM) curve analysis of replicase associated protein and capsid genes." Journal of Virological Methods **237**: 47-57.
- De la Fuente, M., Alcantara, J., Chico, B., Diaz, J. A., Jimenez, J. A. and Morcillo, M. (2016). "Characterisation of rust surfaces formed on mild steel exposed to marine atmospheres using XRD and SEM/Micro-Raman techniques." Corrosion Science **110**: 253-264.

Dear, F. F. and Skinner, G. C. G. (2017). Mechanisms of hydrogen embrittlement in steels: discussion, The Royal Society.

Delaunois, F., Tosar, F. and Vitry, V. (2014). "Corrosion behaviour and biocorrosion of galvanized steel water distribution systems." Bioelectrochemistry **97**: 110-119.

Dickens, G. R., Koelling, M., Smith, D. C. and Schnieders, L. (2007). "Rhizon Sampling of Pore Waters on Scientific Drilling Expeditions: An Example from the IOPDP Expedition 302, Artic Coring Expedition (ACEX)." Scientific Drilling(4): 22-25.

Dinh, H. T., Keuver, J., Mussmann, M., Hassef, A. W., Stratmann, M. and Widdel, F. (2004). "Iron corrosion by novel anaerobic microorganisms." Nature **427**: 829-823.

Dong, Q., Shi, H. and Liu, Y. (2017). "Microbial Character Related Sulfur Cycle under Dynamic Environmental Factors Based on the Microbial Population Analysis in Sewerage System." Frontiers in Microbiology **8**(64): 1-11.

Dong, Y., Jiang, B., Xu, D., Jiang, C., Li, Q. and Gu, T. (2016). "Severe microbiologically influenced corrosion of S32654 super austenitic stainless steel by acid producing bacterium *Acidithiobacillus caldus* SM-1." Bioelectrochemistry **123**: 34-44.

Dong, Z., Zhu, Y., Han, Y., Gu, X. and Jiang, K. (2019). "Study of pyrite oxidation with chlorine dioxide under mild conditions." Minerals Engineering **133**: 106-114.

Dong, Z. H., Shi, W., Ruan, H. M. and Zhang, G. A. (2011). "Heterogeneous corrosion of mild steel under SRB-biofilm characterised by electrochemical mapping technique." Corrosion Science **53**: 2978-2987.

Donlan, R. M. (2001). "Biofilm Formation: A Clinically Relevant Microbiological Process." Healthcare Epidemiology **33**: 1387-1392.

Drissi, S. H., Refait, P., Abdelmoula, M. and Genin, J. M. R. (1995). "The Preparation And Thermodynamic Properties Of Fe(II)-Fe(III) Hydroxide-Carbonate (Green Rust 1); Pourbaix Diagram Of Iron In Carbonate-Containing Aqueous Media." Corrosion Science **37**(12): 2025-2041.

Duan, J., Wu, S., Zhang, X., Huang, G., Du, M. and Hou, B. (2008). "Corrosion of carbon steel influenced by anaerobic biofilm in natural seawater." Electrochimica Acta **54**: 22-28.

Dubiel, M., Hsu, C. H., Chien, C. C., Mansfeld, F. and Newman, D. K. (2002). "Microbial Iron Respiration Can Protect Steel from Corrosion." Applied And Environmental Microbiology **68**(3): 1440-1445.

Dutrow, B. L. (2020). "X-ray Powder Diffraction." Retrieved 24/04/21, 2021, from https://serc.carleton.edu/research_education/geochemsheets/techniques/XRD.html.

Dvorkin, J., Prasad, M., Sakai, A. and Lavoie, D. (1999). "Elasticity of marine sediments: Rock physics modeling." Geophysical Research Letters **26**(12): 1781-1784.

Dzierzewicz, B., Cwalina, B., Chodurek, E. and Wilczok, T. (1997). "The relationship between microbial metabolic activity and biocorrosion of carbon steel." Research in Microbiology **148**: 785-793.

Eashwar, M., Maruthamuthu, S. and Iyer, S. V. (2004). "A possible role for phototrophic sulphur bacteria in the promotion of anaerobic metal corrosion." Current Science **86**(5): 639-641.

Eid, M. E., Duncan, K. E. and Tanner, R. S. (2018). "A semi-continuous system for monitoring microbially influenced corrosion." Journal of Microbiological Methods **150**: 55-60.

Engineering and Construction. (2013). "Sheet Pile Types - Steel Structures." Retrieved 11th March, 2015, from <http://www.thecivilbuilders.com/2013/03/sheet-piles-types-steel-structures.html>.

Enning, D. and Garrelfs, J. (2014). "Corrosion of Iron by Sulfate-Reducing Bacteria: New Views of an Old Problem." Applied and Environmental Microbiology **80**(4): 1226-1236.

Enning, D., Venzlaff, H., Garrelfs, J., Dinh, H. T., Meyer, V., Mayrhofer, K. J. J., Hassel, A. W., Stratmann, M. and Widdel, F. (2012). "Marine sulfate-reducing bacteria cause serious corrosion of iron under electroconductive biogenic mineral crust." Environmental Microbiology **14**(7): 1772-1787.

Faix, O. (1992). Fourier transform infrared spectroscopy. Methods in lignin chemistry. Berlin, Heidelberg, Springer: 83-109.

Fakruddin, M. and Chowdhury, A. (2012). "Pyrosequencing-An Alternative to Traditional Sanger Sequencing." American Journal of Biochemistry and Biotechnology **8**(1): 14-20.

Fan, B., Hao, H., Yang, B. and Li, Y. (2018). "Insights into the inhibition mechanism of a novel supramolecular complex towards the corrosion of mild steel in the condensate water: experimental and theoretical studies." Research on Chemical Intermediates **44**(10): 5711–5736.

Fei, J., Zhao, J., Du, C., Ma, H., Zhang, H. and Li, J. (2013). "Facile 3D Self-Assembly of Porous Iron Hydroxide and Oxide Hierarchical Nanostructures for Removing Dyes from Wastewater." Journal of Materials Chemistry A **1**: 10300–10305.

Feinberg, L. F. (2007). Dissimilatory iron reduction in the hyperthermophilic Archaea Pyrobaculum. Doctor Of Philosophy University of Massachusetts.

Filippov, L. O., Severov, V. V. and Filippova, I. V. (2014). "An overview of the beneficiation of iron ores via reverse cationic flotation." International Journal of Mineral Processing **127**: 62–69.

Fontaine, E. R., Bryant, T. N., Taylor-Robinson, D., Borriello, S. P. and Davies, H. A. (1986). "A Numerical Taxonomic Study of Anaerobic Gram-negative Bacilli Classified as *Bacteroides ureolyticus* Isolated from Patients with Non-gonococcal Urethritis." Journal of General Microbiology **132**: 3137-3146.

Forte Giacobone, A. F., Pizarro, R. A., Rodriguez, S. A., Belloni, M., Croatto, F. J., Ferrari, F., Herrera, C., Mendizabal, M. I., Montes, J., Aliciardi, M. R., Saucedo, R., Ovando, L. E. and Burkart, A. L. (2015). "Biocorrosion at Embalse Nuclear Power Plant. Analysis of the Effect of a Biocide Product." Procedia Materials Science **8**: 101-107.

Forte Giacobone, A. F., Rodriguez, S. A., Burkart, A. L. and Pizarro, R. A. (2011). "Microbiological induced corrosion of AA 6061 nuclear alloy in highly diluted media by *Bacillus cereus* RE 10." International Biodeterioration & Biodegradation **65**: 1161-1168.

Friedrich, M. W. (2002). "Phylogenetic Analysis Reveals Multiple Lateral Transfers of Adenosine-5'-Phosphosulfate Reductase Genes among Sulfate-Reducing Microorganisms." JOURNAL OF BACTERIOLOGY **184**(1): 278–289.

Frost, R. L. and Klopogge, J. T. (1999). "Infrared emission spectroscopic study of brucite." Spectrochimica Acta Part A **55**: 2195–2205.

Fu, H. and Quan, X. (2006). "Complexes of fulvic acid on the surface of hematite, goethite, and akaganeite: FTIR observation." Chemosphere(63): 403–410.

Furukawa, Y. and Barnes, H. L. (1996). "Reactions forming smythite, Fe₉S₁₁." Geochimica et Cosmochimica Acta **60**(19): 3581-3591.

Furukawa, Y., Kim, J.-W., Watkins, J. and Wilkin, R. T. (2002). "Formation of Ferrihydrite and Associated Iron Corrosion Products in Permeable Reactive Barriers of Zero-Valent Iron." Environ. Sci. Technol. **36**: 5469-5475.

Gaines, R. (1910). "Bacterial activity as a corrosive influence in the soil." Ind. Eng. Chem. **2**: 128–130.

Galarce, C., Pineda, F., Fischer, D. A., Flores, M., Vargas, I. T., Sancy, M. and Pizarro, G. E. (2019). "Effect of Hazardous Bacteria Isolated From Copper Plumbing System on

Microbiologically Influenced Corrosion of Copper." Int. J. Electrochem. Sci. **14**: 2305 – 2320.

Galyon Dorman, S. E., Hoff, B. K., Reid, T. A., Collins, S. E. and Henning, D. H. (2014). The Effect of Ralstonia pickettii on Environmental Fatigue Crack Growth of 7xxx Series Aluminum Alloys, Trans Tech Publications Ltd.

Ganachari, S. V., Joshi, V. K., Bhat, R., Deshpande, B., Salimath, B., Rao, N. V. S. and Venkataraman, A. (2012). "Large scale synthesis and characterization of γ -Fe₂O₃ nanoparticles by self-propagating low temperature combustion method." International Journal of Science Research **1**(2): 77-79.

Geets, J., Borremans, B., Diels, L., Springael, D., Vangronsveld, J., van der Lelie, D. and Vanbroekhoven, K. (2006). "DsrB gene-based DGGE for community and diversity surveys of sulfate-reducing bacteria." Journal of Microbiological Methods **66**: 194-205.

Genin, J. R., Christy, A., Kuzmann, E., Mills, S. and Ruby, C. (2014). "Structure and occurrences of green rust related new minerals of the fougérite group, trebeurdenite and mossbauerite, belonging to the hydrotalcite supergroup; how Mossbauer spectroscopy helps XRD." Hyperfine Interact **226**: 459–482.

Gest, H. (2004). "The discovery of microorganisms by Robert Hooke and Antoni van Leeuwenhoek, Fellows of The Royal Society." The Royal Society Journal of the History of Science **58**(2).

Gharizadeh, B. M., Ghaderi, M. and Nyren, P. (2007). "Pyrosequencing technology for short DNA sequencing and whole genome sequencing." Tech. **47**: 129-132.

Ghassa, S., Noaparast, M., Shafaei, S. Z., Abdollahi, H., Gharabaghi, M. and Boruomand, Z. (2017). "A study on the zinc sulfide dissolution kinetics with biological and chemical ferric reagents." Hydrometallurgy **171**: 362–373.

Giblin, A. E. and Howarth, R. W. (1984). "Porewater evidence for a dynamic sedimentary iron cycle in salt marshes." Limnology and Oceanography **29**: 47-63.

Gil, P. P., Pesquera, A. and Velas, F. (1998). "X-ray diffraction, infrared and Mössbauer studies of Fe-rich carbonates." Eur. J. Mineral. **4**: 521-526.

Glomics Inc. (2014). "GeoChip Technology." Retrieved 4th April, 2015, from <http://www.glomics.com/gch-tech.html>.

Gokulakumar, B., Nedunchezian, G., Vijayaraj, C. and Balamurugan, A. (2016). "Fourier Transform Infrared Spectroscopy Studies On Talcum Powders." International Journal of Recent Scientific Research **7**(12): 14505-14507.

- Gomez-Alvarez, V., Revette, R. P. and Santo Domingo, J. W. (2012). "Metagenome analyses of corroded concrete wastewater pipe biofilms reveal a complex microbial system." BMC Microbiology **12**(122).
- Gori, A., Cerboneschi, M. and Tegli, S. (2012). "High-Resolution Melting Analysis as a Powerful Tool to Discriminate and Genotype *Pseudomonas savastanoi* Pathovars and Strains." PLoS ONE **7**(1): 1 - 13.
- Gotic, M. and Music, S. (2007). "Mossbauer, FT-IR and FE SEM investigation of iron oxides precipitated from FeSO₄ solutions." Journal of Molecular Structure **834-836**: 445-453.
- Green, S. J., Leigh, M. B. and Neufeld, J. D. (2010). Denaturing Gradient Gel Electrophoresis (DGGE) for Microbial Community Analysis. Handbook of Hydrocarbon and Lipid Microbiology. K. N. Timmis. Berlin, Heidelberg, Springer Berlin Heidelberg: 4137-4158.
- Griswold, A. (2008). "Genome packaging in prokaryotes: the circular chromosome of *E. coli*." Nature Education **1**(1): 5-7.
- Guerra, J. C., Howland, J. J., Corvo, F., Castañeda, A. and Rodríguez, J. (2018). "Atmospheric corrosion of low carbon steel in a coastal zone of Ecuador: Anomalous behavior of chloride deposition versus distance from the sea." Materials and Corrosion **70**: 444-460.
- Guezennec, J. G. (1994). "Cathodic Protection and Microbially Induced Corrosion." International Biodeterioration and Biodegradation: 275-288.
- Guilbaud, R., White, M. L. and Poulton, S. W. (2013). "Surface charge and growth of sulphate and carbonate green rust in aqueous media." Geochimica et Cosmochimica Acta **108**: 141–153.
- Guo, J., Yuan, S., Jiang, W., Lv, L., Liang, B. and Pehkonen, S. O. (2018). "Polymers for Combating Biocorrosion." Frontiers in Materials **5**(10): 1-15.
- Gurtler, V., Grando, D., Mayall, B. C., Wang, A. and Ghaly-Derias, S. (2012). "A novel method for simultaneous Enterococcus species identification/typing and van genotyping by high resolution melt analysis." Journal of Microbiological Methods **90**: 167-181.
- Guven, D. E. and Akinci, G. (2001). "Comparison of Acid Digestion Techniques To Determine Heavy Metals In Sediment And Soil Samples." Gazi University Journal of Science **29**(1): 29-34.
- Han, J., Lu, Q., Zhou, L., Liu, H. and Xiang, H. (2009). "Identification of the Polyhydroxyalkanoate (PHA)-Specific Acetoacetyl Coenzyme A Reductase among Multiple FabG Paralogs in *Haloarcula hispanica* and Reconstruction of the PHA

- Biosynthetic Pathway in *Haloferax volcanii*." Applied And Environmental Microbiology **75**(19): 6168–6175.
- Hansen, H. C. B. (1989). "Composition, Stabilization, And Light Absorption Of Fe(II)Fe(III) Hydroxy-Carbonate ('Green Rust')." Clay Minerals **24**: 663-669.
- Haosagul, S., Prommeenate, P., Hobbs, G. and Pisutpaisal, N. (2019). "Sulfide-oxidizing bacteria community in full-scale bioscrubber treating H₂S in biogas from swine anaerobic digester." Renewable Energy **150**: 973-980.
- Haque, R. U., Paradisi, F. and Allers, T. (2020). "Haloferax volcanii for biotechnology applications: challenges, current state and perspectives." Applied Microbiology and Biotechnology **104**: 1371–1382.
- Haslett, S. K. (2000). Coastal Systems. New York, NY, Routledge.
- Hausner, D. B., Bhandari, N., Pierre-Louis, A.-M., Kubicki, J. D. and Strongin, D. R. (2009). "Ferrihydrite reactivity toward carbon dioxide." Journal of Colloid and Interface Science **337** 492–500.
- He, Z., Gentry, T. J., Schadt, C. W., Wu, L., Liebich, J., Chong, S. C., Huang, Z., Wu, W., Gu, B., Jardine, P., Criddle, C. and Zhou, J. (2007). "GeoChip: a comprehensive microarray for investigating biogeochemical, ecological and environmental processes." ISME J **1**(1): 67-77.
- He, Z., Zhang, P., Wang, J., Elias, D. A., Adams, P. D., Wu, L., Yan, Q., Watson, D. B., Arkin, A. P., Rocha, A. M., Curtis, D., Adams, M. W. W., Zhou, J., Tu, Q., Ning, D., Shi, Z., Van Nostrand, J. D., Fields, M. W., Wu, B., Wu, L., Alm, E. J., Qin, Y., Yang, Y. and Hazen, T. C. (2018). "Microbial Functional Gene Diversity Predicts Groundwater Contamination and Ecosystem Functioning." American Society for Microbiology **9**(1): 1-15.
- Heather, J. M. and Chain, B. (2016). "The sequence of sequencers: The history of sequencing DNA." Genomics **107**: 1-8.
- Hedrich, S., Schlomann, M. and Johnson, D. B. (2011). "The iron-oxidizing proteobacteria." Microbiology **157**: 1551–1564.
- Heitz, E., Flemming, H. C. and Sand, W. (1996). Microbially Induced Corrosion of Materials. Berlin, Germany, Springer-Verlag GmbH & Co.
- Hennekam, R. and de Lange, G. (2012). "X-ray fluorescence core scanning of wet marine sediments: methods to improve quality and reproducibility of high-resolution paleoenvironmental records." Limnology And Oceanography: Methods **10**: 991–1003.

- Herrera, L. K. and Videla, H. A. (2009). "Role of iron-reducing bacteria in corrosion and protection of carbon steel." International Biodeterioration & Biodegradation **63**: 891–895.
- Herro, H. M. (1998). MIC myths -- Does pitting cause MIC? NACE International. Houston, TX.
- Hewayde, E. and Nehdi, M. (2007). "Effect of mixture design parameters and wetting-drying cycles on resistance of concrete to sulfuric acid attack." Journal of Materials in Civil Engineering **19**(2): 155-163.
- Hjelmsø, M. H., Hansen, L. H., Bælum, J., Feld, L., Holben, W. E. and Jacobsena, C. S. (2014). "High-Resolution Melt Analysis for Rapid Comparison of Bacterial Community Compositions." Applied and Environmental Microbiology **80**(12): 3568-3575.
- Ho, A., Murphy, M., Wilson, S., Atlas, S. R. and Edwards, J. S. (2011). "Sequencing by ligation variation with endonuclease V digestion and deoxyinosine-containing query oligonucleotides." BMC Genomics **12**(598): 1-8.
- Holder, C. F. and Schaak, R. E. (2019). Tutorial on Powder X-ray Diffraction for Characterizing Nanoscale Materials. ACS Nano.
- Homberg, A. M., Leon Morales, C. F., Tinga, T., de Wit, J. H. W. and Mol, J. M. C. (2014). "Detection of microbially influenced corrosion by electrochemical noise transients." Electrochimica Acta **136**: 223-232.
- Hong, S., Wu, Y., Gao, W., Zhang, J., Zhang, Y. and Zhang, Y. (2018). "Slurry erosion-corrosion resistance and microbial corrosion electrochemical characteristics of HVOF sprayed WC-10Co-4Cr coating for offshore hydraulic machinery." International Journal of Refractory Metals & Hard Materials **74**: 7-13.
- Hou, X. and Jones, B. T. (2000). Inductively Coupled Plasma/Optical Emission Spectrometry. Encyclopedia of Analytical Chemistry. R. A. Meyers. Chichester, UK, John Wiley & Sons Ltd: 9468–9485.
- Huang, S., Bergonzi, C., Schwab, M., Elias, M. and Hicks, R. E. (2019). "Evaluation of biological and enzymatic quorum quencher coating additives to reduce biocorrosion of steel." PLOS ONE **14**(5): 1-18.
- Huang, Y. F., Chen, S. C., Chiang, Y. S., Chen, T. H. and Chiu, K. P. (2012). "Palindromic sequence impedes sequencing-by-ligation mechanism." BMC Syst Biol **6**: 1-7.

Huber, B., Herzog, B., Drewes, J. E., Koch, K. and Müller, E. (2016). "Characterization of sulfur oxidizing bacteria related to biogenic sulfuric acid corrosion in sludge digesters." BMC Microbiology **16**(153): 1-11.

Huerta-Diaz, M. A. and Morse, J. W. (1992). "Pyritization of trace metals in anoxic marine sediments." Geochemica Cosmochimica Acta **56**: 2681-2702.

Hui, B. H. and Salimi, M. N. (2019). "Production of Iron Oxide Nanoparticles by Co-Precipitation method with Optimization Studies of Processing Temperature, pH and Stirring Rate." Materials Science and Engineering **743**: 1-13.

Ilhan-Sungur, E., Cansever, N. and Cotuk, A. (2007). "Microbial corrosion of galvanized steel by a freshwater strain of sulphate reducing bacteria (*Desulfovibrio* sp.)." Corrosion Science **49**: 1097-1109.

Industrial Metallurgists LLC. (2020). "Hydrogen Embrittlement Of Steel." Retrieved 31/09/20, from <https://www.imetllc.com/training-article/hydrogen-embrittlement-steel/>.

International Navigation Association Work Group 44 of Maritime Navigation Commission. (2005). "Accelerated low water corrosion." Retrieved 11.04.12, 2012, from http://www.pianc.us/workinggroups/docs_wg/marcom-wg44.pdf.

iSheetPile. (2009). "The Facts on Rust and Corrosion." Retrieved 5th April, 2015, from <http://www.isheetpile.com/articles/corrosion>.

Islander, R. L., Deviny, J. S., Mansfeld, F., Postyn, A. and Shih, H. (1991). "Microbial Ecology of Crown Corrosion in Sewers." Journal Of Environmental Engineering **117**(6): 751 - 770.

Iverson, W. P. (2001). "Research on the mechanisms of anaerobic corrosion." International Biodeterioration and Biodegradation **47**: 63-70.

Jack, T. R., Wilmott, M. J. and Sutherby, R. L. (1995). "Indicator minerals formed during external corrosion of line pipe." Mater. Perform. **34**: 19-22.

Jaen, J. A. and Iglesias, J. (2017). "Corrosion study of steels exposed over five years to the humid tropical atmosphere of Panama." Hyperfine Interact **238**(37): 1-10.

Jagtap, S. D., Tambe, S. P., Choudhari, R. N. and Mallik, B. P. (2013). "Mechanical and anticorrosive properties of non toxic coal-tar epoxy alternative coating." Progress in Organic Coatings **77**(2): 395-402.

Jansen, S., Gerritse, J., van Burgel, M. and Buchler, M. (2017). Cathodic Protection and MIC - Effects of Local Electrochemistry. NACE International Corrosion Conference.

- Javaherdashti, R. (2009). "Microbiological contribution to accelerated low water corrosion of support piles." Port Technology International **29**: 59-63.
- Jia, F., Wang, J., Chen, Y., Zhang, X., Wang, Q., Chen, D. and Zhang, C. (2019). "Effect of oil contents on gluten network during the extrusion processing." Czech Journal of Food Sciences **37**(4): 226–231.
- Jia, R., Unsal, T., Xu, D., Lekbach, Y. and Gu, T. (2019). "Microbiologically influenced corrosion and current mitigation strategies: A state of the art review." International Biodeterioration & Biodegradation **137**: 42–58.
- Jiang, Z., Li, P., Wang, Y., Liu, H., Wei, D., Yuan, C. and Wang, H. (2019). "Arsenic mobilization in a high arsenic groundwater revealed by metagenomic and Geochip analyses." Scientific Reports **9**(12972).
- Jimoh, O. A., Otitoju, T. A., Hussin, H., Ariffin, K. S. and Baharun, N. (2017). "Understanding the Precipitated Calcium Carbonate (PCC) Production Mechanism and Its Characteristics in the Liquid–Gas System Using Milk of Lime (MOL) Suspension." S. Afr. J. Chem. **70**: 1-7.
- Jin, J. and Guan, Y. T. (2014). "The mutual co-regulation of extracellular polymeric substances and iron ions in biocorrosion of cast iron pipes." Bioresource Technology **169**: 387-394.
- Jin, J., Wu, G. and Guan, Y. (2015). "Effect of bacterial communities on the formation of cast iron corrosion tubercles in reclaimed water." Water Research **71** 207-218.
- Jones, A. M., Collins, R. N. and D., W. T. (2017). "Redox characterization of the Fe(II)-catalyzed transformation of ferrihydrite to goethite." Geochimica et Cosmochimica Acta **218**: 257–272.
- Jørgensen, B. B., Findlay, A. J. and Pellerin, A. (2019). "The Biogeochemical Sulfur Cycle of Marine Sediments." Frontiers in Microbiology **10**: 1 - 27.
- Jørgensen, B. B. and Kasten, S. (2006). Sulfur Cycling and Methane Oxidation. Marine Geochemistry.
- Jovanovski, G., Stefov, V., Soptrajanov, B. and Boev, B. (2002). "Minerals from Macedonia. IV. Discrimination between some carbonate minerals by FTIR spectroscopy." N.Jb.Mineral.Abh. **177**(3): 241–253.
- Jung, S. P., Yoon, M., Lee, S., Oh, S., Kang, H. and Yang, J. (2014). "Power Generation and Anode Bacterial Community Compositions of Sediment Fuel Cells Differing in Anode Materials and Carbon Sources." Int. J. Electrochem. Sci. **9**: 315 - 326.

- Kamarisima, Hidaka, K., Miyanaga, K. and Tanji, Y. (2018). "The presence of nitrate- and sulfate-reducing bacteria contributes to ineffectiveness souring control by nitrate injection." International Biodeterioration and Biodegradation **129**: 81-88.
- Kerrigan, Z., Kirkpatrick, J. B. and D'Hondt, S. (2019). "Influence of 16S rRNA Hypervariable Region on Estimates of Bacterial Diversity and Community Composition in Seawater and Marine Sediment." Frontiers in Microbiology **10**: 1-12.
- Kiernan, D. (2020). "Introduction, Simpson's Index and Shannon-Weiner Index." Retrieved 27/04/21, 2021, from <https://stats.libretexts.org/@go/page/2932>.
- Kim, B. H., Lim, S. S., Daud, W. R. W., Gadd, G. M. and Chang, I. S. (2015). "The biocathode of microbial electrochemical systems and microbially-influenced corrosion." Bioresource Technology **190**: 395-401.
- Kim, J. D., Yee, N., Nanda, V. and Falkowski, P. G. (2013). "Anoxic photochemical oxidation of siderite generates molecular hydrogen and iron oxides." PNAS **110**(25): 10073–10077.
- King, R. A. and Miller, J. D. A. (1971). "Corrosion by sulphate-reducing bacteria." Nature **233**: 491-492.
- Kletzin, A. (1988). "Coupled enzymatic production of sulfite, thiosulfate, and hydrogen sulfide from sulfur: Purification and properties of a sulfur oxygenase reductase from the facultatively anaerobic archaeobacterium *desulfurolobus ambivalens*." Journal Of Bacteriology **171**(3): 1638-1643.
- Komatina, M. and Gudenau, H. W. (2004). "The Sticking Problem During Direct Reduction Of Fine Iron Ore In The Fluidized Bed." Metalurgija - Journal of Metallurgy **11**: 309-328.
- Kong, L., Zhang, B. and Fang, J. (2017). "Study on the applicability of bactericides to prevent concrete microbial corrosion." Corrosion and building materials **149**: 1-8.
- Kostka, J. E., Teske, A. P., Joye, S. B. and Head, I. M. (2014). "The metabolic pathways and environmental controls of hydrocarbon biodegradation in marine ecosystems." Frontiers in Microbiology **5**: 1-3.
- Koush, W. A., Farahat, L. A., Labena, A., Mohamed, T. M. and Elsayy, H. (2020). "Microbial Corrosion of C1018 Mild Steel by A Halotolerant Consortium of Sulfate Reducing Bacteria Isolated from an Egyptian Oil Field." Egyptian Journal of Chemistry **63**(4): 1461-1468.
- Kozubal, M. A., Kocar, B. D., Jay, Z. J., Beam, J. P., Malfatti, S. A., Tringe, S. G., Macur, R. E., Borch, T. and Inskeep, W. P. (2012). "Microbial iron cycling in acidic geothermal springs of Yellowstone National Park: integrating molecular surveys,

geochemical processes, and isolation of novel Fe-active microorganisms." Frontiers in Microbiology **3**(109): 1-16.

Kumar, A. and Stephenson, L. D. (2005). "MIC on steel structures in marine environments." Port Technology International **27**: 59-62.

Lamine, G. M. and Azzedine, M. A. (2013). Assessment Of Bacterial Corrosion At The Gas Processing Plants. Offshore Mediterranean Conference. Ravenna, Italy.

Lanzen, A., Lekang, K., Jonassen, I., Thompson, E. M. and Troedsson, C. (2017). "DNA extraction replicates improve diversity and compositional dissimilarity in metabarcoding of eukaryotes in marine sediments." PLOS ONE **12**(6): 1-18.

Lau, S. K. P., Woo, P. C. Y., Woo, G. K. S., Fung, A. M. Y., Wong, M. K. M., Chan, K., Tam, D. M. W. and Yuen, K. (2004). "Eggerthella hongkongensis sp. nov. and Eggerthella sinensis sp. nov., two novel Eggerthella species, account for half of the cases of Eggerthella bacteremia." Diagnostic Microbiology and Infectious Disease **49**: 255–263.

Laurent, F., Grosgeat, B., Reclaru, L., Dalard, F. and Lissac, M. (2000). "Comparison of corrosion behaviour in presence of oral bacteria." Biomaterials **22**: 2273-2282.

Lawler, D. M., Petts, G. E., Foster, I. D. L. and Harper, S. (2006). "Turbidity dynamics during spring storm events in an urban headwater river system: the Upper Tame, West Midlands, UK." Science of the Total Environment **360**(1-3): 109-126.

Lee, A. K. and Newman, D. K. (2003). "Microbial iron respiration: impacts on corrosion processes." Applied Microbiology and Biotechnology **62**: 134-139.

Legrand, L., Abdelmula, M., Gehin, A., Chausse, A. and Genin, J. M. R. (2001). "Electrochemical formation of a new Fe(II)-Fe(III) hydroxy-carbonate green rust: characterisation and morphology." Electrochimica Acta **46**: 1815–1822.

Legrand, L., Mazerolles, L. and Chausse, A. (2004). "The oxidation of carbonate green rust into ferric phases: solid-state reaction or transformation via solution." Geochimica et Cosmochimica Acta **68**(17): 3497–3507.

Lennie, A. R. and Vaughan, D. J. (1996). "Spectroscopic studies of iron sulfide formation and phase relations at low temperatures." Mineral Spectroscopy **5**: 117-130.

Lenntech. (2020). "Iron and water: reaction mechanisms, environmental impact and health effects." Retrieved 24/11/20, from <https://www.lenntech.com/periodic/water/iron/iron-and-water.htm>.

Lerm, S., Westphal, A., Miethling-Graff, R., Alawi, M., Seibt, A., Wolfgramm, M. and Würdemann, H. (2013). "Thermal effects on microbial composition and

microbiologically induced corrosion and mineral precipitation affecting operation of a geothermal plant in a deep saline aquifer." Extremophiles **17**(2): 311-327.

Lerman, L. S., Fischer, S. G., Hurley, J., Silverstein, K. and Lumelsky, N. (1984). "Sequence-determined DNA separations." Annual Review in Biophysics and Bioengineering **13**: 399-424.

Li, J., Nedwell, D. B., Beddow, J., Dumbrell, A. J., McKew, B. A., Thorpe, E. L. and Whitby, C. (2014). "amoA Gene Abundances and Nitrification Potential Rates Suggest that Benthic Ammonia-Oxidizing Bacteria and Not Archaea Dominate N Cycling in the Colne Estuary, United Kingdom." Applied and Environmental Microbiology **81**(1): 159-165.

Li, S., Zhang, Y., Liu, J. and Yu, M. (2008). "Corrosion Behavior of Steel A3 Influenced by Thiobacillus Ferrooxidans." Acta Physico-Chimica Sinica **24**(9): 1553-1557.

Li, X. (2015). "Share corrosion data." Nature **527**: 441-442.

Li, X., Arai, H., Shimoda, I., Kuraishi, H. and Katayama, Y. (2008). "Enumeration of Sulfur-Oxidizing Microorganisms on Deteriorating Stone of the Angkor Monuments, Cambodia." Microbes and Environments **23**(4): 293-298.

Li, Z., Wan, H., Song, D., Liu, X., Li, Z. and Du, C. (2019). "Corrosion behavior of X80 pipeline steel in the presence of *Brevibacterium halotolerans* in Beijing soil." Bioelectrochemistry **126**: 121-129.

Liang, R., Aydin, E., Le Borgne, S., Sunner, J., Duncan, K. E. and Suflita, J. M. (2018). "Anaerobic biodegradation of biofuels and their impact on the corrosion of a Cu-Ni alloy in marine environments." Chemosphere **195**: 427-436.

Liang, R., Davidova, I. A., Marks, C. R., Stamps, B. W., Harriman, B. H., Stevenson, B. S., Duncan, K. E. and Suflit, J. M. (2016). "Metabolic Capability of a Predominant *Halanaerobium* sp. in Hydraulically Fractured Gas Wells and Its Implication in Pipeline Corrosion." Frontiers in Microbiology **7**: 1-10.

Liang, R., Duncan, K. E., Le Borgne, S., Davidova, I., Yakimov, M. M. and Suflita, J. M. (2016). "Microbial activities in hydrocarbon-laden wastewaters: Impact on diesel fuel stability and the biocorrosion of carbon steel." Journal of Biotechnology **256**: 68-75.

Liduino, V. S., Cravo-Laureau, C., Noel, C., Carbon, A., Duran, R., Lutterbach, M. T. and S ervulo, E. F. C. (2019). "Comparison of flow regimes on biocorrosion of steel pipe weldments: Community composition and diversity of biofilm." International Biodeterioration & Biodegradation **143**: 1-10.

Liengen, T., Feron, D., Basseguy, R. and Beech, I. B., Eds. (2014). Understanding Biocorrosion: Fundamentals and Applications, Woodhead Publishing Ltd.

Little, B., Wagner, P., Hart, K., Ray, R., Lavoie, D., Neilson, K. and Aguilar, C. (1998). "The role of biomineralization in microbiologically influenced corrosion." Biodegradation **9**: 1–10.

Little, B. J., Blackwood, D. J., Hinks, J., Lauro, F. M., Marsili, E., Okamoto, A., Rice, S. A., Wadeg, S. A. and Flemming, H. C. (2020). "Microbially influenced corrosion—Any progress?" Corrosion Science **170**: 1-17.

Little, B. J., Gerke, T. L. and Lee, J. S. (2014). "Mini-review: the morphology, mineralogy and microbiology of accumulated iron corrosion products." Biofouling **30**(8): 941-948.

Little, B. J., Gerke, T. L., Ray, R. I. and Lee, J. S. (2015). Minerals, scales and deposits. Oxford, UK, Elsevier.

Little, B. J. and Lee, J. S. (2007). Microbially Influenced Corrosion. Wiley Series in Corrosion. R. W. Revie. Hoboken, USA.

Little, B. J., Lee, J. S. and Ray, R. I. (2007). "Diagnosing Microbiologically Influenced Corrosion: A State-of-the-Art Review." Corrosion Science **62**(11): 1006-1017.

Liu, H. and Fang, H. H. P. (2002). "Extraction of extracellular polymeric substances (EPS) of sludges." Journal of Biotechnology **95**: 249-246.

Liu, H., Fu, C., Gu, T., Zhang, G., Lv, Y., Wang, H. and Liu, H. (2015). "Corrosion behavior of carbon steel in the presence of sulfate reducing bacteria and iron oxidizing bacteria cultured in oilfield produced water." Corrosion Science **100**: 484-495.

Liu, H., Yu, T. and Liu, Y. (2015). "Sulfate reducing bacteria and their activities in oil sands process-affected water biofilm." Science of the Total Environment **536**: 116-122.

Liu, J. F., Lu, Y. W., Liu, X. B., Li, B. G., Sun, Y. F., Zhou, L., Liu, Y. F., Yang, S. Z., Gu, J. D. and Mu, B. Z. (2020). "Dominance of Pseudomonas in bacterial community and inhibition of fumarate addition pathway by injection of nutrients in oil reservoir revealed by functional gene and their transcript analyses." International Biodeterioration & Biodegradation **153**: 1-9.

Liu, Y., Singh, P. and Mustapha, A. (2018). "High-resolution melt curve PCR assay for specific detection of E. coli O157:H7 in beef." Food Control **86**: 275-282.

Logan, M. (2011). "Tutorial 13.2 - Species richness and diversity." Retrieved 27/04/21, 2021, from <https://www.flutterbys.com.au/stats/tut/tut13.2.html>.

- Lovley, D. R. (1993). "Dissimilatory metal reduction." Annual Reviews of Microbiology **47**: 263–290.
- Lovley, D. R., Holmes, D. E. and Nevin, K. P. (2004). Dissimilatory Fe(III) and Mn(IV) Reduction. Advances in microbial physiology. R. K. Poole. **49**.
- Low, A., Ng, C. and He, J. (2016). "Identification of antibiotic resistant bacteria community and a GeoChip based study of resistome in urban watersheds." Water Research **106**: 330-338.
- Lucena-Padros, H., Jimenez, E., Maldonado-Barragan, A., Rodríguez, J. M. and Ruiz-Barba, J. L. (2015). "PCR-DGGE assessment of the bacterial diversity in Spanish-style green table-olive fermentations." International Journal of Food Microbiology: 1-30.
- Luo, J., Tan, X., Liu, K. and Lin, W. (2018). "Survey of sulfur-oxidizing bacterial community in the Pearl River water using soxB, sqr, and dsrA as molecular biomarkers." 3 Biotech **8**(1): pp73.
- Ma, M., Zhang, Y., Yu, W., Shen, H., Zhang, H. and Gu, N. (2003). "Preparation and characterization of magnetite nanoparticles coated by amino silane." Colloids and Surfaces A: Physicochem. Eng. Aspects **212**: 219-226.
- Ma, X., Zhang, Q., Zheng, M., Gao, Y., Yuan, T., Hale, L., Van Nostrand, J. D., Zhou, J., Wan, S. and Yang, Y. (2019). "Microbial functional traits are sensitive indicators of mild disturbance by lamb grazing." The ISME journal **13**(5): 1370-1373.
- Ma, Y., Li, Y. and F., W. (2008). "The effect of *B*-FeOOH on the corrosion behavior of lowcarbon steel exposed in tropic marine environment." Materials Chemistry and Physics **112**: 844–852.
- Machuca, L. L., Jeffrey, R. and Melchers, R. E. (2016). "Microorganisms associated with corrosion of structural steel in diverse atmospheres." International Biodeterioration & Biodegradation **114**: 234-243.
- Madigan, M. T., Martinko, J. M., Dunlap, P. V. and Clark, D. P. (2009). Biology of Microorganisms. San Francisco, CA, USA, Pearson Benjamin Cummings.
- Madirisha, M., Lievens, C., Hack, R. and van der Meer, F. (2020). Bio-corrosion and Acid Stimulation in Geothermal Operations. 3rd International TEP Conference. Zanzibar.
- Magot, M., Ravot, I. G., Campaignolle, X., Ollivier, B., Patel, B. K. C., Fardeau, M. L., Thomas, P., Crolet, J. and Garcia, J. (1997). "Dethiosulfovibrio peptidovorans gen. nov., sp. nov., a New Anaerobic, Slightly Halophilic, Thiosulfate-Reducing Bacterium from Corroding Offshore Oil Wells." International Journal Of Systematic Bacteriology **47**(3): 818-824.

Majzlan, J., Koch, C. B. and Navrotsky, A. (2008). "Hermodynamic properties of feroxyhyte (δ' -FeOOH) " Clays and Clay Minerals **56**(5): 526–530.

Mand, J., Park, H. S., Jack, T. R. and Voordouw, G. (2014). "The role of acetogens in microbially influenced corrosion of steel." Frontiers in Microbiology **5**: 1-14.

Mapsofuk.co.uk. (2015). "Maps Of UK Cities And Regions Pictures." Retrieved 2nd April, 2015, from <http://www.mapsofuk.co.uk/2014/06/simple-maps-of-uk-black-and-white-color.html>.

Marty, D. G. (1993). "Methanogenic bacteria in seawater." Limnol. Oceanogr. **38**(2): 452-456.

Marty, F., Ghliglione, J. F., Païssé, S., Quillet, L., Van Loosdrecht, M. C. M. and Muyzer, G. (2012). "Evaluation and optimization of nucleic acid extraction methods for the molecular analysis of bacterial communities associated with corroded carbon steel." Biofouling **28**(4): 363-380.

Marty, F., Gueuné, H., Malard, E., Sanchez-Amaya, J. M., Sjogren, L., Abbas, B., Quillet, L., van Loosdrecht, M. C. M. and Muyzer, G. (2014). "Identification of key factors in Accelerated Low Water Corrosion through experimental simulation of tidal conditions: influence of stimulated indigenous microbiota." Biofouling **30**(3): 281-297.

Masselink, G., Hughes, M. and Knight, J. (2011). Introduction to Coastal Processes and Geomorphology. UK, Hodder Education.

Masurat, P., Fru, E. C. and Pedersen, K. (2005). "Identification of *Meiothermus* as the dominant genus in a storage system for spent nuclear fuel." Journal of Applied Microbiology **98**: 727–740.

Matthiesen, H., Hilbert, L. R. and Gregory, D. J. (2003). "Siderite as a Corrosion Product on Archaeological Iron from a Waterlogged Environment." Studies in Conservation **48**(3): 183-194.

McBeth, J. M., Little, B. J., Ray, R. I., Farrar, K. M. and Emerson, D. (2011). "Neutrophilic Iron-Oxidizing "Zetaproteobacteria" and Mild Steel Corrosion in Nearshore Marine Environments." Applied and Environmental Microbiology **77**(4): 1405-1412.

Mei, L., Liao, L., Wang, Z. and Xu, C. (2015). "Interactions between Phosphoric/Tannic Acid and Different Forms of FeOOH." Advances in Materials Science and Engineering **2015**: 1-10.

Meincke, M., Krieg, E. and Bock, E. (1989). "Nitrosovibrio spp., the Dominant Ammonia-Oxidizing Bacteria in Building Sandstone." Applied And Environmental Microbiology **55**(8): 2108-2110.

- Melchers, R. E. (2008). "A new interpretation of the corrosion loss processes for weathering steels in marine atmospheres." Corrosion Science **50**: 3446-3454.
- Melchers, R. E. (2013). "Influence of Dissolved Inorganic Nitrogen on Accelerated Low Water Corrosion of Marine Steel Piling." Corrosion **69**(1).
- Melchers, R. E. and Jeffery, R. (2008). "The critical involvement of anaerobic bacterial activity in modelling the corrosion of mild steel in marine environments." Electrochimica Acta **54**: 80-85.
- Melchers, R. E. and Jeffery, R. (2012). "Corrosion of long vertical steel strips in the marine tidal zone and implications for ALWC." Corrosion Science **65**: 26-36.
- Melchers, R. E., Jeffrey, R. J. and Usher, K. M. (2014). "Localized corrosion of steel sheet piling." Corrosion Science **79**: 139-147.
- MEPS International Ltd. (2020). "World steel prices." Retrieved 30/05/20, from <https://worldsteelprices.com/>.
- Merriman, B., Aguinaldo, K. A. N., Alanjary, M. and Altun, G. T. (2012). "Progress in torrent semiconductor chip based sequencing." Electrophoresis **33**: 3397-3417.
- Meteo365.com Ltd. (2015). "Time Tides for Halmstad." Retrieved 13th March, 2015, from <http://www.tide-forecast.com/locations/Halmstad/tides/latest>.
- Mettel, C., Kim, Y., Shrestha, P. M. and Liesack, W. (2010). "Extraction of mRNA from Soil." Applied and Environmental Microbiology **76**(17): 5995–6000.
- Metzker, M. L. (2010). "Sequencing technologies - the next generation." Nature Reviews Genetics **11**: 31-46.
- Meyer, B., Imhoff, J. F. and Kuever, J. (2007). "Molecular analysis of the distribution and phylogeny of the soxB gene among sulfur-oxidizing bacteria – evolution of the Sox sulfur oxidation enzyme system." Environmental Microbiology **9**(12): 2957-2977.
- Meyer, B. and Kuever, J. (2007). "Molecular Analysis of the Diversity of Sulfate-Reducing and Sulfur-Oxidizing Prokaryotes in the Environment, Using aprA as Functional Marker Gene." Applied and Environmental Microbiology **73**(23): 7664-7679.
- Meyers, R. M., Maniatis, T. and Lerman, L. S. (1987). "Detection and localization of single base changes by denaturing gradient gel electrophoresis." Methods in Enzymology **150**: 501-527.

Miletto, M., Bodelier, P. L. E. and Laanbroek, H. J. (2007). "Improved PCR-DGGE for high resolution diversity screening of complex sulfate-reducing prokaryotic communities in soils and sediments." Journal of Microbiological Methods **70**: 103-111.

Mombelli, A., Hashim, D. and Cionca, N. (2018). "What is the impact of titanium particles and biocorrosion on implant survival and complications? A critical review." Clinical Oral Implants Research **29**: 37–53.

Morcillo, M., Alcántara, J., Díaz, I., Chico, B., Simancas, J. and de la Fuente, D. (2015). "Marine atmospheric corrosion of carbon steels." REVISTA DE METALURGIA **51**(2).

Mori, K., Tsurumaru, H. and Harayama, S. (2010). "Iron corrosion activity of anaerobic hydrogen-consuming microorganisms isolated from oil facilities." J Biosci Bioeng **110**(4): 426-430.

Morley, J. and Bruce, D. W. (1983). Survey of steel piling performance in marine environments, Commission of the European Communities.

Morris, E. K., Caruso, T., Buscot, F., Fischer, M., Hancock, C., Maier, T. S., Meiners, T., Müller, C., Obermaier, E., Prati, D., Socher, S. A., Sonnemann, I., Wäschke, N., Wubet, T., Wurst, S. and Rillig, M. C. (2014). "Choosing and using diversity indices: insights for ecological applications from the German Biodiversity Exploratories." Ecology and Evolution **8**(18): 3514-3524.

Mortimer, R. J. G., Harris, S. J., Krom, M. D., Freitag, T. E., Prosser, J. I., Barnes, J., Anschutz, P., Hayes, P. J. and Davies, I. M. (2004). "Anoxic nitrification in marine sediments." Marine Ecology Progress Series **276**: 37-51.

Mos, Y. M., Vermeulen, A. C., Buisman, C. J. N. and Weijma, J. (2018). "X-Ray Diffraction of Iron Containing Samples: The Importance of a Suitable Configuration." Geomicrobiology Journal **35**(6): 511-517.

Müller, B., Sun, L., Westerholm, M. and Schnürer, A. (2016). "Bacterial community composition and fhs profiles of low- and high-ammonia biogas digesters reveal novel syntrophic acetate-oxidising bacteria." Biotechnol Biofuels **9**(48): 1-18.

Murad, E. and Bishop, J. L. (2000). "The infrared spectrum of synthetic akaganéite, β -FeOOH." American Mineralogist **85**: 716–721.

Music, S., Nowik, I., Ristic, M., Orehovec, Z. and Popovic, S. (2004). "The Effect of Bicarbonate/Carbonate Ions on the Formation of Iron Rust." Croatica Chemica Acta **77**: 141-151.

Muyzer, G., De Waal, E. C. and Uitterlinden, A. G. (1993). "Profiling of Complex Microbial Populations by Denaturing Gradient Gel Electrophoresis Analysis of

Polymerase Chain Reaction-Amplified Genes Coding for 16S rRNA." Applied and Environmental Microbiology **59**(3): 695-700.

Nagiub, A. and Mansfeld, F. (2002). "Evaluation of microbiologically influenced corrosion inhibition (MICI) with EIS and ENA." Electrochimica Acta **47**: 2319-2333.

Nasrazadani, S. and Raman, A. (1993). "The Application Of Infrared Spectroscopy To The Study Of Rust Systems--Ii. Study Of Cation Deficiency In Magnetite (Fe₃O₄) Produced During Its Transformation To Maghemite (γ -Fe₂O₃) And Hematite (α -Fe₂O₃)." Corrosion Science **34**(8): 1355-1365.

Nasrazadani, S. and Raman, A. (1993). "Formation and Transformation of Magnetite (Fe₃O₄) on Steel Surfaces Under Continuous and Cyclic Water Fog Testing." Corrosion **49**(4): 294-300.

National Research Council (US) Committee on Metagenomics (2007). The New Science of Metagenomics: Revealing the Secrets of Our Microbial Planet. Washington (DC), National Academies Press.

Navarrette-Bedolla, M., Ballesteros-Almanza, M. L., Sanchez-Yanez, J. M., Valdez-Salas, B. and Hernandez-Duque, G. (1999). "Biocorrosion in a geothermal power plant." Materials Performance **38**(4): 1-8.

Neal, A. L., Techkarnjanaruk, S., Dohnalkova, A., McReady, D., Peyton, B. M. and Geesey, G. G. (2001). "Iron sulfides and sulfur species produced at hematite surfaces in the presence of sulfate-reducing bacteria." Geochimica et Cosmochimica Acta **65**(2): 223-235.

Neihof, R. A. (1988). "Microbes in fuel: An overview with a Naval Perspective." Cited in Chesneau, H. L. and Dorris, M. M. (Eds). Distillate Fuel: Contamination, Storage and Handling (pp. 6-14).

Niu, J., Deng, J., Xiao, Y., He, Z., Zhang, X., Van Nostrand, J. D., Liang, Y., Deng, Y., Liu, X. and Yin, H. (2016). "The shift of microbial communities and their roles in sulfur and iron cycling in a copper ore bioleaching system." Scientific Reports **6**: 1-7.

Obuekwe, C., Westlake, D. and Plambeck, J. (1981). "Corrosion of Mild Steel in Cultures of Ferric Iron Reducing Bacterium Isolated From Crude Oil: Mechanism of Anodic Depolarization. ." Corrosion **37**(11): 632-637.

Odin, G. P., Vanmeert, F., Farges, F., Gand, G., Janssens, K., Romero-Sarmiento, M.-F., Steyer, J.-S., Vantelon, D. and Rouchon, V. (2015). "Alterations in fossil-bearing shale (Autun, France; Permian), Part II: Monitoring artificial and natural ageing by

combined use of S and Ca K-edge XANES analysis, Rock-Eval pyrolysis and FTIR analysis." Annales de Paleontologie **101**: 225-239.

Okabe, S., Odagiri, M., Ito, T. and Satoh, H. (2007). "Succession of Sulfur-Oxidizing Bacteria in the Microbial Community on Corroding Concrete in Sewer Systems." Applied And Environmental Microbiology **73**(3): 971–980.

Oliveira, C. M., Machado, C. M., Duarte, G. W. and Peterson, M. (2016). "Beneficiation of pyrite from coal mining." Journal of Cleaner Production **139**: 821-827.

Otero, E., Bastidas, J. M. and López, V. (2004). "Analysis of a premature failure of welded AISI 316L stainless steel pipes originated by Microbial induced corrosion." Materials and Corrosion **48**(7): 447-454.

Otlewska, A., Adamiak, J., Stryzewska, T., Kańka, S. and Gutarowska, B. (2017). "Factors Determining the Biodiversity of Halophilic Microorganisms on Historic Masonry Buildings." Microbes Environ **32**: 164-173.

Païssé, S., Ghliglione, J. F., Marty, F., Gueuné, H., Sanchez de Amaya, J. M. and Quillet, L. (2012). "Sulfate-reducing bacteria inhabiting natural corrosion deposits from marine steel structures." Applied Microbiology and Biotechnology.

Parthipan, P., Elumalaia, P., Ting, Y. P., Rahmane, P. K. S. M. and Rajasekar, A. (2018). "Characterization of hydrocarbon degrading bacteria isolated from Indian crude oil reservoir and their influence on biocorrosion of carbon steel API 5LX." International Biodeterioration & Biodegradation **129**: 67–80.

Pekov, I. V., Chukanov, N. V., Britvin, S. N., K., K. Y., Gottlicher, J., Yakaskurt, V. O., Zadov, A. E., Krivovichev, S. V., Schuller, W. and Ternes, B. (2012). "The sulfite anion in ettringite-group minerals: a new mineral species hielscherite, $\text{Ca}_3\text{Si}(\text{OH})_6(\text{SO}_4)(\text{SO}_3) \cdot 11\text{H}_2\text{O}$, and the thaumasite-hielscherite solid-solution series." Mineralogical Magazine **76**(5): 1133–1152.

Peulon, S., Legrand, L., Antony, H. and Chausse, A. (2003). "Electrochemical deposition of thin films of green rusts 1 and 2 on inert gold substrate." Electrochemistry Communications **5**: 208–213.

Pholwat, S., Stroupa, S., Gratz, J., Trangan, V., Foongladda, S., Kumburuc, H., Jumac, S. P., Kibiki, G. and Houpt, E. (2014). "Pyrazinamide susceptibility testing of *Mycobacterium tuberculosis* by high resolution melt analysis." Tuberculosis **94**: 20-25.

Phull, B. (2010). Marine corrosion. Amsterdam, The Netherlands, Elsevier Science.

Pile Buck International Inc. (2015). "Types of sheet piling." Retrieved March 7th, 2015, from <http://www.pilebuckinternational.com/specs-2/>.

- Pineau, S., Sabot, R., Quillet, L., Caplat, C., Dupont-Morrall, I. and Refait, P. (2008). "Formation of Fe (II-III) hydroxysulphate greenrust during marine corrosion of steel associated to molecular detection of dissimilatory sulphite-reductase." Corrosion Science **50**: 1099-1111.
- Plaza, G. and Achal, V. (2020). "Biosurfactants: Eco-Friendly and Innovative Biocides against Biocorrosion." International Journal of Molecular Sciences **21**: 1-11.
- Porcellato, D., Gronnevik, H., Rudi, K., Narvhus, J. and Skeie, S. B. (2012). "Rapid lactic acid bacteria identification in dairy products by high-resolution melt analysis of DGGE bands." Letters in Applied Microbiology **54**: 344–351.
- Pozebon, D. and Martins, P. (2002). "Marine Sediment Analysis Using Inductively Coupled Plasma Optical Emission Spectrometry." Atomic Spectroscopy **23**(4): 111-118.
- Procópio, P. (2019). "The role of biofilms in the corrosion of steel in marine environments." World Journal of Microbiology and Biotechnology **35**: 73-81.
- Pugliese, L., Casabianca, S., Perini, F., Andreoni, F. and Penna, A. (2017). "A high resolution melting method for the molecular identification of the potentially toxic diatom *Pseudo-nitzschia* spp. in the Mediterranean Sea." Scientific Reports **7**: 1 - 10.
- Rahman, Z., Rahman, M. U., Usman, M., Hasanain, S. K., Rahman, Z. U., Ullah, A. and Kim, I. W. (2014). "Static Magnetic Properties of Maghemite Nanoparticles." Journal of the Korean Physical Society **65**(11): 1925-1929.
- Raiswell, R. and Canfield, D. E. (1998). "Sources of Iron For Pyrite Formation In Marine Sediment." American Journal of Science **298**: 219-245.
- Rajala, P., Huttunen-Saarivirta, E., Bomberg, M. and Carpén, L. (2019). "Corrosion and biofouling tendency of carbon steel in anoxic groundwater containing sulphate reducing bacteria and methanogenic archaea." Corrosion Science **159**: 1-16.
- Rajasekar, A. (2017). Biodegradation of Petroleum Hydrocarbon and Its Influence on Corrosion with Special Reference to Petroleum Industry. Singapore, Springer.
- Ramirez, G. A., Graham, D. and D'Hondt, S. (2018). "Influence of commercial DNA extraction kit choice on prokaryotic community metrics in marine sediment." Limnology and Oceanography: Methods **16**: 525–536.
- Rampadarath, S., Bandhoa, K., Puchooa, D., Jeewon, R. and Bal, S. (2017). "Early bacterial biofilm colonizers in the coastal waters of Mauritius." Electronic Journal of Biotechnology **29**: 13–21.
- Rasheed, A. P., Jabbar, K. A., Rasool, K., Pandey, R. P., Sliem, M. H., Helal, M., Samara, A., Abdullah, A. M. and Mahmoud, K. A. (2018). "Controlling the

Biocorrosion of Sulfate-Reducing Bacteria (SRB) on Carbon Steel using ZnO/Chitosan Nanocomposite as an Eco-Friendly Biocide." Corrosion Science **3**: 1-10.

Ravin, A., Rouchon, V. and Blanchet, D. (2017). "Determination of organic degradation rates in 100 My old sediments: Application to Cretaceous black shale intervals from Demerara Rise, ODP Leg 207." Organic Geochemistry **113**: 128–140.

Refait, P., Abdelmoula, M., Genin, J. M. R. and Sabot, R. (2006). "Green rusts in electrochemical and microbially influenced corrosion of steel." Comptes Rendus Geoscience **338**: 476-487.

Refait, P., Grolleu, A. M., Jeannin, M., Fancois, E. and Sabot, R. (2018). "Corrosion of mild steel at the seawater/sediments interface: Mechanisms and kinetics." Corrosion Science **130**: 76-84.

Refait, P., Memet, J. B., Bon, C., Sabot, R. and Genin, J. M. R. (2003). "Formation of the Fe(II)-Fe(III) hydroxysulphate green rust during marine corrosion of steel." Corrosion Science **45**: 833-845.

Reig, F. B., Adelantado, J. V. G. and Moreno, M. C. M. M. (2000). "FTIR quantitative analysis of calcium carbonate (calcite) and silica (quartz) mixtures using the constant ratio method. Application to geological samples." Talanta **58**: 811-821.

Reji, L., Tolar, B. B., Smith, J. M., Chavez, F. P. and Francis, C. A. (2019). "Depth distributions of nitrite reductase (nirK) gene variants reveal spatial dynamics of thaumarchaeal ecotype populations in coastal Monterey Bay." Environmental Microbiology **21**(11): 4032–4045.

Rémazeilles, C. and Refait, P. (2009). "Fe(II) hydroxycarbonate Fe₂(OH)₂CO₃ (chukanovite) as iron corrosion product: Synthesis and study by Fourier Transform Infrared Spectroscopy." Polyhedron **28**: 749–756.

Remmas, N., Melidis, P., Katsioui, E. and Ntougias, S. (2016). "Effects of high organic load on amoA and nirS gene diversity of an intermittently aerated and fed membrane bioreactor treating landfill leachate." Bioresource Technology **220**: 557–565.

Reyes-Bozo, L., Escudey, M., Vyhmeister, E., Higuera, P., Godoy-Faúndez, A., Salazar, J. L., Valdés-González, H., Wolf-Sepúlveda, G. and Herrera-Urbina, R. (2015). "Adsorption of biosolids and their main components on chalcopyrite, molybdenite and pyrite: Zeta potential and FTIR spectroscopy studies." Minerals Engineering **78** 128–135.

Ribeiro, D. V. and Abrantes, J. C. C. (2016). "Application of electrochemical impedance spectroscopy (EIS) to monitor the corrosion of reinforced concrete: A new approach." Construction and Building Materials **111**: 98–104.

Rickard, D. and Luther, G. W. (2007). "Chemistry of Iron sulfides." Chem. Rev. **107**: 514–562.

Roberge, P. R. (1999). Handbook of Corrosion Engineering, McGraw-Hill.

Roberge, P. R. (2006). Corrosion Basics—An Introduction,. Houston, TX.

Roberts, A. P. and Turner, G. M. (1993). "Diagenetic formation of ferrimagnetic iron sulphide minerals in rapidly deposited marine sediments, South Island, New Zealand." Earth and Planetary Science Letters **115**: 257-273.

Roberts, D. J., Nica, D., Zuo, G. and Davis, J. J. (2002). "Quantifying microbially induced deterioration of concrete: initial studies." International Biodeterioration and Biodegradation **49**: 227-234.

Robertson, T., Bibby, S., O'Rourke, D., Belfiore, T., Lambie, H. and Noormohammadi, A. H. (2009). "Characterization of Chlamydiae species using PCR and high resolution melt curve analysis of the 16S rRNA gene." Journal of Applied Microbiology **107**: 2017–2028.

Rodríguez-Rodríguez, C. E., Rodríguez-Cavallini, E. and Blanco, R. (2009). "Bacterial contamination of automotive fuels in a tropical region: the case of Costa Rica." Rev. Biol. Trop. **57**(3): 489-504.

Rosero-Navarro, N. C., Pellice, S. A., Castro, Y., Aparicio, M. and Durán, A. (2009). "Improved corrosion resistance of AA2024 alloys through hybrid organic–inorganic sol–gel coatings produced from sols with controlled polymerisation." Surface & Coatings Technology **203**: 1897–1903.

Rothberg, J., Hinz, W. and Reartik, T. (2011). "An integrated semiconductor device enabling non-optical genome sequencing." Nature **475**: 348-352.

Rouchon, V., Badet, H., O., B., Bonnerot, O., Lavedrine, B., Michard, J.-G. and Miska, S. (2012). "Raman and FTIR spectroscopy applied to the conservation report of paleontological collections: identification of Raman and FTIR signatures of several iron sulfate species such as ferrinatriite and sideronatriite." Journal of Raman Spectroscopy **43**: 1265-1274.

Rousell, B. (2012). Hall's Aggregate Wharf Dive Survey 2011. Shoreham Port Engineering Department.

Ruff Project. (2020). "Halite R070292." Retrieved 25/06/20, from <https://ruff.info/halite/display=default/R070292>.

- Salerno, J. L., Little, B., Lee, J. and Hamdan, L. J. (2018). "Exposure to Crude Oil and Chemical Dispersant May Impact Marine Microbial Biofilm Composition and Steel Corrosion." Frontiers in Marine Science **5**: 1-14.
- San, N. O., Nazir, H. and Donmez, G. (2012). "Microbially influenced corrosion of NiZn alloy coatings by *Delftia acidovorans* bacterium." Corrosion Science **64**: 198-203.
- Sánchez, R. G. P., Quintero, J. A. L., Pereira, M. M. and Agudelo-Flórez, P. (2017). "High-Resolution Melting Curve Analysis of the 16S Ribosomal Gene to Detect and Identify Pathogenic and Saprophytic *Leptospira* species in Colombian Isolates." Am. J. Trop. Med. Hyg. **96**(5): 1031-1038.
- Santo Domingo, J. W., Revetta, R. P., Iker, B., Gomez-Alvarez, V., Garcia, J., Sullivan, J. and Weast, J. (2011). "Molecular survey of concrete sewer biofilm microbial communities." Biofouling **27**(9): 1-4.
- Sarin, P., Snoeyink, V. L., Lytle, D. A. and Kriven, W. M. (2004). "Iron Corrosion Scales: Model for Scale Growth, Iron Release, and Colored Water Formation." Journal Of Environmental Engineering **130**(4): 365-373.
- Satoh, H., Odagiri, M., Ito, T. and Okabe, S. (2009). "Microbial community structures and in situ sulfate-reducing and sulfur-oxidizing activities in biofilms developed on mortar specimens in a corroded sewer system." Water Research **43**: 4729-4739.
- Schiffirin, D. J. and De Sanchez, S. R. (1985). "The Effect of Pollutants and Bacterial Microfouling on the Corrosion of Copper Base Alloys in Seawater " Corrosion **41**(1): 31-38.
- Schroder, I., Johnson, E. and de Vries, S. (2003). "Microbial ferric iron reductases." FEMS Microbiology Reviews **27**: 427-447.
- Schwertmann, U. and Fechter, H. (1993). "The Formation Of Green Rust And Its Transformation To Lepidocrocite." Clay Minerals **29**: 87-92.
- SciMed. (2021). "What is X-Ray Diffraction (XRD)." Retrieved 24/04/21, 2021, from <https://www.scimed.co.uk/education/what-is-x-ray-diffraction-xrd/>.
- Seifert, V. A., Clarke, B. J., Crossland, J. P. and Bemis, L. T. (2016). "A method to distinguish morphologically similar *Peromyscus* species using extracellular RNA and high-resolution melt analysis." Analytical Biochemistry **508**: 65-72.
- Shi, J., Yu, Z., Chen, B. and Zheng, J. (2015). "Preparation and Mechanical Properties of Composites Based on Rigid Polyvinyl Chloride Filled with Organic Modified Illite Powder." Journal of Macromolecular Science, Part B: Physics **54**: 507–516.

Shi, X., Xie, N. and Gong, J. (2011). "Recent Progress in the Research on Microbially Influenced Corrosion: A Bird's Eye View through the Engineering Lens." Recent Patents on Corrosion Science **1**: 118-131.

Shopska, M., Cherkezova-Zheleva, Z. P., Paneva, D. G., Iliev, M., Kadinov, G. B., Mitov, I. G. and Groudeva, V. I. (2013). "Biogenic iron compounds: XRD, Mossbauer and FTIR study." Central European Journal of Chemistry **11**(2): 215-217.

Shoreham Port. (2013). "Shoreham support renewable energy plans at the port." Retrieved 2nd April, 2015, from <http://www.shoreham-port.co.uk/Latest-News/shoreham-support-renewable-energy-plans-at-the-port>.

Shoreham Port. (2015). "Commodities." Retrieved 2nd April, 2015, from <http://www.shoreham-port.co.uk/Commodities>.

Sikkema-Raddatz, B., Johansson, L. F., de Boer, E. N., Almomani, R., Boven, L. G., van den Berg, M. P., van Spaendonck-Zwarts, K. Y., van Tintelen, J. P., Sijmons, R. H., Jongbloed, J. D. H. and Sinke, R. J. (2013). "Targeted Next-Generation Sequencing can Replace Sanger Sequencing in Clinical Diagnostics." Human Mutation **34**(7): 1035-1042.

Skyline Steel LLC. (2014). "Steel Sheet Piling." Retrieved 22nd March, 2015, from <http://www.skylinesteel.com/globalnav/products/steel-sheet-piling>.

Smith, C. J., Nedwell, D. B., Dong, L. F. and Osborn, A. M. (2007). "Diversity and Abundance of Nitrate Reductase Genes (narG and napA), Nitrite Reductase Genes (nirS and nrfA), and Their Transcripts in Estuarine Sediments " Applied and Environmental Microbiology **73**(11): 3612-3622.

Smith, M., Bardiau, M., Brennan, R., Burgess, H., Caplin, J., Ray, S. and Urios, T. (2019). "Accelerated low water corrosion: the microbial sulfur cycle in microcosm." npj Materials Degredation **3**(1): 1-11.

Smith, W. R. and Paul, S. (2015). "Natural Deposit Coatings on Steel during Cathodic Protection and Hydrogen Ingress." Coatings **5**: 816-829.

Snow, D. A. (2001). Plant Engineer's Reference Book, Butterworth-Heinemann.

Souza, R. A. and Falcão, J. P. (2012). "A novel high-resolution melting analysis-based method for *Yersinia pseudotuberculosis* genotyping." Journal of Microbiological Methods **91**: 329-335.

Sowards, J. W. and Mansfield, E. (2014). "Corrosion of copper and steel alloys in a simulated underground storage-tank sump environment containing acid-producing bacteria." Corrosion Science **87**: 460-471.

Stamps, B. W., Bojanowski, C. L., Drake, C. A., Nunn, H. S., Lloyd, P. F., Floyd, J. G., Emmerich, K. A., Neal, A. R., Crookes-Goodson, W. J. and Stevenson, B. S. (2020). "In situ Linkage of Fungal and Bacterial Proliferation to Microbiologically Influenced Corrosion in B20 Biodiesel Storage Tanks." Frontiers in Microbiology **11**(167): 1-13.

Stetter, K. and Gaag, G. (1983). "Reduction of molecular sulphur by methanogenic bacteria." Nature **305**: 309–311.

Stoffyn-Egli, P. and Buckley, D. E. (1993). "The Titanic: from metals to minerals." Can Chem News **45**: 26–28.

Summer, E. J., Duggleby, S., Janes, C. and Liu, M. (2014). Microbial Populations in the O&G: Application of this Knowledge. Corrosion 2014, NACE International.

Sun, H., Shi, B., Lytle, D. A., Baia, Y. and Wang, D. (2014). "Formation and release behavior of iron corrosion products under the influence of bacterial communities in a simulated water distribution system." Environmental Science: Processes & Impacts **16**: 576–585.

Suo, Z., Deliorman, M., Lucas, K., Loetterle, L., Yang, X., Celikkol, S., Beech, I., Sunner, J. and Avci, R. (2012). Rapid Anaerobic Degradation of Carbon Steel Exposed to *Desulfoglaeba Alkanexedens* Media. CORROSION 2012, NACE International.

Swaroop, B. S., Victoria, S. N. and Manivannan, R. (2016). "Azadirachta indica leaves extract as inhibitor for microbial corrosion of copper by *Arthrobacter sulfureus* in neutral pH conditions—A remedy to blue green water problem." Journal of the Taiwan Institute of Chemical Engineers **64**: 269–278.

Sztyler, M. K. (2014). Molecular analysis of microbial communities from oil industry environments. Doctor of Philosophy, University of Portsmouth.

Takeuchi, M., Hamana, K. and Hiraishi, A. (2001). "Proposal of the genus *Sphingomonas sensu stricto* and three new genera, *Sphingobium*, *Novosphingobium* and *Sphingopyxis*, on the basis of phylogenetic and chemotaxonomic analyses." International Journal of Systematic and Evolutionary Microbiology **51**: 1405–1417.

Telegdi, J., Shaban, A. and Trif, L. (2017). Microbiologically influenced corrosion (MIC). Trends in oil and gas corrosion research and technologies, Woodhead Publishing: 191-214.

Thermo Fisher Scientific. (2018). "High Resolution Melting (HRM)." Retrieved 26/05/18, 2018, from <https://www.thermofisher.com/ar/en/home/life-science/pcr/real-time-pcr/real-time-pcr-applications/genetic-variation-analysis-using-real-time/high-resolution-melting-hrm.html>.

Thermo Fisher Scientific. (2021). "CRISPR Gene Editing Confirmation with Sanger Sequencing." Retrieved 22.04.21, 2021, from <https://www.thermofisher.com/uk/en/home/life-science/sequencing/sanger-sequencing/applications/crispr-talen-genome-editing-sanger-sequencing.html>.

Thomas, A. N., Eiche, E., Göttlicher, J., Steininger, R., Benning, L. G., Freeman, H. M., Dideriksen, K. and Neumann, T. (2018). "Products of Hexavalent Chromium Reduction by Green Rust Sodium Sulfate and Associated Reaction Mechanisms." Soil Systems **2**(58): 1-19.

Thomas, T., Gilbert, J. and Meyer, F. (2012). "Metagenomics - a guide from sampling to data analysis." Microbial Informatics and experimentation **2**(3).

ThyssenKrupp GfT Bautechnik. (2008). "Sheet Piling Handbook." Retrieved 11 March, 2015, from http://www.thyssenkrupp-bautechnik.com/fileadmin/Leistungen/01_Spundwandprofile/media/english/2008_08_21_steel_piling_handbook_Design_englisch.pdf.

Tironi, A., Trezza, M. A., Irassar, E. F. and Scian, A. N. (2012). "Thermal treatment of kaolin: effect on the pozzolanic activity." Procedia Materials Science **1**: 343 – 350.

Titov, I., Tsybanov, S. and Malogolovkin, A. (2015). "Genotyping of classical swine fever virus using high-resolution melt analysis." Journal of Virological Methods **224**: 53–57.

Todorova, M. (2020). "Ab initio study of corrosion: Adsorbate phases on surfaces and phase diagrams." Retrieved 24/05/20, from <https://www.mpie.de/2954362/Corrosion>.

Tomlinson, M. and Woodward, J. (2014). Pile Design and Construction Practice. Abingdon, Oxon, UK, Taylor & Francis.

Tu, K. and Cottis, R. A. (2009). Controlling the components of calcareous deposit to protect steel structures from alwc with dc and pulse current. NACE International.

Tu, Q., Yu, H., He, Z., Deng, Y., Wu, L., Van Nostrand, J. D., Zhou, A., Voordeckers, J., Lee, Y. J., Qin, Y., Hemme, C. L., Shi, Z., Xue, K., Yuan, T., Wang, A. and Zhou, J. (2014). "GeoChip 4: a functional gene-array-based high-throughput environmental technology for microbial community analysis." Molecular Ecology Resources **14**(5): 914-928.

Uddin, H., Khalid, R. S., Alaama, M., Abdulkader, A. M., Kasmuri, A. and Abbas, S. A. (2016). "Comparative study of three digestion methods for elemental analysis in traditional medicine products using atomic absorption spectrometry." Journal of Analytical Science and Technology **7**(6): 1-7.

- Ul-Hasan, S., Bowers, R. M., Figueroa-Montiel, A., Licea-Navarro, A. F., Beman, J. M., Woyke, T. and Nobile, C. J. (2019). "Community ecology across bacteria, archaea and microbial eukaryotes in the sediment and seawater of coastal Puerto Nuevo, Baja California." *PLOS ONE* **14**(2): 1-19.
- Urubschurov, V., Stroebel, C., Günther, E., Romanowski, K., Büsing, K. and Zeyner, A. (2019). "Effect of oral supplementation of probiotic strains of *Lactobacillus rhamnosus* and *Enterococcus faecium* on the composition of the faecal microbiota of foals." *J Anim Physiol Anim Nutr.* **103**: 915–924.
- Usher, K. M., Kaksonen, A. H. and MacLeod, I. D. (2014). "Marine rust tubercles harbour iron corroding archaea and sulphate reducing bacteria." *Corrosion Science* **83**: 189-197.
- Usman, M., Byrne, J. M., Chaudhary, A., Orsetti, S., Hanna, K., Ruby, C., Kappler, A. and Haderlein, S. B. (2018). "Magnetite and Green Rust: Synthesis, Properties, and Environmental Applications of Mixed-Valent Iron Minerals." *Chemical Reviews* **118**: 3251–3304.
- Valipour, R., Boegman, L., Bouffard, D. and Rao, Y. R. (2017). "Sediment resuspension mechanisms and their contributions to high-turbidity events in a large lake." *Limnol. Oceanogr.* **62**: 1045–1065.
- van der Maarel, M. J. E. C., Sprenger, W., Haanstra, R. and Forney, L. J. (1999). "Detection of methanogenic archaea in seawater particles and the digestive tract of a marine fish species." *FEMS Microbiology Letters* **173**: 189-194.
- Van Nostrand, J. D., Liang, Y., He, Z., Li, G. and Zhou, J. (2009). GeoChip: A High Throughput Genomic Tool for Linking Community Structure to Functions. *Handbook of Hydrocarbon and Lipid Microbiology*. K. N. Timmis. Berlin, Heidelberg, Springer.
- Van Nostrand, J. D., Wu, W. M., Wu, L., Deng, Y., Carley, J., Carroll, S., He, Z., Gu, B., Luo, J., S., C. C., Watson, D. B., Jardine, P. M., Marsh, T. L., Tiedje, J. M., Hazen, T. C. and Zhou, J. (2009). "GeoChip-based analysis of functional microbial communities during the reoxidation of a bioreduced uranium-contaminated aquifer." *Environmental Microbiology* **11**(10): 2611-2626.
- Vangriesheim, A., Khripounoff, A. and Crassous, P. (2009). "Turbidity events observed in situ along the Congo submarine channel." *Deep Sea Research Part II: Topical Studies in Oceanography* **56**(23): 2208-2222.
- vanLoon, G. W. and Duffy, S. J. (2005). *Environmental Geochemistry - a Global Perspective*, Oxford University Press.

Varliero, G., Bienhold, C., Schmid, F., Boetius, A. and Molari, M. (2019). "Microbial Diversity and Connectivity in Deep-Sea Sediments of the South Atlantic Polar Front." Frontiers in Microbiology **10**: 1-18.

Vaughan, D. J. (2006). "Sulfide Mineralogy and Geochemistry." Reviews in Mineralogy and Biochemistry **61**: 2-713.

Veerasingam, S., Venkatachalapathy, R. and Ramkumar, T. (2014). "Distribution of clay minerals in marine sediments off Chennai, Bay of Bengal, India: Indicators of sediment sources and transport processes." International Journal of Sediment Research **29**: 11-23.

Veneranda, M., Aramendia, J., Bellot-Gurlet, L., Colomban, P., Castro, K. and Madariaga, J. M. (2018). "FTIR spectroscopic semi-quantification of iron phases: A new method to evaluate the protection ability index (PAI) of archaeological artefacts corrosion systems." Corrosion Science **133**: 68-77.

Venzlaff, H., Enning, D., Srinivasan, J., Mayrhofer, K. J. J., Hassel, A. W., Widdel, F. and Stratmann, M. (2013). "Accelerated cathodic reaction in microbial corrosion of iron due to direct electron uptake by sulfate-reducing bacteria." Corrosion Science **66**: 88–96.

Verma, M. K., Ahmed, V., Gupta, S., Kumar, J., Pandey, R., Mandhan, V. and Chauhan, N. S. (2018). "Functional metagenomics identifies novel genes ABCPPP, TMSRP1 and TLSRP1 among human gut enterotypes." Nature Scientific Reports **8**(1397): 1-11.

Videla, H. A. (2001). "Microbially Induced Corrosion: an Updated Overview." International Biodeterioration and Biodegradation **48**: 176-201.

Videla, H. A. (2002). "Prevention and control of biocorrosion." International Biodeterioration & Biodegradation **49**: 259–270.

Videla, H. A. and Herrera, L. K. (2005). "Microbiologically influenced corrosion: looking to the future." International Microbiology **8**: 169-180.

Villalobos, M. and Leckie, J. O. (2001). "Surface Complexation Modeling and FTIR Study of Carbonate Adsorption to Goethite." Journal of Colloid and Interface Science **235**: 15-32.

Vlachos, N., Skopelitis, Y., Psaroudaki, M., Konstantinidou, V., Chatzilazarou, A. and Tegou, E. (2006). "Applications of Fourier transform-infrared spectroscopy to edible oils." Analytica Chimica Acta **573–574**: 459–465.

- Voordouw, G., Nemati, M. and Jenneman, G. (2002). Use of Nitrate Reducing, Sulfide Oxidizing Bacteria to Reduce Souring in Oil Fields: Interactions with SRB and Effects on Corrosion CORROSION 2002. Denver, Colorado.
- Walden, C., Carbonerob, F. and Zhang, W. (2017). "Assessing impacts of DNA extraction methods on next generation sequencing of water and wastewater samples." Journal of Microbiological Methods **141**: 10-16.
- Wall, H. and Wadso, L. (2013). "Corrosion rate measurements in steel sheet pile walls in marine environment." Marine Structures **33**: 21-33.
- Walsh, E. A., Kirkpatrick, J. B., Rutherford, S. D., Smith, D. C., Sogin, M. and D'Hondt, S. (2016). "Bacterial diversity and community composition from seafloor to subseafloor." The ISME Journal **10**: 979-989.
- Wang, H., Hu, C., Hu, X., Yang, M. and Qu, J. (2012). "Effects of disinfectant and biofilm on the corrosion of cast iron pipes in a reclaimed water distribution system." Water Research **46**: 1070-1078.
- Wang, H., Hu, C., Zhang, L., Li, X., Zhang, Y. and Yang, M. (2014). "Effects of microbial redox cycling of iron on cast iron pipe corrosion in drinking water distribution systems." Water Research **65**: 363-370.
- Wang, H., Wang, X., Zhang, T. and Zhou, H. (1995). "Comparison between conformational change and inactivation rates of aminoacylase during denaturation in urea solutions." Science in China **38**(3): 328-335.
- Wang, M., Deng, B., Fu, X., Sun, H. and Xu, Z. (2019). "Characterizations of microbial diversity and machine oil degrading microbes in machine oil contaminated soil." Environmental Pollution **255**: 1-10.
- Wang, P., Zhou, H., Meng, J., Peng, X., Jiang, L., Sun, S., Zhang, C., Van Nostrand, J. D., Deng, Y., He, Z., Wu, L., Zhou, J. and Xiao, X. (2009). "GeoChip-based analysis of metabolic diversity of microbial communities at the Juan de Fuca Ridge hydrothermal vent " Proc Natl Acad Sci USA **106**(12): 4840-4845.
- Wang, S., Tang, Y., Schobert, H. H., Guo, Y., Gao, W. and Lu, X. (2013). "FTIR and simultaneous TG/MS/FTIR study of Late Permian coals from Southern China." Journal of Analytical and Applied Pyrolysis **100**: 75–80.
- Wang, X., Xia, Y., Wen, Y., Yang, Y. and Zhou, J. (2014). "Microbial Community Functional Structures in Wastewater Treatment Plants as Characterized by GeoChip." PLoS ONE **9**(3): e93422.
- Waragai, T. (2016). "The effect of rock strength on weathering rates of sandstone used for Angkor temples in Cambodia." Engineering Geology **207**: 24-35.

- Weatherill, J. S., Morris, K., Bots, P., Stawski, T. M., Janssen, A., Abrahamsen, L., Blackham, R. and Shaw, S. (2016). "Ferrihydrite Formation: The Role of Fe₁₃ Keggin Clusters." Environmental Science and Technology **50**: 9333–9342.
- Weerasooriya, R., Makehelwala, M. and Bandara, A. (2010). "Probing reactivity sites on pyrite-oxidative interactions with 4-chlorophenol." Colloids and Surfaces A: Physicochem. Eng. Aspects **367**: 65-69.
- Weisburg, W. G., Barns, S. M., Pelletier, D. A. and Lane, D. J. (1991). "16S Ribosomal DNA Amplification for Phylogenetic Study." Journal of Bacteriology **173**(2): 697-703.
- Woksepp, H., Jernberg, C., Tarnberg, M., Ryberg, A., Brolund, A., Nordvall, M., Olsson-Liljequist, B., Wisell, K. T., Monstein, H.-J., Nilsson, L. E. and Schon, T. (2011). "High-Resolution Melting-Curve Analysis of Ligation-Mediated Real-Time PCR for Rapid Evaluation of an Epidemiological Outbreak of Extended-Spectrum-Beta-Lactamase-Producing Escherichia coli." Journal of Clinical Microbiology **49**(12): 4032-4039.
- Wolska, K. I., Grudniak, A. M., Rudnicka, Z. and Markowska, K. (2016). "Genetic control of bacterial biofilms." J Appl Genetics **57**: 225–238.
- Wolzogen-Kuhr, G. A. H. and Van der Vlugt, L. R. (1934). "The graphitization of cast iron as an electrochemical process in anaerobic soil." Water **18**: 147.
- Wormser, G. P. and Bottone, E. J. (1983). "Cardiobacterium hominis: Review of Microbiologic and Clinical Features." Reviews of Infectious Diseases **5**(4): 680–691.
- Wu, Y., Hayes, V. M., Osinga, J., Mulder, I. M., Looman, M. W. G., Buys, C. H. C. M. and Hofstra, R. M. W. (1998). "Improvement of fragment and primer selection for mutation detection by denaturing gradient gel electrophoresis." Nucleic Acids Research **26**(23): 5432–5440.
- Xiao, H., Ye, W., Song, X., Ma, Y. and Li, Y. (2017). "Evolution of Akaganeite in Rust Layers Formed on Steel Submitted to Wet/Dry Cyclic Tests." Materials **10**(1262): 1-14.
- Xie, J., He, Z., Liu, X., Liu, X., Van Nostrand, J. D., Deng, Y., Wu, L., Zhou, J. and Qiu, G. (2011). "GeoChip-Based Analysis of the Functional Gene Diversity and Metabolic Potential of Microbial Communities in Acid Mine Drainage." Applied and Environmental Microbiology **77**(3): 991-999.
- Xu, C., Zhang, Y., Cheng, G. and Zhu, W. (2007). "Localized corrosion behavior of 316L stainless steel in the presence of sulfate-reducing and iron-oxidizing bacteria." Materials Science and Engineering A **443**: 235–241.

- Xu, Z., Liang, J. and Zhou, L. (2013). "Photo-Fenton-like degradation of azo dye methyl orange using synthetic ammonium and hydronium jarosite." Journal of Alloys and Compounds **546**: 112–118.
- Yakovchuk, P., Protozanova, E. and Frank-Kamenetskii, M. D. (2006). "Base-stacking and base-pairing contributions into thermal stability of the DNA double helix." Nucleic Acids Research **34**(2): 564-575.
- Yamashita, M., Hara, S., Kamimura, T., Miyuki, H. and Sato, M. (2007). "X-ray Diffraction Analysis of Rust Layer on a Weathering Steel Bridge with Surface Treatment Using Synchrotron Radiation." Materials Transactions **48** (3): 579-583.
- Yang, F., Shi, B., Bai, Y., Sun, H., Lytle, D. A. and Wang, D. (2014). "Effect of sulfate on the transformation of corrosion scale composition and bacterial community in cast iron water distribution pipes." Water Research **59**: 46-57.
- Yang, Y., Liu, W., Bhargava, S. K., Zeng, W. and Chen, M. (2016). "A XANES and XRD study of chalcopyrite bioleaching with pyrite." Minerals Engineering **89**: 157–162.
- Yang, Y., Scantlebury, J. D. and Koroleva, E. V. (2015). "A Study of Calcareous Deposits on Cathodically Protected Mild Steel in Artificial Seawater." Metals **5**: 439-456.
- Yuk, S., Kamarisima, Azamd, A. H., Miyanagaa, K. and Tanji, Y. (2020). "The contribution of nitrate-reducing bacterium *Marinobacter* YB03 to biological souring and microbiologically influenced corrosion of carbon steel." Biochemical Engineering Journal **156**: 1-9.
- Zegeye, A., Huguet, L., Adbelmoula, M., Carteret, C., Mullet, M. and Jorand, F. (2007). "Biogenic hydroxysulfate green rust, a potential electron acceptor for SRB activity." Geochimica et Cosmochimica Acta **71**(22): 5450-5462.
- Zhang, L., De Schryver, P., De Gusseme, B., De Muynck, W., Boon, N. and Verstraete, W. (2008). "Chemical and biological technologies for hydrogen sulfide emission control in sewer systems: A review." Water Research **42**: 1-12.
- Zhang, T. and Fang, H. H. P. (2001). "Quantification of extracellular polymeric substances in biofilms by confocal laser scanning microscopy." Biotechnology Letters **23**: 405-409.
- Zhang, W., Ding, W., Li, Y. X., Tam, C., Bougouffa, S., Wang, R., Pei, B., Chiang, H., Leung, P., Lu, Y., Sun, J., Fu, H., Bajic, V. B., Liu, H., Webster, N. S. and Qian, P. Y. (2019). "Marine biofilms constitute a bank of hidden microbial diversity and functional potential." Nature Communications **10**(517): 1-10.

- Zhang, Y., Douglas, G. B., Kaksonen, A. H., Cui, L. and Ye, Z. (2019). "Microbial reduction of nitrate in the presence of zero-valent iron." Science of the Total Environment **646**: 1195–1203.
- Zhao, X., Chen, K., Yang, J., Xi, G., Tian, H. and Chen, Q. (2019). "Effects of Three Kinds of Hydrocarbon Degrading Bacteria on Biocorrosion Behavior of 16Mn Steel in the Bacteria-Containing Media." Int. J. Electrochem. Sci. **14**: 886 – 896.
- Zhao, X., Wang, Z., Zhou, X., Qi, N., Chen, F., Li, D. and Li, X. (2019). "Full length obtains of hydA and phylogenetic analysis of bio-hydrogen production new species of Clostridium based on efficient hydA degenerate primers." International Journal of Hydrogen Energy **44**: 29493-29499.
- Zhilina, T. N., Zavarzin, G. A., Rainey, I. F. A., Pikuta, E. N., Osipov, I. G. A. and Kostrikina, N. A. (1997). "Desulfonatovibrio hydrogenovorans gen. nov., sp. nov., an Alkaliphilic, Sulfate-Reducing Bacterium." International Journal Of Systematic Bacteriology **47**(1): 144-149.
- Zhou, J., He, Z., Van Nostrand, J. D., Wu, L. and Deng, Y. (2010). "Applying GeoChip Analysis to Disparate Microbial Communities." Microbe **5**(2): 60-65.
- Zhou, J., He, Z., Yang, Y., Deng, Y., Tringe, S. G. and Alvarez-Cohen, L. (2015). "High-Throughput Metagenomic Technologies for Complex Microbial Community Analysis: Open and Closed Formats." mBio **6**(1): e02288-02214.
- Zhu, B.-S., Jia, Y., Jin, Z., Sun, B., Luo, T., Kong, L.-T. and Liu, J.-H. (2015). "A facile precipitation synthesis of mesoporous 2-line ferrihydrite with good fluoride removal properties." RSC Advances **5**: 84389–84397.
- Zhu, X. Y., Lubeck, J. and Kilbane, J. J. (2003). "Characterization of Microbial Communities in Gas Industry Pipelines." Applied and Environmental Microbiology **69**(9): 5354-5363.
- Zhu, Y., Wang, H., Li, X., Hu, C., Yang, M. and Qu, J. (2014). "Characterization of biofilm and corrosion of cast iron pipes in drinking water distribution system with UV/Cl₂ disinfection." Water Research **60**: 174-181.
- Zumft, W. G. (1997). "Cell biology and molecular basis of denitrification." Microbiology and Molecular Biology Reviews **61**(4): 533–616.
- Zyka, K. and Mohajerani, A. (2016). "Composite piles: A review." Construction and Building Materials **107**: 394–410.

Appendix A - Membrane filtration protocol

1. Filter 2 x 500 ml seawater samples using vacuum manifold, filtration assembly and 0.45 μm membrane.
2. Place filter membrane in centrifuge tube with 10 ml STE buffer, and vortex for 10 minutes.
3. Remove filter membrane, and centrifuge the sediment/buffer solution at 4°C for 30 minutes at 10000 g.
4. Pipette off 6 to 8 ml of supernatant and resuspend the sediment pellet in remaining buffer.
5. Add to MoBio PowerSoil bead beating tube and conduct standard DNA extraction protocol (see Appendix B).

Appendix B - MoBio PowerSoil protocol

1. To the PowerBead Tubes provided, add 0.25 grams of sample.
2. Gently vortex to mix.
3. Check Solution 1. If solution 1 is precipitated, heat gently solution to 60°C until dissolved before use.
4. Add 60 µl of Solution 1 and invert several times or vortex briefly.
5. Secure PowerBead Tubes horizontally using the MoBio Vortex Adapter tube holder for the vortex. Vortex at maximum speed for 10 minutes.
6. Make sure the PowerBead Tubes rotate freely in your centrifuge without rubbing. Centrifuge tubes at 10000 g for 30 seconds at room temperature.
7. Transfer the supernatant to a clean 2 ml Collection Tube
8. Add 250 µl of Solution 2.
9. Centrifuge the tubes at room temperature for 1 minute at 10000 g
10. Avoiding the pellet, transfer up to, but no more than 600 µl of supernatant to a clean 2 ml collection tube
11. Add 200 µl of Solution 3 and vortex briefly. Incubate at 4°C for 5 minutes.
12. Centrifuge tubes at room temperature for 1 minute at 10000 g.
13. Avoiding the pellet, transfer up to 750 µl of supernatant into a clean 2 ml collection tube.
14. Shake to mix Solution 4 before use. Add 1200 µl of Solution 4 to the supernatant and vortex for 5 seconds.
15. Load approximately 675 µl onto a Spin Filter and centrifuge at 10000 g for 1 minute at room temperature. Discard the flow through and add an additional 675 µl of supernatant to the spin filter and centrifuge for 10000 g for 1 minute at room temperature. Load the remaining supernatant onto the Spin Filter and centrifuge at 10000 x g for 1 minute at room temperature.
16. Add 500 µl of Solution 5; centrifuge at room temperature for 30 seconds at 10000 g.
17. Discard the flow through.
18. Centrifuge again at 10000 g for 1 minute at room temperature.
19. Carefully place spin filter in a clean 2 ml Collection Tube. Avoid splashing any Solution 5 onto the Spin Filter.

Appendix B - MoBio PowerSoil protocol (continued)

19. Add 100 μ l of Solution 6 to the centre of the white filter membrane.
20. Centrifuge at room temperature for 30 seconds at 10000 g.
21. Discard the Spin Filter.

Appendix C - GeoChip methodology

1. 1 µg of each DNA template was incubated at 99.9 °C for 5 minutes before being chilled on ice. They were then labelled with Cy3 fluorescent dye using random octamer primers, dNTP mix, and Klenow fragment. Each sample mixture was incubated for 37 °C for 6 hours and then incubated at 95 °C for 3 minutes.
2. Samples were purified using QIAquick PCR purification kit, then dehydrated using a Savant ISS110 SpeedVac solvent evaporator.
3. Prior to hybridization each sample was rehydrated using a unique Cy3-labelled 48 mer oligonucleotide , at 50 °C for 5 minutes.
4. The labelled templates were hybridised at 42°C for 16 hours with the GeoChip TM 5.0 on a MAUI hybridisation station (BioMicro, USA).
5. After hybridisation, microarrays were scanned using a microarray scanner and the intensity of each spot was determined.
6. To call probes positive, a floating signal-to-noise ratio (SNR) was used so that the hyperthermophile probes accounted for 5% of the positive signals. The probes were assigned as negative if the signal was <1.3 times the background.
7. The signal intensity was then normalised by dividing the signal intensity of each spot by the mean intensity of the microarray.

Adapted from Van Nostrand et al. (2009) and Tu et al. (2014).

Appendix D - Alpha Diversity tests

Simpson Index

$$D = 1 - \sum \frac{n(n-1)}{N(N-1)}$$

Where D = Simpson Index

n = Total number of organisms of one group

N = Total number of organisms of all groups

Shannon Index

$$H = \sum \frac{n}{N} \ln \frac{n}{N}$$

Where H = Shannon Index

n = Total number of organisms of one group

N = Total number of organisms of all groups

Shannon evenness

$$J = \frac{H}{\ln S}$$

Where J = Shannon evenness

H = Shannon Index

ln S = Natural logarithm of the total number of groups

Appendix E - PCR primers

Target gene	Primer reference	Sequence (5' to 3')	Notes	Reference
<i>dsrB</i>	dsrB2060F	CAACATCGTYCAYACCCAGGG	HRM forward primer	Dong et al. (2017)
<i>dsrB</i>	dsrB2060F-GC	CGCCCGCCGCGCGCGGCGGGC GGGGCGGGGGCACGGGGGGC AACATCGTYCAYACCCAGGG	DGGE forward primer	
<i>dsrB</i>	dsrB4R	GTGTAGCAGTTACCGCA	HRM/ DGGE reverse primer	
<i>aprA</i>	AprA-1-FW	TGGCAGATCATGATY MAYGG	HRM forward primer	Blazejak et al. (2005)
<i>aprA</i>	aprA-5-RV	GCGCCAACYGGRCRTA	HRM reverse primer	
<i>soxB</i>	SoxB432F	GAYGGNGGNGAYACNTGG	HRM forward primer	Anandham et al. (2008)
<i>soxB</i>	soxB1446B	CATGTCNCCNCCRTGYTG	HRM reverse primer	
<i>16S</i>	16S-341f	CCTAYGGGRBGCASCAG	HRM forward primer	Behrendt et al. (2012)
<i>16S</i>	16S-806r	GGACTACNNGGGTATCTAAT	HRM reverse primer	

Legend: **B** = C/G/T; **M** = A/C; **N** = A/C/G/T; **R** = A/G; **S** = C/G and **Y** = C/T

Appendix F - PCR preparation

HRM:

1 μ l DNA template (undiluted)

1 μ l Forward Primer (10 μ M dilution)

1 μ l Reverse Primer (10 μ M dilution)

12.5 μ l SsoAdvanced Universal SYBR Green Supermix solution

9.5 μ l Nuclease-free water

DGGE:

1 μ l DNA template (undiluted)

1 μ l Forward primer (with G-C clamp) (10 μ M dilution)

1 μ l Reverse primer (10 μ M dilution)

12.5 μ l ThermoFisher 2X MasterMix solution

9.5 μ l Nuclease-free water

Appendix G - Thermocycler protocols

dsrB (HRM) (Seifert et al., 2016, Dong et al., 2017)

One cycle:	95°C for 5 minutes (Initial denaturation)
Twenty cycles:	95°C for 40 seconds (Denaturation) 60°C for 30 seconds (Annealing) Decrease temperature by 0.5°C per cycle 72°C for 1 minute (Elongation)
Twenty-nine cycles:	95°C for 40 seconds (Denaturation) 50°C for 30 seconds (Annealing) 72°C for 1 minute (Elongation)
One cycle:	72°C for 10 minutes (Final elongation)
One cycle:	50°C for 90s (Pre-melt conditioning)
Four hundred and sixty cycles:	50°C for 2 seconds (Melting) Increase temperature by 0.1°C per cycle
One cycle:	4°C for ∞ minutes (Hold cycle)

dsrB (DGGE) (Dong et al., 2017)

One cycle:	95°C for 5 minutes (Initial denaturation)
Twenty cycles:	95°C for 40 seconds (Denaturation) 60°C for 30 seconds (Annealing) Decrease temperature by 0.5°C per cycle 72°C for 1 minute (Elongation)
Twenty-nine cycles:	95°C for 40 seconds (Denaturation) 50°C for 30 seconds (Annealing) 72°C for 1 minute (Elongation)
One cycle:	72°C for 10 minutes (Final elongation)
One cycle:	4°C for ∞ minutes (Hold cycle)

Appendix G – Thermocycler protocols (continued)

aprA (HRM) (Seifert et al., 2016, Badamchi et al., 2017)

One cycle:	94°C for 5 minutes (Initial denaturation)
Thirty-five cycles:	94°C for 1 minute (Denaturation)
	48°C for 1 minute (Annealing)
	72°C for 90 seconds (Elongation)
One cycle:	72°C for 10 minutes (Final elongation)
One cycle	50°C for 90s (Pre-melt conditioning)
Four hundred and sixty cycles:	50°C for 2 seconds (Melting)
	Increase temperature by 0.1°C per cycle
One cycle:	4°C for ∞ minutes (Hold cycle)

soxB (HRM) (Seifert et al., 2016, Luo et al., 2018)

One cycle:	95°C for 30 seconds (Initial denaturation)
Forty cycles:	95°C for 10 seconds (Denaturation)
	55°C for 30 seconds (Annealing)
	72°C for 45 seconds (Elongation)
One cycle:	72°C for 1 minute (Final elongation)
One cycle	50°C for 90s (Pre-melt conditioning)
Four hundred and sixty cycles:	50°C for 2 seconds (Melting)
	Increase temperature by 0.1°C per cycle
One cycle:	4°C for ∞ minutes (Hold cycle)

Appendix G – Thermocycler protocols (continued)

16S (HRM) (Behrendt et al., 2012, Seifert et al., 2016)

One cycle:	95°C for 5 minutes (Initial denaturation)
Thirty-five cycles:	94°C for 30 seconds (Denaturation)
	50°C for 45 seconds (Annealing)
	72°C for 2 minutes (Elongation)
One cycle:	72°C for 5 minutes (Final elongation)
One cycle:	72°C for 10 minutes (Final elongation)
One cycle	50°C for 90s (Pre-melt conditioning)
Four hundred and sixty cycles:	50°C for 2 seconds (Melting)
	Increase temperature by 0.1°C per cycle
One cycle:	4°C for ∞ minutes (Hold cycle)

Appendix H - FTIR spectra (1650 cm⁻¹ to 550 cm⁻¹)

	Wave number (cm ⁻¹)	Reference
Magnetite (Fe₃O₄)	695 (Fe-O stretch), 631 (Fe-O stretch), 592-568 (Fe-O stretch)	Chaki et al. (2015), Cui et al. (2013), Ma et al. (2003), Veneranda et al. (2018)
Hematite (α-Fe₂O₃)	577-572 (Fe-O stretch)	Balasubramaniam and Kumar (2000), Balasubramaniam et al. (2003), Gotic and Music (2007)
Maghemite (γ-Fe₂O₃)	694 (Fe-O stretch), 560-555 (Fe-O stretch)	Chauhan et al. (2013), Ganachari et al. (2012), Hui and Salimi (2019)
Goethite (α-FeOOH)	1386 (Fe-O-H bend), 905-882 (Fe-O-H bend), 800-795 (Fe-O-H bend), 650-615 (Fe-O stretch)	Cui et al. (2013), Shopska et al. (2013), Veneranda et al. (2018), Xiao et al. (2017)
Akaganeite (β-FeOOH)	1401 (Fe-O-H bend), 1126 (Fe-O-H bend), 847-844 (Fe-O-H bend), 696-693 (Fe-O stretch), 648-638 (Fe-O stretch),	Fu and Quan (2006), Murad and Bishop (2000), Veneranda et al. (2018), Xiao et al. (2017)
Lepidocrocite (γ-FeOOH)	1164-1150 (Fe-O-H bend), 1023-1020 (Fe-O-H bend), 759-743 (Fe-O-H bend), 616-615 (Fe-O stretch),	Cui et al. (2013), Music et al. (2004), Veneranda et al. (2018), Xiao et al. (2017)
Feroxyhyte (δ-FeOOH)	1120 (Fe-O-H bend), 975 (Fe-O-H bend)	Jaen and Iglesias (2017), Mei et al. (2015)
Ferrihydrite (Fe₅HO₆·4H₂O)	1055 (Fe-O-H bend), 705 (Fe-O-H bend), 582-565 (Fe-O stretch)	Hausner et al. (2009), Zhu et al. (2015)
Sulfate green rust (GR(SO₄²⁻))	1551-1550 (H-O-H bend), 1185 (S-O stretch), 1150 (S-O asymmetric stretch), 1085 (S-O asymmetric stretch), 880-876 (Fe-O-H bend), 780-776 (Fe-O-H bend), 663 (Fe-O stretch), 618 (Fe-O stretch)	Peulon et al. (2003), Zegeye et al. (2007),
Carbonate green rust (GR(CO₃²⁻))	1563 (H-O-H bend), 1390 (O-C-O asymmetric stretch), 1345 (O-C-O symmetric stretch), 854 (Fe-O-H bend), 774 (Fe-O-H bend)	Peulon et al. (2003), Zegeye et al. (2007)
Chloride green rust (GR(Cl⁻))	1561 (H-O-H bend), 804 (Fe-O-H bend), 707-680 (Fe-O stretch),	Peulon et al. (2003)
Siderite (FeCO₃)	865-859 (C-O asymmetric stretch)	Gil et al. (1998), Matthiesen et al. (2003)
Iron (II) hydroxide (Fe(OH)₂)	1360 (Fe-O-H bend), 1053 (Fe-O-H bend), 980-950 (Fe-O-H bend), 875 (Fe-O-H bend), 840 (Fe-O-H bend)	Chernyshova (2003), Rémazeilles and Refait (2009), Weerasooriya et al. (2010)

Appendix H - FTIR spectra (1650 cm⁻¹ to 550 cm⁻¹) (continued)

	Wave number (cm ⁻¹)	Reference
Brucite (Mg(OH)₂)	1400 (Mg-O-H bend), 568-560 (Mg-O stretch)	Boev et al. (2009), Gokulakumar et al. (2016), Frost and Kloprogge (1999)
Sulfate ion (SO₄²⁻)	1252-1223 (O-S-O asymmetric stretch), 1190 (S-O stretch), 1085 (S-O asymmetric stretch), 1055 (S-O asymmetric stretch), 1012-993 (S-O symmetric stretch)	Boyatzis et al. (2016), Rouchon et al. (2012), Reyes-Bozo et al. (2015), Xu et al. (2013)
Sulfite ion (SO₃²⁻)	1220 (S-O stretch), 1090 (S-O stretch), 1036 (S-O asymmetric stretch), 1017 (S-O symmetric stretch), 930-916 (S-O stretch)	Borda et al. (2003), Chernyshova (2003), Pekov et al. (2012), Weerasooriya et al. (2010)
Thiosulfate ion (S₂O₃²⁻)	1140-1120 (S-O asymmetric stretch), 1000-994 (S-O symmetric stretch), 950 (S-O symmetric stretch)	Borda et al. (2003), Chernyshova (2003), Weerasooriya et al. (2010)
Calcite (CaCO₃)	1454-1433 (O-C-O asymmetric stretch), 1390 (O-C-O asymmetric stretch), 875-874 (C-O asymmetric stretch), 713-712 (Ca-C-O bend)	Jimoh et al. (2017), Reig et al. (2000), Villalobos and Leckie (2001)
Aragonite (CaCO₃)	1445-1430 (O-C-O asymmetric stretch), 1083 (C-O symmetric stretch), 854-844 (C-O stretch), 712-700 (Ca-C-O bend), 565 (Fe-O stretch)	Chakrabarty and Mahapatra (1999), Jovanovski et al. (2002)
Nahcolite (NaHCO₃)	1493 (O-C-O asymmetric stretch), 1365-1358 (C-O-H symmetric stretch), 1015 (C-O stretch)	Music et al. (2004), Villalobos and Leckie (2001)
Kaolinite (Al₂Si₂O₅(OH)₄)	1115 (Si-O stretch), 1040-1032 (Si-O stretch), 1009 (Si-O stretch), 960-910 (Al-O-H stretch), 789-748 (Si-O-Al bend), 696-690 (Mg/Al-O-H bend)	Odin et al. (2015), Tironi et al. (2012)
Illite (K,H₃O)(Al,Mg,Fe)₂(Si,Al)₄[(OH)₂,H₂O]	936-910 (Al-O-H stretch), 822-796 (Si-O-Al bend), 752 (Si-O-Al bend), 694 (Si-O-Al bend)	Odin et al. (2015), Shi et al. (2015)
Silica (SiO₂)	1090-1050 (Si-O asymmetric stretch), 797-796 (Si-O stretch), 779-775 (Si-O symmetric stretch)	Odin et al. (2015), Reig et al. (2000)
Water (H₂O)	1650-1620 (H-O-H bend)	Cui et al. (2013), Gotic and Music (2007), Shopska et al. (2013), Veneranda et al. (2018)